Seismic Design of Low-Damage Post-Tensioned Timber Wall Systems

Francesco Sarti

A thesis submitted in partial fulfilment of the requirements for the Degree
of Doctor of Philosophy in Civil Engineering
at the University of Canterbury
Christchurch, New Zealand
November 2015

Abstract

The recent Canterbury earthquake sequence in 2010-2011 highlighted a uniquely severe level of structural damage to modern buildings, while confirming the high vulnerability and life threatening of unreinforced masonry and inadequately detailed reinforced concrete buildings. Although the level of damage of most buildings met the expected life-safety and collapse prevention criteria, the structural damage to those building was beyond economic repair. The difficulty in the post-event assessment of a concrete or steel structure and the uneconomical repairing costs are the big drivers of the adoption of low damage design.

Among several low-damage technologies, post-tensioned rocking systems were developed in the 1990s with applications to precast concrete members and later extended to structural steel members. More recently the technology was extended to timber buildings (Pres-Lam system).

This doctoral dissertation focuses on the experimental investigation and analytical and numerical prediction of the lateral load response of dissipative post-tensioned rocking timber wall systems.

The first experimental stages of this research consisted of component testing on both external replaceable devices and internal bars. The component testing was aimed to further investigate the response of these devices and to provide significant design parameters.

Post-tensioned wall subassembly testing was then carried out. Firstly, quasi-static cyclic testing of two-thirds scale post-tensioned single wall specimens with several reinforcement layouts was carried out.

Then, an alternative wall configuration to limit displacement incompatibilities in the diaphragm was developed and tested. The system consisted of a Column-Wall-Column configuration, where the boundary columns can provide the support to the diaphragm with minimal uplifting and also provide dissipation through the coupling to the post-tensioned wall panel with dissipation devices.

Both single wall and column-wall-column specimens were subjected to drifts up to 2% showing excellent performance, limiting the damage to the dissipating devices. One of the objectives of the experimental program was to assess the influence of construction detailing, and the dissipater connection in particular proved to have a significant influence on the wall's response.

The experimental programs on dissipaters and wall subassemblies provided exhaustive data for the validation and refinement of current analytical and numerical models.

The current moment-rotation iterative procedure was refined accounting for detailed response parameters identified in the initial experimental stage. The refined analytical model proved capable of fitting the experimental result with good accuracy.

A further stage in this research was the validation and refinement of numerical modelling approaches, which consisted in rotational spring and multi-spring models. Both the modelling approaches were calibrated versus the experimental results on post-tensioned walls subassemblies. In particular, the multi-spring model was further refined and implemented in OpenSEES to account for the full range of behavioural aspects of the systems.

The multi-spring model was used in the final part of the dissertation to validate and refine current lateral force design procedures.

Firstly, seismic performance factors in accordance to a Force-Based Design procedure were developed in accordance to the FEMA P-695 procedure through extensive numerical analyses. This procedure aims to determine the seismic reduction factor and over-strength factor accounting for the collapse probability of the building. The outcomes of this numerical analysis were also extended to other significant design codes.

Alternatively, Displacement-Based Design can be used for the determination of the lateral load demand on a post-tensioned multi-storey timber building. The current DBD procedure was used for the development of a further numerical analysis which aimed to validate the procedure and identify the necessary refinements.

It was concluded that the analytical and numerical models developed throughout this dissertation provided comprehensive and accurate tools for the determination of the lateral load response of post-tensioned wall systems, also allowing the provision of design parameters in accordance to the current standards and lateral force design procedures.

Acknowledgments

Firstly, I would like to acknowledge my supervisors Assoc. Prof. Alessandro Palermo and Prof. Stefano Pampanin. Without their guidance, technical discussions and support this work would not have been possible. In addition I would like to thank the input of Prof. Andy Buchanan. Although not a direct part of my supervisory team, his input was invaluable.

I would also like to acknowledge Assoc. Prof. Jeffrey Berman, Dr. Mohammad Malakoutian and Dr. Jonathan Weigand for their technical support during my exchange period at the University of Washington.

The financial support of the Structural Timber Innovation Company (STIC) made this research possible.

I would like to thank Dr. David Carradine who helped me in the very first stages of my experimental research.

To the technical staff of the Civil and Natural Resources Engineering Department for their technical advice during the experimental testing of this dissertation, in particular to Mr. John Maley who provided a great help during the dissipater testing and to Mr. Mosese Fifita whose technical skills and good company made the lab work and the long testing hours much easier.

To Dr. Robert Finch and Maxim Millen, thank you for your assistance proofreading parts of this dissertation and helping me to improve my Italian English.

To my friends and colleagues (or ex colleagues) Dr. Tobias Smith, Daniel Moroder, Dr. Andrew Baird, Dr. Denis Pau, Gareth Morris, Maxim Millen (again), Harry Johnston, Chris Watson, Zeinab Chegini, Simona Giorgnini, Audsley Jones, Dr. James O'Neil, Sam MacHattie, Varun Joshi, Tom Armstrong, Andrew Dunbar, the formal Fridays, the Friday drinks, the BYOs and, of course, our technical (or not so technical) discussions were a great help throughout this PhD.

Last but not the least, I would like to thank my family for supporting me through my PhD studies from quite a distance.

Contents

Notation

A	Cross-sectional area
a_1, a_2, a_3, a_4	Menegotto-Pinto rule experimentally calibrated parameters
ACMR	Adjusted Collapse Margin Ratio
$ACMR_{10\%}$	Acceptable ACMR value at 10% collapse probability
$ACMR_{20\%}$	Acceptable ACMR value at 20% collapse probability
$A_{eff,fill}$	Fuse-type dissipater tube steel equivalent filler cross-sectional area
A_{ex}	Fuse-type dissipater external area
A_{fill}	Fuse-type dissipater filler cross-sectional area
A_{fuse}	Fuse-type dissipater fuse area
$A_{pt,i}$	Cross-section area of the i-th post-tensioning reinforcement layer
A_s	Steel bar cross-sectional area
$A_{s,i}$	Cross-section area of the i-th tension dissipative layer
$A'_{s,i}$	Cross-section area of the i-th compression dissipative layer
A_t	Timber cross-sectional area
A_{ts}	Timber shear area
A_{tube}	Fuse-type dissipater tube cross-sectional area
b	Section width
B_I	Damping coefficient
b_u	Width of the U-shape Flexural Plate section
c	Neutral axis depth
C	Elastic site hazard spectrum
c_1, c_2	Integration constants
$C_{1,T}$	Seismic coefficient accounting for mid-height higher modes moment amplification
$C_{2,T}$, $C_{3,T}$	Seismic coefficient accounting for higher modes shear amplification
C_d	Deflection amplification factor
C_h	Spectral shape factor
CMR	Collapse Margin Ratio
$C_{s,i}$	Force in the i-th compression dissipater
C_t	Timber compressive force
C_{vi}	Vertical distribution factor
d	Dowel diameter
d_b	Bar diameter
D_{conn}	Fuse-type dissipater connection diameter
$D_{eff,fill}$	Filler effective diameter
$D_{eff,fuse}$	Fuse effective diameter
D_{ex}	Fuse-type dissipater external diameter
$D_{ex,tube}$	Fuse-type dissipater tube external diameter
D_{fuse}	Fuse-type dissipater fuse diameter
D_{fuse}	Fuse diameter
D_h	Hole diameter

DI	Damage accumulation index
$D_{int,tube}$	Fuse-type dissipater tube internal diameter
D_n	Nominal diameter
D_u	Average diameter of the U-shape Flexural plate
E	Modulus of elasticity
E_{con}	Connection modulus
E_{fill}	Fuse-type dissipater filler modulus of elasticity
E_{pt}	Post-tensioning steel elastic modulus
E_s	Steel modulus of elasticity
$E_{s,t}$	Steel tangent modulus of elasticity
E_t	Timber modulus of elasticity
F	Force
F_0	Asymptotic intersection force (Menegotto-Pinto rule)
F_i	Applied force at the i-th story
F_{max}	Maximum force
F_n	Force acting at the n-th story
F_r	Reversal force (Menegotto-Pinto rule)
$f_{s,i}$	Stress in the i-th dissipater
F_{st}	Force shift of the yield asymptote (Menegotto-Pinto rule)
f_{sy}	Steel yield strength
f_{tu}	Timber crushing strength
F_u	U-shape Flexural Plate yield force
F_y	Yield force
f_y	Yield strength
G_t	Timber shear modulus
H	Inter-story height
h	Section depth
H_i	i-th inter-story height
h_i	i-th story height
h_i	Height of the i-th level
h_i	Height of the i-th storey
h_n	n-th story height
h_n	Height of the top storey
I	Second moment of area
I_c	Column second moment of area
$I_{eff,fill}$	Fuse-type dissipater tube steel equivalent filler second moment of area
I_{fuse}	Fuse-type dissipater fuse second moment of area
I_{tube}	Fuse-type dissipater tube second moment of area
k	exponent related to the structure period
k_0	U-shape Flexural Plate initial stiffness
k_1	Earthquake record scale factor
k_a	Fuse-type dissipater elastic stiffness correction factor
$k_{anti\text{-}buck.}$	Fuse-type dissipater anti-buckling system stiffness
k_b	Fuse-type dissipater post-yield stiffness correction factor
	Bending elastic drift correction factor
k_{comp}	Fuse-type dissipater composite stiffness
k_{con}	Connection flexibility
$k_{contact}$	Contact stiffness
k_{diss}	Fuse-type dissipater total elastic stiffness
k_{dyn}	Hysteretic damping correction factor based on non-linear time-history analyses
K_e	Secant stiffness
k_{el}	Displacement contribution factor due elastic deflections

k_{fuse}	Fuse-type dissipater fuse stiffness
$k_{fuse,t}$	Fuse-type dissipater fuse tangent stiffness
$k_{mspring}$	Multi-spring element total stiffness
k_{pt}	Post-tensioning spring axial stiffness
k_s	Shear elastic drift correction factor
K_{ser}	Total slip modulus
k_{wall}	Wall panel axial stiffness
k_θ	Connection rotational stiffness
k_μ	Inelastic spectrum scaling factor
k_ξ	Area based hysteretic viscous damping modification factor
L	Length
	centerline-centerline separation between coupled walls
L_{cant}	Cantilever length
L_{conn}	Fuse-type dissipater connection length
L_{ex}	Fuse-type dissipater external length
L_{fuse}	Fuse-type dissipater fuse length
l_{sp}	Strain penetration length
$l_{sp,para}$	Parallel-to-grain strain penetration length
L_{tot}	Fuse-type dissipater total length
L_{tube}	Fuse-type dissipater tube length
l'_{ub}	Dissipater unbonded length
$l_{ub,i}$	Unbonded length of the i-th post-tensioning reinforcement layer
m, ε_0	Low-cycle fatigue material parameter
M_0	Yield load moment
M_0, M_1	Multi-linear elastic calibration moments
$M_{0.5Hn,NLTHA}$	Moment at mid-height resulting from non-linear time-history analyses
M_b	Base moment
$M_{b,NLTHA}$	Base moment resulting from non-linear time-history analyses
M_c	Boundary column moment
M_{con}	Connection moment
M_{dec}	Connection moment
m_e	Effective mass
m_i	Mass of the i-th significant mass location
$M_{mspring}$	Multi-spring element moment
M_p	Plastic moment
M_{pt}	Post-tensioning moment contribution
M_{sy}	Dissipative yielding moment
M_{tot}	Total Moment
M_{w1}, M_{w2},	
M_{w3}	Base moment demand
N	Axial force
n	Total number of stories, total number of dowels
N(T,D)	Near-fault factor
N_f	Number of cycles to failure
NM_i	Normalization factor for th i-th record
$NTH_{1,i}$	Normalized i-th record, horizontal component 1
$NTH_{2,i}$	Normalized i-th record, horizontal component 2
OTM	Overturning moment
$PGV_{PEER,i}$	Peak ground velocity of the i-th record
Q	Riveted connection capacity
r	Post-yielding stiffness factor
R	Ramberg-Osgood factor
	Return period factor

	Response modification factor
R, R_0	Elastic-plastic transition curvature parameter (Menegotto-Pinto rule)
R_ξ	Reduction factor given as a function of the equivalent viscous damping of the structure
s	Relative slip
s_1	Slip at maximum bond stress
$SA_{component}$	Component spectrum
SA_{target}	Target spectrum
S_{CT}	Median collapse spectral acceleration
S_d	Spectral displacement
S_{MT}	Maximum Credible Event spectral acceleration
S_p	Structural performance factor
SSF	Spectral Shape Factor
T	Period
T^*_{pt0}	Multi-spring model preload force
T_e	Secant period
$TH_{1,i}$	i-th record, horizontal component 1
$TH_{2,i}$	i-th record, horizontal component 2
T_i	Elastic fundamental period of the structure
T_{min}, T_{max}	Period range of interest for record scaling purposes
$T_{pt,i}$	Post-tensioning force of the i-th post-tensioning bar
$T_{pt,i}$	Force in the i-th post-tensioning reinforcement layer
T_{pt0}	Initial post-tensioning force
$T_{pt0,i}$	Initial post-tensioning force of the i-th bar
$T_{s,i}$	Force in the i-th tension dissipater
t_u	Thickness of the U-shape Flexural Plate section
V	Seismic base shear
V_b	Base shear
V_{max}	Maximum base shear capacity
V^o_{Base}	Over-strength design base shear
V^o_n	Over-strength top shear
V_p	Demand of a coupling element
w	Transverse displacement
W_i	Storey weight
x	Abscissa
$y_{pt,i}$	Edge distance of the i-th post-tensioning reinforcement layer
$y_{s,i}$	Edge distance of the i-th tension dissipative layer
$y'_{s,i}$	Edge distance of the i-th compression dissipative layer
Z	Hazard factor
Z_t	Timber section modulus
α	Post-yielding slip factor
α_{con}	Connection stiffness-to-dissipater stiffness ratio
β, λ	Re-centering ratio
β_{DR}	Design requirements uncertainty
β_{MDL}	Modelling uncertainty
β_{RTR}	Record-to-record uncertainty
β_{TD}	Test data uncertainty
β_{TOT}	Total system uncertainty
γ_p	Post-tensioning steel stress-to-strength ratio
γ_t	Timber stress-to-strength ratio
Δ	Displacement
δ	Riveted connection elastic displacement
Δ_0	Asymptotic intersection displacement (Menegotto-Pinto rule)

Δ_1, Δ_n	Elongation of the multi-spring edge elements
δ_b	Elastic bending deflection contribution
Δ_c	Displacement at the critical storey
δ_c	Inelastic mode shape at the critical storey
$\Delta_{cant,i}$	Displacement of a vertical cantilever
Δ_d	Design displacement
δ_{gap}	Wall displacement due to gap opening
$\Delta_{gap,i}$	Displacement given by the gap opening
Δ_i	Displacement of the i-th significant mass location
δ_i	Inelastic mode shape at the i-th storey
$\delta_{initial}$	Multi-spring model initial shortening
Δ_m	Maximum displacement achieved in the stabilized force-displacement loops
Δ_{max}	Maximum displacement
$\Delta_{pt,i}$	Elongation of the i-th post-tensioning reinforcement layer
Δ_r	Reversal displacement (Menegotto-Pinto rule)
Δ_s	Steel reinforcement displacement
δ_s	Elastic shear deflection contribution
$\Delta_{s,i}$	Displacement due to gap opening of the i-th tension dissipative layer
$\Delta'_{s,i}$	Displacement due to gap opening of the i-th compressive dissipative layer
Δ_{sp}	Additional slip due to tensile strain penetration
$\Delta_{sp,i}$	Displacement due to strain penetration of the i-th compressive dissipative layer
δ_{tot}	Wall total displacement
$\Delta T_{pt,i}$	Change in post-tensioning force of the i-th bar
δ_u	Ultimate roof drift displacement
Δ_y	Yield displacement
$\delta_{y,eff}$	Effective yield roof drift displacement
$\Delta\varepsilon_{pt,i}$	Change in strain of the i-th post-tensioning bar
ε_e	Elastic strain
ε_i	Dissipater strain amplitude
ε_{max}	Maximum strain of U-shape flexural plates
ε_{onset}	Fuse-type dissipater onset average strain
ε_p	Plastic strain
ε_s	Steel strain
ε_s	Dissipater strain
$\varepsilon_{s,i}$	Strain in the i-th dissipater
ε_{sy}	Steel yield strain
ε_t	Timber strain
ε_t	Timber strain
ε_{t0}	Timber strain at maximum strength
ε_{trig}	Fuse-type dissipater interaction onset average strain
ε_{tu}	Timber strain at maximum strength
θ	Rotation
θ_0, θ_1	Multi-linear elastic calibration rotations
θ_y	Yielding rotation
θ_d	Design drift
θ_{imp}	Imposed connection rotation
θ_w	Total elastic drift contribution
λ_{eff}	Fuse-type dissipater composite slenderness ratio
λ_{fuse}	Fuse slenderness ratio
μ	Ductility
μ_T	Period-based ductility
ξ	Difference between asymptotic intersection and reversal displacement

	(Menegotto-Pinto rule)
ξ, EVD	Equivalent Viscous Damping
ξ_{el}	Elastic damping
ξ_{el}	Elastic damping
ξ_{hyst}	Hysteretic viscous damping
ξ_{hyst}	Hysteretic damping
ρ	Timber mean density
Σ_0	Steel bar circumference
σ_s	Steel bar stress
σ_t	Timber stress
τ	Bond stress
τ_{max}	Maximum bond stress
ϕ_{dec}	Decompression curvature
ϕ^o	Over-strength factor
Ω	Over-strength factor
Ω_0	System over-strength factor
ω_V	Dynamic amplification factor

Part 1:

Background knowledge

1 Introduction

The recent Canterbury earthquake sequence in 2010-2011 highlighted a uniquely severe level of structural damage to modern buildings, while confirming the high vulnerability and life threatening nature of unreinforced masonry and inadequately detailed reinforced concrete buildings. After the 22nd February earthquake, the most serious event in terms of damage to the buildings and the resultant loss of life, more than 45% of buildings in Christchurch Central Business District were classified as unsafe or restricted use (red- or yellow-tag respectively) (Figure 1-1). As a result, a total number of approximately 1300-1400 buildings were demolished (Kam *et al.*, 2010).

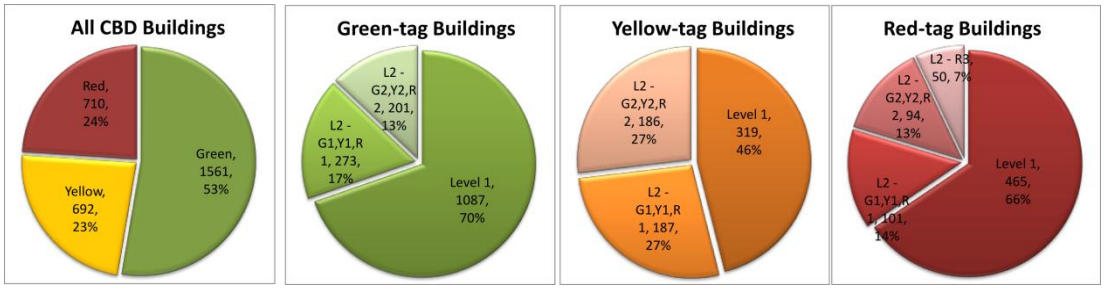

Figure 1-1. Distribution of building tagging statistics in Christchurch CBD after 22nd February Earthquake (Kam et al., 2010)

Traditional reinforced concrete and structural steel buildings rely on the plastic deformation of the structural elements (frames or walls) to limit the earthquake-induced actions on the structure. During the February 2011 event, although the level of damage met the expected life-safety and collapse prevention criteria in all but a couple of isolated cases, the structural damage to those building was beyond economic repair (Figure 1-2).

The difficulty with the post-event assessment of a concrete or steel structure and the associated uneconomical repairing costs are big drivers of the adoption of low damage design technology.

As recommended by the Canterbury Earthquakes Royal Commission Final Report new technologies should be used to improve the seismic performance of new buildings, in particular reducing the structural (and non-structural) damage, thus allowing for limited

repairing cost and time and minimizing the downtime (The Canterbury Earthquakes Royal Commission, 2012). A number of different technologies can be considered, including base isolation, energy dissipation or supplemental damping devices, as well as PRESSS-technology with possible application to concrete (Priestley *et al.*, 1999), steel (Christopoulos *et al.*, 2002) and timber (Palermo *et al.*, 2006) buildings.

Figure 1-2. Shear walls damage during February earthquake (Kam et al., 2010).

1.1 Research Motivations

Innovative post-tensioned seismic damage-resistant solutions were first investigated in the 1990s as a main outcome of the PREcast Seismic Structural Systems (PRESSS) program, coordinated by the University of California, San Diego (Priestley, 1991; Priestley, 1996; Nakaki *et al.*, 1999).

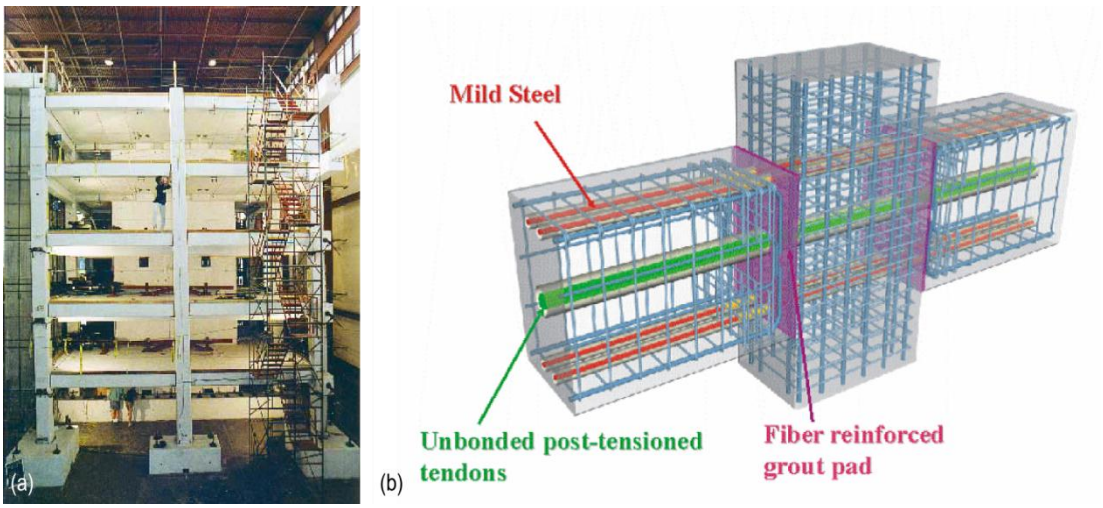

Figure 1-3. (a) PRESSS five-story building (Priestley et al., 1999) and (b) hybrid beam-column joint (c/o Ms. S. Nakaki).

Among different technologies developed in the PRESSS program, the hybrid rocking system (Figure 1-3b) proved to be a promising and efficient solution and capable of concentrating damage at the interface between either beam-to-column or wall-to-foundation interface.

In recent years the PRESSS-technology has been extended to timber (engineered wood) structural systems (Palermo *et al.*, 2005). This extension expanded to new structural systems, referred to as Pres-Lam (i.e. Pre-stressed Laminated) systems, which consists of large timber structural frames or walls made of engineered wood products such as LVL, glulam, Cross-Lam (CLT) etc., are capable of resisting seismic actions with minimal damage to timber element.

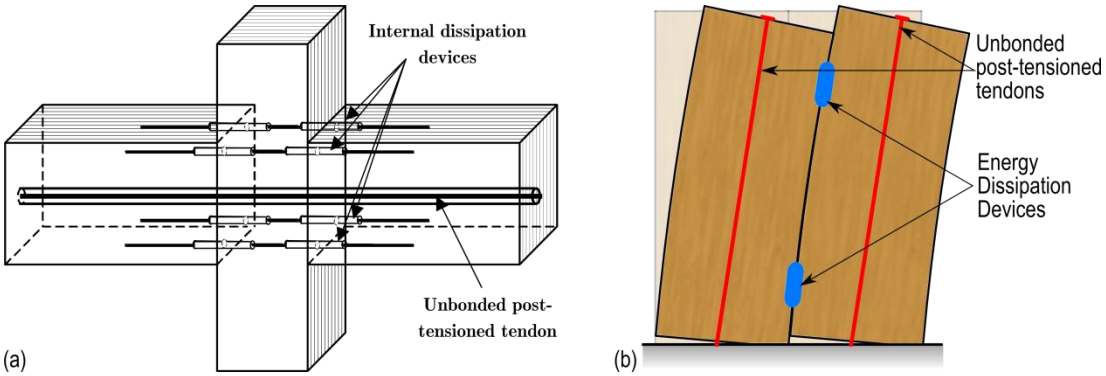

Figure 1-4. Pres-Lam systems for (a) frames (modified from Palermo et al. (2005)) and (b) walls

Following extensive research programmes at the University of Canterbury (Palermo *et al.*, 2006; Iqbal *et al.*, 2007; Smith *et al.*, 2007; Newcombe *et al.*, 2008; Newcombe *et al.*, 2010), a few Pres-lam multi-storey commercial timber buildings have been recently designed and constructed. The world's first commercial building which adopted this technology was the NMIT (Nelson Marlborough Institute of Technology) building (Figure 1-5a), constructed in Nelson, New Zealand (Devereux *et al.*, 2011). Post-tensioned coupled walls resist horizontal loads in each direction. Steel U-shaped Flexural Plates (Kelly *et al.*, 1972) link the pairs of structural walls together and provide dissipative capacity to the system (Buchanan *et al.*, 2011).

The Carterton Events Centre (Figure 1-5b), located 100km north of Wellington, is the second building in the world to adopt the Pres-Lam concept. Single post-tensioned rocking walls were designed as the lateral load resisting system (Dekker *et al.*, 2012). Post-tensioned bars provide re-centering and dissipation is given by internally epoxied mild steel rods.

Figure 1-5. (a) NMIT building (b) Carterton Event Centre

Whilst Pres-Lam buildings have been currently designed and constructed, mostly only small scale testing has been carried out, and it is crucial for researchers to further investigate and validate the system performance, and therefore accounting for design parameters related to its construction details. This can be achieved by a further research phase aimed at experimentally investigating the system behaviour of large-scale post-tensioned timber walls with realistic and practical construction detailing. Moreover, as highlighted by the Canterbury earthquake events, displacement incompatibilities can be a severe issue, undermining the structural integrity of the diaphragm system and thus of the whole building. Several solutions have been developed for concrete structures and can be extended to timber, but further development and validation of the concept must be undertaken.

Whilst experimental research is an essential step to fully understand and validate the behaviour of any new structural system, the implementation of the new system requires practical and simple design guidelines. The experimental research outcomes provide a solid support for numerical investigations aimed at developing practical design procedure to be subsequently included in current design standards.

1.2 Scope and Objectives

The scope of this research is the investigation and prediction of the lateral load response of dissipative post-tensioned rocking timber (Laminated Veneer Lumber) walls. The research focuses on the behaviour of single Laminated Veneer Lumber (LVL) post-tensioned wall systems with several reinforcement layouts. Within the scope of this dissertation, an alternative system for diaphragm interaction mitigation is developed and its behaviour investigated. The system consists of a post-tensioned single wall coupled with end columns which provide the support for the diaphragm avoiding its uplifting.

Whilst some research work developed and presented in the dissertation is applicable to lateral load design in general, this research is focussed on the behaviour of the system subjected to earthquake loading.

The main objective of this research is to refine the understanding of the response of post-tensioned timber wall systems, from the detailed behaviour of their components to the connection response. This aims to provide practical design guidelines in accordance with current seismic design procedures and standards.

The objectives can be broken down into three main research areas: dissipation devices, wall connection performance and wall system performance. For each of these areas, the research objectives are listed below.

Dissipation devices

1. Determine the main failure mechanisms governing the response of external tension-compression yield fuse-type dissipaters
2. Develop and calibrate a numerical model capable of simulating the key behavioral aspects of the dissipaters in order to determine significant design procedures and parameters
3. Develop and validate simplified analytical models to predict the external dissipaters' response
4. Experimentally determine the response of internal bars in terms of tensile strain penetration effects
5. Determine a simplified formulation for the strain penetration length to be used in design

Wall connection performance

6. Experimentally determine the lateral load response of large-scale single post-tensioned timber walls with several reinforcement configurations
7. Assess the influence on the structural response of construction details such as the dissipaters' connection to the structural element
8. Develop an alternative solution to minimize the vertical interaction with the diaphragm system and investigate its behavior

9. Refine the current analytical models incorporating design parameters developed and validated in previous stages and validate its capabilities to predict the wall response

10. Validate and refine current numerical modelling approaches for the prediction of the seismic response of post-tensioned wall systems as well as simulating the full range of behavioral aspects

Wall system performance

11. Determine the collapse probability of multi-storey buildings adopting post-tensioned rocking timber wall systems

12. Propose Force-Based Design parameters such as seismic reduction factors, over-strength factors and deflection amplification factors in accordance with current seismic design codes

13. Validate and refine significant Displacement-Based Design parameters and equations of post-tensioned timber wall systems with particular focus on displacement profile, equivalent viscous damping reduction and higher modes amplification factors

1.3 Dissertation outline

Chapter 2 presents the research background for the study of dissipative post-tensioned timber walls. An overview of the development of the dissipative post-tensioned rocking system is presented, from its early concepts introduced for precast concrete structures to the latest applications to timber buildings. An overview of the most common dissipating devices used in post-tensioned rocking structures will also be presented.

Chapter 3 shows the experimental programme on fuse-type buckling-restrained dissipaters. The dissipater is a tension-compression yield device to be used at the rocking base of the wall. A comprehensive testing is presented and the experimental results are used to calibrate both analytical and numerical models. The latter are used in the final part of the chapter to calibrate significant design parameters.

Chapter 4 shows the experimental work performed on internal tension-compression yield dissipaters. The experimental program aims to calibrate design parameters accounting for parallel-to-the-grain strain penetration effects of glued-in bars in timber.

Chapter 5 describes the construction detailing and experimental testing of a two-thirds scale post-tensioned Laminated Veneer Lumber wall. Several reinforcement layouts are

considered in the experimental program and the results are also discussed with reference to the influence of the different layouts to the global response.

In **Chapter 6** an alternative wall configuration aimed at reducing diaphragm interaction (in particular vertical displacement incompatibility), referred to as CWC (Column-Wall-Column) system is developed and tested. The system consists of a single wall configuration coupled with boundary columns which provide the support for the diaphragm as well as the dissipater connections. The experimental results are discussed and compared with the more "traditional" single wall system presented in Chapter 5.

Chapter 7 summarizes the current analytical model for post-tensioned rocking walls and proposes some refinements based on findings from this research. A simplified analytical approach for the CWC system is also shown and discussed in the last part of the chapter.

Chapter 8 provides the overview of current modelling approaches and the validation of such models against experimental results on post-tensioned walls connection. Among the available modelling approaches, the multi-spring model (Spieth *et al.*, 2004) is further developed for use in OpenSEES (McKenna, 2011) and refined to simulate the full range of behavioural aspects of the system.

Chapter 9 shows the determination of the seismic performance factors of dissipative post-tensioned rocking wall systems in accordance with the FEMA P695 (ATC, 2009) procedure and to be used in the design in accordance with ASCE/SEI 7-10 (2010). The numerical results are also extended to other significant standards such as NZS 1170.5 (2004) and EN 1998-1 (2004).

In **Chapter 10** a set of case study buildings are designed in accordance with current Displacement-Based Design procedures for post-tensioned timber walls. Non-linear time-history analyses are carried out to validate the current design assumptions and propose refined design parameters.

Chapter 11 provides a final summary and recommendations for the seismic design of dissipative post-tensioned rocking wall systems with reference to significant results shown in the previous chapters.

Chapter 12 presents the main conclusions drawn from the research and provides future research recommendations.

1.4 References

American Society of Civil Engineers and S. E. Institute. 2010. *Minimum design loads for buildings and other structures*. American Society of Civil Engineers and S. E. Institute. Reston, (VA), American Society of Civil Engineers, Structural Engineering Institute.

Applied Technology Council for the Federal Emergency Management Agency (ATC). 2009. *Quantification of building seismic performance factors*. Applied Technology Council for the Federal Emergency Management Agency (ATC). Washington, D.C.], Washington, D.C. : U.S. Dept. of Homeland Security, FEMA.

Buchanan, A.H., Bull, D., Dhakal, R., MacRae, G., Palermo, A., Pampanin, S. 2011. *Base Isolation and Damage-Resistant Technologies for Improved Seismic Performance of Buildings*. Technical report University of Canterbury. Christchruch, New Zealand.

Christopoulos, C., Filiatrault, A., Uang, C.M., Folz, B. 2002. Post-tensioned Energy Dissipating Connections for Moment Resisting Steel Frames. *ASCE Journal of Structural Engineering* 128(9): 1111-1120.

Dekker, D., Chung, S., Palermo, A. 2012. Carterton Events Centre Auditorium Pres-Lam Wall Design and Construction. *New Zeland Society of Earthquake Engineering Annual Conference*, Christchurch.

Devereux, C.P., Holden, T.J., Buchanan, A.H., Pampanin, S. 2011. NMIT Arts & Media Building - Damage Mitigation Using Post-Tensioned Timber Walls. *9th Pacific Conference on Earthquake Engineering*, Auckland, New Zealand.

Eurocode 8 - Design of structures for earthquake resistance - Part 1: General rules, seismic actions and rules for buildings. European Committee for Standardization. 2004. Brussels, Belgium, European Committee for Standardization.

Iqbal, A., Pampanin, S., Buchanan, A.H., Palermo, A. 2007. Improved Seismic Performance of LVL Post-tensioned Walls Coupled with UFP devices. *8th Pacific Conference on Earthquake Engineering*, Singapore.

Kam, W.Y., Pampanin, S., Elwood, K. 2010. Seismic Performance Of Reinforced Concrete Buildings In The 22 February Christchurch (Lyttelton) Earthquake. *Bulletin of the New Zeland National Society for Eartquake Engineering* 44(4): 279-296.

Kelly, J.M., Skinner, R.I., Heine, A.J. 1972. Mechanisms of Energy Absorbtion in Special Devices for use in Earthquake Resistant Structures. *Bulletin of the New Zealand Society for Eathquake Engineering* 5(3): 63-88.

McKenna, F. 2011. OpenSees: A Framework for Earthquake Engineering Simulation. *Computing in Science and Engg.* 13(4): 58-66.

Nakaki, S.D., Stanton, J.F., Sritharan, S. 1999. An overview of the PRESSS five-story precast test building. *PCI journal* 44(2): 26-26.

Newcombe, M.P., Pampanin, S., A.Buchanan, Palermo, A. 2008. Section Analysis and Cyclic Behavior of Post-Tensioned Jointed Ductile Connections for Multi-Story Timber Buildings. *Journal of Earthquake Engineering* 12(1): 83–110.

Newcombe, M.P., Pampanin, S., Buchanan, A.H. 2010. Global Response of a Two Storey Pres-Lam Timber Building. *2010 New Zealand Society for Earthquake Engineering Conference*, Wellington, New Zealand.

Palermo, A., Pampanin, S., Buchanan, A., Newcombe, M. 2006. Seismic Design of Multi-Storey Buildings using Laminated Veneer Lumber (LVL). *NZ Society of Earthquake Engineering, Annual National Conference*, Wairakei, New Zealand, University of Canterbury. Civil Engineering.

Palermo, A., Pampanin, S., Buchanan, A.H., Newcombe, M.P. 2005. Seismic design of multi-storey buildings using laminated veneer lumber (LVL). *New Zealand Society of Earthquake Engineering, Annual Conference*, Wairakei, New Zealand, University of Canterbury. Civil Engineering.

Priestley, M.J.N. 1991. Overview of PRESSS research program. *PCI Journal* 36(4): 50-57.

Priestley, M.J.N. 1996. The PRESSS program - Current Status and Proposed Plans for Phase III. *PCI Journal* 41(2): 22-40.

Priestley, M.J.N., Sritharan, S., Conley, J.R., Pampanin, S. 1999. Preliminary Results and Conclusions from the PRESSS Five-Story Precast Concrete Test Building. *PCI Journal* 44.

Smith, T., Ludwig, F., Pampanin, S., Fragiacomo, M., Buchanan, A., Deam, B., Palermo, A. 2007. Seismic Response of Hybrid-LVL Coupled Walls Under Quasi-Static and Pseudo-Dynamic Testing. *2007 New Zealand Society for Earthquake Engineering Conference*, Palmerston North, New Zealand.

Spieth, H.A., Carr, A.J., Pampanin, S., Murahidy, A.G., Mander, J.B. 2004. *Modelling of Precast Prestressed Concrete Frame Structures with Rocking Beam-Column Connections.* Technical report Report 2004-01. Christchurch, New Zealand, University of Canterbury.

NZS 1170.5: Structural Design Actions - Part 5: Earthquake actions. Standards New Zealand. 2004.

The Canterbury Earthquakes Royal Commission. 2012. *Final Report*. Technical report. Christchurch, New Zealand**:** 64.

2 Literature review

2.1 Introduction

The objective of this chapter is to provide a comprehensive overview of past research on post-tensioned rocking systems. This was achieved through a thorough literature review of the relevant research work published in literature.

The relevant literature briefly summarized in the chapter is structured as follows:

- *The post-tensioned technology origins and recent developments* gives an overview of the early and most recent research developments on the post-tensioned rocking system applied to precast concrete structures
- *The post-tensioned rocking system mechanics* shows a detailed description of the system behaviour addressing the significant parameters influencing the system response
- *The Pres-Lam system* provides a comprehensive overview of the experimental research on post-tensioned rocking timber systems.
- *Supplemental damping devices* briefly reports the past research on a number damping devices used in post-tensioned rocking structures.
- *Pres-Lam built examples* describes the built applications of the Pres-Lam system.

2.2 Post-tensioning technology origins and recent developments

The modern development of prestressed concrete is attributed to Eugene Freyssinet who started using high strength steel wires for post-tensioning concrete beams in 1928. By 1939, he had designed the Freyssinet system with conical wedges for anchoring wires at the ends of prestressed members as well as special jacks for use in stressing and anchoring the wires.

Post-tensioning technologies were widely used over those first 50 years, demonstrating the advantages derived from post-tensioned concrete; nevertheless, the use and development of precast concrete structures in seismic areas has been limited, until the late 1990s, by the absence of rational and flexible seismic design code provisions in major model building codes (New Zealand Concrete Society, 2010).

In the late 1990s a revolutionary alternative technological solution capable of achieving high seismic performance at low-cost has been introduced as the main outcome of the U.S. PRESSS program (New Zealand Concrete Society, 2010).

The research program was in progress for ten years, and since the very beginning all of the research teams involved in the program have focused on two primary objectives:

- The development of comprehensive and rational design recommendations needed for a broader acceptance of precast concrete construction in different seismic zones and,
- The development of new materials, concepts, and technologies for precast concrete construction in different seismic zones (Nakaki *et al.*, 1999).

The third phase of the program consisted of the seismic design and analysis of a five-story precast/prestressed concrete building (see Figure 2-1) using dry jointed construction.

Among different technologies developed and tested, the hybrid technology proved to be the most stable and promising. The hybrid connection comprises of a combination of re-centering and dissipation, which are provided by post-tensioning and mild steel reinforcement respectively. The combination of those contributions generates a flag-shaped hysteresis loop, which ensures the residual displacements are minimized. In addition, the use of mild steel reinforcement provides the system with significant dissipation, concentrating the damage at the connection interface.

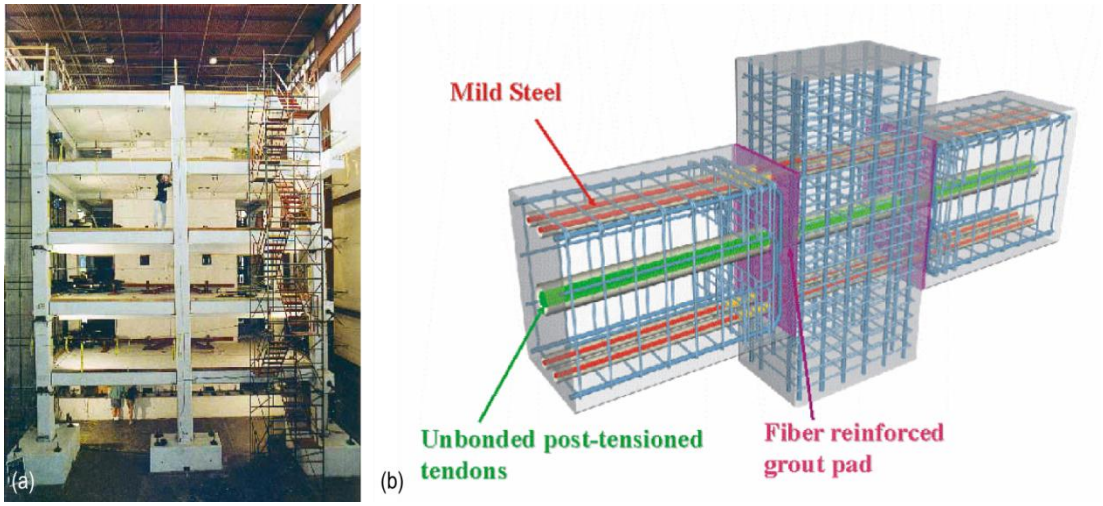

Figure 2-1. (a) PRESSS five-story building (Priestley et al., 1999) and (b) hybrid beam-column joint (c/o Ms. S. Nakaki).

2.3 The post-tensioned rocking system concept and mechanism

The basic concept of a post-tensioned rocking system is to activate a "controlled rocking" motion between two structural members (beam-column or wall-foundation). This is generally achieved by subjecting the element to a compressive load.

The post-tensioning load enables a moment-resisting connection at the element end while allowing separation to occur between either the beam-column or the wall-foundation interface.

Separation between the elements occurs as the connection moment increases beyond the decompression value, M_{dec}, given by Equation (2-1).

In general, the axial load is imposed using post-tensioned high-strength steel bars while some contribution can also derive from the gravity loads. From this the load P in Equation (2-1) can be given by the sum of the initial post-tensioning force, T_{pt0}, and the gravity load, N.

$$\frac{P}{A}+\frac{M}{Z}=0\rightarrow M_{dec}=P\frac{Z}{A}=\left(T_{pt}+N\right)\frac{Z}{A} \qquad (2\text{-}1)$$

Where P = the total axial load acting on the section
M = the connection moment
Z = the section modulus
A = the cross-section area

As shown in Equation (2-1) this happens when virtual tension stresses develop in the section.

Before the decompression occurs the deformation of the element is purely elastic and it results from the bending and shear deformation of the wall panel. This is highlighted by the linear elastic behaviour observed in the force-displacement response (Figure 2-2b).

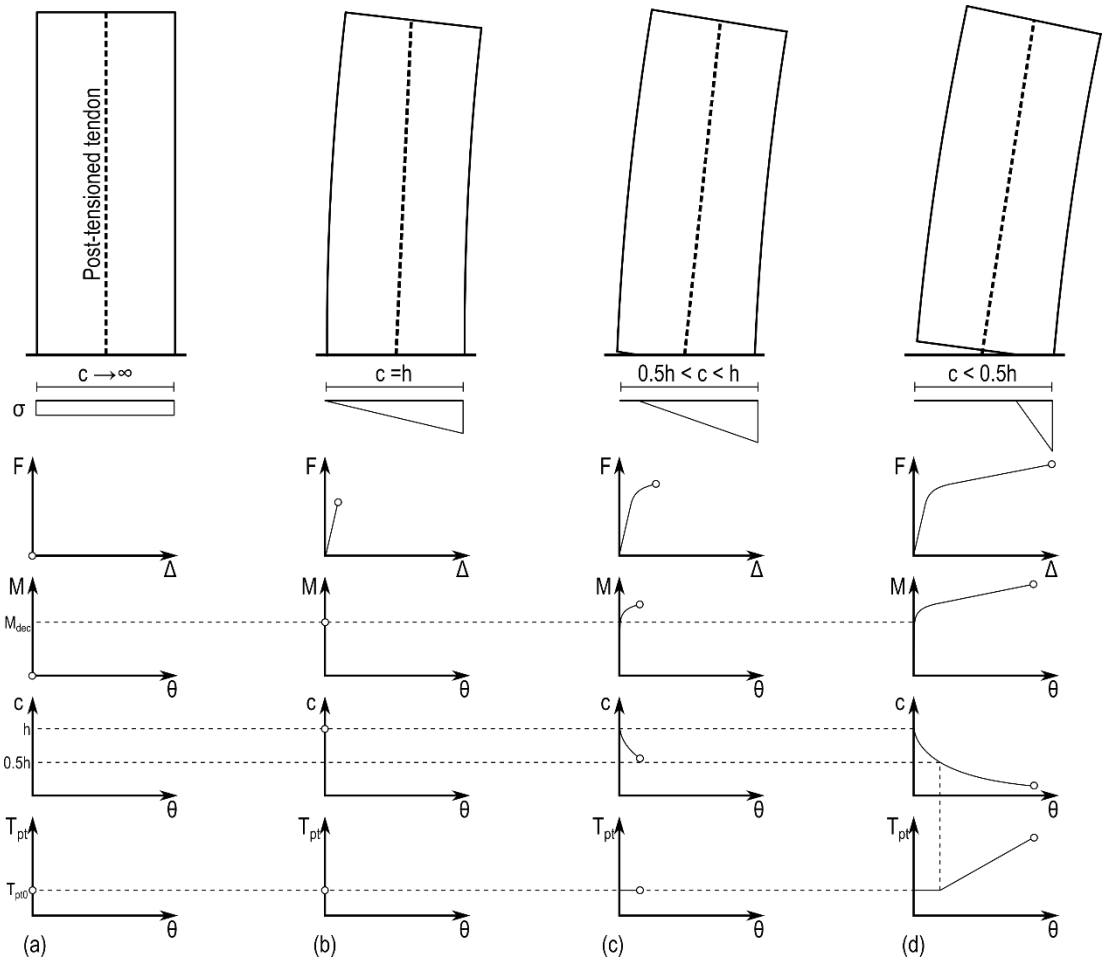

Figure 2-2. Post-tensioned rocking mechanism. (a) Initial state; (b) Decompression; (c) non-linearity; (d) tendon elongation.

After the gap has opened (i.e. non-zero connection rotation), the compression zone depth, referred to as neutral axis depth, varies with a negative decreasing slope as shown in Figure 2-2c. With reference to either the force-displacement or the moment-rotation response, this results in a non-linear trend for low connection rotation values.

For small connection rotation values the neutral axis depth is bigger than the section's half-depth and no post-tensioning force increase is observed. As soon as the neutral axis depth reaches that value the post-tensioning force increases resulting in a linear behaviour as shown in Figure 2-2d (T_{pt}-θ chart).

The increase in post-tensioning force as well as the decreasing neutral axis depth contributes to determine the post-decompression stiffness of the connection as shown in Figure 2-2d (M-θ chart).

When pure post-tensioned rocking sections are used, typical multi-linear elastic hysteresis is observed and no hysteretic damping is provided by the system.

When a dissipative post-tensioned rocking system is used, damping devices are connected to the element and provide the hysteretic dissipation. The system's mechanics in Figure 2-3 show similarities to the pure post-tensioned rocking connection.

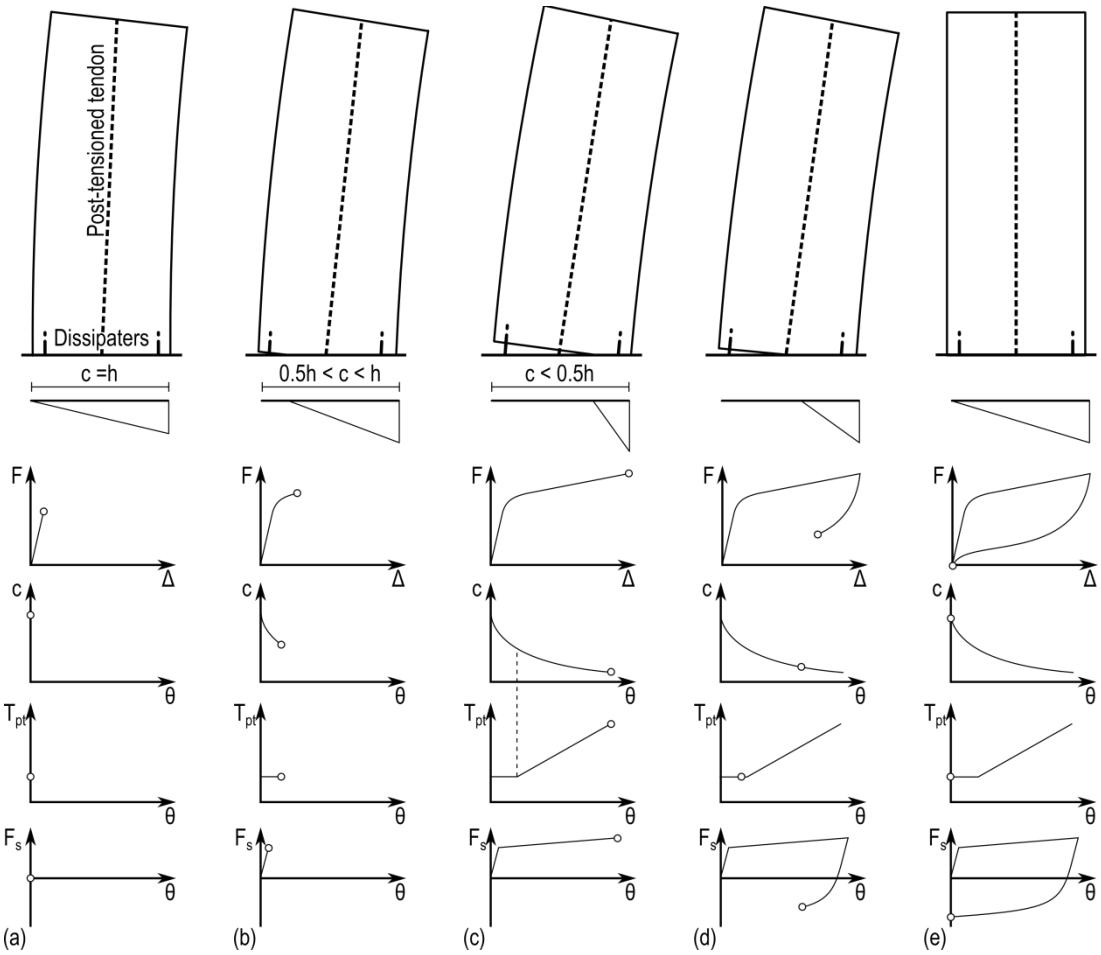

Figure 2-3. Dissipative post-tensioned rocking mechanism. (a) Decompression; (b) tensile yielding; (c) tendon elongation; (d) compressive yielding; (e) re-centering.

At the decompression point (Figure 2-3a) no connection rotation develops, consequently, the dissipaters are not activated. As soon as the gap opens and the dissipater's yielding displacement is developed, the dissipater yields in tension (Figure 2-3b).

For increasing connection rotations the tendons elongate and the dissipaters further extend developing ductility and hysteretic damping. On the reversing cycle the dissipater yield in compression (Figure 2-3d) and the system re-centers revealing the typical flag-shaped hysteresis.

The neutral axis depth trend is similar to the post-tensioned only solution and it is not generally strongly influenced by the use of dissipation devices. In fact those devices usually develop similar forces once yielded, having a negligible influence on the force balance which governs the neutral axis depth value.

As shown above, the typical force-displacement loop of a dissipative post-tensioned rocking connection is a flag-shaped hysteresis which is given by a combination of a multi-linear elastic and bi-linear hysteresis rules as shown in Figure 2-4a.

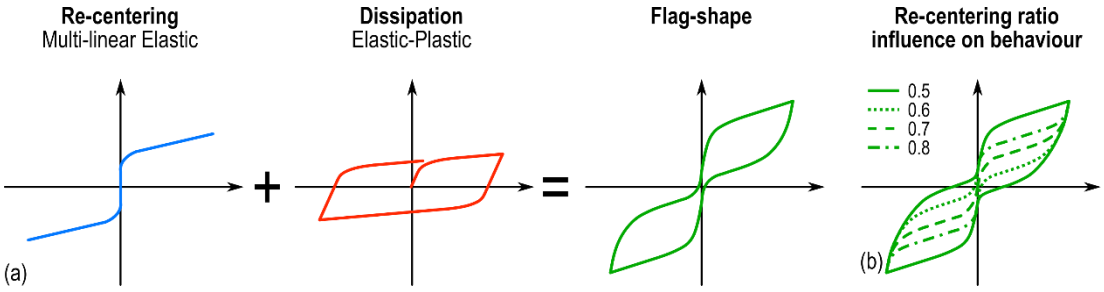

Figure 2-4. (a) Flag-shaped hysteresis; (b) influence of the re-centering ratio on the behaviour.

The hysteresis' shape is governed by the re-centering ratio, β or λ, as defined by Equation (2-2).

$$\beta = \frac{M_{pt}}{M_{tot}};\ \lambda = \frac{M_{pt}}{M_s} \qquad (2\text{-}2)$$

Where M_{pt} = the post-tensioning moment contribution

M_s = the dissipative moment contribution

M_{tot} = the total moment distribution

Figure 2-4b qualitatively shows the influence of this parameter on the hysteric behaviour of the connection. For a unit value of β, the connection behaves following a multi-linear elastic (post-tensioned only) relationship, with no dissipation; instead, for $\beta = 0$ $(\lambda = 0)$ the connection is a mild steel only option with very high hysteretic damping and significant residual displacement. A minimum value of β = 0.55 (λ = 1.15) is suggested, ensuring acceptable levels of dissipation and negligible residual displacements (Standards New Zealand, 2006).

2.4 The Pres-Lam system

Extensive research on the PRESSS system was carried out by a number of researchers further developing the precast post-tensioned rocking system (Kurama *et al.*, 1999; Kurama *et al.*, 2004; Marriott, 2009; Amaris Mesa, 2010): moreover, the system was extended to different structural materials such as structural steel (Christopoulos *et al.*, 2002) and timber (Palermo *et al.*, 2005a) demonstrating it to be material independent.

The extension of the post-tensioned rocking hybrid connection to timber, with particular emphasis on Laminated Veneer Lumber (LVL), brought new solutions for multi-storey frame or shear wall systems. The system was reffered to as the Pres-Lam (Prestressed Laminated Timber) system (Figure 2-5).

An extensive research program was carried out to investigate the seismic performance of innovative LVL connections relying on the extension of the concepts from reinforced concrete precast hybrid systems.

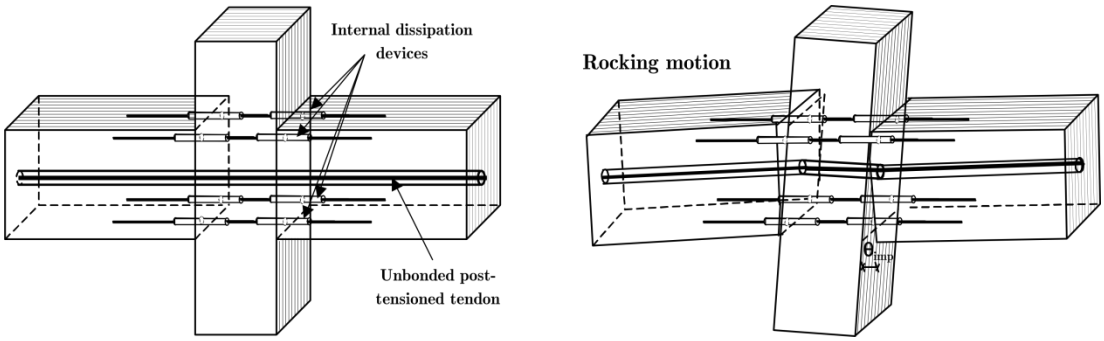

Figure 2-5. Application of Hybrid Concept to LVL frame systems (modified from Palermo et al. (2005a)).

The experimental results showed the advantages of using timber for hybrid connections. The lack of damage in the structural elements, combined with appropriate energy dissipation capacity provided by the dissipaters and self-centering provided by the unbonded post-tensioned tendons guaranteed improved seismic performance when compared with the traditional solutions for timber construction (Palermo *et al.*, 2005a).

2.4.1 Experimental research on post-tensioned timber frames

As part of the first experimental testing program on the Pres-Lam system, Palermo et al. (2005a) tested a post-tensioned rocking beam-column joint with different reinforcement configurations. Firstly, a post-tensioned only solution was tested showing a non-linear elastic behaviour with an "equivalent yielding", which is due to geometrical non-linearity, not

related to material non-linearity. The geometrical non-linearity results from a reduction of section stiffness due to a sudden relocation of the neutral axis position (2005a).

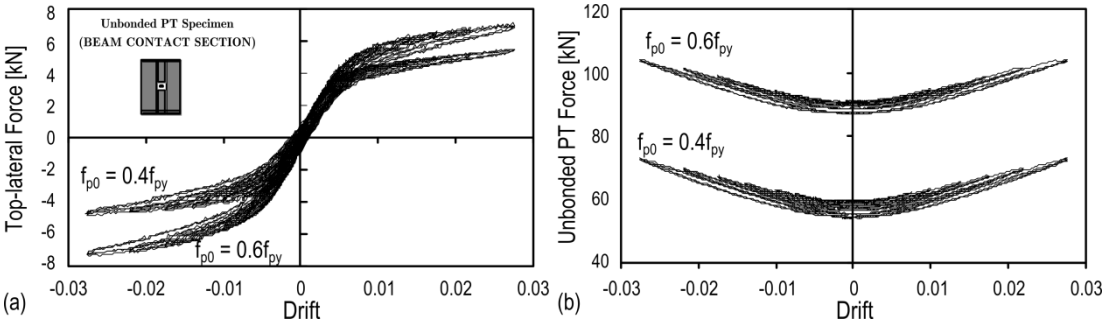

Figure 2-6. Unbonded post-tensioned solution: (a) lateral force-drift;(b) post-tensioning force vs. drift (modified after Palermo et al. (Palermo et al., 2005a))

The hybrid solution was also tested and consisted of the same beam-column joint configuration with additional internal bars as dissipation devices. The experimental results showed a very stable flag-shape hysteresis (see Figure 2-7a).

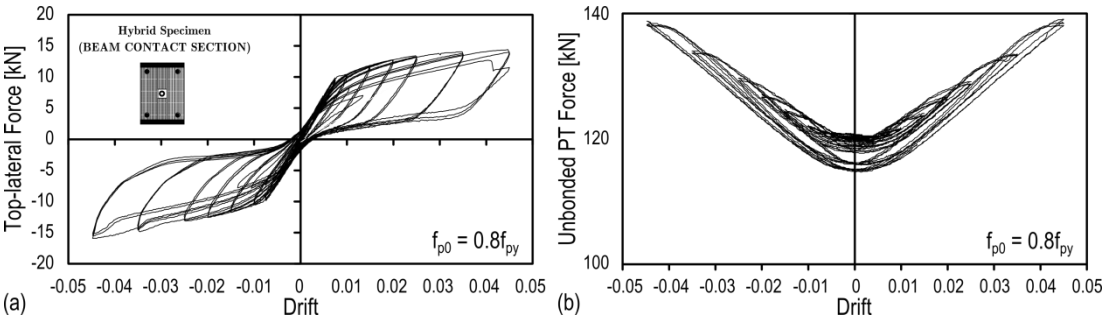

Figure 2-7. Hybrid solution: (a) lateral force-drift;(b) post-tensioning force vs. drift (modified after Palermo et al. (Palermo et al., 2005a)).

Further experimental testing on beam-column joints was carried out by Iqbal et al. (2010). Both post-tensioned only and hybrid solutions were tested and the dissipation devices used in this experimental program were mounted externally (see Figure 2-8a). Similarly to previous research, the beam-column joint showed good performance, providing hysteretic dissipation and full re-centering after testing.

To protect the column from perpendicular-to-grain compressive damage, two reinforcing solutions were considered in the experimental program. Both steel armouring plates and screws were used for this purpose proving effective in increasing the stiffness of the joint panel as well as limiting the damage in the column (Iqbal *et al.*, 2010).

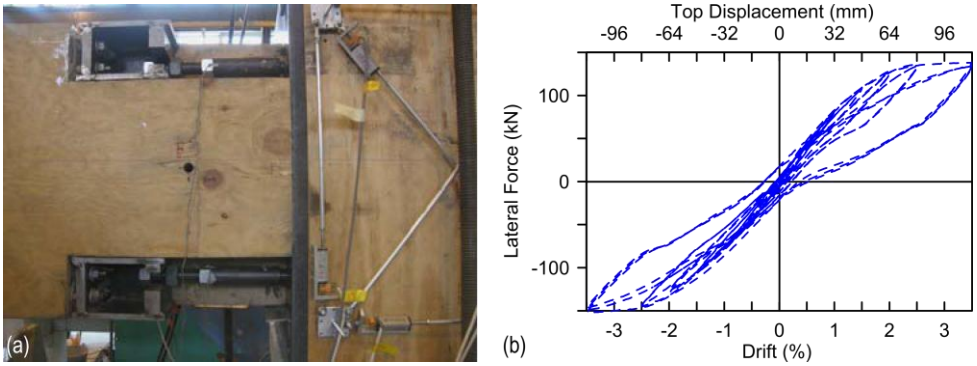

Figure 2-8. (a) Beam-column joint with external dissipaters; (b) Force-displacement response of the joint (modified after Iqbal et al. (2010)).

More recently Smith et al. (2013) tested a post-tensioned Glulam (Glued Laminated Timber) beam-column joint (Figure 2-9), extending the system to a different engineered wood product. The connection used a different type of mild steel dissipater consisting of a steel angle with reduced section at significant locations to localize yielding (Di Cesare *et al.*, 2013).

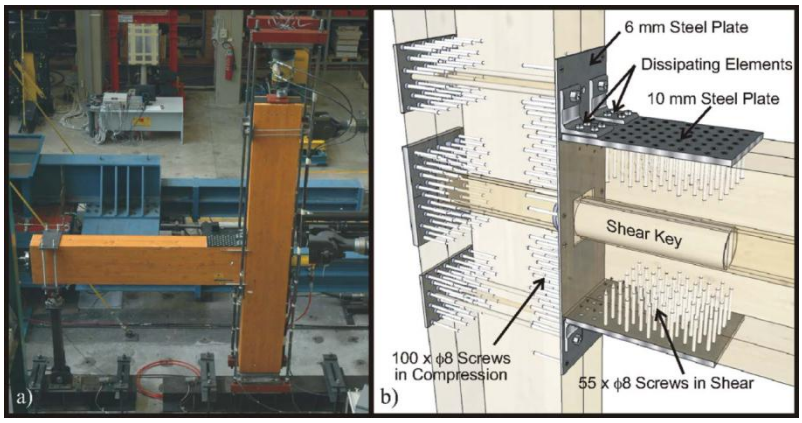

Figure 2-9. (a) Beam-column joint and (b) details of beam-column joint showing dissipating elements and shear transfer system (Smith et al., 2013).

The experimental results on a number of different reinforcement configurations confirmed the application of the Pres-Lam concept to Glulam structural elements. Testing with and without dissipative elements has been performed displaying the same damage-free performance similar to previous results with LVL timber (Smith et al., 2013).

2.4.2 Experimental research on post-tensioned timber walls

Tests on wall-to-foundation subassemblies were also carried out by Palermo et al. (Palermo *et al.*, 2005a; 2006a). The specimen consisted of the Laminated Veneer Lumber (LVL) wall shown in Figure 2-10.

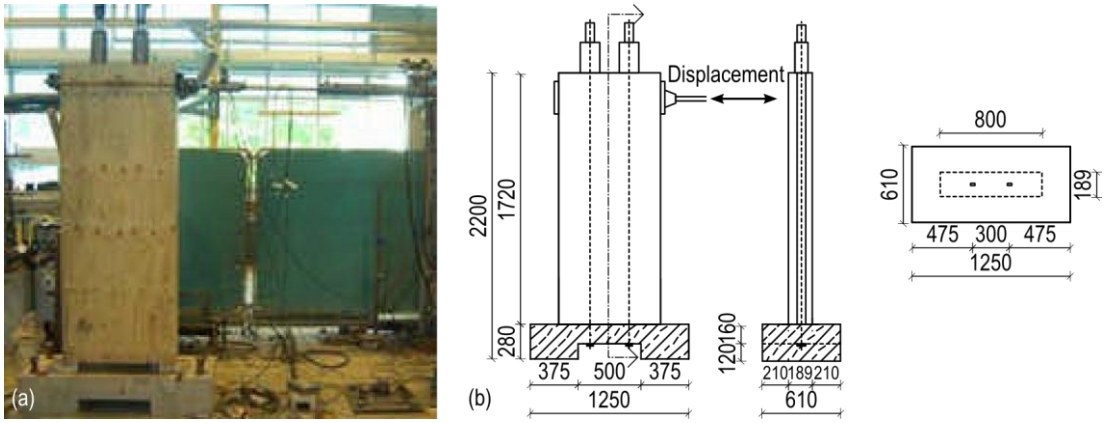

Figure 2-10. (a) Test setup and(b) specimen geometry detail (modified from Palermo et al. (2006a)).

Different post-tensioning levels were considered, and two dissipation options, internal and external mild steel bars (see Figure 2-11), were tested in the experimental program. Internal dissipaters consisted of mild steel fused bars, and external dissipation devices were 63mm thick LVL blocks and pre-tensioned rods connected to the wall specimen, with D6mm epoxied deformed bars inserted (Figure 2-11c).

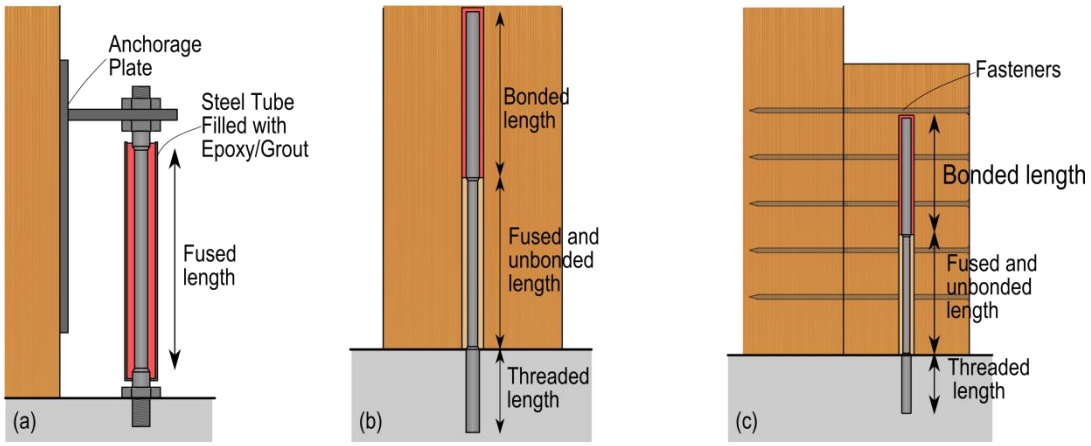

Figure 2-11.Pres-Lam walls dissipation options. (a) Fuse-type external dissipater; (b) Internal glued-in bars; (c) External glued-in bars.

The specimen with lower post-tensioning forces developed a greater dissipation capacity despite a reduced re-centering capability. Tests with internal dissipaters (see Figure 2-12a) showed stiffness degradation at higher drift levels. This was mainly due to bond deterioration between the dissipaters and the LVL specimen. A similar behaviour was observed for the specimen with external dissipaters (Figure 2-12b).

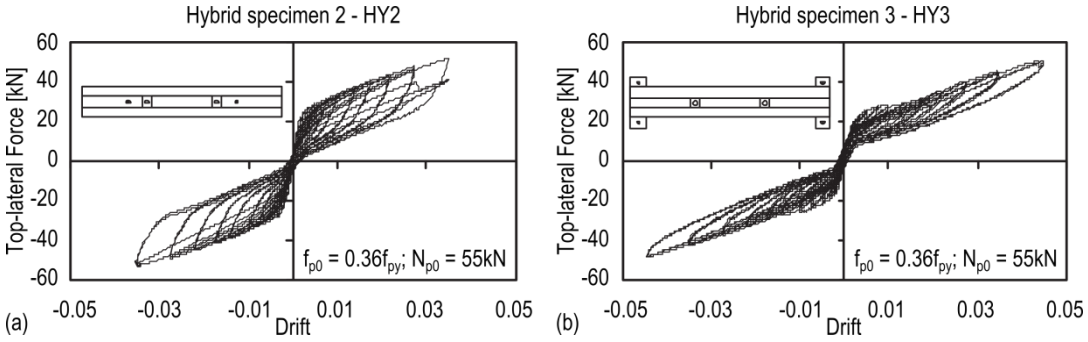

Figure 2-12. Force-Drift loops for (a) internal dissipaters (Figure 2-11b) and (b) timber external dissipaters (Figure 2-11c) (modified from Palermo et al. (2006b)).

Further quasi-static and pseudo dynamic testing of post-tensioned timber walls was performed by Smith et al. (2007). A single wall solution with external dissipaters was tested as well as an alternative configuration consisting of coupled walls.

The results on the single wall specimens confirmed the good performance of externally mounted longitudinal mild steel dissipaters as shown in the hysteretic curved of Figure 2-13b (Smith *et al.*, 2007).

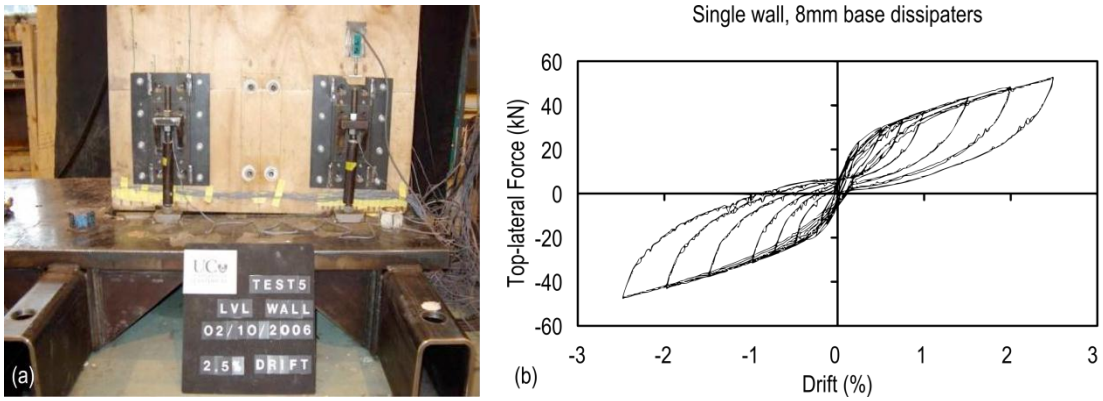

Figure 2-13. (a) Hybrid wall-to-foundation specimen; (b) Force-Drift experimental results (modified from Smith et al. (2007)).

An alternative dissipation method was adopted for a coupled system. The walls were coupled with a nailed plywood panel, which provided dissipation through the nails (Figure 2-14a).

The force-displacement behaviour of the specimen shown in Figure 2-14b highlighted stiffness degradation resulting from the pinching behaviour of the nailed connection, leading to a reduced dissipation contribution of the whole system.

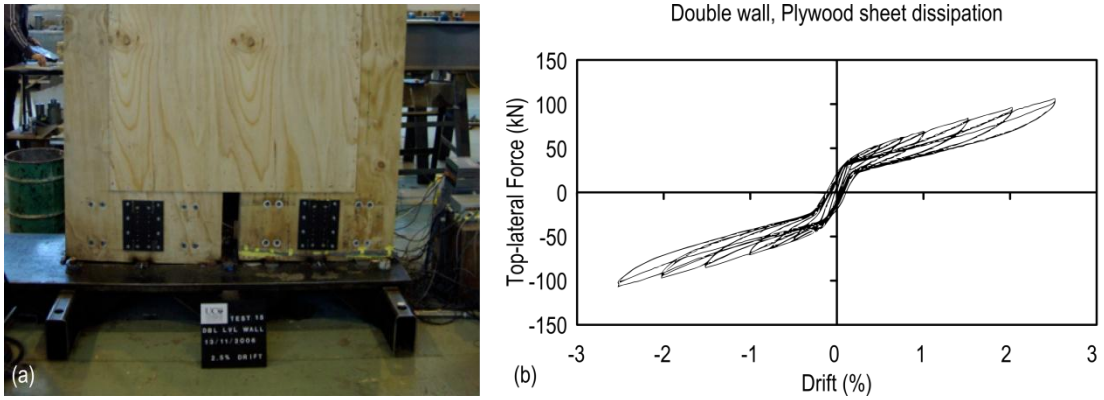

Figure 2-14. (a) Coupled walls specimen; (b) force vs. drift experimental results (modified from Smith et al. (2007)).

More research on coupled walls was carried out by Iqbal et al. (2007) (see Figure 2-15). The dissipation and coupling devices used were U-shaped Flexural Plates (UFPs, Figure 2-15,c), which were first proposed and tested by (Kelly *et al.*, 1974). Walls with different arrangements of couplers were subjected to quasi-static and pseudo-dynamic regimes.

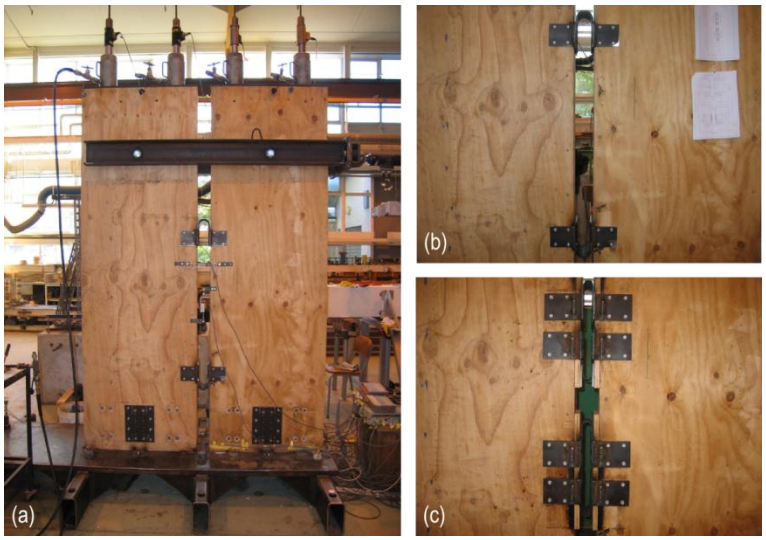

Figure 2-15. (a) Coupled walls system and arrangements of UFPs, (b) single and (c) double (modified from Iqbal et al. (2007)).

The results of quasi-static testing (Figure 2-16) showed the typical non-linear elastic and Flag Shape hysteresis loops for the pure unbonded post-tensioned and hybrid solutions respectively. The strength and hysteretic damping of the overall system could be controlled as per design by varying the UFP properties. It is noticeable that similar levels of peak lateral force but different overall dissipation were reached through the combination of different arrangements of UFP with different post-tensioning loads (Iqbal *et al.*, 2007).

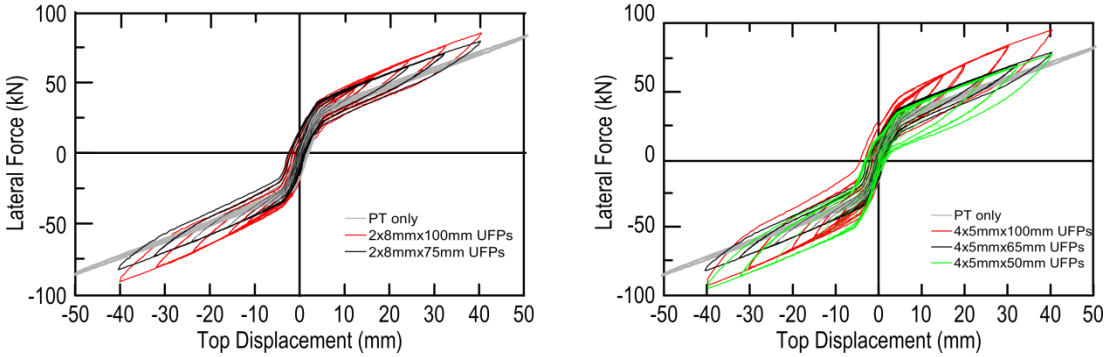

Figure 2-16. Coupled walls force-displacement experimental results (modified from Iqbal et al. (2007)).

While extensive experimental research had been carried out on several post-tensioned rocking walls configuration, the experimental programs were performed following quasi-static regimes. Marriot (2009) designed a timber post-tensioned single wall as a retrofit solution and tested it under high-speed cyclic push-pull displacement control to investigate the effects of velocity dependant dampers and to further understand the behaviour of rocking systems. Two types of damping devices were used: mild steel dampers (TCY, Figure 2-17 c,d) and fluid viscous dampers (FVD, Figure 2-17e).

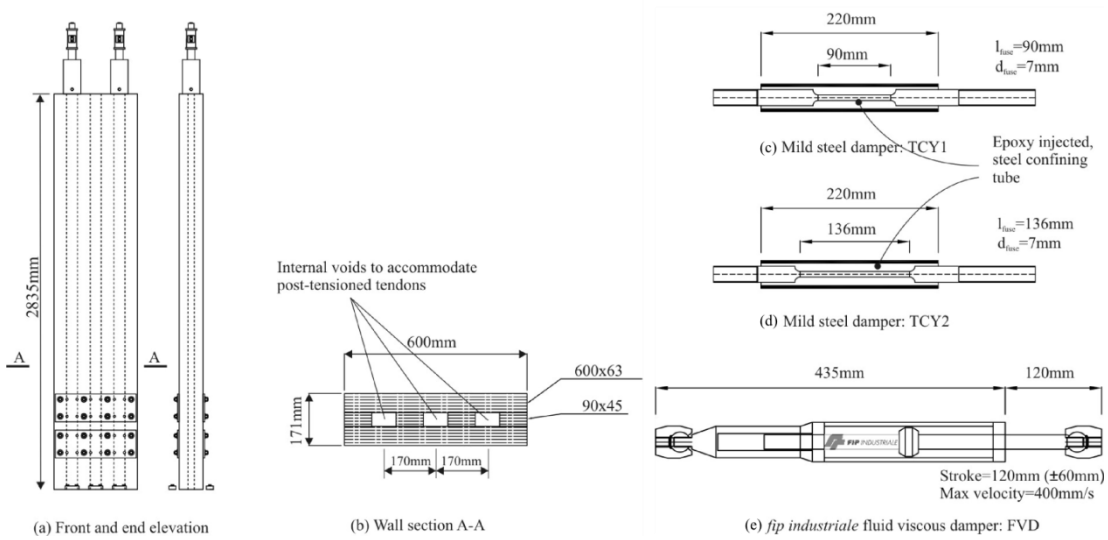

Figure 2-17. (a-b) Geometry of the post-tensioned wall. (c-e) Dissipation devices (Marriott, 2009).

Experimental results on high-speed tests highlighted a very stable hysteresis of all the configurations. Damage was entirely confined to the external dissipaters and full re-centering was achieved in all the systems (Marriott, 2009).

2.4.3 Large-scale testing

The first large scale dynamic testing program on Pres-Lam structures was carried out by Pino et al. (2010a; 2010b) and consisted of unidirectional dynamic tests of a ¼ scale building (Figure 2-18a). The test specimens were 3- and 5-storeys structures, and lateral load resistance was provided by post-tensioned moment-resisting frames (Figure 2-18b). The test results highlighted good dynamic performance and showed only minor permanent perpendicular-to-grain compression at the beam-column interface (Pino *et al.*, 2010a)

Figure 2-18.(a) Completded structure on the shake table; (b) Specimen under construction (Pino et al., 2010b).

Bi-directional quasi-static testing was carried out by Newcombe et al. (2010b; 2010a) on a 2/3 scale two-storey structure, which had independent post-tensioned frames and coupled post-tensioned walls in the two directions. (see Figure 2-19).

Figure 2-19. (a) Building overview and (b) test apparatus (2010a).

Experimental results from the two-storey building highlighted the excellent seismic performance of post-tensioned rocking structures. Elastic deformation of the frame represented a much larger proportion of the total displacement that would occur in a similar

reinforced concrete frame. The largest component of elastic displacement was shear deformation of the beam-column joint zone (Newcombe *et al.*, 2010b).

No significant damage was observed at 2% drift, but stress concentration around the energy dissipation anchorages caused the fracture of one column at 3% drift (Newcombe *et al.*, 2010b).

More recently, Smith et al. (2014) performed dynamic shake table tests on a Glulam three-storey structure which used Pres-Lam frames to resist the horizontal action (Figure 2-20). Similarly to the quasi-static testing performed on a glulam beam-column joint by Smith et al. (2013), the test building used dissipative mild-steel angles to provide hysteretic damping to the system.

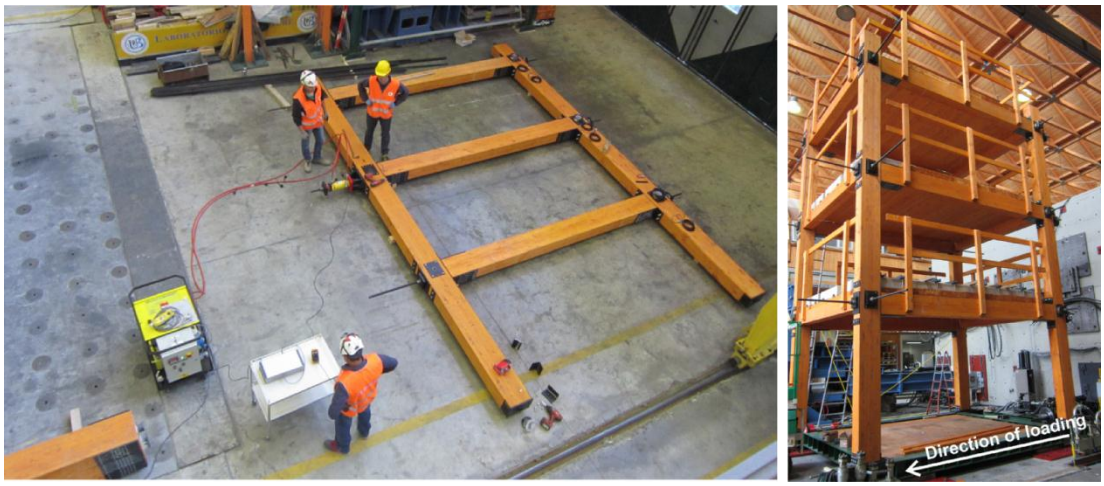

Figure 2-20. Pres-Lam glulam dynamic test specimen (Smith et al., 2014).

Both post-tensioned only and dissipative solutions were tested, and their results compared. While dynamic test results showed that the presence of dissipative devices did not impact on serviceability level response, with higher demands the addition of damping elements allows a reduction of drift and accelerations (Smith *et al.*, 2014).

2.5 Supplemental damping devices

In post-tensioned rocking systems, including Pres-Lam, the connection relies upon the combination of post-tensioning unbonded strand or bars and some type of dissipation. Different devices have been adopted in past research and the influence on the hysteretic behaviour of the connection is qualitatively shown in Figure 2-21.

With respect to the different dissipative options shown in Figure 2-21 the following sections give a brief overview on the past research carried out on mild steel (elastic-plastic), friction and viscous dissipating devices.

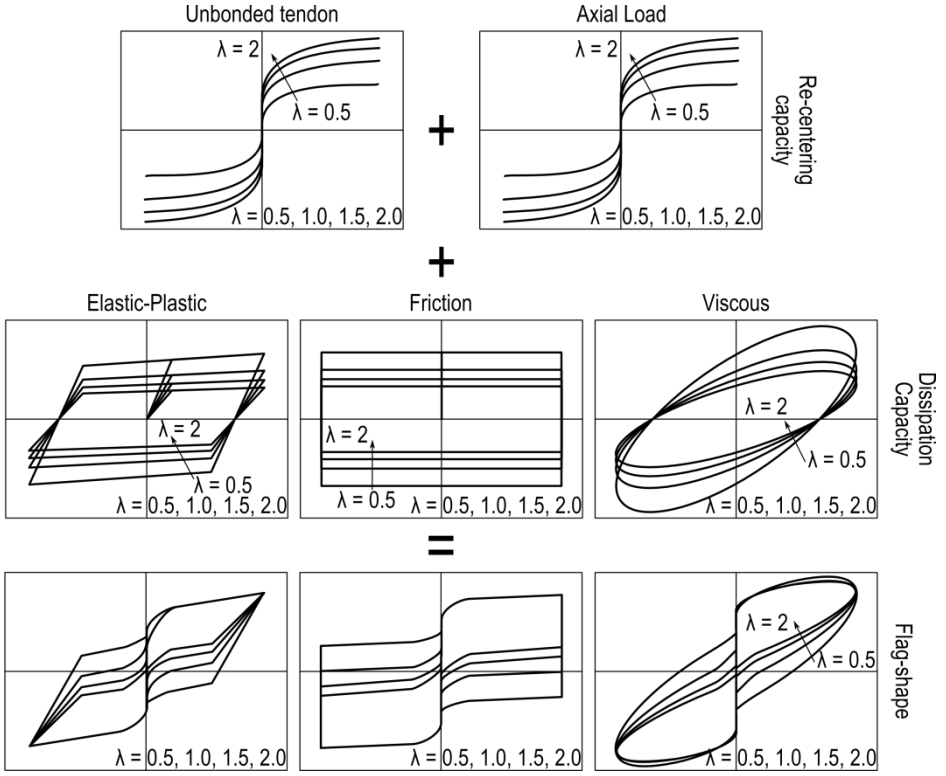

Figure 2-21. Flag-shape hysteresis for different dissipation devices: elastic-plastic, friction and viscous (modified from Palermo et al. (2005b)).

2.5.1 Tension-compression yield mild steel dissipaters

Internal dissipaters

As part of an experimental campaign on post-tensioned concrete and timber systems, an option for providing dissipation in the system is to use internal grouted/glued bars (Figure 2-22a). This type of dissipation option is convenient from an architectural point of view, since no space is needed around the wall for placing the dissipaters. Some stiffness

degradation due to bond degradation is usually present as shown in experimental tests (Figure 2-22b).

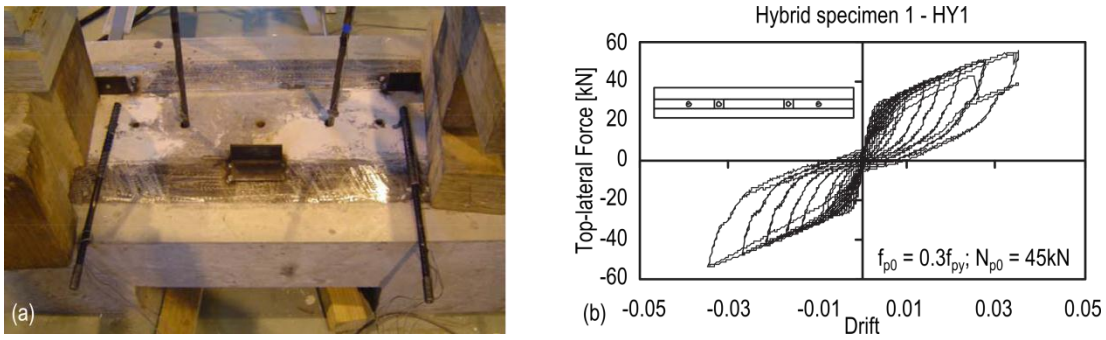

Figure 2-22. (a) Internal dissipaters in a wall-to-foundation timber subassembly (Newcombe, 2007); (b) Force-displacement of the subassembly (modified from Palermo et al. (2006)).

External dissipaters

External tension-compression yield mild steel dissipaters have been tested as part of component testing for post-tensioned concrete or timber subassemblies (Marriott, 2009; Iqbal, 2011). A brief summary of tests carried out is summarized in this section.

Component testing was carried out by Amaris (2010). The geometry of tested dissipaters is shown in Figure 2-23.

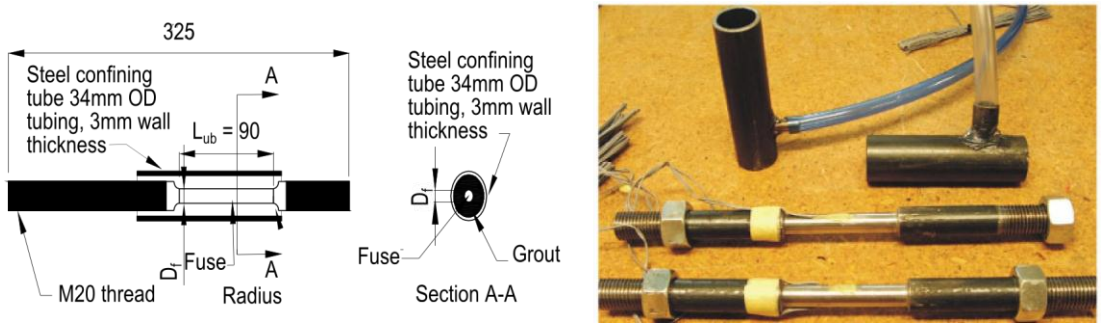

Figure 2-23. Dissipaters details (modified from Amaris Mesa (2010)).

The specimens were expected to undergo both positive and negative displacements; therefore a symmetric loading protocol was adopted.

Results reported in Figure 2-24 show a reduced dissipation capacity due to a buckling mechanism occurring at relatively low displacements. Additionally, an increase in stiffness is observed in the negative range of displacements.

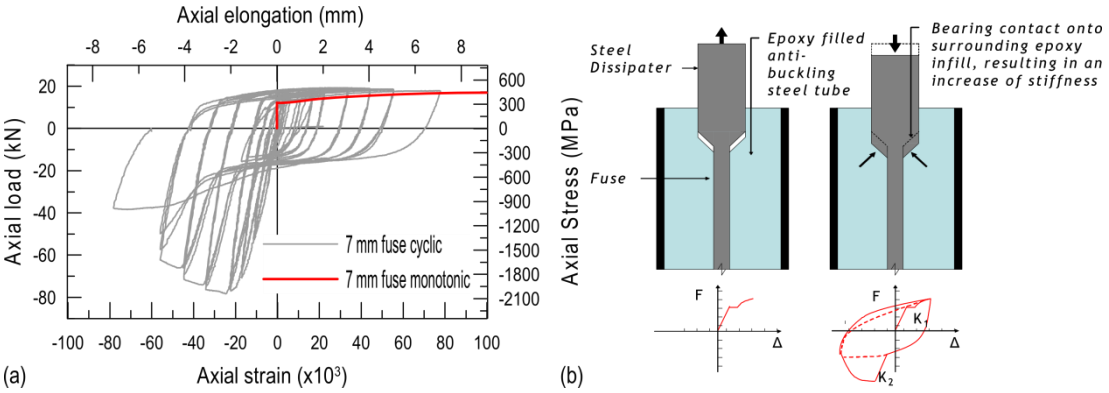

Figure 2-24. (a) Cyclic and monotonic dissipater test; (b) and behaviour in compression (Amaris Mesa, 2010)

Marriott (2009) tested three different group of Tension-Compression-Yield (TCY) dampers with 13.5, 10.0 and 8.0mm fuse diameter, and 75mm, 75mm and 115mm fuse length respectively. A 34mm (outside diameter) pipe, with a wall thickness of 2mm, was used as confining tube to prevent premature buckling.

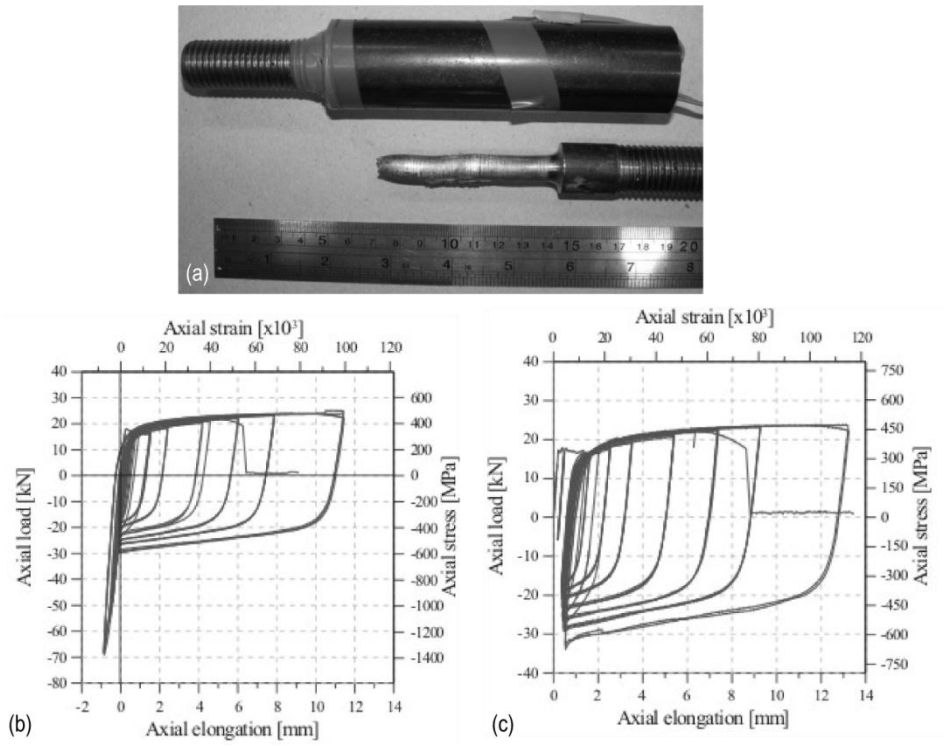

Figure 2-25. (a) Failure mode of TCY dampers; hysteresis loops for 8.0mm fuse dissipaters (b) non-symmetric and (c) symmetric load (Marriott, 2009).

The typical failure mechanism of the TCY damper was rupture of the mild steel within the fused region due to low-cycle fatigue. While buckling was observed, the buckled length is very short (Figure 2-25a) indicating an effective buckled length of approximately 3-3.5 bar diameters. This allowed the damper to yield efficiently in compression during unloading

(Marriott, 2009). Testing results showed stable hysteresis for most specimens as shown in Figure 2-25b.

Some specimens were subjected to symmetric load protocols. The experimental results showed a sudden increase in stiffness when the specimen was subjected to negative displacements (Figure 2-25c). This effect was due to the larger diameter of the bar coming into contact with the surrounding epoxy, increasing the stiffness of the damper in compression (Marriott, 2009). A similar behaviour was observed also by Amaris (2010) as shown in Figure 2-24b.

2.5.2 U-shaped flexural plates

U-shaped flexural plates (UFPs) were first developed in the 1970s by Skinner et al. (1974) with the main purpose of separating the load carrying function of the building from the energy absorbing function (Kelly *et al.*, 1974; Skinner *et al.*, 1974).

The experimental campaign performed by Kelly et al. (1974) comprised of 9mm wide strips which ranged in thickness from 0.75mm to 2.00mm. Four spacings were used, namely 9, 11, 13 and 15mm, allowing a wide variation in the thickness-radius ratio.

The UFPs were tested under quasi static displacement controlled cycles, and the peak load, the energy dissipated per cycle and the number of cycles to failure were the results of interest.

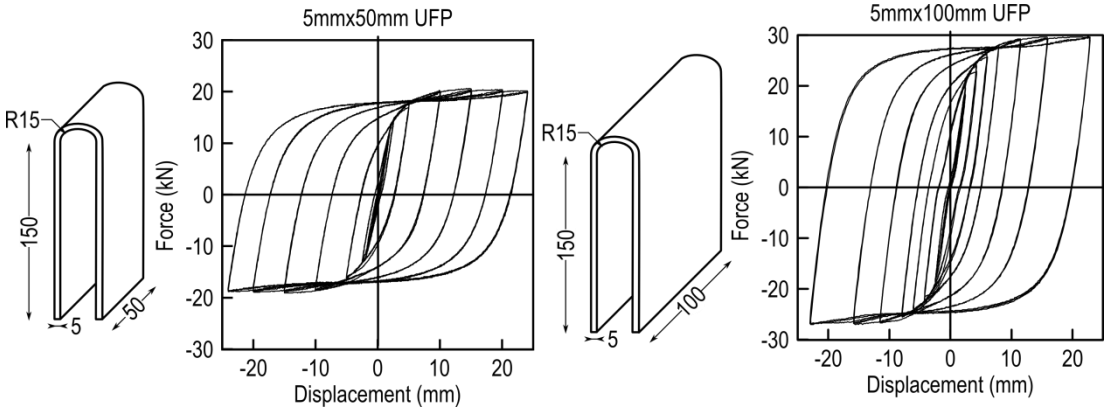

Figure 2-26. Force vs. displacement plots for UFPs (modified from Iqbal (2011)).

Iqbal et al. (2007) carried on more experimental research on UFP devices as part of testing campaign on coupled LVL walls. Three different UFP sizes were considered. A thickness of 5mm and radius of curvature of 15mm were adopted for the three devices and the widths were 50mm, 65mm and 100mm. Quasi static cyclic tests with increasing level of

displacement (symmetric loading protocol) were carried out (Iqbal *et al.*, 2007). The dissipaters showed highly dissipative and stable hysteresis loops as shown in Figure 2-26.

Additional numerical research was carried out by Baird et al. (2014) and the analytical models first proposed by Skinner et al. (1974) were refined on the basis of Finite Element modelling results.

2.5.3 Friction dampers

Friction dampers were developed for post-tensioned precast concrete structures by Morgen et al. (2004; 2007; 2009). (see Figure 2-27).

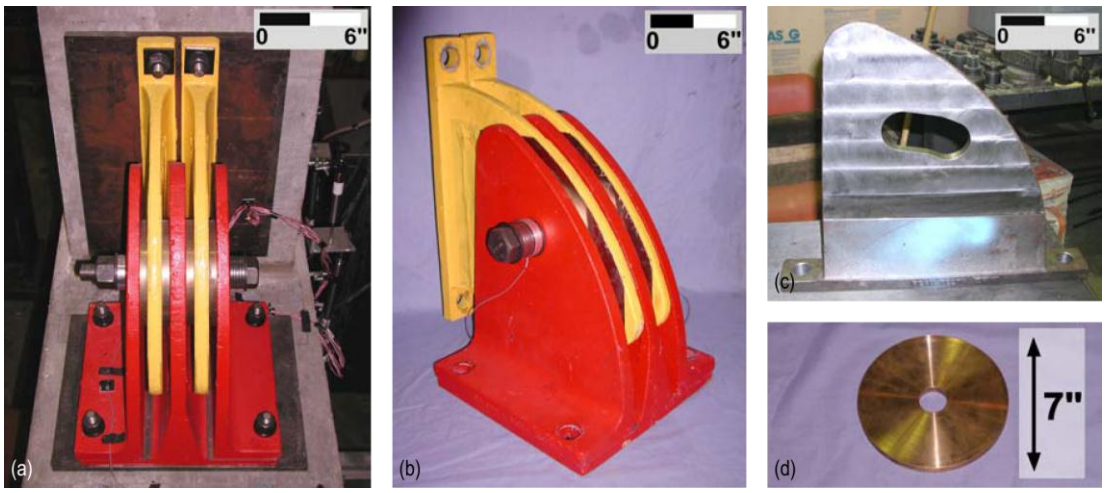

Figure 2-27. Prototype damper details – (a) beam-to-column joint; (b) damper; (c) damper component that connects to the beam; (d) leaded-bronze disk (Morgen et al., 2004).

The dampers use the friction developed between adjacent metallic surfaces as gaps open and close at the beam-to-column interfaces in an unbonded post-tensioned precast frame. Knowledge gained from past implementation of friction dampers in structural applications (Grigorian *et al.*, 1993) led to the use of two types of friction interfaces: (1) leaded-bronze against stainless steel; and (2) leaded-bronze against alloy steel. These configurations were previously shown to provide consistent and repeatable damper slip force-displacement characteristics (Morgen *et al.*, 2004).

Experimental results (some reported in Figure 2-28) showed: (1) repeatable and reliable damper hysteretic behaviour that was relatively independent of excitation velocity and displacement amplitude (assuming that the dampers are used indoors under controlled environmental conditions); (2) close-to-rectangular damper force versus displacement characteristics providing a large amount of energy dissipation per cycle; and (3) large damper initial stiffness allowing slip to occur early in the response, and thus, providing

energy dissipation beginning at small lateral displacements of the structure (Morgen *et al.*, 2009).

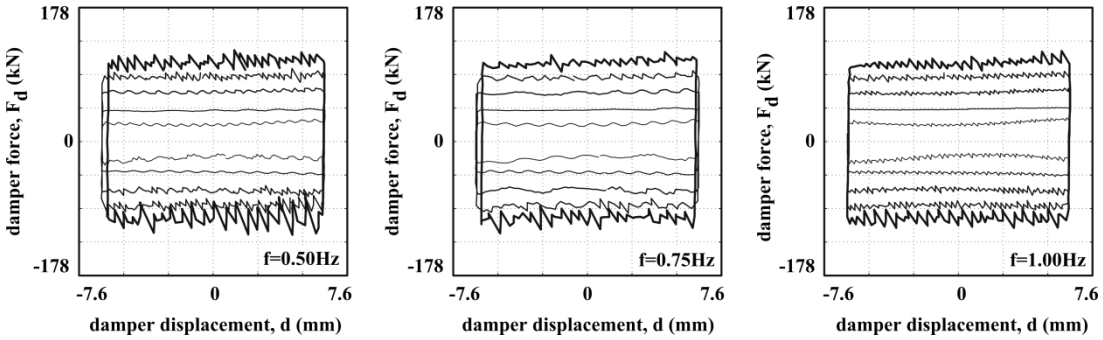

Figure 2-28. Damper force-displacement behaviour for increasing frequencies (Morgen et al., 2009).

2.5.4 Viscous dampers

Some viscous dampers (Figure 2-29a) were tested as part of the high-speed testing of a post-tensioning concrete wall by Marriott (2009). Some minor dependency from the frequency was observed as shown in Figure 2-29b,c. More importantly, some of the dampers indicated some slipping within the hysteretic response due to mechanical clearances within the ball-joint connection at each end of the damper (see Figure 2-29c).

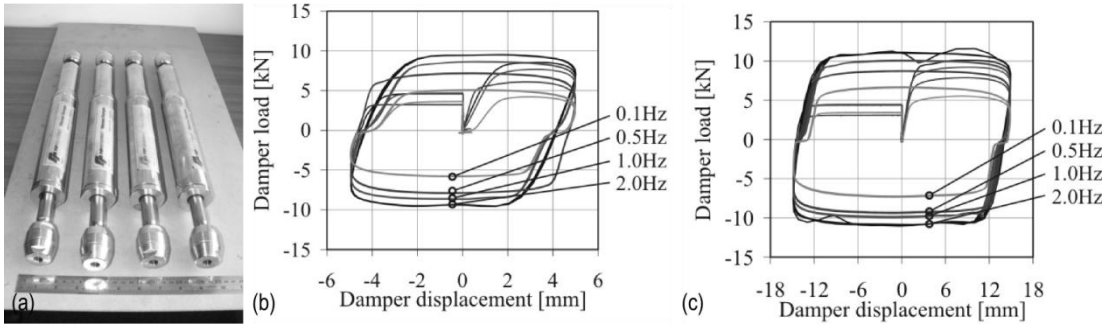

Figure 2-29. (a) viscous dampers; (b-c) damper force-displacement loops (Marriott, 2009).

2.6 Pres-Lam built examples

Following the extensive research discussed in the previous section, a few post-tensioned multi-storey timber buildings have been designed and constructed in New Zealand.

The Nelson and Marlborough Institute of Technology in Nelson (Figure 2-30a) was the first post-tensioned building constructed worldwide; it is a three storey timber building with coupled walls resisting the horizontal actions (Devereux *et al.*, 2011) which uses U-shaped flexural plates (UFPs) (Skinner *et al.*, 1974) as coupling mechanism and additional dissipative source between the walls (Figure 2-30b).

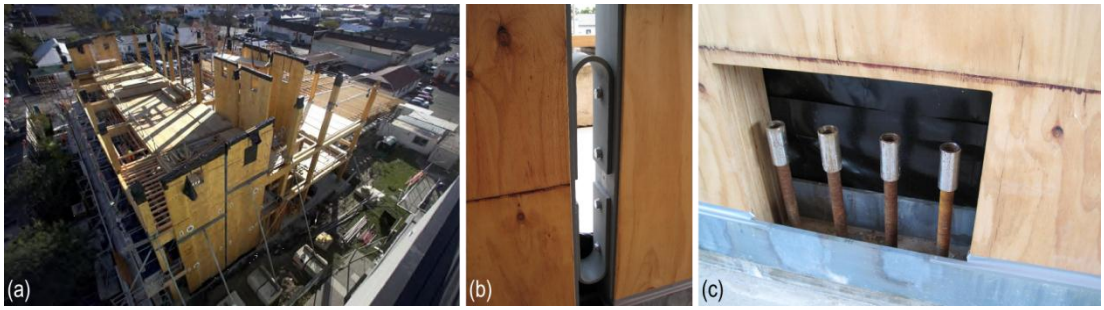

Figure 2-30. Nelson and Marlborrough Institute of Technology (NMIT) building (Devereux et al., 2011): (a) aerial view of the construction site; (b) UFP and (c) post-tensioning couplers detail.

Figure 2-31a shows the Carterton Events Center, a single story building with large timber trusses for carrying the gravity loads and single walls with internal dissipaters resisting the seismic loading (Palermo *et al.*, 2012). The supplemental dissipative reinforcement was cast into the foundation and some debonding was provided as shown in Figure 2-31b. After the wall was positioned, the post-tensioning bars could be connected through a cut in the wall panel (see Figure 2-31c), and the internal dissipaters epoxy glued in predrilled holes in the timber section.

Figure 2-31. Carterton Events Centre (Carterton) (Palermo et al., 2012): (a) view of the building under construction; (b) wall base detail under erection; (c) post-tensioning coupling.

The Trimble building (Figure 2-32a), was one of the first Pres-Lam building of the Christchurch Rebuild. The building comprises post-tensioned LVL timber frames in one direction (Figure 2-32b), which support the gravity loads of the roof and suspended floor and post-tensioned coupled timber LVL shear walls (Figure 2-32c) in the orthogonal direction (Brown *et al.*, 2012). The post-tensioned timber walls comprise of coupled panels using UFPs. Additional dissipation is provided by tension-compression yield mild steel (referred to as fuse-type dissipaters or Plug & Play devices) dissipaters connected at the base.

Figure 2-32. Trimble building (Christchurch): (a) architectural render (Brown et al., 2012); (b) beam-column joint; (c) view of the coupled walls (c/o D. Moroder) .

More recently, the Kaikoura District Council building (Figure 2-33a) was designed and is currently under construction. The building is a three-storey timber structure and is the first adopting post-tensioned Cross-Laminated Timber (CLT) rocking walls (Figure 2-33b). The dissipation is provided by tension-compression yield mild steel dissipaters (Figure 2-33c).

Figure 2-33. Kaikoura District Council Building: (a) architectural render; (b) view of the post-tensioned walls under construction (c/o A. Buchanan); (c) detail of the dissipaters base connection (c/o A. Buchanan).

2.7 References

Amaris Mesa, A.D. 2010. Developments of Advanced Solutions for Seismic Resisting Precast Concrete Frames. *Doctor of Philosophy*, University of Canterbury.

Baird, A., Smith, T., Palermo, A., Pampanin, S. 2014. Experimental and Numerical Study of U-Shaped Flexural Plate (UFP) Dissipators. *New Zealand Society for Earthquake Engineering Annual Conference*, Auckland, New Zealand.

Brown, A., Lester, J., Pampanin, S., Pietra, D. 2012. Pres-Lam in practice - A damage-limiting rebuild project. *New Zealand Society of Structural Engineers Conference*, Auckland, New Zealand.

Christopoulos, C., Filiatrault, A., Uang, C.M., Folz, B. 2002. Post-tensioned Energy Dissipating Connections for Moment Resisting Steel Frames. *Journal of Structural Engineering* 128(9): 1111-1120.

Devereux, C., Holden, T., Buchanan, A., Pampanin, S. 2011. NMIT Arts & Media Building-Damage Mitigation Using Post-tensioned Timber Walls.

Di Cesare, A., Ponzo, F.C., Nigro, D., Simonetti, M., Smith, T., Pampanin, S. 2013. Experimental testing and numerical analysis of steel angles as hysteretic energy dissipating devices. *Il XV Convegno di Ingegneria Sismica, Associazione Nazionale di Ingegneria Sismica*, Padua, Italy.

Grigorian, C.E., Yang, T.S., Popov, E.P. 1993. Slotted Bolted Connection Energy Dissipators. *Earthquake Spectra* 9(3): 491-504.

Iqbal, A., Pampanin, S., Buchanan, A.H., Palermo, A. 2007. Improved Seismic Performance of LVL Post-tensioned Walls Coupled with UFP devices. *8th Pacific Conference on Earthquake Engineering*, Singapore.

Iqbal, A., Pampanin, S., Palermo, A., Buchanan, A.H. 2010. Seismic Performance Of Full-Scale Post-tensioned Timber Beam-Column Joints. *World Conference on Timber Engineering*, Riva del Garda, Trentino, Italy.

Iqbal, M.A. 2011. Seismic response and design of subassemblies for multi-storey prestressed timber buildings. *Doctor of Philosophy*, University of Canterbury.

Kelly, J.M., Skinner, R.I., Heine, A.J. 1974. Mechanism of Energy Absorption in Special Devices for Use in Earthquake Resistant Structures. *Bulletin of the New Zealand Society of Earthquake Engineering* 5(3): 63-88.

Kurama, Y., Sause, R., Pessiki, S., Lu, L.-W. 1999. Lateral load behavior and seismic design of unbonded post-tensioned precast concrete walls. *ACI Structural Journal* 96(4).

Kurama, Y.C., Shen, Q. 2004. Posttensioned hybrid coupled walls under lateral loads. *Journal of structural Engineering* 130(2): 297-309.

Marriott, D.J. 2009. The Development of High-Performance Post-Tensioned Rocking Systems for the Seismic Design of Structures. *Doctor of Philosophy*, Universtiy of Canterbury.

Morgen, B., Kurama, Y. 2004. A friction damper for post-tensioned precast concrete beam-to-column joints. *PCI J* 49(4): 112-133.

Morgen, B., Kurama, Y. 2009. Characterization of two friction interfaces for use in seismic damper applications. *Materials and Structures* 42(1): 35-49.

Morgen, B.G., Kurama, Y.C. 2007. Seismic Design of Friction-Damped Precast Concrete Frame Structures. *Journal of Structural Engineering* 133(11): 1501-1511.

Nakaki, S.D., Stanton, J.F., Sritharan, S. 1999. An overview of the PRESSS five-story precast test building. *PCI journal* 44(2): 26-26.

New Zealand Concrete Society 2010. *PRESSS Design Handbook*.

Newcombe, M.P., Pampanin, S., Buchanan, A.H. 2010a. Design, fabrication and assembly of a two-storey post-tensioned timber building. *World Conference on Timber Engineering*.

Newcombe, M.P., Pampanin, S., Buchanan, A.H. 2010b. Global Response of a Two Storey Pres-Lam Timber Building. *New Zealand Society of Earthquake Engineering, Annual Conference*.

Palermo, A., Pampanin, S., Buchanan, A., Newcombe, M. 2006a. Seismic Design of Multi-Storey Buildings using Laminated Veneer Lumber (LVL). *New Zealand Society of Earthquake Engineering, Annual Conference*, Wairakei, New Zealand, University of Canterbury. Civil Engineering.

Palermo, A., Pampanin, S., Buchanan, A.H., Newcombe, M.P. 2005a. Seismic design of multi-storey buildings using laminated veneer lumber (LVL). *New Zealand Society of Earthquake Engineering, Annual Conference*, Wairakei, New Zealand, University of Canterbury. Civil Engineering.

Palermo, A., Pampanin, S., Calvi, G.M. 2005b. Concept and development of hybrid solutions for seismic resistant bridge systems. *Journal of Earthquake Engineering* 9(6): 899-921.

Palermo, A., Pampanin, S., Fragiacomo, M., Buchanan, A.H., Deam, B. 2006b. Innovative Seismic Solutions for Multi-Storey LVL Timber Buildings. *9th World Conference on Timber Engineering*, Portland, Oregon, USA.

Palermo, A., Sarti, F., Baird, A., Dekker, D. 2012. From theory to practice: design, analysis and construction of dissipative timber rocking post-Tensioning wall system for Carterton Events Centre, New Zealand. *World Conference on Earthquake Engineering*, Lisbon, Portugal.

Pino, D., Pampanin, S., Buchanan, A., Carradine, D., deam, B. 2010a. Shake Table Test Response of Multi-Storey Post-Tensioned Timber Buildings. *New Zealand Society for Earthquake Engineering Annual Conference*, Wellington, New Zealand.

Pino, D., Pampanin, S., Carradine, D., Deam, B., Buchanan, A.H. 2010b. Dynamic Response of a Multi-Storey Post-Tensioned Timber Building. *World Conference on Timber Engineering*, Riva del Garda, Trentino, Italy.

Skinner, R.I., Kelly, J.M., Heine, A.J. 1974. Hysteretic dampers for earthquake-resistant structures. *Earthquake Engineering & Structural Dynamics* 3(3): 287-296.

Smith, T., Ludwig, F., Pampanin, S., Fragiacomo, M., Buchanan, A., Deam, B., Palermo, A. 2007. Seismic Response of Hybrid-LVL Coupled Walls Under Quasi-Static and Pseudo-Dynamic Testing. *NZSEE Conference*.

Smith, T., Pampanin, S., Di Cesare, A., Ponzo, F., Simonetti, M., Nigro, D., Carradine, D. 2014. Shaking table testing of a multi-storey post-tensioned timber building *NZSEE Conference*, Auckland, New Zealand.

Smith, T., Ponzo, F.C., Di Cesare, A., Pampanin, S., Carradine, D., Buchanan, A.H., Nigro, D. 2013. Post-Tensioned Glulam Beam-Column Joints with Advanced Damping Systems: Testing and Numerical Analysis. *Journal of Earthquake Engineering* 18(1): 147-167.

Standards New Zealand. 2006. *NZS 3101: Concrete structures standard*. Standards New Zealand. Wellington, New Zealand, Standards New Zealand.

Part 2:

Dissipation devices

3 Fused-type buckling-restrained dissipaters: testing and modelling

3.1 Introduction

This chapter aims to answer the following research objectives as anticipated in Chapter 1 of this dissertation.

1. Determine the main failure mechanisms governing the response of external tension-compression yield dissipaters
2. Develop and calibrate a numerical models capable of simulating the significant behavioral aspects of the dissipater in order to determine significant design parameters
3. Develop and validate simplified analytical models to predict the external dissipater's response

To address this research questions the chapter presents an extensive experimental campaign on tension-compression yield dissipaters. The dissipaters comprised of necked-down mild steel round bars, where the buckling was prevented by a filled steel tube, and the dissipaters were referred to as Fuse-type buckling-restrained (FBR) devices. To provide a comprehensive understanding of the dissipaters' structural behaviour, several specimens were tested under a quasi-static cyclic protocol. Since the dissipaters were not expected to undergo significant compressive displacements, the quasi-static schedule subjected the specimens to net tension displacements only.

Firstly, the chapter discusses the testing methodology and experimental results, which are used for the calibration of a fiber elements-based model developed in OpenSEES (McKenna, 2011). The model aims to simulate the buckling behaviour observed during experimental testing and used to define significant design parameters and to provide the calibration of a force-displacement macro-model for the dissipaters.

In the final part of the chapter analytical models are proposed and validated against the experimental results, and a cyclic force-displacement hysteretic rule is developed also accounting for numerical analyses outcomes.

3.2 Past research and early developments of the FBR dissipater

Post-tensioned low-damage technologies were first developed for pre-cast concrete structures in high-seismic region in the late 1990s as part of the Precast Prestressed Structural Systems (PRESSS) program (Priestley, 1991). One of the most stable solutions tested in the final experimental stage of the research program was the hybrid connection, which provides a combination of re-centering and dissipative contributions. The former is given by post-tensioning unbonded strands; the latter is provided by tension compression yield (TCY) mild steel reinforcement (Nakaki *et al.*, 1999; Priestley *et al.*, 1999). In the first applications the dissipative reinforcement was in the form of internal bonded bars, and an unbonded length was provided at the beam-column or column-foundation interface to limit the strain demand during the rocking mechanism at the critical interface.

The research into post-tensioning PRESSS systems was further developed in the last decade at the University of Canterbury. Marriott *et al.* (2009) and Amaris (2010) carried out experimental programs and numerical studies on post-tensioned precast bridge piers and walls (Marriott *et al.*, 2007; Marriott *et al.*, 2008; Marriott, 2009), and post-tensioned beam-column joints and frames (Pampanin *et al.*, 2006; Amaris Mesa, 2010).

The post-tensioned hybrid technology was more recently extended to engineered timber (i.e. Laminated Veneer Lumber and Glued Laminated timber) structural systems (Palermo *et al.*, 2006a) and referred to as Pres-Lam (Prestressed Laminated timber) system. Further research was carried out on walls by Iqbal (2007) and Smith (2007), and post-tensioned timber frames (Iqbal *et al.*, 2010). Glue Laminated timber was also used in beam-column subassemblies (Smith *et al.*, 2013).

In both precast concrete and timber post-tensioning internal as well as external dissipaters were used. In the original concept of hybrid systems, the reinforcement was generally bonded into the concrete element providing some de-bonding at either the beam-column or the wall-foundation interface to limit the strain demand due to the rocking mechanism and protect the steel reinforcing bars from premature buckling. In later applications to timber elements (Palermo *et al.*, 2006a) the same concept was applied, and mild steel bars were epoxied inside the timber sections. Although this type of system is rather suitable from a constructability as well as an architectural point of view, experimental results showed that relying on bond can lead to stiffness degradation due to the degrading bond-slip behaviour; more importantly, the internal dissipater is not of easy replacement after a seismic event, and

some alternative dissipation device can be externally connected to the structural element in the post-event repairing.

To favour the post-event replaceability, an external fuse-type dissipater has been developed and first implemented into a precast concrete beam-column joint with draped post-tensioning (Amaris Mesa, 2010). The external fuse-type dissipater concept is in general similar to a Buckling Restrained Brace (BRB), composed of a ductile steel core, designed to yield both in tension and compression. To preclude global buckling in compression, the steel core is first placed inside a steel casing before the casing is filled with mortar or concrete. Generally a BRB is composed of (1) a restrained yielding segment, (2) restrained non-yielding element, (3) unrestrained non-yielding segment, (4) unbonding agent and expansion material and (5) buckling-restraining system (Uang *et al.*, 2004) (see Figure 3-1).

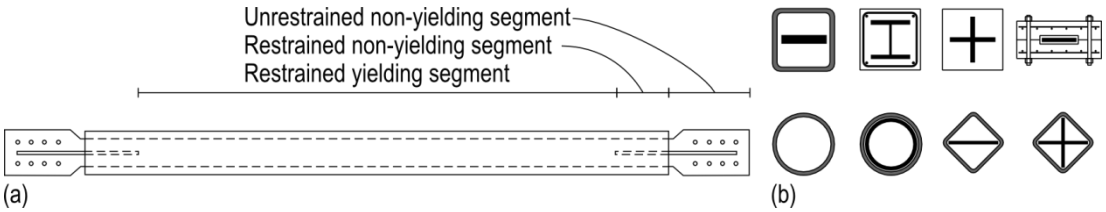

Figure 3-1. (a) Component of BRB; (b) Cross sections of various BRBs (modified from Uang et al., 2004 (Uang et al., 2004))

The very first experimental investigations on a BRB system were performed by Wakabayashi et al. (1973) who tested flat steel plates braces encased between a pair of precast reinforced concrete panels. Further and extensive research was later carried out on different cross-sectional shapes encased in concrete-filled steel profiles proving good cyclic performance (Clark *et al.*; Fujimoto *et al.*, 1988; Nagao *et al.*, 1990; Horie *et al.*, 1993; Inoue *et al.*, 1993; Suzuki *et al.*, 1994; Sabelli *et al.*, 2003; Black *et al.*, 2004).

Similarly, the fuse-type buckling-restrained dissipater is a mild steel round bar milled to a reduced diameter to create a controlled "fuse" action; an external part of bigger diameter with threaded ends allows the dissipater connection to the structural element to be protected from the over-strength of the fuse part. Some buckling restraint must be provided as the dissipater undergoes significant cyclic stresses in compression. A round mild steel tube is filled with either grout or epoxy, and provides the restraint needed (Figure 3-2).

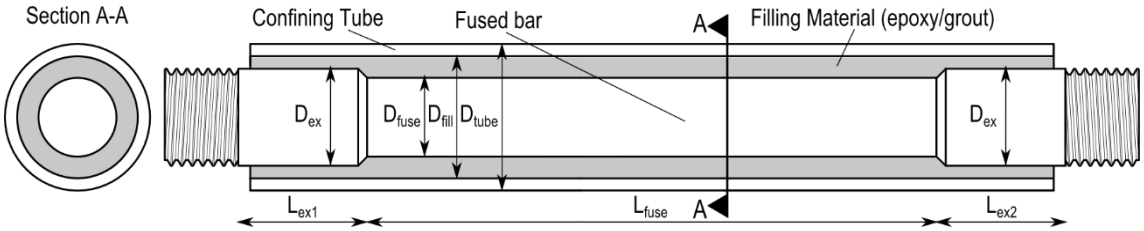

Figure 3-2. Fuse-type dissipater.

Several fuse-type dissipaters were tested as part of connection/system testing for post-tensioned concrete elements and subassemblies. Marriott (2010) performed component testing on several dissipaters with fuse diameters of 13.5mm, 10.0mm and 8.0mm, and with fuse length of 75mm, 75mm and 115mm respectively. The dissipaters' experimental performance showed very stable hysteresis and proved capable of providing significant dependable energy dissipation. Some specimens were subjected to negative displacements, and the test results indicated a sudden increase in stiffness. This phenomenon can be explained with the illustration in Figure 3-3b. As the damper is compressed into the negative displacements range, the larger diameter of the bar comes into contact with the surrounding epoxy increasing the stiffness of the damper in compression (Marriott, 2009).

Amaris (2010) also tested fuse-type dissipaters as part of the component testing of a larger experimental campaign. Three different fuse diameters (7mm, 10mm and 13mm) were considered with a fuse length of 90mm. The steel confining tube had an external diameter of 34mm and thickness of 3mm. The testing results (Figure 3-3a) showed reduced energy dissipation capacity when the dissipater was displaced into net negative displacements and that was reduced further by buckling at relatively low displacements and strain level.

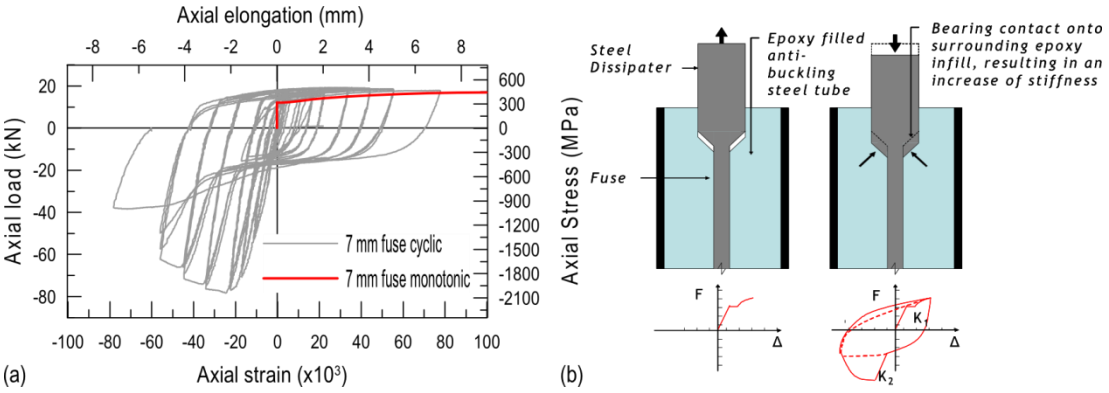

Figure 3-3. (a) Cyclic and monotonic dissipater test and (b) behaviour in compression (Amaris Mesa, 2010).

Following extensive experimental and numerical investigation on post-tensioned concrete and timber technologies, several buildings were designed and constructed applying this innovative low-damage post-tensioning technology.

The first post-tensioned concrete building adopting the fused-type (or "Plug-and-Play" (Pampanin, 2005)) dissipater was the Learning and Research Building at Victoria University in Wellington (Figure 3-4 left). The building has six three-bay post-tensioned concrete frames, spanning 8.4m, carrying double-tee flooring units spanning 9.9m. Energy dissipation is provided by external replaceable devices bolted to the pre-cast beams and columns after erection (Cattanach *et al.*, 2008).

Figure 3-4. Fuse-type dissipater applications. (a) Learning and Research building, Victoria University, Wellington (Cattanach et al., 2008); (b) Young Hunter House , Christchurch; (c) Trimble Navigation offices (Brown et al., 2012)

More recently a Pres-Lam building, the Young Hunter House in Christchurch, New Zealand (Figure 3-4 right), was constructed. The building is a three storey timber structure with post-tensioned frames spanning 8.8m in one direction. Fuse-type dissipaters are bolted at the beam-column and column-foundation interfaces to provide both dissipation and additional moment capacity under both gravity and seismic loading.

The Trimble Navigation Offices in Christchurch, New Zealand was also a Christchurch Rebuild project incorporating the Pres-Lam system and the fuse-type dissipaters. A portion of the coupled walls is shown in Figure 3-4c highlighting the use of the dissipation devices at the wall-foundation interface as additional dampers (Brown *et al.*, 2012).

Experimental testing on fuse-type dissipaters carried out by Amaris (2010) and Marriott et al. (2008) was mainly focussed on component testing as part of subassemblies tests and the device was also used in post-tensioned timber subassemblies tests by Palermo et al. (2006b) and Armstrong et al. (2014).

3.3 Experimental testing

3.3.1 Materials

Different options are available in terms of the structural steel grades to be used in the fabrication of the fuse-type dissipater. In past research in post-tensioned rocking systems applications mainly Grade300 and Grade500 mild steel were used (Marriott *et al.*, 2008; Amaris Mesa, 2010; Newcombe *et al.*, 2010).

The experimental work presented in the paper focussed solely on Grade300 mild steel, and AS/NZS 1163 Grade C250L0 circular hollow sections were used as confining tubes as readily available materials. The filling material between the fuse bar and the tube was either cement grout or epoxy. Table 3-1 gives the characteristic properties of the materials used (provided by the manufacturer).

Table 3-1. Material properties

Material	**Modulus of elasticity** *(GPa)*	**Strength** *(MPa)*
Grade300 Steel (fused bar)	200	300
Grade C250L0 steel (confining tube)	200	250
Cement grout (filler)	30	40
Epoxy (filler)	1.5	83

3.3.2 Testing schedule

One of the main research objectives was to investigate the expected failure mechanisms of the dissipaters mainly based on the dissipater's geometry. Among the parameters to be considered were the dissipater slenderness, the anti-buckling system strength and difference in fuse vs. external diameters.

To accomplish the research objectives, different geometric parameters were taken into account. Four different geometries were tested for a fuse slenderness ratio of 60 ($\lambda_{fuse} = 4L_{fuse}/D_{fuse}$). The fuse length, L_{fuse}, for those specimens was 180, 300, 360 and 390mm for a fuse diameter, D_{fuse}, of 12, 20, 24 and 26mm respectively. A variation in fuse slenderness (75 and 90) was considered for the largest fuse diameter of 26mm; therefore, the last two specimens' fuse length was 488 and 585mm, respectively. A constant difference in fuse and external diameter, D_{ext}, of 4mm to 8mm was taken into account for the test specimens. The summary of the testing schedule is reported in Table 3-2 and nomenclature is shown in Figure 3-2. Different filling materials (cement grout and epoxy grout) were considered to assess the influence of different elastic modulus values on the dissipater's behaviour.

Table 3-2. Testing schedule.

ID No.	D_{ex} [mm]	D_{fuse} [mm]	L_{ex} [mm]	L_{fuse} [mm]	λ_{fuse} [-]	λ_{eff} [-]	$D_{ex,tube}$ [mm]	$D_{int,tube}$ [mm]	L_{tube} [mm]
D12L180	16	12	40	180	60	25.7	21.7	26.9	256
D20L300	24	20	40	300	60	27.9	36	42.4	377
D24L360	32	24	40	360	60	29.4	40.3	48.3	440
D26L390	32	26	40	390	60	32.2	40.3	48.3	468
D26L488	32	26	40	488	75	40.2	40.3	48.3	566
D26L585	32	26	40	585	90	48.4	40.3	48.3	665

NOTE: λ_{eff} effective slenderness ratio, see Equation (3-4).

3.3.3 Test setup and protocol

A Dartec 10MN Universal Testing Machine (UTM) was used as shown Figure 3-5b. The testing machine had a maximum force of 10MN, with a maximum actuator stroke of 300mm and maximum and minimum velocities of 16 and 0.002 mm/s respectively. For the purposes of the experimental campaign the testing was carried out at 40mm/min.

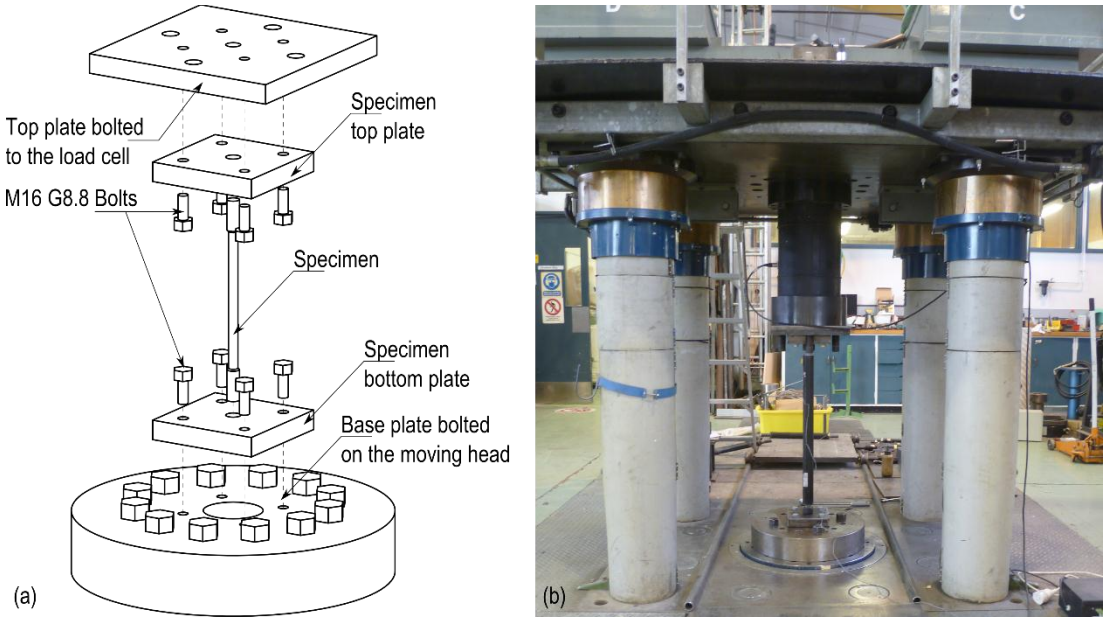

Figure 3-5. (a) Test setup 3D view and (b) testing machine.

Steel plates were fabricated in order to obtain the necessary flexibility of the test setup due to the large range of dissipater sizes. The testing rig consisted of a series of 40mm thick Grade300 steel plates. Two main connecting plates were joined with 1.5" bolts to the 1000kN load cell and the moving head of the hydraulic machine. M16 Grade 8.8 bolts

connected a set of smaller plates (135mm×135mm) which provided the dissipater connection (see Figure 3-5a). This setup allowed the easy replacement of the specimen following testing.

As the observed behaviour of the dissipaters under net negative displacements showed a significant increase in the dissipater's stiffness (Marriott, 2009; Amaris Mesa, 2010), the testing protocol subjected the specimens to tension displacements only. This is an acceptable assumption also considering the behaviour of the dissipater in real applications. In post-tensioned rocking systems the device undergoes very small or no compressive displacements. In fact, for increasing connection rotations, the neutral axis depth decreases to values as low as 20% of the section depth (this value depends on the rate of initial post-tensioning force); furthermore, the dissipater's connection system has some flexibility which also reduces the device's displacement.

The testing protocol is shown in Figure 3-6 was a modified version of the ACI ITG-5.1-07 (ACI Innovation Task Group 5, 2008) protocol: the maximum displacement of the first three amplitudes does not exceed 60% of the design displacement ($\Delta_d = 0.02L_{fuse}$); the maximum displacement of the subsequent cycle amplitudes is between 1.25 and 1.5 times the previous maximum displacement.

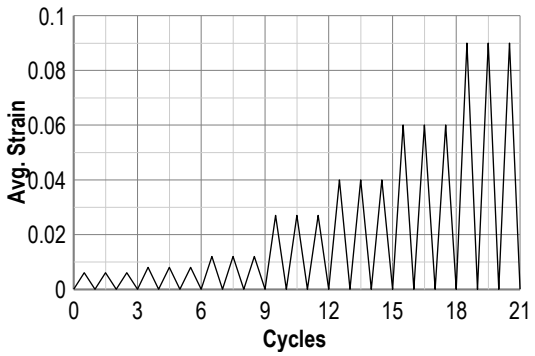

Figure 3-6. Loading protocol.

3.3.4 Results

The experimental results in Figure 3-7 show that most of the specimens displayed stable hysteresis loops within a maximum average strain of 6%, with the exception of the most slender specimens.

Two failure mechanisms were observed in the experimental program. For low effective slenderness ratio values (i.e. specimen D18L180, $\lambda_{eff} = 25.7$) axial low cycle fatigue caused the fracture of the fused portion after many loading cycles (see Figure 3-8c).

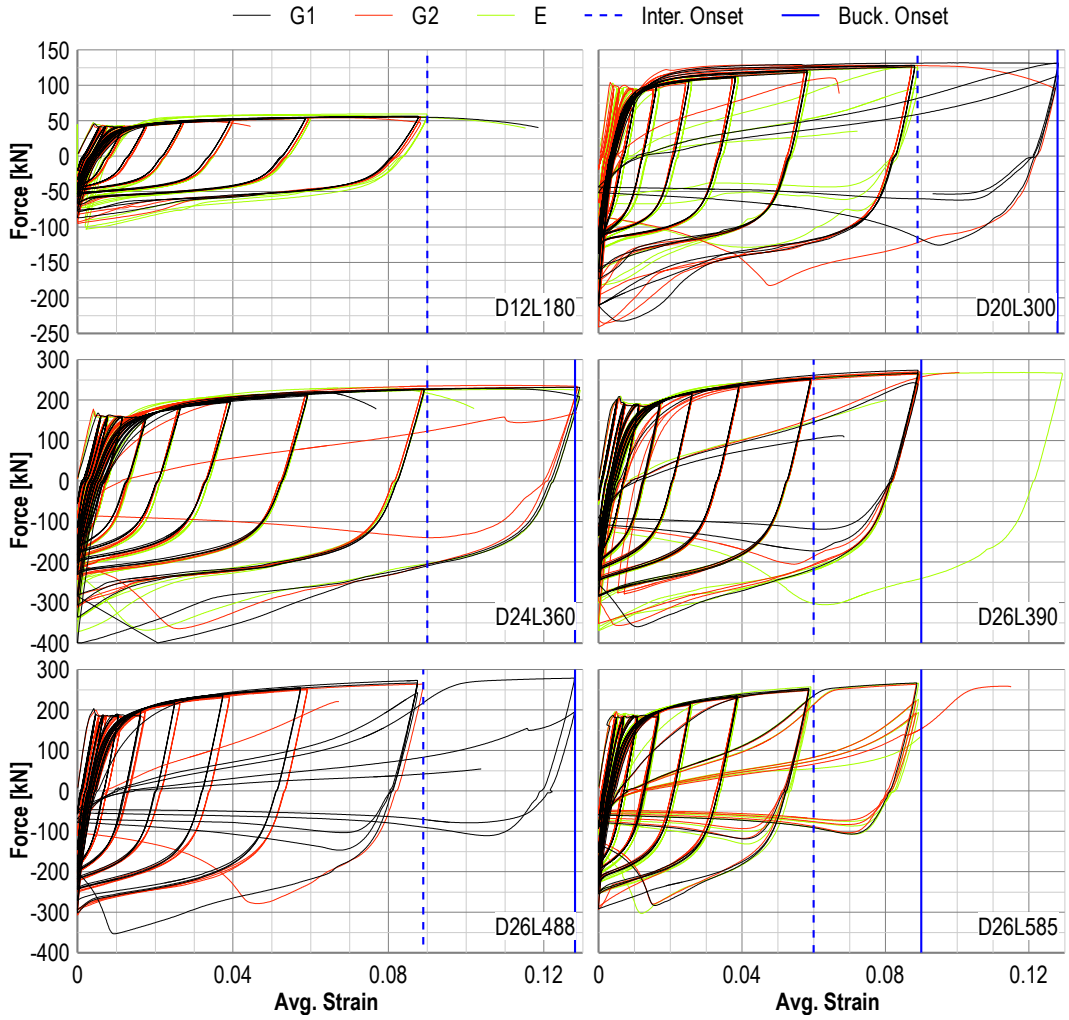

Figure 3-7. Experimental test results

Figure 3-8. Specimen D26L585. (a) Sway mechanism during testing; (b) permanent deformation after testing; (c) test specimen after testing.

A second failure mechanism consisted of a buckling/sway mechanism of the device as shown in Figure 3-8a,b. At higher displacements the devices developed an increased force in the unloading branch of the cycle. This highlights that some part of the load is taken by the

confining system, which was not designed for this load, and the increased load eventually caused the plasticization of the confining tube; as a consequence, the entire device displayed a sway mechanism. Figure 3-8a,b shows the sway mechanism of the D26L585 grouted specimen during testing and the residual deformation observed after testing.

The experimental results suggested that the sway behaviour was mainly influenced by the effective slenderness ratio, λ_{eff} as defined later in Equation (3-4). As expected more slender specimens ($\lambda_{eff} \geq 32$) displayed lower buckling onset average strain, ε_{onset}. The experimental correlation between the two parameters is plotted in Figure 3-9 and highlights a linear trend of the average results across the three different specimens.

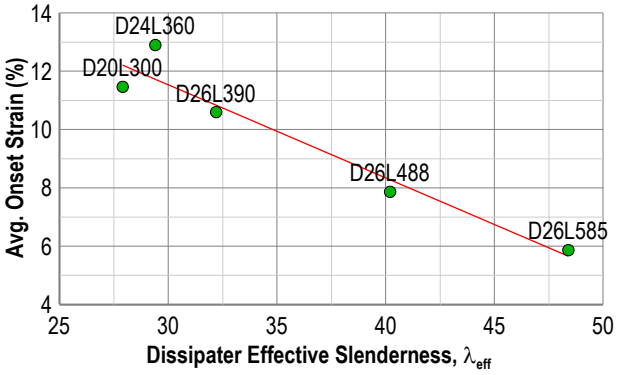

Figure 3-9. Onset strain vs. dissipater slenderness.

The issue is further investigated through numerical analyses in the final part of the paper.

As an indication of the fuse-tube interaction mechanism, the experimental force vs. average strain loops of Figure 3-7 shows the interaction onset strain in thicker dashed lines. The onset strain is defined as the maximum strain the device was subjected to before the interaction was triggered. For most of the specimens the onset strain was in the range of 9%; the experimental values are shown in Table 3-3 for all the specimens.

In general, the filling material, i.e. grout vs. epoxy, did not have any significant influence either on the overall force-displacement behaviour of the device or the failure mechanism displayed. Similar values of onset strain and maximum compressive force are observed, regardless of the filling material, as shown in Table 3-3.

Table 3-3. Summary of test results

ID No.	Filler material	Slenderness ratio		Max. Aver. Strain	Interaction Onset Avg. strain	Buckling Onset Avg. strain	Yield Force (F_y)	Max. Compr. Force (F_{max})	F_{max}/F_y
		Fuse	*Effective*	*(%)*	*(%)*	*(%)*	*(kN)*	*(kN)*	*(kN)*
D12L180	Grout 1	60	25.7	11.8	-	-	41.4	87.3	2.11
	Grout 2	60	25.7	8.8			42.3	94.8	2.24
	Epoxy	60	25.3	11.5			42.7	103.3	2.42
D20L300	Grout 1	60	27.9	12.8	8.9	8.9	97.7	232.8	2.38
	Grout 2	60	27.9	12.7	9.0	12.7	98.5	241.3	2.45
	Epoxy	60	27.6	8.9	8.9	8.9	95.4	182.5	1.91
D24L360	Grout 1	60	29.4	12.9	8.9	12.9	160.1	402.3	2.51
	Grout 2	60	29.4	12.9	8.9	12.9	160.2	364.8	2.28
	Epoxy	60	29.2	12.9	8.9	12.9	157.4	372.7	2.37
D26L390	Grout 1	60	32.2	8.9	5.9	8.9	207.0	360.0	1.74
	Grout 2	60	32.2	10.0	5.9	8.9	193.8	357.0	1.84
	Epoxy	60	32.1	12.9	5.9	8.8	208.0	305.3	1.47
D26L488	Grout 1	75	40.3	12.8	5.8	8.8	185.8	353.5	1.90
	Grout 2	75	40.2	8.9	5.9	8.9	185.6	307.2	1.66
D26L585	Grout 1	90	48.4	8.9	4.1	5.9	181.0	291.9	1.61
	Grout 2	90	48.4	11.5	3.9	5.8	187.5	293.0	1.56
	Epoxy	90	48.2	9.0	4.0	5.9	189.6	303.1	1.60

Fuse-tube interaction

Given the complexity of the interaction mechanisms between the fused bar and the anti-buckling system the phenomenon was further studied with an analytical model considering the contact stiffness, $k_{contact}$. This model was calibrated against experimental data using the parameters shown in Figure 3-10a and the approximated scheme reported in Figure 3-10b.

According to these assumptions, the device's overall stiffness is equal to the fused bar stiffness only until interaction with the anti-buckling tube is triggered.

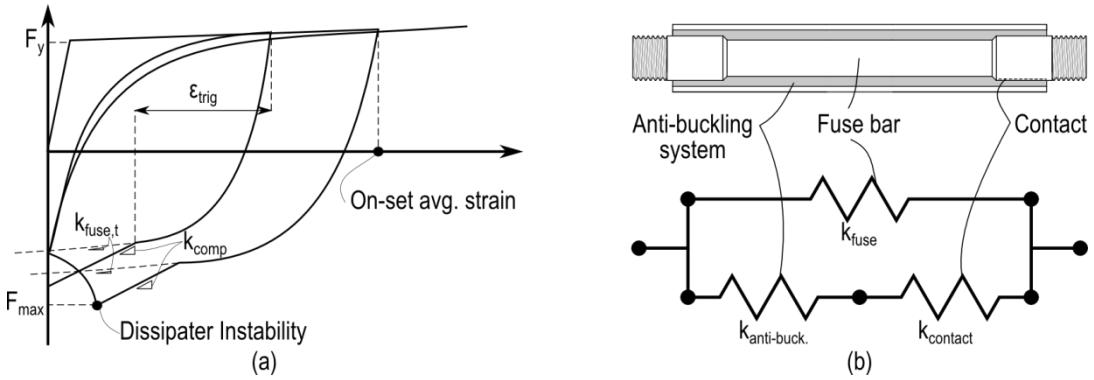

Figure 3-10. (a) Interaction parameters; (b) composite stiffness.

In the simplified analytical model, the device is idealized as two parallel springs where the first spring is the fused-bar stiffness and the second spring is the combination of the anti-buckling system and the contact stiffness; therefore, the total stiffness of the device is given as:

$$k_{comp} = k_{fuse,t} + \left(\frac{1}{k_{contact}} + \frac{1}{k_{anti-buck.}} \right)^{-1} \quad (3\text{-}1)$$

Where k_{comp} = the composite stiffness

$k_{fuse,t}$ = the fuse tangent stiffness

$k_{contact}$ = the contact stiffness

$k_{anti\text{-}buck.}$ = the anti-buckling system stiffness

The contact stiffness was experimentally determined using equation (3-1).

The fused bar stiffness was evaluated using tangent properties (i.e. inelastic) as shown in Equation (3-2).

$$k_{fuse,t} = \frac{E_{s,t} A_{fuse}}{L_{fuse}} \quad (3\text{-}2)$$

Where $E_{s,t}$ = the steel tangent modulus of elasticity

A_{fuse} = the fuse area

L_{fuse} = the fuse length

The stiffness of the anti-buckling system was evaluated considering both the confining tube and filling material properties using Equation (3-3).

$$k_{anti-buckl.} = \frac{E_s A_{tube}}{L_{tube}} + \frac{E_{fill} A_{fill}}{L_{tube}} \quad (3\text{-}3)$$

Another significant parameter for characterizing the interaction behaviour is the difference between the onset strain and the strain level at which the interaction is triggered, defined as ε_{trig}. This parameter was determined from experimental results as shown in Figure 3-10a.

Table 3-4. Dissipater interaction properties.

ID No.	λ_{eff}	Filling material	ε_{trig}	$k_{fuse,t.}$ (kN/mm)	k_{tot} (kN/mm)	$k_{anti\text{-}buck.}$ (kN/mm)	$k_{contact}$ (kN/mm)
	25.7	Grout	6.0%	1.8	9.3	185.2	7.9
D12L180	25.7	Grout	5.4%	2.0	9.1	185.2	7.5
	25.3	Epoxy	5.3%	2.7	7.2	156.6	4.6
	27.9	Grout	5.2%	3.3	10.2	265.1	8.1
D20L300	27.9	Grout	5.3%	3.1	15.3	265.1	12.1
	27.6	Epoxy	3.7%	4.1	7.8	211.9	3.7
	29.4	Grout	6.7%	3.3	14.2	255.8	11.3
D24L360	29.4	Grout	7.2%	3.2	9.3	309.2	7.1
	29.2	Epoxy	6.8%	4.0	6.9	309.2	4.7
D26L390	32.2	Grout	6.0%	4.3	11.7	240.3	7.7
	32.1	Epoxy	5.1%	4.4	9.2	285.6	4.8
D26L488	40.3	Grout	6.6%	3.2	12.8	236.2	10.1
	40.2	Grout	6.3%	3.5	7.1	236.2	3.7

3.4 Numerical Modelling and parametric analysis

A simplified physical model was developed using OpenSees (McKenna, 2011) to account for the different behavioural aspects of the dissipaters, including low cycle fatigue, higher modes buckling behaviour, anti-buckling system interaction effects.

To model the entire device the anti-buckling system must be taken into account. A second pinned beam was introduced, and the section defined with fiber elements for both the tube and the filler as shown in Figure 3-11. The transversal displacements of the fuse bar and the anti-buckling system were rigidly coupled to impede relative displacement between the two elements.

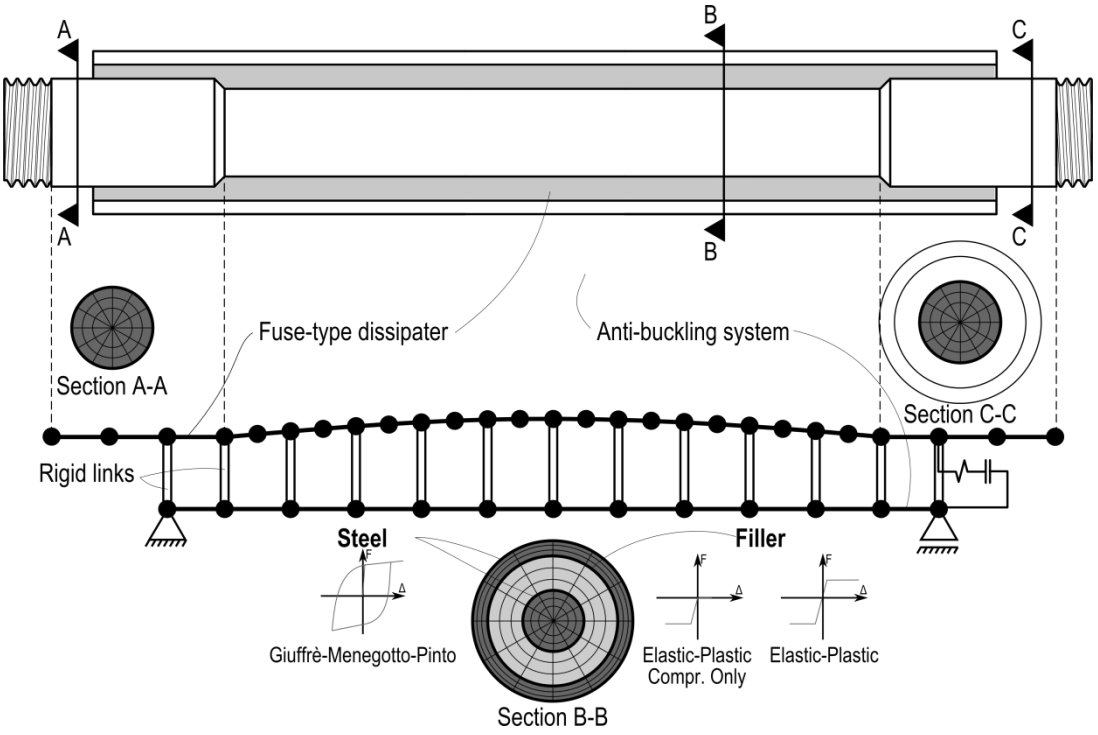

Figure 3-11. Dissipater model summary

Different stress-strain relationships were accounted for in the model. Steel elements followed a Menegotto-Pinto relationship (Menegotto *et al.*, 1973). The low-cycle fatigue model, proposed by Uriz (Uriz, 2008) and implemented in OpenSees, was used to predict low-cycle fatigue failure of the dissipaters tested.

Elastic-perfectly plastic compression only material for grout and elastic-perfectly plastic non-symmetric material for epoxy were used. The latter accounted for the different strength values of the epoxy used in the experimental campaign (see Section 3.3.1).

The interaction (in the axial direction) between the fused bar and the surrounding anti-buckling system, as observed in the experimental tests, was modelled using an elastic compression only gap spring connecting the tube and the dissipater. The gap and the stiffness values of the spring were calibrated against the experimental observations shown in Table 3-4. The spring element was activated in the model as soon as the dissipater strain reached the gap value ε_{trig} and it activated on the reversal branch of the cycle as soon as the gap value was reached.

Figure 3-12 shows that the numerical model can predict with good accuracy the behaviour of the device. The calibrated steel hysteresis can capture accurately the isotropic strain hardening occurring before the interaction is triggered. The numerical results after the interaction occurs are in good agreement with observed experimental behaviour; both the increased stiffness and the sway mechanism occurrence are captured.

Finally, the implemented low cycle fatigue model allowed the prediction of cycles to failure observed in experimental tests.

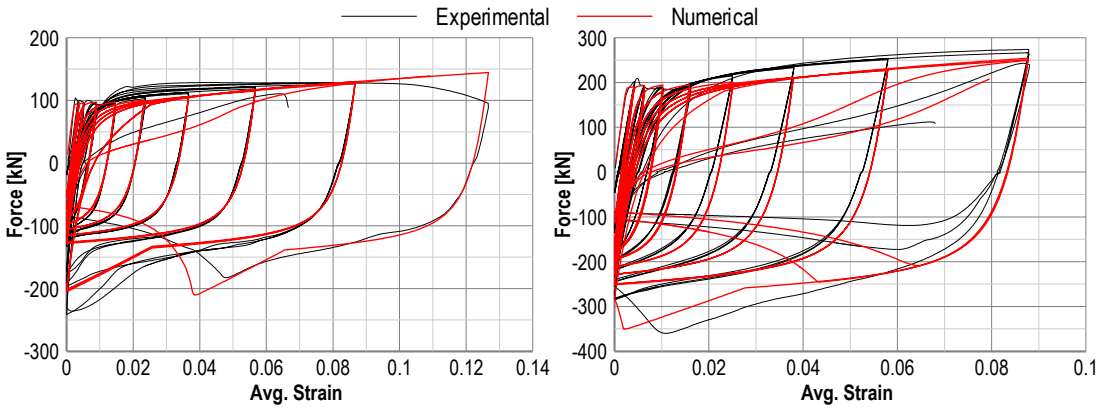

Figure 3-12. Experimental-Numerical comparison of specimens D20L300 (left) and D24L390 (right)

3.4.1 Parametric analysis

An extensive parametric analysis was carried out using the developed model calibrated versus experimental data as shown above.

The main objective of the parametric analysis was to investigate in more detail the occurrence of the failure mechanisms observed in the experimental campaign. In particular the parametric analysis was aimed at suggesting significant design parameters influencing the failure mechanisms of the device in order to support its design and detailing.

The two key design parameters are the onset average strain, ε_{trig}, and the maximum total compressive force, F_{max}. The former is defined as the maximum average strain (i.e. dissipater

displacement-to-fuse length ratio) before the entire dissipater instability phenomenon occurs. Figure 3-10 shows the two parameters on a qualitative force vs. average strain loop.

From the experimental results, these two parameters were observed to have a main influence in the failure behaviour of the device and deemed fundamental in the design and detailing of the device.

As part of this parametric study, the geometric parameters influencing the behaviour of the dissipater were considered more extensively. In particular, different fuse slenderness ratios ranging from 50 to 90 were investigated. Similarly to the experimental study, the geometric parameters chosen for the sensitivity analysis were: a) the fuse diameter, b) the filler diameter and c) the tube thickness. Three fuse diameters, namely 12mm, 18mm and 24mm, were chosen; the filler diameters were varied from 1.2, 1.5 or 2 times the fuse diameter; the tube thickness values of 2mm, 3mm or 4mm were considered. The variation of the geometrical properties of the connection parts was not investigated in this study: the diameter and lengths of the connection parts were set with the same proportions for each specimen with the length of the external part being $L_{ext} = 0.4L_{fuse}$ and the diameter $D_{ex} = 1.33D_{fuse}$.

The properties of the interaction spring were calibrated to the average values of the onset strain, $\varepsilon_{trig,}$ and the contact stiffness, $k_{contact}$,resulting from the experimental data (see Table 3-4), being 0.06 and 8.0kN/mm, respectively.

As the experimental data highlighted that the filling material did not have significant influence on the dissipater behaviour, cement grout only was considered in the parametric study.

The results of the parametric numerical analyses are plotted in terms of onset average strain, ε_{trig}, and maximum compressive force ratio in Figure 3-13.

The effective slenderness ratio, λ_{eff}, was used as a significant parameter to represent the combination of the different geometric and material properties of the dissipater's components. λ_{eff} is defined in Equation (3-4).

$$\lambda_{tot} = L_{fuse}\sqrt{\frac{A_{fuse} + A_{tube} + A_{eff,fill}}{I_{fuse} + I_{tube} + I_{eff,fill}}} \qquad (3\text{-}4)$$

Where L_{fuse} = the fuse length

A_{fuse} = the fuse cross-sectional area

A_{tube} = the tube cross-sectional area

A^*_{fill} = the filler steel-equivalent cross-sectional area

I_{fuse} = the fuse second moment of area

I_{tube} = the tube second moment of area

I^*_{fill} = the filler steel-equivalent second moment of area

$$A_{eff,fill} = nA_{fill},\ n = \frac{E_{fill}}{E_s} \tag{3-5}$$

$$I_{eff,fill} = \left(D^4_{eff,fill} - D^4_{eff,fuse}\right)\frac{\pi}{64} \tag{3-6}$$

Where $D_{eff,fill}$ and $D_{eff,fuse}$ are the effective filler and fuse diameters given in Equation (3-7).

$$\begin{aligned} D_{eff,fuse} &= 0.5\left[D_{fill} + D_{fuse} - n\left(D_{fill} - D_{fuse}\right)\right] \\ D_{eff,fill} &= 0.5\left[D_{fill} + D_{fuse} + n\left(D_{fill} - D_{fuse}\right)\right] \end{aligned} \tag{3-7}$$

Numerical results reported in Figure 3-13 were fitted with exponential functions and the proposed equations for the onset average strain and maximum compressive force ratio are reported below as a function of the section composite slenderness ratio.

$$\varepsilon_{onset} = 0.537\lambda_{eff}^{-0.537} \tag{3-8}$$

$$\frac{F_{max}}{F_y} = 30.9\lambda_{eff}^{-0.759} \tag{3-9}$$

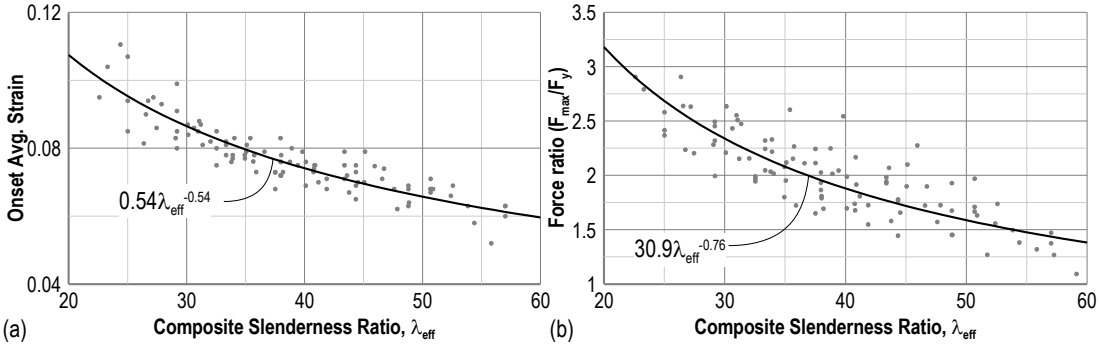

Figure 3-13. Parametric analysis results. (a) onset average strain and (b) maximum compressive force vs. composite slenderness ratio

3.5 Analytical models

To capture the monotonic behaviour (i.e. backbone curve) of the device, the different displacement contributions of the dissipater shall be taken into account.

The major contribution is the fuse displacement, yet the yield displacement of the device can be significantly underestimated by considering only this contribution.

Equation (3-10) gives the total dissipater contribution in the elastic range of stresses:

$$\Delta = \frac{FL}{EA} = \sum \frac{FL_{ex,i}}{EA_{ex,i}} + \sum \frac{FL_{conn,i}}{EA_{conn,i}} + \frac{FL_{fuse}}{EA_{fuse}} \qquad (3\text{-}10)$$

Where F = the applied force
E = the steel elastic modulus
$L_{ex,i}$ = the external length
$L_{conn,i}$ = the connection length
$A_{ex,i}$ = the external cross-sectional area
$A_{conn,i}$ = the connection cross-sectional areas

In most cases the dissipater external and connection lengths and areas are equal; therefore, the yield displacement of the dissipater can be simplified as follows:

$$\Delta = \frac{F}{E}\left(\frac{L_{tot} - L_{fuse}}{A_{ex}} + \frac{L_{fuse}}{A_{fuse}}\right) = \frac{FL_{fuse}}{EA_{fuse}}\left[1 + \left(\frac{L_{tot}}{L_{fuse}} - 1\right)\frac{D_{fuse}^2}{D_{ex}^2}\right] \qquad (3\text{-}11)$$

Where L_{tot} = the total dissipater length
D_{fuse} = the fuse diameter
D_{ex} = the external diameter

A correction factor k_a was defined to account for the additional displacement contributions coming from the connection parts of the dissipater.

$$k_a = 1 + \left(\frac{L_{tot}}{L_{fuse}} - 1\right)\frac{D_{fuse}^2}{D_{ex}^2} \qquad (3\text{-}12)$$

Similarly, a correction factor, k_b, for the post-yield stiffness of the dissipater can be worked out considering an elastic-plastic stress-strain relationship and assuming the yielding concentrates in the fused portion only.

$$k_b = \left[\frac{1}{r} + \left(\frac{D_{fuse}}{D_{ex}}\right)^2\left(\frac{L_{tot}}{L_{fuse}} - 1\right)\right] \qquad (3\text{-}13)$$

Substituting the latter, the total displacement distribution post-yield can be given as:

$$\Delta = \frac{k_a f_y L_{fuse}}{E} + \frac{k_b \left(f_s - f_y \right) L_{fuse}}{E} = \left[\left(k_a - k_b \right) f_y + k_b f_s \right] \frac{L_{fuse}}{E} = \left[\left(1 - \frac{1}{r} \right) f_y + k_b f_s \right] \frac{L_{fuse}}{E} \qquad (3\text{-}14)$$

Table 3-5 shows the comparison of the analytical results versus the experimentally measured stiffness and yielding forces.

Table 3-5. Experimental vs. analytical model comparison, corrected dissipater stiffness.

ID No.	D_{ex}	D_{fuse}	k_{fuse}	k'	k_{exp}	$\Delta_{y,fuse}$	$\Delta_{y,a}$	$\Delta_{y,exp}$	F_y	error mod.	error fuse
	mm	*mm*	*kN/mm*	*kN/mm*	*kN/mm*	*mm*	*mm*	*kN/mm*	*kN*	*%*	*%*
D12L180	16	12	126	81	69	0.34	0.52	0.61	42	-14.9	-45
D20L300	24	20	209	113	121	0.47	0.87	0.81	98	7.3	-42
D24L360	32	24	251	123	129	0.62	1.28	1.24	156	3.0	-50
D26L390	32	26	272	178	173	0.67	1.07	1.10	190	-3.3	-37
D26L488	32	26	218	153	168	0.87	1.23	1.13	188	8.8	-23
D26L585	32	26	182	134	128	1.03	1.39	1.52	187	-7.9	-32

The analytical results are in good agreement with the experimental data with a maximum deviation of 15% from the observed values and an average deviation of 7.5%. When considering the fuse contribution alone a more significant deviation is observed as values of Table 3-5 show. The maximum and average deviation from the experimental values are 50% and 38%, respectively (Sarti *et al.*, 2013).

3.6 Cyclic analytical force-displacement curve

Based on experimental observations and numerical and analytical modelling results, a force-displacement hysteresis can be calibrated accounting for the different behavioural aspects highlighted in the laboratory test results.

3.6.1 The Giuffrè-Menegotto-Pinto rule

For modelling the mild steel used in the experimental campaign the Giuffrè-Menegotto-Pinto rule was adopted and calibrated versus the experimental results. The model was first proposed by Giuffrè and Pinto (1970) and later modified by Menegotto and Pinto (1973). Alternatively different hysteretic rules suitable for modelling the steel cyclic behaviour such as Dodd-Restrepo (1995) can be used.

Equation (3-15) represents the transition curve from the elastic to the inelastic asymptote of the force-displacement trend.

$$F^* = r\Delta^* + \frac{(1-r)\Delta^*}{\left(1+\Delta^{*R}\right)^{\frac{1}{R}}} \tag{3-15}$$

Where

$$\Delta^* = \frac{\Delta - \Delta_r}{\Delta_0 - \Delta_r} \tag{3-16}$$

And

$$F^* = \frac{F - F_r}{F_0 - F_r} \tag{3-17}$$

Where F_0, Δ_0 and F_r, Δ_r are the coordinates of the intersection point of the two asymptotes of the strain reversal point respectively (see Figure 3-14).

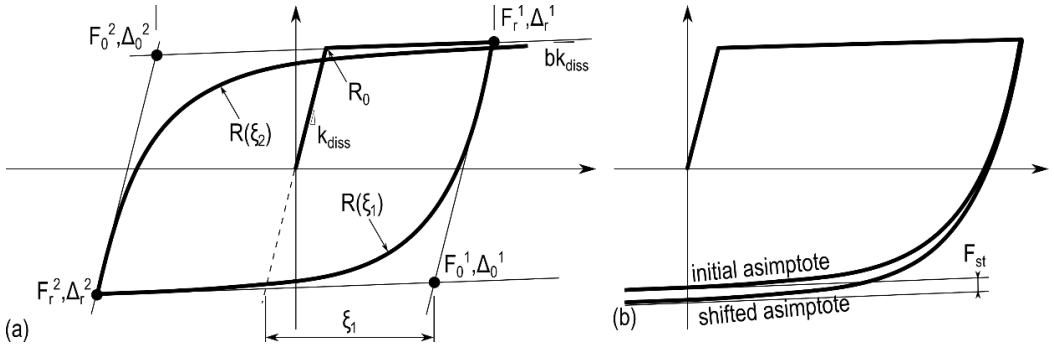

Figure 3-14. Giuffrè-Menegotto-Pinto hysteresis rule nomenclature (modified from Filippou et al. (1983)).

Figure 3-14 shows the behaviour and key parameters of the hysteretic force-displacement loop. The initial stiffness, k_{diss}, is taken accordingly to analytical models, and reported in Equation (3-18).

$$k_{diss} = \frac{EA_{fuse}}{k_a L_{fuse}},\ k_a = 1 + \left(\frac{L_{tot}}{L_{fuse}} - 1\right)\frac{D_{fuse}^2}{D_{ex}^2} \tag{3-18}$$

The dissipater's post-yielding stiffness factor, r, was defined using the modification factors k_a and k_b as follows:

$$r = \frac{k_a}{k_b} = \left[1 + \left(\frac{L_{tot}}{L_{fuse}} - 1\right)\frac{D_{fuse}^2}{D_{ex}^2}\right] \Big/ \left[\frac{1}{r} + \left(\frac{L_{tot}}{L_{fuse}} - 1\right)\frac{D_{fuse}^2}{D_{ex}^2}\right] \tag{3-19}$$

The curvature of the elastic-plastic transition, R, of Equation (3-20) is dependent on the displacement difference, ξ, between the current asymptote intersection point, Δ_0, and the previous load reversal point, Δ_r.

$$R = R_0 - \frac{a_1 \xi}{a_2 + \xi} \qquad (3\text{-}20)$$

Where a_1, a_2 = experimentally determined parameters to be defined together with R_0 (Filippou *et al.*, 1983).

The strain hardening highlighted in the force-displacement loops was modelled by shifting the yield asymptote using the relation of Equation (3-21).

$$\frac{F_{st}}{F_y} = a_3 \left(\frac{\Delta_{max}}{\Delta_y} - a_4 \right) \qquad (3\text{-}21)$$

Where Δ_{max} =the maximum displacement at the instant of strain reversal

a_3, a_4 = experimental determined parameters.

3.6.2 Interaction properties

The interaction of the tube and fused bar was modelled using a simplified approach as shown in Section 3.3.4. An interaction spring of stiffness $k_{contact}$ was activated as soon as the contact interaction was triggered; consequently, the composite stiffness, k_{comp}, was evaluated as:

$$k_{comp} = k_{fuse,t} + \left(\frac{1}{k_{contact}} + \frac{1}{k_{anti-buck.}} \right)^{-1}$$

The interaction was triggered when the displacement Δ_{trig} was reached on the reversal cycle as shown in Figure 3-15.

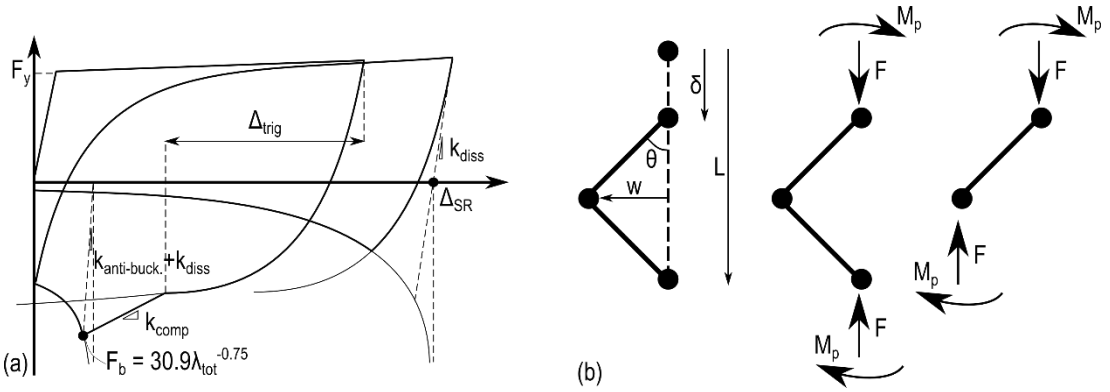

Figure 3-15. (a) Buckling path. (b) Equilibrium of a buckled bar (modified from (Gomes et al., 1997))

3.6.3 Instability

The approach proposed by Gomes and Appleton (1997) was used to predict the instability mechanism of the dissipater. The model assumed that a plastic hinge was developing at the mid-span of the bar, and the displacement compatibility between the transversal displacement and vertical displacement was defined.

The equilibrium of the buckled bar can is defined by Equation (3-22)

$$F = \frac{2M_p}{w} \tag{3-22}$$

Where w = the transversal displacement of the buckled bar

M_p = the plastic moment of the dissipater

The compatibility between the transversal displacement, the longitudinal displacement δ and the rigid body rotation θ can be expressed in Equation (3-23)

$$w = \frac{L}{2}\sin\theta,\ \Delta = L(1-\cos\theta) \tag{3-23}$$

Expanding in series and ignoring the third- and higher-order terms gives (Gomes *et al.*, 1997):

$$F = \frac{2\sqrt{2}M_p}{\sqrt{L}}\frac{1}{\sqrt{\Delta}} \tag{3-24}$$

To include in Equation (3-24) in the global force-displacement relationship the curve vertical asymptote was shifted with respect to the zero force point Δ_{SR}. The latter was determined by the zero force point of either the composite section (dissipater and anti-buckling system) if the global instability has not occurred; the global buckling load can be determined using Equation (3-9) resulting from the parametric analysis. Once the restraining system has buckled, the zero force point of the fused bar shall be taken into account as shown in Figure 3-15a.

3.6.4 Experimental results comparison

Experimental data presented in paragraph 3.3.4 was used to calibrate the parameters presented in the preceding paragraphs. The Giuffrè-Menegotto-Pinto parameters used in the analysis were: (a) $a_1 = 18.5$; (b) $a_2 = 0.2$; (c) $a_3 = 0.02$; (d) $a_4 = 7$.

The following interaction properties were used accordingly to the average values observed in the experimental tests: $\Delta_{trig} = 0.06L_{fuse}$ and $k_{contact} = 6kN/m$.

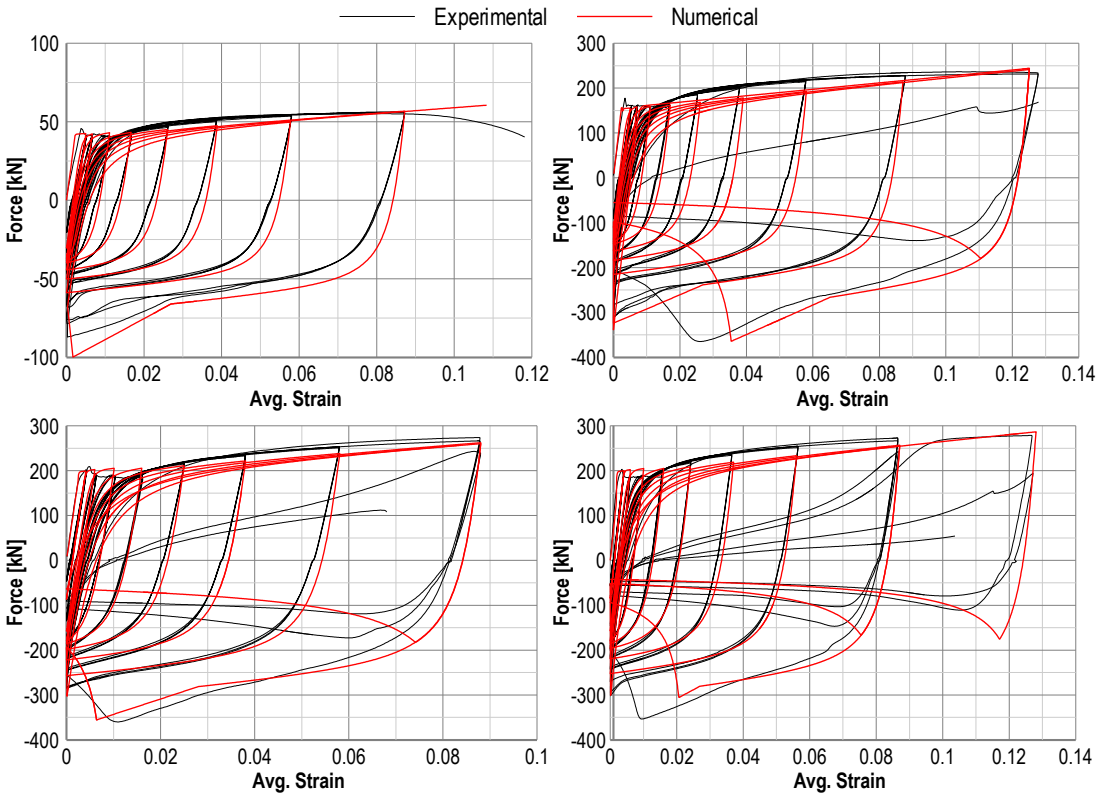

Figure 3-16. Macro-model vs. experimental results. (a) D12L180, (b) D24L360, (c) D26L390, (d) D26L488.

The comparison charts of the proposed hysteretic force-displacement rule against experimental results are plotted in Figure 3-16. During the testing of the specimen D12L180 the fused bar-anti-buckling system interaction was triggered, but the sway mechanism did not occur. In fact, according to Equation (3-8) the instability load from numerical analysis would be:

$$F_{max} = 30.9\lambda_{tot}^{-0.759} F_y = 30.9 \cdot 25.7^{-0.759} \cdot 42kN = 111kN \qquad (3\text{-}25)$$

The value above was not reached during testing and no instability mechanism occurred.

For more slender specimens the sway mechanism occurred and the macro-model developed was capable of predicting the failure mechanism and similar stiffness degradation as shown in Figure 3-16(b-d).

3.7 Conclusions

The chapter presented the experimental and numerical study of the fuse-type buckling-restrained mild steel dissipater. The dissipater has been most commonly used in jointed ductile precast concrete and timber post-tensioning technologies in recent years.

The main objective of this experimental program was to provide a comprehensive set of experimental and numerical data to support the dissipater design and to calibrate a hysteretic rule presented in the final part of the chapter.

The experimental program included several geometric parameters such as fuse diameter, fuse length and anti-buckling system geometry, and was performed using a standard quasi-static protocol for tension-only displacements.

The experimental results highlighted a stable behaviour up to 6% average strain (i.e. displacement-fuse length ratio). When the specimen underwent higher displacements, the sway mechanism of the internal bar caused interaction between the fused bar and the anti-buckling system. The contact between the two systems subjected the anti-buckling system to compressive load which caused a sway mechanism in the restraining tube as well.

Experimental results showed that a fuse slenderness ratio, λ_{fuse}, lower than 60 is preferred. For higher slenderness values the anti-buckling system must be detailed considering interaction of the fused bar and the filler.

A numerical model was developed using OpenSees in order to capture the different mechanisms observed in the laboratory tests. The numerical results showed the model can accurately predict the behaviour and failure mechanisms observed during experimental testing.

The parametric analysis considered a more comprehensive variation of the significant parameters. The numerical study allowed the evaluation of significant design parameters. In particular, the latter are the onset average strain and the maximum compressive force in the dissipater.

The results of the parametric analysis as well as the analytical models provided the calibration for the hysteretic force-displacement rule proposed in the final part of the chapter.

3.8 References

ACI Innovation Task Group 5 2008. *Acceptance criteria for special unbonded post-tensioned precast structural walls based on validation testing and commentary : an ACI standard*. Farmington Hills, Mich., American Concrete Institute.

Amaris Mesa, A.D. 2010. Developments of Advanced Solutions for Seismic Resisting Precast Concrete Frames *PhD Dissertation*, University of Canterbury, Christchurch, New Zealand.

Armstrong, T., Smith, T., Buchanan, A., Pampanin, S. 2014. Experimental testing of alternative beam-column joints in post-tensioned timber frames. *NZSEE Conference*, Auckland, New Zealand.

Black, C., Makris, N., Aiken, I. 2004. Component Testing, Seismic Evaluation and Characterization of Buckling-Restrained Braces. *Journal of Structural Engineering* 130(6): 880-894.

Brown, A., Lester, J., Pampanin, S., Pietra, D. 2012. Pres-Lam in practice - A damage-limiting rebuild project. *New Zealand Society of Structural Engineers Conference*, Auckland, New Zealand.

Cattanach, A., Pampanin, S. 2008. 1st Century Precast: the Detailing and Manufacture of NZ's First Multi-Storey PRESSS-Building. *NZ Concrete Industry Conference*, Rotorua.

Clark, P., Aiken, I., Kasai, K., Kimura, I. Large-Scale Testing of Steel Unbonded Braces for Energy Dissipation. *Advanced Technology in Structural Engineering***:** 1-5.

Dodd, L., Restrepo-Posada, J. 1995. Model for predicting cyclic behavior of reinforcing steel. *Journal of Structural Engineering* 121(3): 433-445.

Filippou, F.C., Popov, E.P., Bertero, V.V. 1983. Effects of bond deterioration on hysteretic behavior of reinforced concrete joints.

Fujimoto, M., Wada, A., Saeki, E., Watanabe, A., Hitomi, Y. 1988. A study on the unbonded brace encased in buckling-restraining concrete and steel tube. *Journal of Structural and Construction Engineering, AIJ* 34: 249-258.

Giuffrè, A., Pinto, P. 1970. Il comportamento del cemento armato per sollecitazioni cicliche di forte intensità. *Giornale del Genio Civile* 5(1): 391-408.

Gomes, A., Appleton, J. 1997. Nonlinear cyclic stress-strain relationship of reinforcing bars including buckling. *Engineering Structures* 19(10): 822-826.

Horie, T., Yabe, Y., Hori, T., Nakamura, S. 1993. Elasto-plastic behavior of steel brace with restraint system for post buckling. *Annual Technical Papers of Steel Structures* 1: 187-194.

Inoue, K., Sawaizumi, S., Higashibata, Y., Inoue, K. 1993. Stiffening design at the edge of reinforced concrete panel including unbonded steel diagonal braces. *Journal of Structural Engineering* 443: 137-146.

Iqbal, A., Pampanin, S., Buchanan, A.H. 2010. Seismic Performance of Prestressed Timber Beam-Column Sub-Assemblies. *New Zealand Society for Earthquake Engineering, Annual Conference*, Wellington, New Zealand.

Iqbal, A., Pampanin, S., Buchanan, A.H., Palermo, A. 2007. Improved Seismic Performance of LVL Post-tensioned Walls Coupled with UFP devices. *8th Pacific Conference on Earthquake Engineering*, Singapore.

Marriott, D., Pampanin, S., Bull, D.K., Palermo, A. 2007. Improving the Seismic Performance of Existing Reinforced Concrete Buildings using Advanced Rocking Wall Solutions. *NZSEE Conference*, Palmerston North, New Zealand.

Marriott, D.J. 2009. The Development of High-Performance Post-Tensioned Rocking Systems for the Seismic Design of Structures *PhD Dissertation*, Universtiy of Canterbury, Christchurch, New Zealand.

Marriott, D.J., Pampanin, S., Bull, D., Palermo, A. 2008. Dynamic Testing of Precast, Post-Tensioned Rocking Wall Systems with Alternative Dissipating Solutions. *Bulletin of the New Zeland Society for Eartquake Engineering* 41(2): 90-103.

McKenna, F. 2011. OpenSees: A Framework for Earthquake Engineering Simulation. *Computing in Science and Engg.* 13(4): 58-66.

Menegotto, M., Pinto, P.E. 1973. Method of Analysis for Cyclically Loaded Reinforced Concrete Plane Frames Including Changes in Geometry and Non-elastic Behavior of Elements Under Combined Normal Force and Bending. *IABSE Symposium on the Resistance and Ultimate Deformability of Structures Acted on by Well-Defined Repeated Loads, Lisbon*.

Nagao, N., Takahashi, S. 1990. A study on the elasto-plastic behavior of unbonded composite bracing (Part 1: experiments on isolated members under cyclic loading). *Journal of Structural Engineering* 415: 105-115.

Nakaki, S.D., Stanton, J.F., Sritharan, S. 1999. An overview of the PRESSS five-story precast test building. *PCI journal* 44(2): 26-26.

Newcombe, M.P., Pampanin, S., Buchanan, A.H. 2010. Design, fabrication and assembly of a two-storey post-tensioned timber building. *World Conference on Timber Engineering*.

Palermo, A., Pampanin, S., Buchanan, A.H. 2006a. Experimental Investigations on LVL seismic resistant wall and frame subassemblies. *First European Conference on Earthquake Engineering and Seismology*, Geneva, Switzerland.

Palermo, A., Pampanin, S., Fragiacomo, M., Buchanan, A.H., Deam, B. 2006b. Innovative Seismic Solutions for Multi-Storey LVL Timber Buildings. *9th World Conference on Timber Engineering*, Portland, Oregon, USA.

Pampanin, S. 2005. Emerging solutions for high seismic performance of precast/prestressed concrete buildings. *Journal of Advanced Concrete Technology* 3(2): 207-223.

Pampanin, S., Amaris Mesa, A.D., Palermo, A. 2006. Implementation and Testing of Advanced Solutions for Jointed Ductile Seismic Resisting Frames. *Second International fib Congress*, Naples, Italy.

Priestley, M.J.N. 1991. Overview of PRESSS research program. *PCI Journal* 36(4): 50-57.

Priestley, M.J.N., Sritharan, S., Conley, J.R., Pampanin, S. 1999. Preliminary Results and Conclusions from the PRESSS Five-Story Precast Concrete Test Building. *PCI Journal* 44(6): 42-67.

Sabelli, R., Mahin, S., Chang, C. 2003. Seismic demands on steel braced frame buildings with buckling-restrained braces. *Engineering Structures* 25(5): 655-666.

Sarti, F., Smith, T., Palermo, A., Pampanin, S., Carradine, D.M. 2013. Experimental and analytical study of replaceable Buckling-Restrained Fused-type (BRF) mild steel dissipaters. *New Zealand Society for Earthquake Engineering Annual Conference*, Wellington, New Zealand.

Smith, T., Ludwig, F., Pampanin, S., Fragiacomo, M., Buchanan, A., Deam, B., Palermo, A. 2007. Seismic Response of Hybrid-LVL Coupled Walls Under Quasi-Static and Pseudo-Dynamic Testing. *NZSEE Conference*.

Smith, T., Ponzo, F.C., Di Cesare, A., Pampanin, S., Carradine, D., Buchanan, A.H., Nigro, D. 2013. Post-Tensioned Glulam Beam-Column Joints with Advanced Damping Systems: Testing and Numerical Analysis. *Journal of Earthquake Engineering* 18(1): 147-167.

Suzuki, N., Kono, R., Higasibata, Y., Sasaki, T., Segawa, T. 1994. Experimental study on the H-section steel brace encased in RC or steel tube. *Summaries of Technical Papers of Annual Meeting, Architectural Institute of Japan*.

Uang, C.-M., Nakashima, M., Tsai, K.-C. 2004. Research and application of buckling-restrained braced frames. *International Journal of Steel Structures* 4(4): 301-313.

Uriz, P. 2008. *Toward earthquake-resistant design of concentrically braced steel-frame structures*, Pacific Earthquake Engineering Research Center.

Wakabayashi, M., Nakamura, T., Kashibara, A., Morizono, T., Yokoyama, H. 1973. Experimental study of elasto-plastic properties of precast concrete wall panels with built-in insulating braces. *Summaries of Technical Papers of Annual Meeting, Architectural Institute of Japan*.

4 Investigation on the strain penetration length in internal epoxied bars for energy dissipation

4.1 Introduction

The chapter has the main objectives to experimentally determine the response of internal bars in terms of tensile strain penetration effects, and determine a simplified formulation for the slip due to strain penetration effects.

The chapter addresses the research objectives through a comprehensive set of experimental tests on epoxied bar loaded in the parallel-to-the-grain direction.

After briefly discussing past research on the subject, the chapter presents the testing methodology. Several specimens were tested in the experimental campaign accounting for different geometric and material properties. In particular several bar diameters were accounted for as well as two different steel grades were used in the experimental program.

The strain profile along the bond region was recorded through strain gauges fixed to the epoxied bars before the specimens were assembled and those provided the experimental results for the calibration of the simplified analytical model.

The chapter then shows the experimental data fitting methodology which is based on bond theory of reinforced concrete, and it is used to evaluate the slip due to tensile strain penetration effects.

In the final part of the chapter, the experimental results are used to develop simplified design equations for the determination of the slip due to strain penetration effects.

4.2 Strain penetration in past research

The concept of an equivalent strain penetration length was first introduced for flexural analysis of concrete elements and the definition of the element's plastic hinge length. Theoretical values for the equivalent plastic hinge length based on the integration of the curvature distribution for typical members would make such length directly proportional to the total length of the element. Such values do not, however, agree well with experimentally measured lengths. This is because, as shown in Figure 4-1c and d, the theoretical curvature distribution ends abruptly at the base of the cantilever, while steel tensile strains continue, due to finite bond stress, for some depth into the footing. The elongation of bars beyond the theoretical base leads to additional rotation and deflection. The phenomenon is referred to as tensile strain penetration (Paulay *et al.*, 1992).

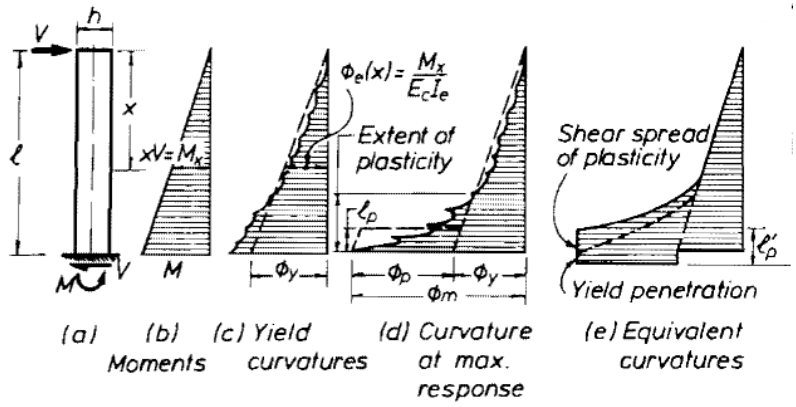

Figure 4-1. Moment, curvature and deflection relationships for a prismatic reinforced concrete or masonry cantilever (modified from Paulay and Priestley (1992)).

Based on experimental research carried out by Sritharan (1998), Equation (4-1) reports the calibrated equivalent strain penetration length for bonded steel reinforcing bars.

$$l_{sp} = 0.022 f_y d_b \,(mm) \qquad (4\text{-}1)$$

Where f_y= bar's tensile strength (MPa)

d_b= bar diameter (mm)

The calibrated analytical model is widely adopted in literature for the design of reinforced concrete elements (Paulay *et al.*, 1992; Priestley *et al.*, 2007).

Grouted bars have also been extensively used in post-tensioned rocking elements developed during the PREcast Seismic Structural Systems Program (PRESSS) (Priestley, 1991) and the analytical formula in Equation (4-1) was adopted to correctly determine the strain in partially unbonded bars used as dissipative source. In PRESSS systems internal bars are used

in combination to unbonded post-tensioning tendons providing a combination of dissipation and re-centering capabilities.

In more recent year the PRESSS system concept was extended to structural steel elements (Christopoulos *et al.*, 2002) and Laminated Veneer Lumber elements (Pres-Lam systems) (Palermo *et al.*, 2005).

In Pres-Lam elements, similarly to PRESSS systems, internal epoxied bars have been used as dissipative reinforcement (Figure 4-2a) (Palermo *et al.*, 2005; Newcombe, 2007).

Extensive experimental research on the behaviour of epoxied connections in timber have been carried out by Buchanan and Fairweather (1993) and Buchanan (2001) proving the high damping capabilities of such connections. Design provisions for epoxied bar in glulam and Laminated Veneer Lumber (LVL) have been provided by experimental research by Deng (1997) and Van Houtte (2003), respectively.

Whilst this research had been focusing on the strength of such connection type, limited research has been carried out on its stiffness.

The derivation of an approximate strain penetration length for mild steel bars embedded in timber was firstly attempted by Newcombe (2007) as part of a post-tensioned timber beam-column subassembly test.

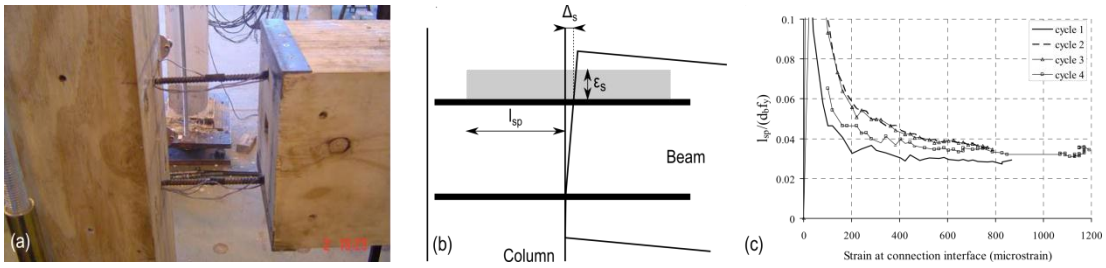

Figure 4-2.(a) Beam-column subassembly with internal bars; (b) assumed strain distribution for fully bonded energy dissipation system; (c) Average normalised strain penetration length assuming a uniform strain distribution within the bonded region for a beam-column connection vs. versus drift (modified from Newcombe (2007)).

Fully bonded epoxied bars were used as internal energy dissipation for beam-column subassembly. Three strain gauges were placed along the internal energy dissipaters in the attempt to measure the extent of the strain penetration (Figure 4-2a). By testing fully bonded energy dissipation it could be assumed that all the deformation was due to strain penetration. The latter was then inferred by assuming a constant strain profile over the strain penetration length as shown in Figure 4-2b.

Observing Figure 4-2c it was noted that the strain penetration length converged to an asymptote as the deformation increased. The average asymptotic value was approximately 130mm (or $0.032f_yd_b$ if it assumed that the strain penetration length is related to yield strength and bar diameter as it is for cement grout) (Newcombe, 2007):

$$l_{sp} = 0.032 f_y d_b \ (mm) \qquad (4\text{-}2)$$

Where f_y = yield strength of the bar (MPa)

d_b = bar diameter (mm)

Therefore, for fully bonded energy dissipation system the maximum strain, ε_s, at the connection interface can be approximated as:

$$\varepsilon_s = \frac{\Delta_s}{2l_{sp}} = \frac{\Delta_s}{0.064 f_y d_b} \qquad (4\text{-}3)$$

Where Δ_s = bar displacement from gap opening (see Figure 4-2b)

It is to be clarified that the average strain penetration length above is only valid for beam-column joints, where both parallel and perpendicular to the grain contributions are present. Newcombe (2007) observed from experimental results that the strain within the beam (i.e. parallel to the grain) is approximately 40% of the total (Newcombe, 2007); therefore, the strain penetration parallel to the grain can be calculated as:

$$l_{sp,para} = 0.024 f_y d_b \qquad (4\text{-}4)$$

4.3 Testing methodology

4.3.1 Testing schedule

To provide a comprehensive set of specimens, different bar types and geometric properties were considered in the experimental campaign. Both threaded and deformed bars were used, in particular M16, M20 and M24 (SP16t, SP20t and SP24t in Table 4-1) threaded bars and 20mm and 25mm diameter deformed bars were tested. The testing schedule is summarized in Table 4-1, which also reports the significant geometric properties of the specimens with reference to Figure 4-3.

Two main sets of specimens for each geometry were tested. At first, monotonic tests were carried out, and cyclic tests were then performed to assess whether degradation in the bond behaviour occurs.

The specimen dimensions in Table 4-1 were governed by the minimum edge distance according to Buchanan (2007) and also by standard profiles provided by the manufacturers.

A set of specimens were also designed to create a pull-out failure (BondSlip specimens in Table 4-1), so a shorter embedment length of 80mm was provided.

As anticipated, the experimental program was oriented to calibrate parallel-to-grain strain penetration effects; therefore, only this grain direction was considered in this study.

Table 4-1. Testing schedule.

ID	**Nom. Diam. (D_n)** *(mm)*	**Hole Diam. (D_h)** *(mm)*	**Spec. Length (L)** *(mm)*	**Spec. Section (b×h)** *(mm)*	**Fuse Diam. (D_{fuse})** *(mm)*	**Strain Gauge Spacing** *(mm)*
BondSlip	16	20	80	135×140	n/a	n/a
SP16t	16	20	290	135×140	14	25
SP20t	20	26	370	135×140	16	30
SP24t	24	30	550	180×190	20	35
SP20d	20	26	550	135×140	14	30
SP25d	25	32	800	180×190	16	35

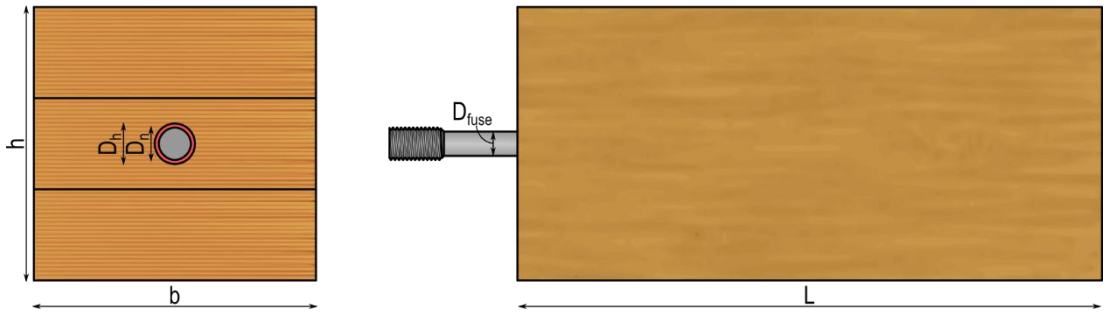

Figure 4-3. Specimen geometry.

4.3.2 Fabrication of the specimens

The specimens were fabricated out of LVL11 (Nelson Pine Industries Limited, 2012) standards profiles. To provide the required edge distance, different 63mm thick panels were glued together and a hole was drilled in the centre of the section allowing the bar to be inserted and glued. A hole was drilled at the bottom side of the specimen, allowing an optimal injection of the epoxy from the bottom up (Figure 4-4a).

Before gluing, some machining of the bars was necessary. To attach the specimen to the machine, a threaded end was to be provided. The threaded bar was readily available for threaded bars, yet for reinforcing bars that had to be machined from the deformed bars.

A fuse length was provided in the specimens and the reduced diameter was rounded down from the net diameter of the thread.

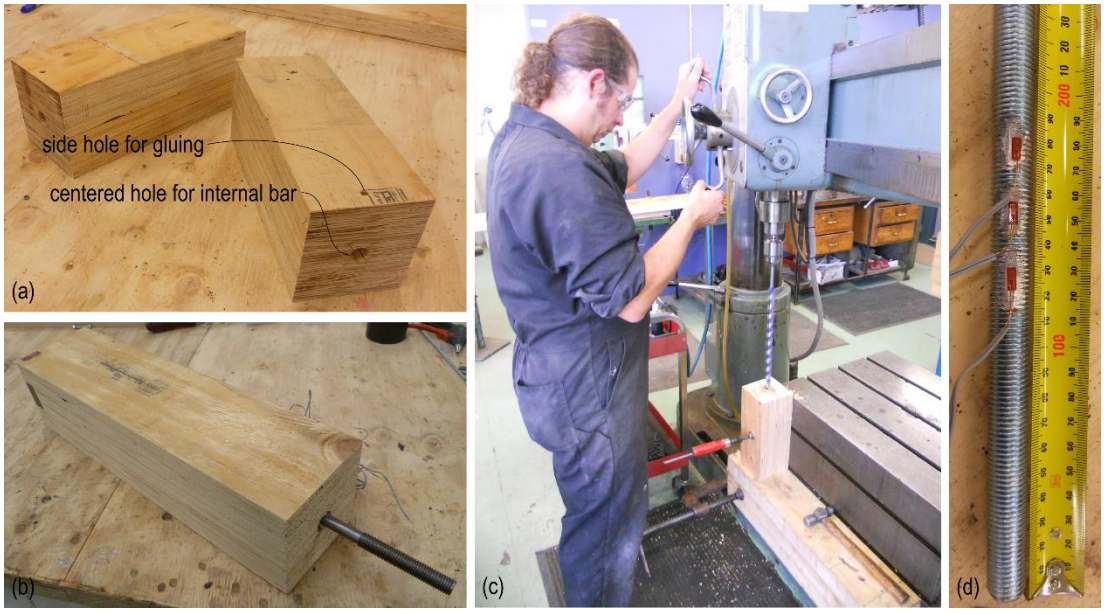

Figure 4-4. Fabrication of the specimens. (a) Timber blocks; (b) finished specimen; (c) drilling of the timber blocks; (d) strain gauges setup.

Instrumentation comprised of strain gauges glued on the bar; consequently, those were part of the fabrication process. To allow the strain gauges to be successfully glued on the bars, some surface preparation was necessary. For deformed bars, the surface had to be sanded to provide an even surface for the instruments. Differently, in the case of threaded bars (see Figure 4-4d), few threads needed to be grinded. The strain gauges were positioned at even distances in the specimens, using different spacing for each diameter. In particular, a spacing of 25mm, 30mm and 35mm was chosen for specimens SP16t, SP20t and SP24t respectively and 30mm and 35mm for specimens SP20d and SP25d.

4.3.3 Materials

The timber blocks were fabricated out of LVL11 standard profiles glued using resorcinol glue. The block was then machined to create the space allowing for clearance for the bar positioning. The bars were fixed to the timber element using epoxy resin Hilti HIT-RE500.

Two different steel grades were tested. At first Grade300E reinforcing steel bars were used, but also threaded mild steel bars were used (Grade 4.6). The nominal properties of the aforementioned materials are summarized in Table 4-2.

Table 4-2. Material nominal properties.

Laminated Veneer Lumber (LVL)		
Property		Value
Modulus of Elasticity	E_t	11000MPa
Bending strength	f_{bt}	38MPa
Compression strength	f_{ct}	45MPa

Epoxy resin (Hilti HIT-RE500)		
Property		Value
Compressive strength	f_c	82.7MPa
Tensile strength	f_t	43.5MPa
Modulus of Elasticity	E_{fill}	1.493GPa

Reinforcing steel (Grade300E)		
Property		Value
Yield stress	f_{ys}	300MPa
Ultimate stress	f_{us}	450MPa
Modulus of Elasticity	E_s	200GPa

Threaded bar steel (Grade 4.6)		
Property		Value
Yield stress	f_{ys}	320MPa
Ultimate stress	f_{us}	400MPa
Modulus of Elasticity	E_s	200GPa

4.3.4 Test setup and protocol

A Dartec 10MN Universal Testing Machine (UTM) was used as shown in Figure 4-5b. The testing machine had a maximum force of 10MN, with a maximum actuator stroke of 300mm and maximum and minimum velocities of 16 and 0.002 mm/s respectively. For the purposes of the experimental campaign the testing was carried out at 40mm/min.

The test setup (Figure 4-5b) included a set of steel connecting plates. Two plates were connected using 1.5" bolts to the 1000kN load cell and the moving head of the machine. The attachment of the specimen to the moving head at the bottom of the test setup comprised of a set of different interchangeable 135mm×135mm, 40mm thick plates. At the centre of the plate a threaded hole was drilled and tapped. Four M16 Grade 8.8 bolts connected the smaller plate to the moving head of the machine.

To connect the timber block, two 40mm thick plates were bolted to the load cell at the top of the machine using M24 G8.8 threaded bars. The specimen was then clamped between the two plates. Figure 4-5a shows the 3D view of the test setup with the indication of the different components.

The experimental testing comprised of both monotonic and cyclic protocols. The former was carried out by increasing the tensile displacement up to failure of the glued bar.

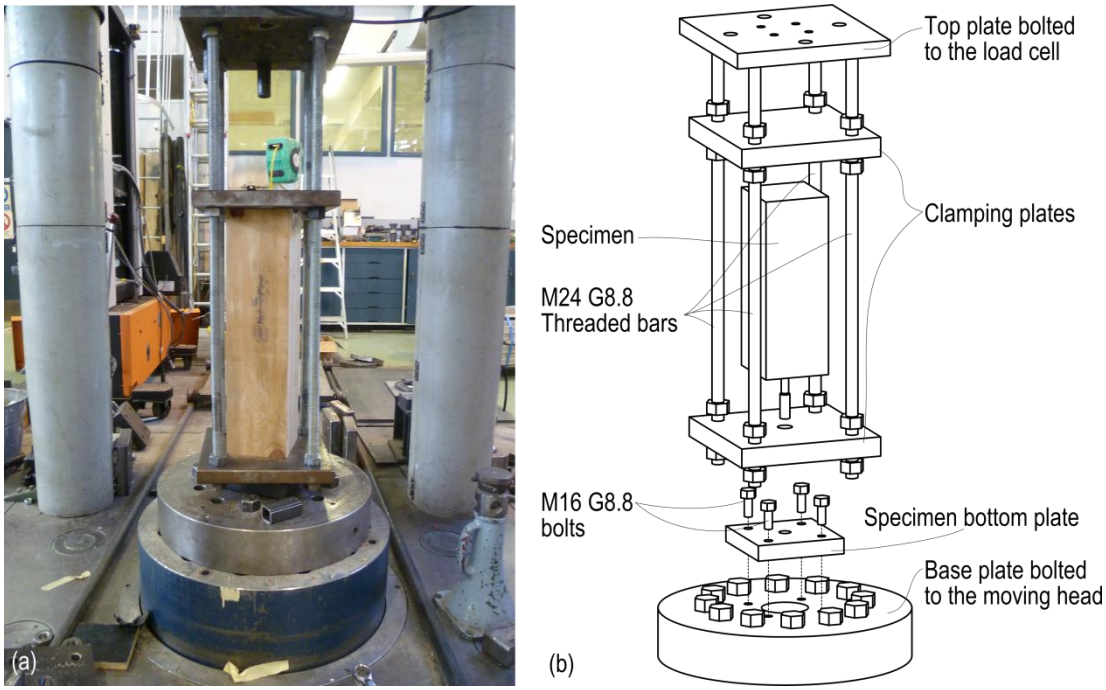

Figure 4-5. (a) Test setup 3D view and (b) testing machine.

Since tensile strain penetration effects investigation was targeted in the cyclic testing, only tension displacement were necessary and a modified regime based on ACI ITG-5.1-07 protocol (ACI Innovation Task Group 5, 2008) was used (see Figure 4-6).

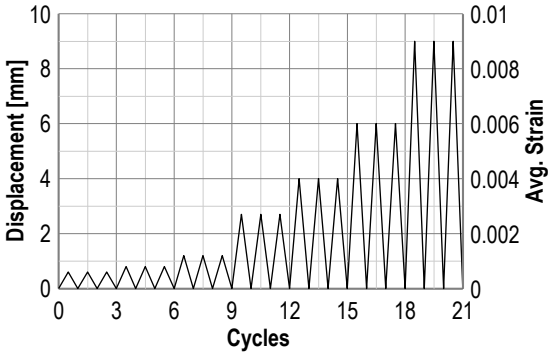

Figure 4-6. Testing protocol.

4.4 Determination of the bond stress-slip relationship

The first set of tests in the experimental program aimed to determine the bond stress-slip relationship for internal bars in timber. To achieve the purpose, the specimens were designed to have a short embedment length in order to trigger the pull-out failure mechanism.

The slip, s, was measured at the top of the specimen, while the force recorded by the load cell was converted into the average bond stress, τ, by dividing the force by the bond surface:

$$\tau = \frac{F}{D_h \pi L} \qquad (4\text{-}5)$$

Where F = recorded force

D_h = hole diameter (see Figure 4-3)

L = specimen length

Figure 4-6b shows the experimental results of the pull-out tests. The experimental force-slip charts show a brittle failure is occurring soon after the maximum bond stress is reached; therefore the bond stress-slip relationship can be approximated by a linear function.

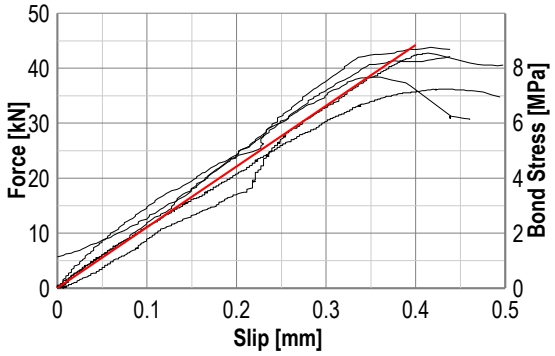

Figure 4-7. Force-slip pull-out tests experimental results

Based on the average results of the experimental tests the bond stress-slip relationship is:

$$\tau(s) = \frac{\tau_{max}}{s_1} s \qquad (4\text{-}6)$$

Where τ_{max} = maximum bond stress

s_1 = slip at maximum bond stress

Based on experimental results an average maximum bond stress of 8.8MPa and slip of 0.4mm were observed.

4.5 Instrumentation and data analysis

To analyse the experimental strain data, a theoretical approach was adopted and the differential equations governing the bond behaviour were considered (Fédération internationale du béton, 2000).

The instrumentation apparatus was mainly set up to determine the strain profile in the bond region; therefore, in addition to the general force-displacement behaviour recorded by the testing machine, multiple strain readings were recorded by the strain gauges glued on the bars as shown in Figure 4-4c.

The equations used in this chapter are based on the assumption of perfect elasticity for both the reinforcing steel and the timber in the bond region; moreover, long member behaviour was considered (Figure 4-8). According to this assumption a portion of the anchorage is ineffective because of slip absence (Fédération internationale du béton, 2000).

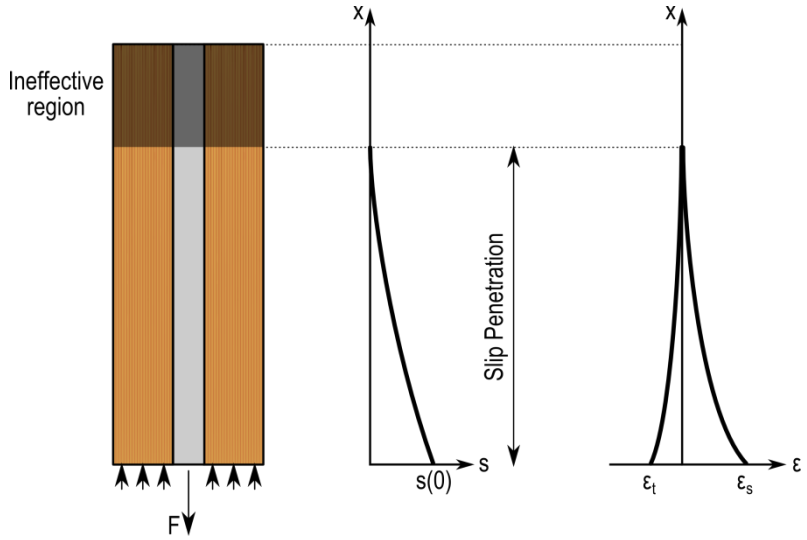

Figure 4-8. Long-member behaviour and approximate slip and strain distributions.

Assuming axial symmetry with respect to the bar axis and neglecting the radial dimension, the differential equations are summarized below. For the purposes of the experimental data analysis of this chapter, the glue layer was considered to perfectly transfer the stresses and was therefore neglected.

By means of the differential equations reported below, a fitting function could be worked out and used to fit experimental data and extrapolate significant parameters such as the slip at the start of the bond region and the slip penetration (see Figure 4-8).

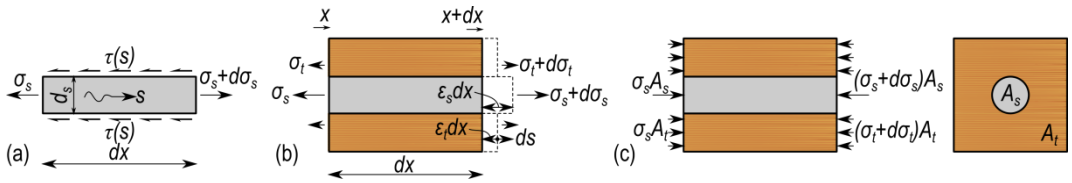

Figure 4-9. (a) Stresses acting on a reinforcing bars; (b)stresses in and strain in the bar in the timber block; (c) force acting on a reinforced-timber element.

The reinforcing bar equilibrium can be defined in Equation (4-7) with reference to Figure 4-9a as:

$$A_s \frac{d\sigma_s(x)}{dx} = \Sigma_0 \tau(s) \qquad (4\text{-}7)$$

Where A_s = the bar cross-sectional area
Σ_0 = the bar circumference
σ_s = the steel stress
$\tau(s)$ = the bond stress
s = the relative slip

Figure 4-9b shows the stress and strain in the bar and the difference between the strain of the bar and that of the timber can be written as the strain-displacement relation of Equation (4-8):

$$\varepsilon_s - \varepsilon_t = \frac{ds}{dx} = s' \qquad (4\text{-}8)$$

Where ε_s = the steel strain
ε_t = the average strain in the timber embedment

$$A_t \frac{d\sigma_t}{dx} = A_s \frac{d\sigma_s}{dx} \qquad (4\text{-}9)$$

Where A_t = timber cross-section
σ_t = timber stress

The derivation of (4-8) substituting (4-7) and (4-9) gives Equation (4-10).

$$\frac{d^2 s}{dx^2} - \chi\tau\left[s(x)\right] = 0 \qquad (4\text{-}10)$$

Where: $\chi = (1+\xi)\Sigma_0 / A_s E_{s,t}$

As shown in Section 4.4, the bond stress-slip relationship can be assumed as linear; therefore, Equation (4-10) can be re-written as follows.

$$\frac{d^2 s}{dx^2} - \chi \frac{\tau_{max}}{s_1} s(x) = 0 \qquad (4\text{-}11)$$

The solution of Equation (4-11) is given in Equation (4-12):

$$s(x) = c_1 e^{x\sqrt{\chi \frac{\tau_{max}}{s_1}}} + c_2 e^{-x\sqrt{\chi \frac{\tau_{max}}{s_1}}} \qquad (4\text{-}12)$$

Where c_1, c_2 = integration constants
x = the abscissa along the bar bond region

Equation (4-8) can also be written integrating Equation (4-12):

$$\varepsilon_s - \varepsilon_t = \sqrt{\chi \frac{\tau_{max}}{s_1}} \left(c_1 e^{x\sqrt{\chi \frac{\tau_{max}}{s_1}}} - c_2 e^{-x\sqrt{\chi \frac{\tau_{max}}{s_1}}} \right) \quad (4\text{-}13)$$

Equation (4-13) was used as a fitting function of the experimental strain gauge readings in the bonded region and the integration constants c_1 and c_2 were determined for each loading step.

Once the integration constants were known, the slip at the base of the bond region (i.e. x = 0) was determined and the resulting slip due to strain penetration was plotted against the strain in the unbonded portion of the bar.

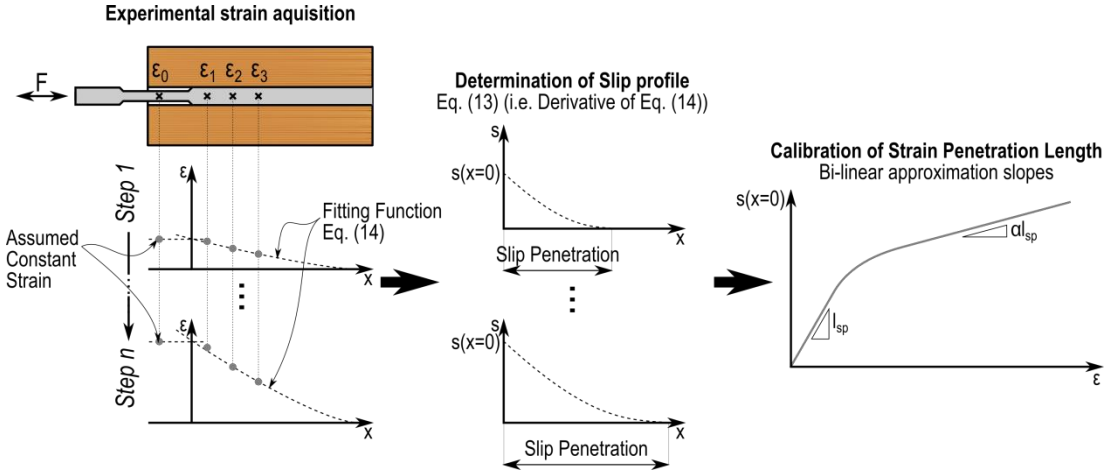

Figure 4-10. Data analysis flowchart

Figure 4-10 shows the analysis framework for the calibration of the equivalent strain penetration length. The recorded strain points at each loading step were fitted using Equation (4-13). This was then derived into Equation (4-12) and the slip due to strain penetration at the base of the bond region (x = 0) was determined.

The slip, s(x=0), was then plotted versus the maximum strain at the same point; this experimental plot was then fitted with a bi-linear curve and the slope of the elastic portion of this curve represented the equivalent strain penetration length.

4.6 Results

Figure 4-11 shows the experimental monotonic results for the specimens SP16t, SP20t and SP24t in terms of force-displacement; strain along the embedment length, slip penetration and total slip, also plotted versus the maximum strain measured externally in the fused portion of the bar. As expected the bar force-displacement did not show the yielding plateau being mild Grade 4.6 steel. The strain measurements were consistent for the three specimens

tested. From a more detailed observation of the variation of the strain in the embedment length, it can be observed that the deeper strain gauges recorded nearly constant strains after yielding, when most of the strain is concentrated in the yielding section external of the timber block. This is also consistent with the observed trend of the slip penetration (Figure 4-11c,g,k). The latter is defined as the zero of the slip function (Equation (4-12)), i.e. the abscissa indicating the equivalence of the timber and steel strains.

The behaviour in terms of strain distribution along the bond region for deformed bars (Figure 4-12b, f) showed a slight difference. Some strain increase was observed also beyond yield. This is confirmed by the constant trend of the slip penetration (Figure 4-12c, g).

The proposed analytical model was calibrated using the slip values extrapolated from experimental results. The experimental values of Figure 4-11 are plotted against the bar maximum strain at the start of the bond length and it shows a bilinear trend for all the specimens.

A similar behaviour was observed for deformed bars, but the strain readings (Figure 4-12b, f) in the bond region tended to increase even when plastic maximum strain was developed in the fused portion of the bar. This was also confirmed by the evaluated slip penetration (Figure 4-12c, g), which shows a constant trend.

The specimens were also tested cyclically to assess whether any degradation in the behaviour was occurring and Figure 4-13 summarizes the results of the specimens SP16t and SP20d in terms of slip versus maximum strain in the bar. Experimental results on cyclic testing shows no degradation (i.e. cyclic increase of bar slip) occurred; therefore, the monotonic test results were used in the following paragraph to work out the proposed analytical model for strain penetration in internally glued bars.

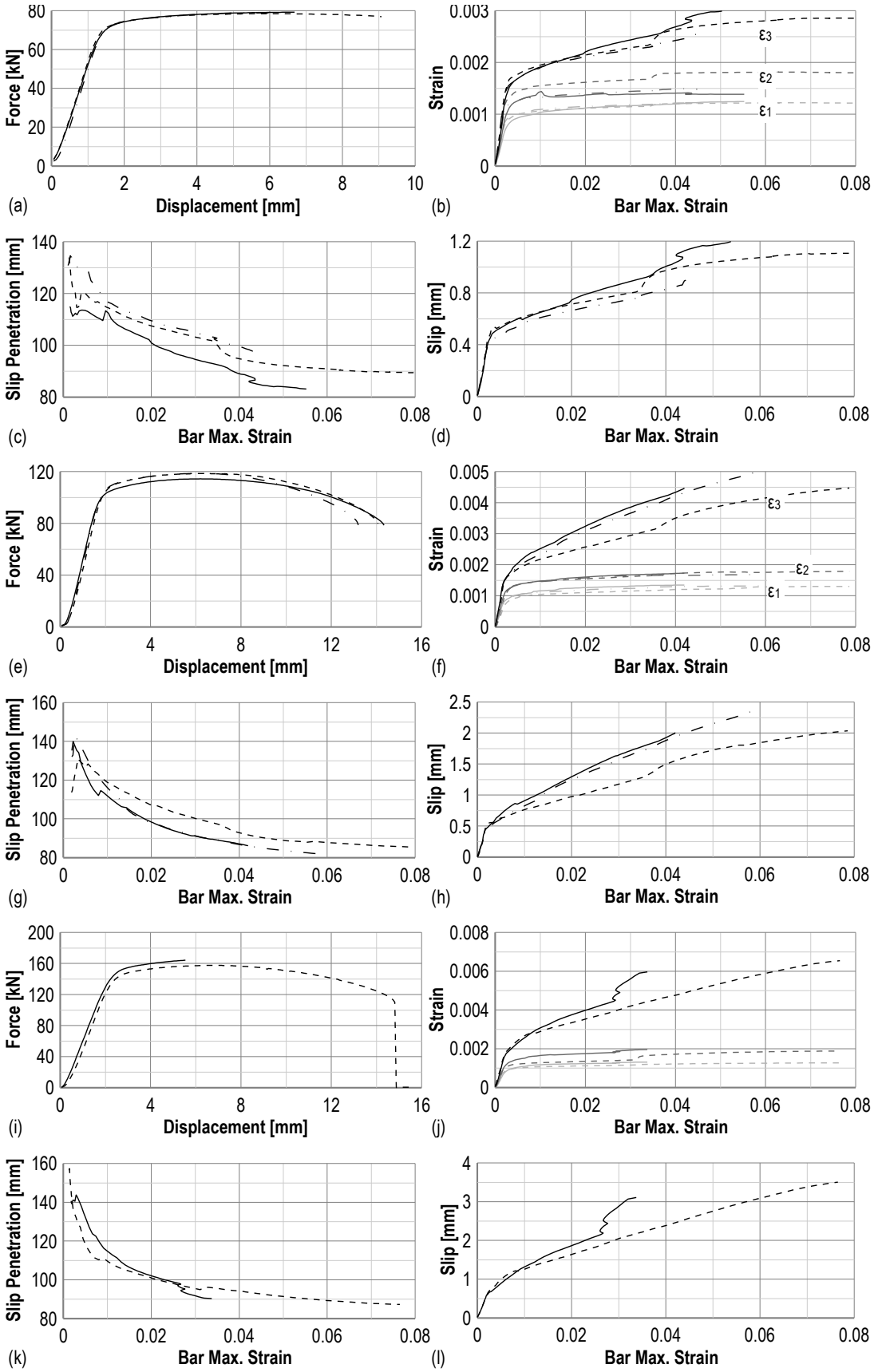

Figure 4-11. Experimental data monotonic results: (a-d) SP16t; (e-h) SP20t; (i-l) SP24t

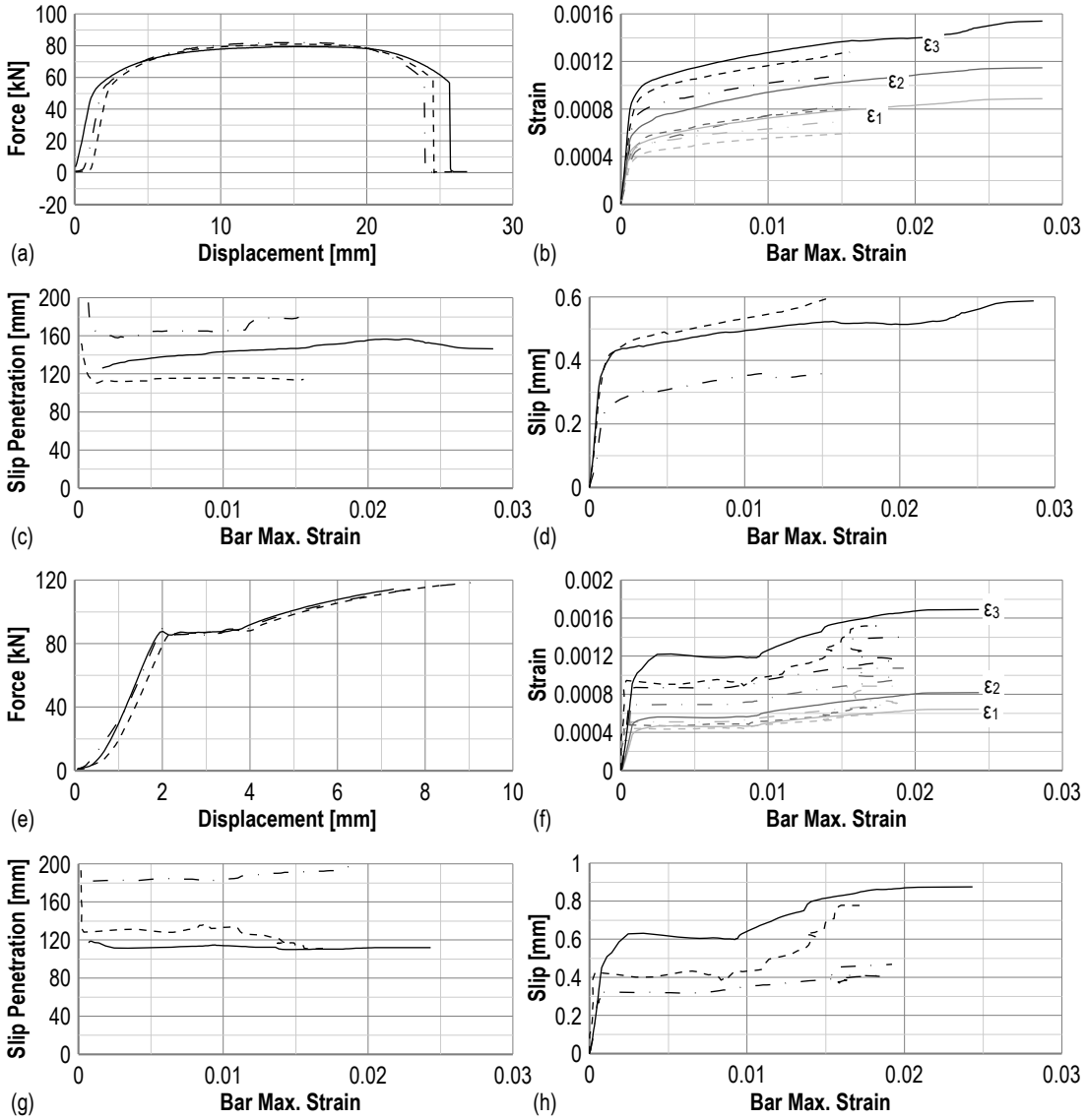

Figure 4-12. Experimental data monotonic results: (a-d) SP20d; (e-h) SP25d

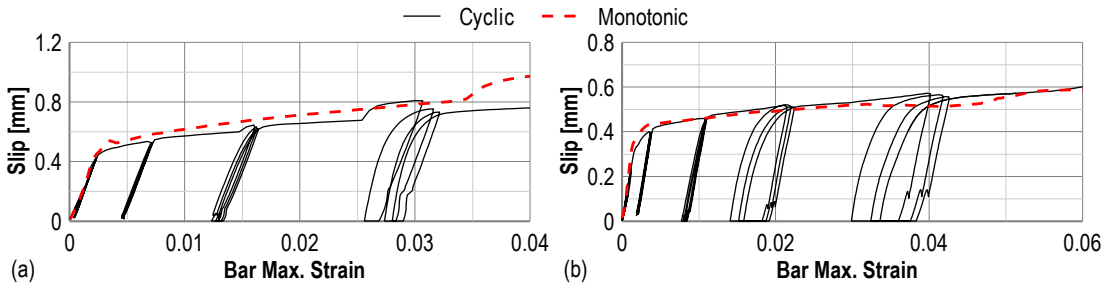

Figure 4-13. Experimental data cyclic results: (a) SP16t; (b) SP20d

4.7 Proposed analytical model

The proposed model is defined in terms of additional slip due to strain penetration, Δ_{sp}. This contribution can be consistently defined as a function of the maximum strain measured at the

start of the bonded length. A bilinear relationship was observed, so the slip due to strain penetration, Δ_{sp}, is defined as:

$$\Delta_{sp} = l_{sp}\varepsilon_e + \alpha l_{sp}\varepsilon_p \qquad (4\text{-}14)$$

Where l_{sp} = strain penetration length

ε_e, ε_p = elastic and plastic strains

α = post-yielding slip factor

As proposed in past research, the strain penetration length is expressed as a function of the yield strength and diameter of the bar; the experimental results in terms of slip-maximum strain were normalized accordingly.

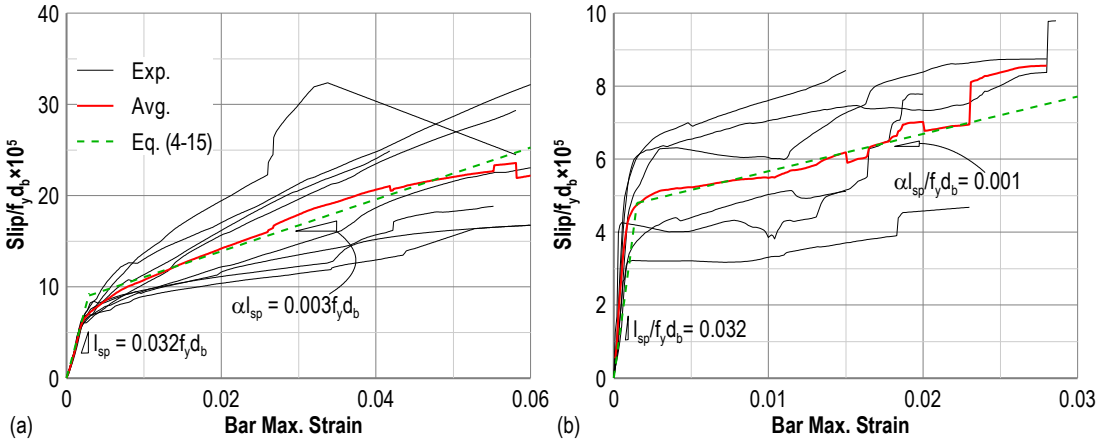

Figure 4-14. Normalized slip and strain penetration length formulation.

Figure 4-14 shows the normalized slip results of the threaded and deformed bars specimens. The experimental test data shows consistent results of the slip in the elastic range of strain, yet a significant difference in the slope is evident for plastic deformations. From averaging the experimental results (Figure 4-14 thick solid plot) a bi-linear approximation was used and the slopes of the two branches give the calibrated values.

Therefore, the strain penetration length parameters for internal bars are given below:

$$l_{sp} = 0.032 f_y d_b, \alpha = \begin{cases} 0.094 & \text{threaded} \\ 0.031 & \text{deformed} \end{cases} \qquad (4\text{-}15)$$

Equation (4-16) shows the proposed formulation of the slip due to strain penetration

$$\Delta_{sp} = 0.032 f_y d_b \begin{cases} \left(\varepsilon_e + 0.094\varepsilon_p\right) & \text{threaded} \\ \left(\varepsilon_e + 0.031\varepsilon_p\right) & \text{deformed} \end{cases} \qquad (4\text{-}16)$$

4.8 Conclusions

The chapter presented the experimental program carried out to quantify the tensile strain penetration effects occurring in internally glued bars in timber.

The most significant parameter, the strain penetration length, l_{sp}, was determined considering different geometries and steel grades. In particular, threaded (Grade 4.6) and deformed bars (Grade 300E) were used in different diameters (16, 20, and 24/25mm, the latter for either threaded or deformed bars).

A key design parameter when designing internal dissipative reinforcement in dissipative post-tensioned rocking sections is the strain penetration length, l_{sp}, which was defined as the elastic slope of the slip due to strain penetration effects, Δ_{sp}, versus the bar strain. A value of $0.032 f_y d_b$ was proposed and is close to concrete reinforcement values.

As shown later in Chapter 7 strain penetration effects are an important parameter in the design of post-tensioned rocking sections. Accounting for strain penetration effects allows the correct estimation of the strain in internal bars used as dissipation devices. When strain penetration effects are neglected the dissipater strain, thus the section ductility, is over-estimated resulting in an unconservative design.

4.9 References

ACI Innovation Task Group 5 2008. *Acceptance criteria for special unbonded post-tensioned precast structural walls based on validation testing and commentary : an ACI standard*. Farmington Hills, Mich., American Concrete Institute.

Buchanan, A., Moss, P., Wong, N. 2001. Ductile moment-resisting connections in glulam beams. *New Zealand Society of Earthquake Engineering, Annual Conference*, Taupo, New Zealand.

Buchanan, A.H. 2007. *Timber design guide*. Wellington, New Zealand, New Zealand Timber Industry Federation.

Buchanan, A.H., Fairweather, R.H. 1993. Design of Glulam Structures. *Bulletin of the New Zeland Natoinal Society for Eartquake Engineering* 26(4): 415-436.

Christopoulos, C., Filiatrault, A., Uang, C.M., Folz, B. 2002. Post-tensioned Energy Dissipating Connections for Moment Resisting Steel Frames. *Journal of Structural Engineering* 128(9): 1111-1120.

Deng, X. 1997. Strength of the epoxy bonded steel connection *PhD Dissertation*, University of Canterbury, Christuchurch, New Zealand.

Fédération internationale du béton. 2000. *Bond of Reinforcement in Concrete: State-of-art Report. Bulletin. State-of-art report, 10*. Technical report, International Federation for Structural Concrete.

Nelson Pine Industries Limited. 2012. *Specific Engineering Design Guide*. Technical report NPIL/LVL 04, Nelson Pine Industries Limited. Richmond, Nelson, New Zealand.

Newcombe, M. 2007. Seismic design of multistorey post-tensioned timber buildings. *Master of Engineering. Master thesis*, Università degli Studi di Pavia, Pavia, Italy.

Palermo, A., Pampanin, S., Buchanan, A.H., Newcombe, M.P. 2005. Seismic design of multi-storey buildings using laminated veneer lumber (LVL). *New Zealand Society of Earthquake Engineering, Annual Conference*, Wairakei, New Zealand, University of Canterbury. Civil Engineering.

Paulay, T., Priestley, M.J.N. 1992. *Seismic design of reinforced concrete and masonry buildings*. New York, Wiley.

Priestley, M.J.N. 1991. Overview of PRESSS research program. *PCI Journal* 36(4): 50-57.

Priestley, M.J.N., Calvi, G.M., Kowalsky, M.J. 2007. *Displacement-based seismic design of structures*, IUSS Press.

Sritharan, S. 1998. *Analysis of concrete bridge joints subjected to seismic actions*, University of California, San Diego.

Van Houtte, A. 2003. Innovative connections in laminated veneer lumber using epoxied steel rods *Master Thesis*, University of Canterbury, Christchurch.

Part 3:

Wall connection performance

5 Quasi-static testing of post-tensioned timber wall systems

5.1 Introduction

The objective of this chapter is the determination of the lateral load response of single post-tensioned large-scale timber walls with several reinforcement configurations, and to assess the influence of construction details such as the dissipater connection to the structural element.

Whilst past research on Pres-Lam walls focused on small-scale specimens, large-scale testing was considered necessary to achieve the research objectives; moreover, this allowed investigating the influence on the system response of realistic construction details.

After discussing the testing methodology, the chapter focuses on the construction detailing which was considered crucial to achieve the objectives of this experimental work. In fact, the use of realistic construction detailing can lead to an increased flexibility of the dissipaters, which may affect the connection response.

A set of 2/3 scaled single Pres-Lam walls was tested with several reinforcement layouts (i.e. initial post-tensioning force and dissipation devices) and was subjected to a quasi-static cyclic testing regime with an imposed triangular distribution of forces to assess the seismic load response of the system. An alternative configuration to the more traditional single wall was also tested. This solution, referred to as "Heel-and-Toe", consists of lifting the wall panel on steel plates to concentrate the compressive stress over a fixed area and is aimed to optimize the system performance.

The chapter provides a detailed discussion on the observed test results of the different specimens in terms of overall force-displacement response and detailed parameters such as the neutral axis depth, post-tensioning force variation and dissipaters connection flexibility. In particular, the influence of the latter on the overall behaviour was assessed in terms of hysteretic damping.

5.2 Test specimens detailing

5.2.1 Wall optimized section and post-tensioning anchorage

The timber section of the specimen (Figure 5-1a) was 0.189m×1.57m and made of standard 63mm thick Laminated Veneer Lumber (LVL) profiles chosen to optimize the section. The voids created for the post-tensioning bars were reduced to a minimum to maximize the bearing area for the post-tensioning anchorage at the top of the wall.

Figure 5-1b shows the wall before erection, highlighting the detail of the anchorage plate. A Grade300 60mm thick steel plate was used.

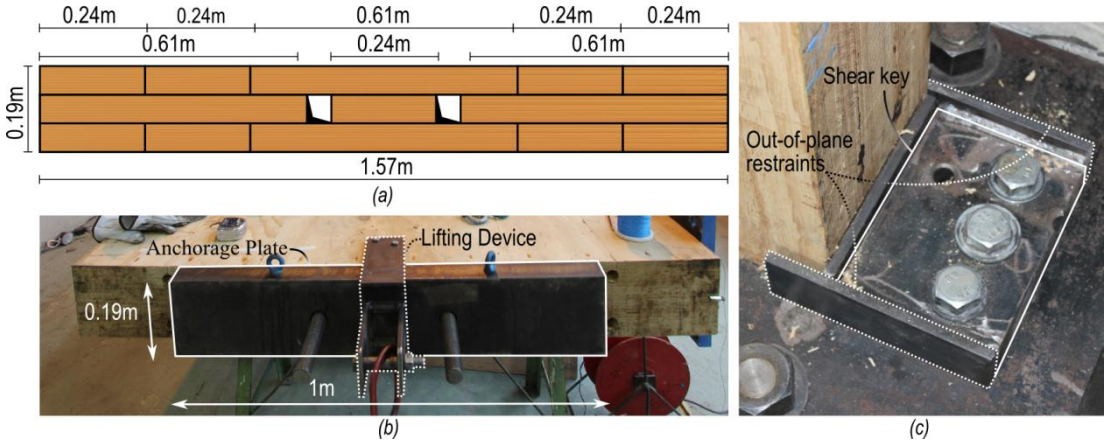

Figure 5-1. (a) Wall section. (b) Post-tensioning plate detail; (c) shear key

5.2.2 Shear key

Although a large amount of friction was expected to be developed at the base of the wall due to the high compressive forces, Appendix B of NZS3101:2006 (2006) does not permit resisting of shear by friction, differently from ACI 318-11 (2011); therefore, external shear keys were introduced to provide more robustness to the system and prevent sliding both in the in-plane and out-of plane directions. 40mm thick plates were used to prevent in-plane sliding and thinner 6mm plates were welded on the sides to prevent out-of-plane displacements. To allow for construction tolerance, slotted holes were drilled for connecting the shear key to the foundation. The detail of the shear key is shown in Figure 5-1c.

5.2.3 Dissipater connections

When using external dissipation devices, the dissipater-to-wall connection must be carefully detailed in order to provide the required strength, as well as to limit the deflection associated with the connection stiffness. The latter can delay the activation of the dissipaters reducing the system's moment and dissipation capacity at the design target drift. Common practice in

timber engineering is the use of metallic fasteners such as screws, bolts or timber rivets. The latter represents a good solution for this type of application, since they enable a connection with high stiffness, with no significant overdesign. Figure 5-2 shows the details of the connection. A 6mm thin plate was connected to the wall element using 90mm long timber rivets. A 20mm thick plate was welded to the riveted plate providing the connection setup for the dissipaters (Figure 5-2a).

The dissipation device were tension-compression yield (TCY) fuse-type dissipater and consisted of a mild steel rebar, milled down to a reduced diameter to concentrate the damage within a fuse (gauge) length, whilst maintaining the connecting parts in the elastic range (Marriott *et al.*, 2008). To avoid buckling, a restraining system made of a circular hollow section (CHS60.3×3.6) filled with epoxy was used (see Figure 5-2c). Extensive experimental testing on this type of dissipater was carried out by Sarti *et al.* (2013) and the device was also used in post-tensioning concrete applications in the past (Marriott *et al.*, 2008).

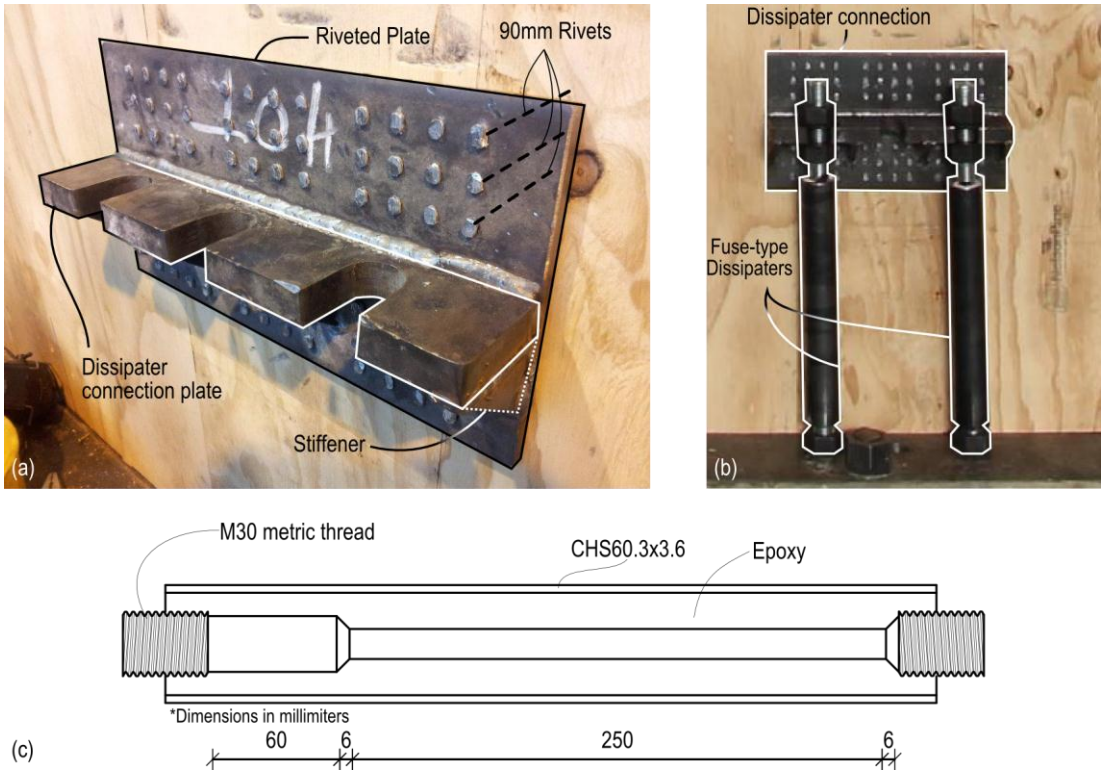

Figure 5-2. Fuse-type dissipater connection: (a) detail of the connection; (b) final setup.

Internal dissipaters were used as well and they were glued in the timber section using epoxy resin. 26mm diameter holes were drilled in the wall section in order to provide the positioning tolerance. The holes were drilled 800mm deep into the section providing the required embedment length for epoxied bars, in accordance with Buchanan (2007). This also provided for the unbonded length of 300mm.

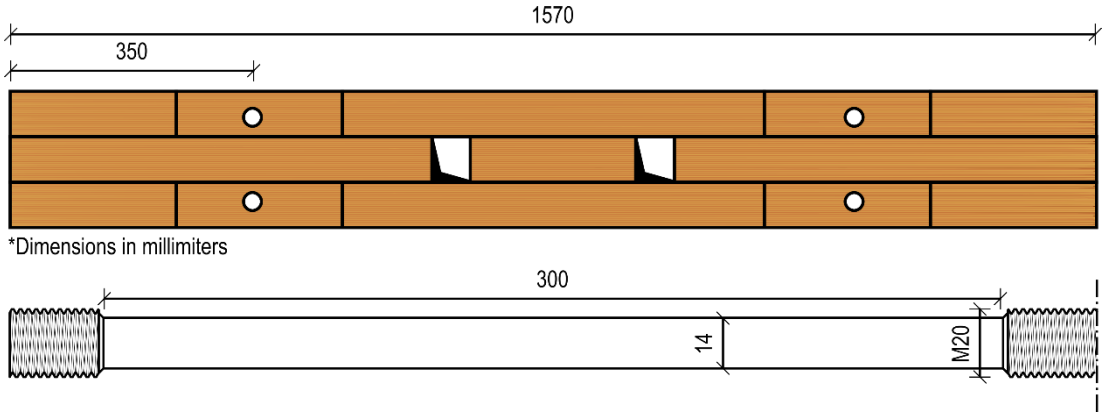

Figure 5-3. Internal dissipater details.

For the internal dissipation devices a threaded bar was used and gauged down to a fuse diameter of 14mm (Figure 5-3). The threaded portions allowed the connection of the dissipater in the foundation plate via threaded holes (see the foundation details below) and also the bonding surface inside the timber section. Figure 5-3 shows the positioning of the holes and the dissipater details.

5.2.4 Foundation details

The concrete block was 0.53m deep, 0.76m wide and 2.66m long. Several ducts were created in the foundation to allow the connection to the strong floor with anchoring bolts. A pocket was created in the bottom part of the concrete block to accommodate the post-tensioning anchorage devices into the foundation. The latter consisted of a shorter threaded bar portion anchored at the bottom of the foundation with standard connections composed of a 125mm×125mm×25mm steel plate and post-tensioning nut and washer.

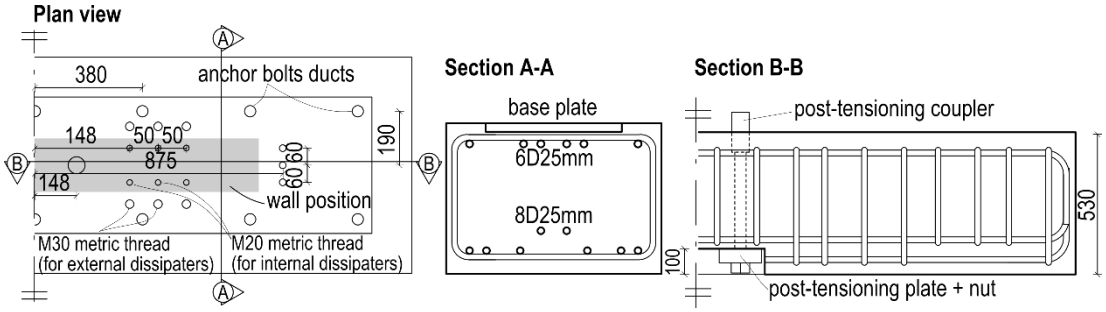

Figure 5-4. Concrete block foundation details.

A 32mm thick steel plate was positioned on the top of the foundation to create an even surface for the wall base as well as the necessary threaded holes for the connections. Additional holes were drilled to connect the shear keys as well as to provide flexible positioning of the dissipaters (either internal or external). The details of the foundation are shown in Figure 5-4.

5.3 Testing methodology

The testing schedule was developed starting from the reinforcement design presented in Appendix A. The reinforcement configuration was varied in terms of the initial post-tensioning force applied and mild steel reinforcement layout. Several tests on the post-tensioned only configuration specimens were carried out, varying the initial post-tensioning forces from 200kN to 400kN and 600kN. Those post-tensioning forces were chosen to provide the post-tensioned only experimental curve to compare to the hybrid specimens.

Hybrid (i.e. providing re-centering and dissipation) post-tensioned tests were performed with different numbers of dissipaters to assess the influence of the re-centering ratio.

A variation of the single wall solution was the Heel-and-Toe (HT) configuration which was an alternative to the traditional configuration of a single wall, where steel plates were placed underneath the wall section. The plates allow the wall to bear on a reduced surface and to limit the neutral axis depth variation. For this configuration the same post-tensioning only specimens were tested for comparison and the equivalent hybrid test of S-Hy600-4 was carried out. The testing schedule is reported in Table 5-1.

Table 5-1.Post-tensioned walls testing schedule.

Test ID	PT Initial	Dissipaters	Re-centering Ratio
S200	200kN	n/a	1.0
S400	400kN	n/a	1.0
S600	600kN	n/a	1.0
S400-8	400kN	8D14mm	0.6
S400-4	400kN	4D14mm	0.7
S600-4	600kN	4D14mm	0.8
S600-4i	600kN	4D14mm (internal)	0.8
HT200	200kN	n/a	1.0
HT400	400kN	n/a	1.0
HT600	600kN	n/a	1.0
HT600-4	600kN	4D14mm	0.8

As the test setup in Figure 5-5 shows, the wall was loaded simulating a triangular distribution of forces accordingly to the case study design which assumes the top floor mass concentrated at the second level. The applied point loads were achieved using a 2m long distribution beam (250UC89.5) which was linked to the wall and the actuator through steel hinges. The centre-to-centre distance between the top and bottom pin hinges was 2m and the pin hinge connecting the distribution beam to the hydraulic actuator was positioned at 0.64m from the top pin hinge (see Figure 5-5a).

The reaction frame consisted of a built-up column made of a double 300PFC profile, further stiffened along the length by welded plates; lateral stability was provided by two struts (SHS100 and SHSH200).

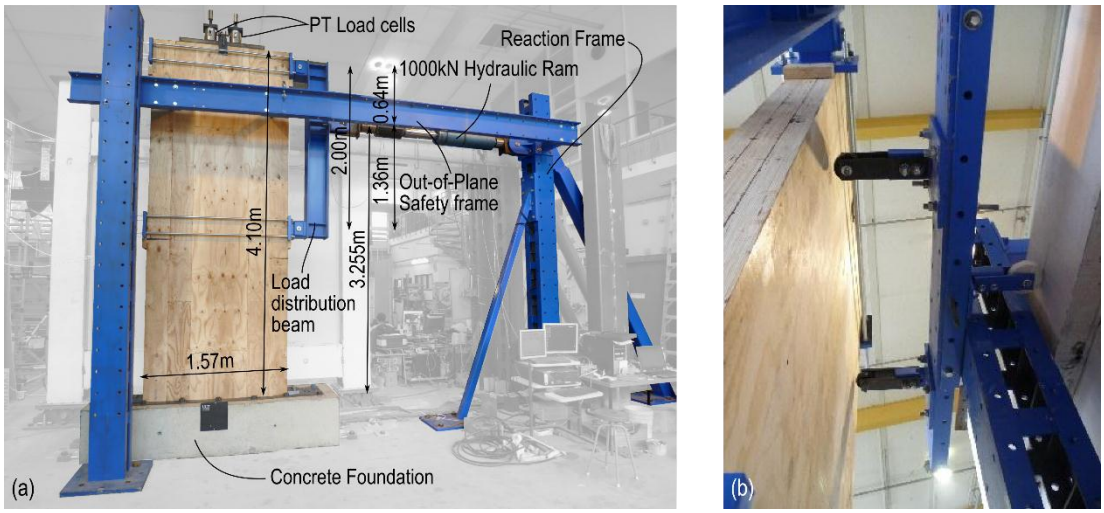

Figure 5-5. (a) Test setup. (b) out-of plane restraining beam detail.

The load was applied by a 1000kN hydraulic actuator mounted at the height of 3.7m from the strong floor (3.2m from the bottom of the wall).

For safety purposes the out-of-plane displacement of the wall was restrained by sliders consisting of small steel plates with a rubber wheel bolted on 300PFC (Parallel Flange Channel) profiles (Figure 5-5b). To provide support for the PFC profiles, an additional column was connected on the front side of the test setup (see Figure 5-7a), while on back of the specimen an existing column from a different test setup was used. The quasi-static displacement loading consisted of sequential displacement-controlled cycles according to ACI ITG-5.1-07 protocol (ACI Innovation Task Group 5, 2008): the maximum displacement of the first three cycles did not exceed 60% of the design displacement (0.040m or 1%); the maximum displacement of the subsequent cycles was between 1.25 and 1.5 times the previous maximum displacement. A maximum drift of 2% was imposed which corresponds to the Maximum Credible Event (MCE) scenario according to a capacity demand spectrum method (Chopra *et al.*, 1999).

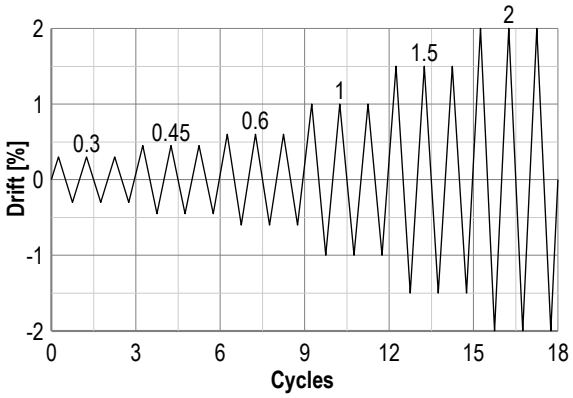

Figure 5-6. Loading protocol.

5.3.1 Instrumentation

The experimental test was a displacement controlled setup and the top displacement was measured using a rotary potentiometer (D in Figure 5-7a). The applied load was recorded through the 1000kN load cell (LC in Figure 5-7a) mounted on the hydraulic actuator.

The post-tensioned forces were monitored by two 1000kN load cells at the top of the wall (PT1 and PT2).

Figure 5-7. Instrumentation setup (left) and instrumentation for detailing (right).

A key design and response parameter of a post-tensioning rocking connection is the neutral axis depth. In fact, during the rocking mechanism, the structural wall, rather than displaying a rigid body motion pivoting around the corners, develops a compressive region within the rocking interface.

The neutral axis depth was measured using six spring loaded potentiometers (NA1 to NA6, Figure 5-7a) fixed at the wall base. A linear function was used to fit the potentiometer

readings. The neutral axis depth corresponded to the zero of the linear fitting function and the connection rotation (gap opening) was the slope of such function.

When using external dissipaters some type of connection to the structural element must be provided. Although over-designed for strength, the flexibility of the dissipaters' connections must be taken into account when assessing the behaviour of post-tensioned rocking sections. A set of potentiometers were used to measure the relative displacement between the riveted connection plate and the wall and to measure the net displacement of the dissipaters. When more than one dissipater was connected through the same plate the loading pattern on the connection was eccentric, so the potentiometers were positioned at the edges of the connection plate to capture the plate's rotation. Two sets of potentiometers were used: DISS1 and DISS2 captured the net displacement of the dissipaters, while DS1 and DS2 (see Figure 5-7b) measured the relative slip occurring between the connection plate and the wall.

The elastic displacement contribution of the riveted connection can have a major effect on the overall system behaviour since it may delay the activation of the dissipaters until higher drift, thus affecting the overall ductility and energy dissipation. The influence of this parameter is assessed and discussed in the final part of the chapter.

5.4 Dissipaters fabrication and testing

The fuse-type dissipaters for this experimental study were fabricated from M32 G4.6 mild steel bars and milled down to 14mm fuse diameter with a fuse length of 250mm (see Figure 5-8a). The anti-buckling system comprised of a CHS60.3×3.6 steel profile (grade C250L0) filled with epoxy resin. The dissipaters were fabricated and tested as explained in Chapter 3 of this dissertation (see the test setup in Figure 5-8b).

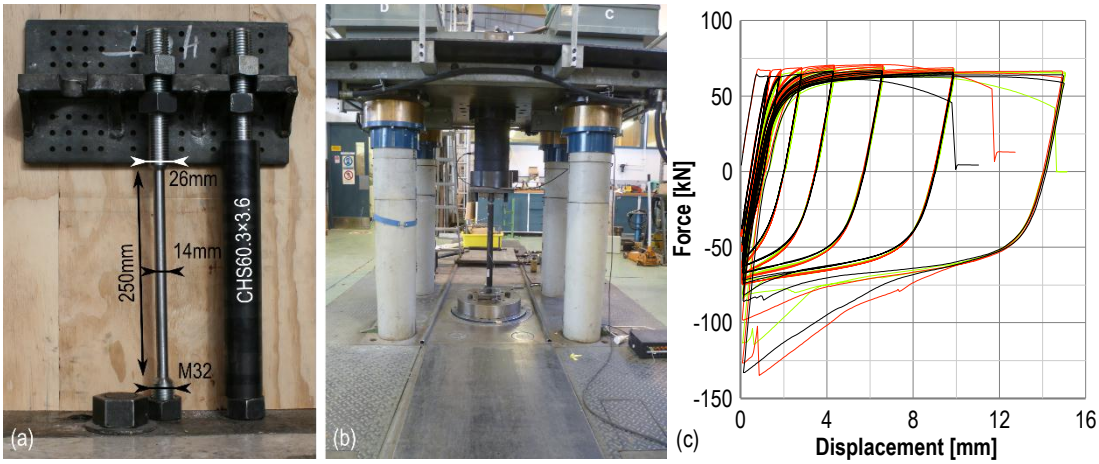

Figure 5-8. (a) Fuse-type dissipater; (b) component test setup; (c) experimental results.

Experimental results for the two dissipater types are shown in Figure 5-8c. Similarly to the testing results documented in Chapter 3, the fuse-type dissipater showed stable hysteresis up to a displacement of 10mm (5% average strain) and for higher displacements some interaction between the dissipater and the restraining system occurs. Observation of those specimens that failed suggested that the failure mode was low-cycle fatigue.

5.5 Test results

5.5.1 Single wall

Pure post-tensioned rocking

The test results are discussed with reference to the different reinforcement configurations. The experimental program started with tests on post-tensioned only configurations. Since no dissipation device was used in this phase as supplemental reinforcement, the behaviour was expected to be non-linear elastic as typical of a rocking and re-centering system.

In a pure post-tensioned rocking solution no connection rotation is occurring until the decompression moment, M_{dec}, is reached, where M_{dec} is given by;

$$\frac{M_{dec}}{Z_t} - \frac{N + \sum T_{pt,i}}{A_t} = 0 \rightarrow M_{dec} = \left(N + \sum T_{pt,i}\right)\frac{Z_t}{A_t} \qquad (5\text{-}1)$$

Where Z_t and A_t are the timber section modulus and cross-sectional area respectively. For rectangular sections $Z_t/A_t = h/6$, where h is the section depth.

As shown in the moment-rotation loop (Figure 5-9b), before the decompression moment is achieved, no rotation occurs at the base connection. The force-displacement loop in Figure 5-9a shows that the system flexibility is given by the elastic bending and shear deflections of the cantilever wall (i.e. fully fixed base) before the gap opens.

Once past the decompression point, the wall displayed the typical non-linear elastic behaviour up to 1.5% drift. For higher drifts some minor hysteresis was displayed in the moment-rotation for all the post-tensioned only specimens (see Figure 5-9). This was assumed to be caused by the minor post-tensioning losses possibly due to two main factors; (i) minor plastic deformations occurring on the surface of the bearing plates due to highly concentrated stresses on the reduced area of the washer; (ii) the yielding stress (835MPa) of manufacturer's specifications is defined as 0.1% proof stress; therefore, small plastic

deformations are anticipated. This was confirmed by the increased post-tensioning losses in specimen S600 in Figure 5-9 (black line).

Post-tensioning losses at the end of the test for each of the three specimens were 42kN, 40kN and 67kN (21%, 10% and 11% of the initial post-tensioning force) for the 200kN, 400kN and 600kN initial post-tensioning forces respectively.

More significant degradation behaviour was observed for specimen S600 where it is assumed that the effect was caused by both the minor plastic deformation of the post-tensioning bars and by some inelastic deformation of the timber section at the base connection. Timber plastic deformation was observed only for the specimens with the highest post-tensioning stress levels (S600), whilst the compressive stresses for the other specimens remained within the elastic limit.

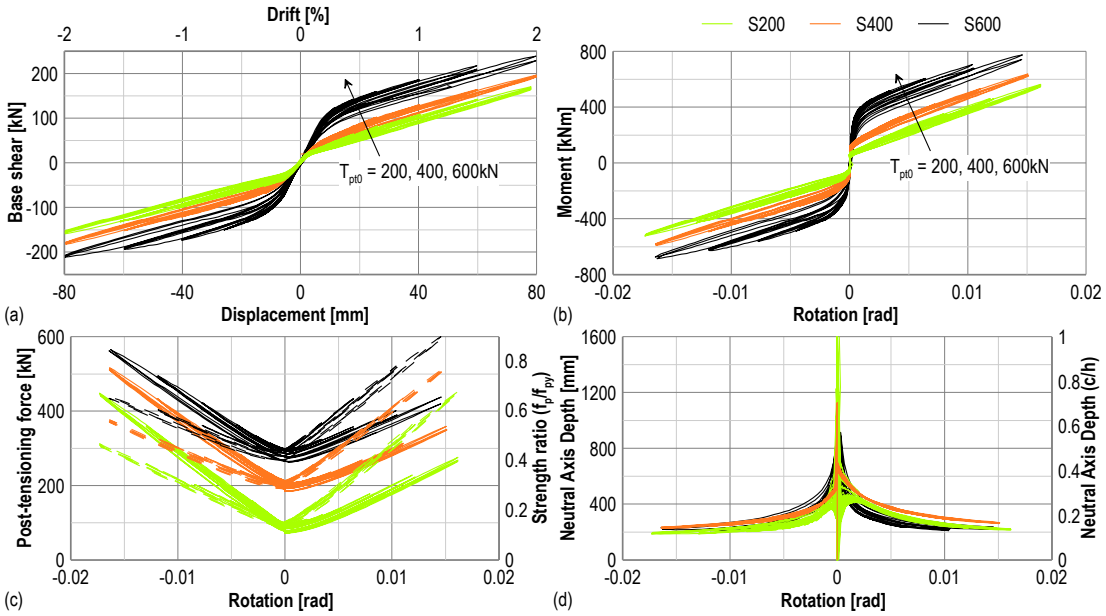

Figure 5-9. Single wall post-tensioned only experimental results.

Figure 5-9c,d also shows the typical post-tensioning force and neutral axis depth variation. As soon as the gap opens between wall and foundation, the tendon elongation causes an increase in the post-tensioning force. As expected, this led to higher capacity of the specimens, but the neutral axis depth was not significantly influenced by the increased axial load reaching approximately 25% of the section depth at design drift.

Dissipative post-tensioned rocking – External Dissipaters

In the second phase of the experimental program, hybrid (i.e. post-tensioned and dissipative) configurations were tested. This was achieved by adding some dissipating devices with

different configurations and reinforcing ratios (re-centering ratios, $\beta = M_{pt}/M_{tot}$, 0.6, 0.7 and 0.8). Several tests were carried out using the external mild steel type dissipaters and finally the equivalent configuration as S600-4 was tested using internal dissipaters (i.e. S400-6i).

The dissipaters were positioned at 350mm from the either edge of the wall. This design choice was made to optimize the system behaviour accounting for the different characteristics of the dissipater response. The dissipater would give a greater moment contribution when positioned at the wall edges; however, the strain demand is much greater and, as a result, the dissipaters would need to have a longer fuse length to prevent premature ultimate tensile failure. Additionally a longer fuse length corresponds to a higher slenderness and this would increase the buckling propensity of the dissipater.

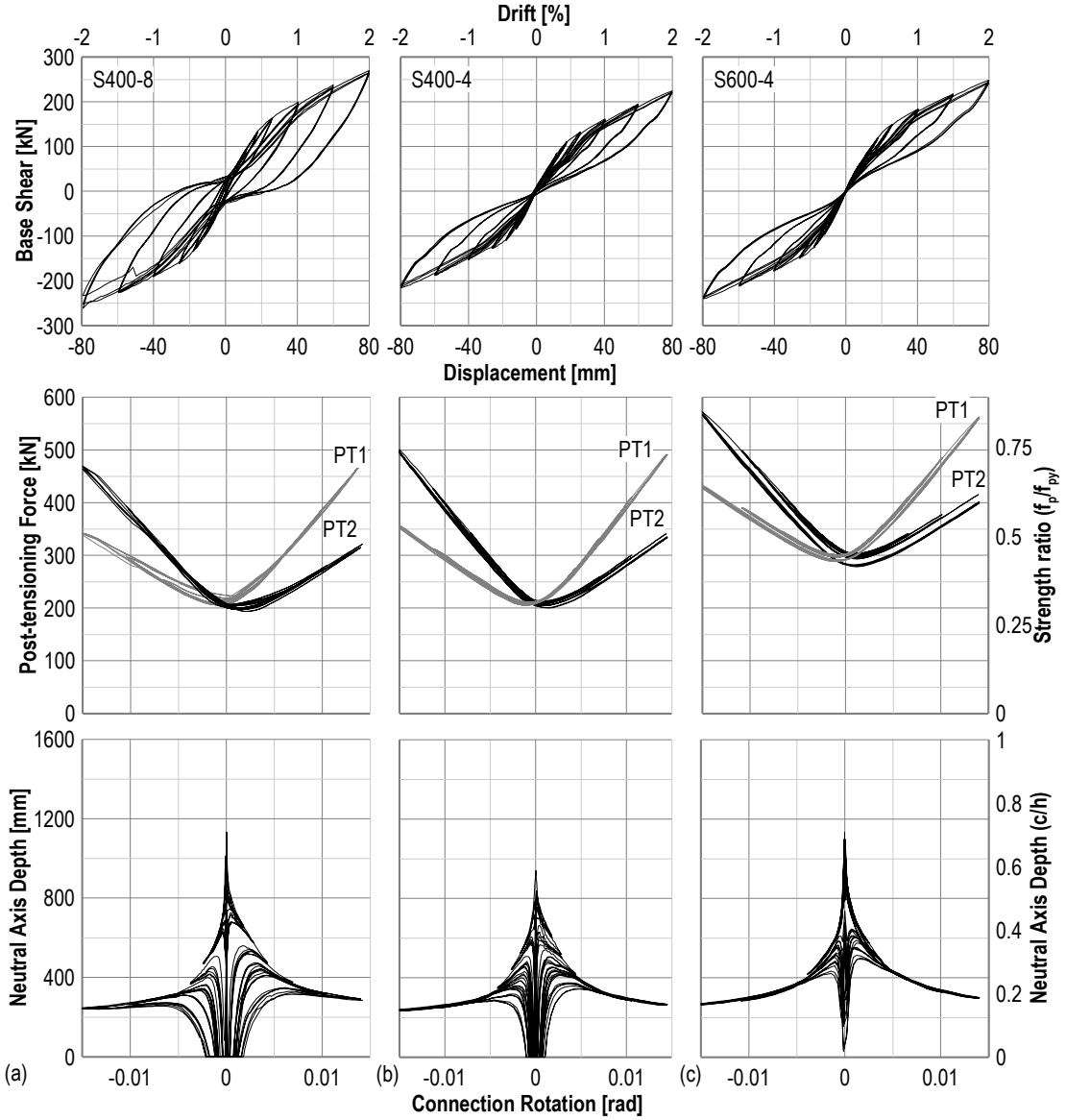

Figure 5-10. Experimental results. (a) S400-8; (b) S400-4; (c) S600-4.

The hybrid specimen S400-8 experimental results are shown in Figure 5-10a. The results display a flag-shaped hysteresis, despite full re-centering not being accomplished. In fact, the solution was designed with a re-centering ratio $\beta = M_{pt}/M_{tot} = 0.6$ (60% re-centering and 40% dissipative contribution respectively) at design drift (i.e. 1%), the experimental results show a re-centering ratio of about 0.5. This decreased value was due to over-strength in the mild steel which developed higher yielding stress than the nominal value considered in the design phase. Also, increased compressive forces are observed in the dissipaters due to isotropic strain hardening, which were not accounted for in the section design. As a result, a residual drift of 0.6% was observed after testing.

Some stiffness degradation was observed and that was due to some flexibility of the dissipater's connection as well as the ratcheting behaviour of the dissipaters. This effect is further discussed later in the chapter.

The hybrid specimen S600-4 was designed to achieve the same capacity as the S400-8 specimen but with a different re-centering/dissipative ratio (β = 0.8). The flag-shape hysteresis was thinner due to the reduced dissipation contribution. Furthermore, the same stiffness degradation was present, but the effect was reduced because of the lower force acting on the connection. No residual deformations were observed for this configuration.

Dissipative post-tensioned rocking – Internal Dissipaters

The same configuration as the S600-4 specimen was tested with internal dissipaters (S600-4i) and the results are shown in Figure 5-11d.

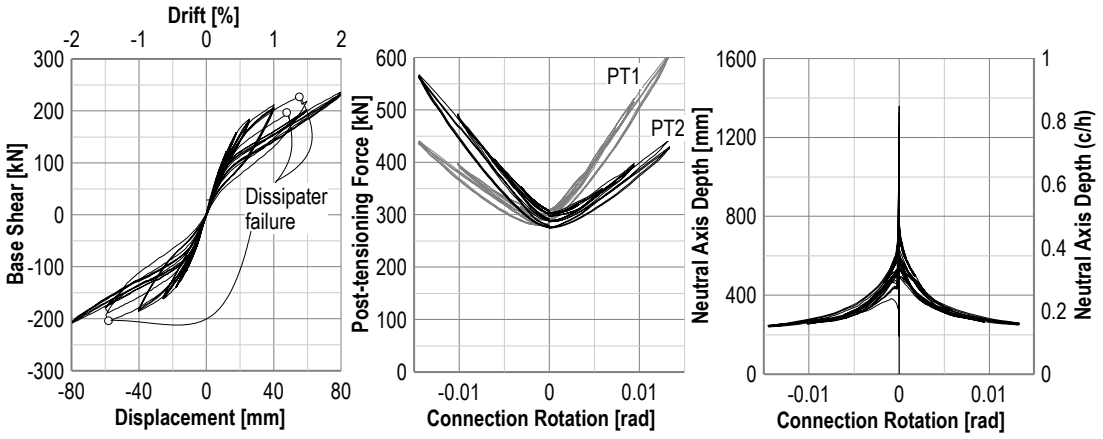

Figure 5-11. Experimental results S600-4i

The specimen shows very similar results to the equivalent solution with external dissipaters up to the design drift level of 1%. With subsequent amplitude cycles (up to 1.5%) the internal dissipaters fractured and in the final cycles at 2% drift (MCE level) the hysteresis

loop showed the elastic bi-linear trend of the post-tensioned only solution, still maintaining a substantial residual capacity, corresponding to the full contribution of the post-tensioned steel.

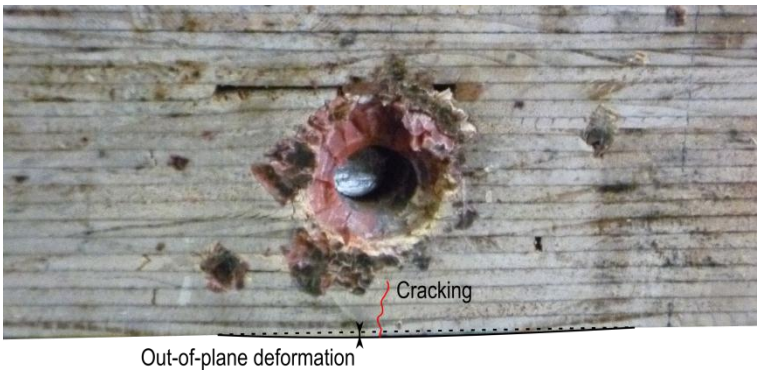

Figure 5-12. Internal bar out-of-plane behaviour evidence.

A closer inspection after testing showed that the edge distance of the internally epoxied dissipater did not provide the necessary buckling restraint; consequently, the dissipaters deformed transversally causing a premature low-cycle fatigue failure. This phenomenon is highlighted in Figure 5-12 by the out-of-plane deformation and the crack formation observed after testing.

The post-tensioning force and neutral axis depth shown in Figure 5-10 demonstrate a similar behaviour to that observed in the pure post-tensioning rocking solutions. In particular, the initial post-tensioning stress for the specimens tested was in the range $0.3\text{-}0.5f_{py}$ (see strength ratio on the right axis). This corresponded to an initial timber stress of approximately 1.5-2MPa (approximately 5% of the timber compressive strength). This low initial stress level in the timber section results in a smaller neutral axis depth, thus optimizing the system response (i.e. increased tendon elongation and dissipater activation).

5.5.2 Heel-and-Toe Solution

The aim of the Heel-and-Toe configuration was to concentrate the timber stresses onto a reduced area by creating a double-hinge mechanism reducing the neutral axis depth. Figure 5-13 shows the qualitative stress distribution for increasing connection rotations. As the picture highlights the stress is concentrated over a reduced area, increasing the lever arm. A similar concept was proposed and tested for concrete post-tensioned frames (Amaris Mesa, 2010).

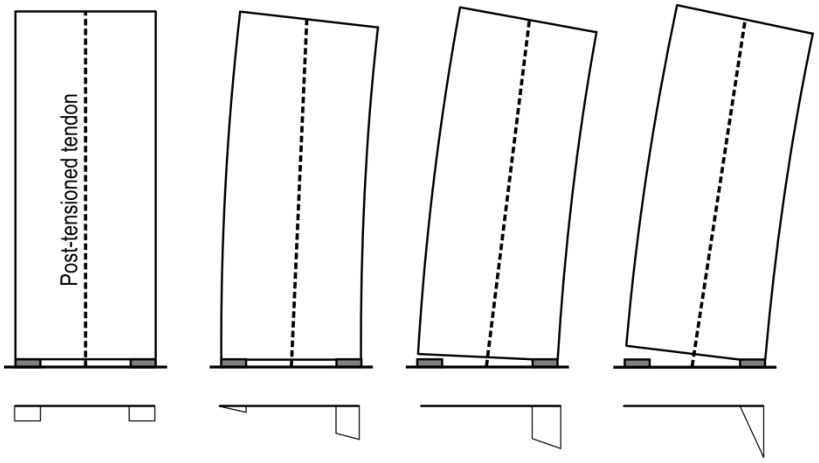

Figure 5-13. Double-hinging mechanism qualitative stress distribution.

The double-hinge configuration for timber walls was achieved by positioning two 20mm thick plates at the wall edges. To avoid excessive timber stresses, the length of the plates was designed to be no shorter than the minimum neutral axis values observed in previous tests (see Figure 5-14).

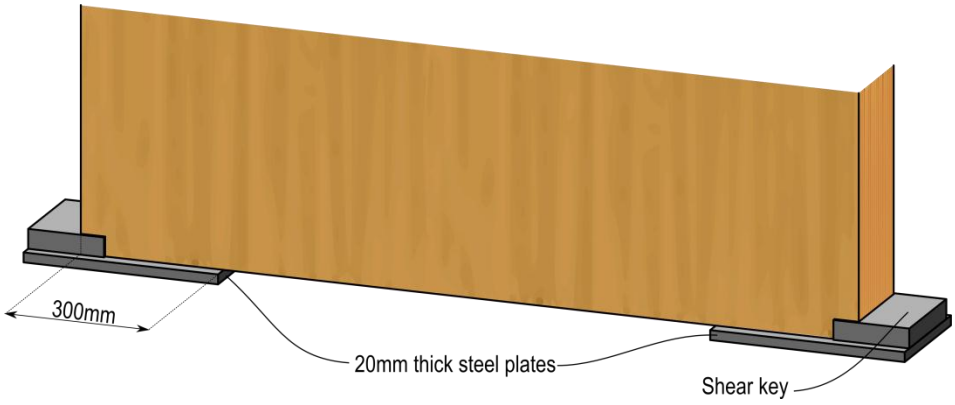

Figure 5-14. Setup of the heel-and-toe solution.

The results of the post-tensioned only and hybrid heel-and-toe (HT) configurations are shown in Figure 5-15. Similar capacity was accomplished by this alternative configuration, and no major difference in the behaviour was observed. The heel-and-toe hybrid specimen shows a stable flag-shape hysteresis and a full re-centering as shown in the force-displacement results in Figure 5-15.

The lateral load response of the system was compared to the single wall solutions, and the experimental results do not show significant differences in the overall capacity of the system.

Figure 5-15 shows the experimental backbone curves of the single and heel-and-toe post-specimens for comparison, which show that a small difference in the decompression point occurs.

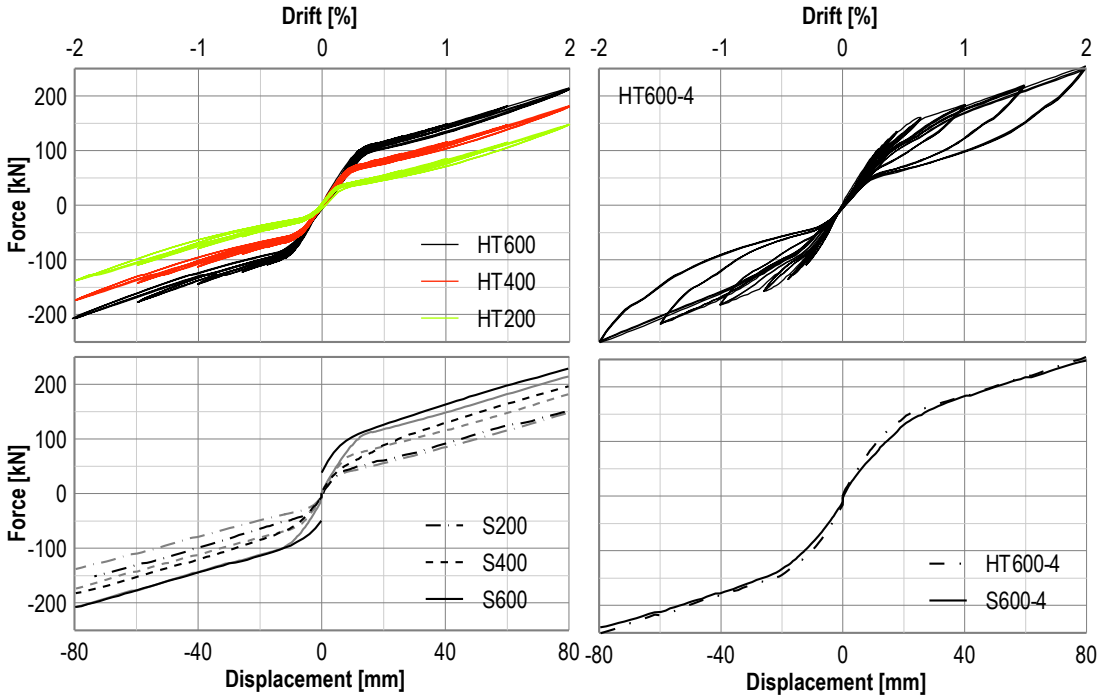

Figure 5-15. Heel-and-Toe system force-displacement experimental results and comparison with single wall system.

5.5.3 Dissipater stiffness

As shown in section 5.3.1 some instrumentation was used to record the detailed behaviour of the external fuse-type dissipaters. Since the dissipater's yield displacement, thus its activation, is rather small (in the order of 0.4mm), the stiffness contribution of the connection is a key point of the system behaviour.

The riveted connection was designed using an over-strength factor of 1.5 and assuming that a maximum of three dissipaters were bolted to the connection. The connection used in the test setup, consisting of 12 rows and 6 columns of 90mm long timber rivets, had a design capacity Q = 295kN (Zarnani *et al.*, 2014).

The estimated connection elastic displacement, δ, can be evaluated using Equation (5-2) (Zarnani *et al.*, 2014):

$$\delta = 4\left(1-\sqrt{1-\frac{F}{Q}}\right) \qquad (5\text{-}2)$$

Where F = force in the connection

Q = connection capacity.

Figure 5-16a shows the dissipater and connection displacement experimental results from the S400-8 specimen. Since the dissipater force could not be directly recorded during testing a force-displacement loop was analytically inferred (Figure 5-16b). As shown below the inherent flexibility of the connection does not allow the dissipater to return to zero net displacement, causing minor stiffness degradation in the overall force-displacement response (see Figure 5-16d).

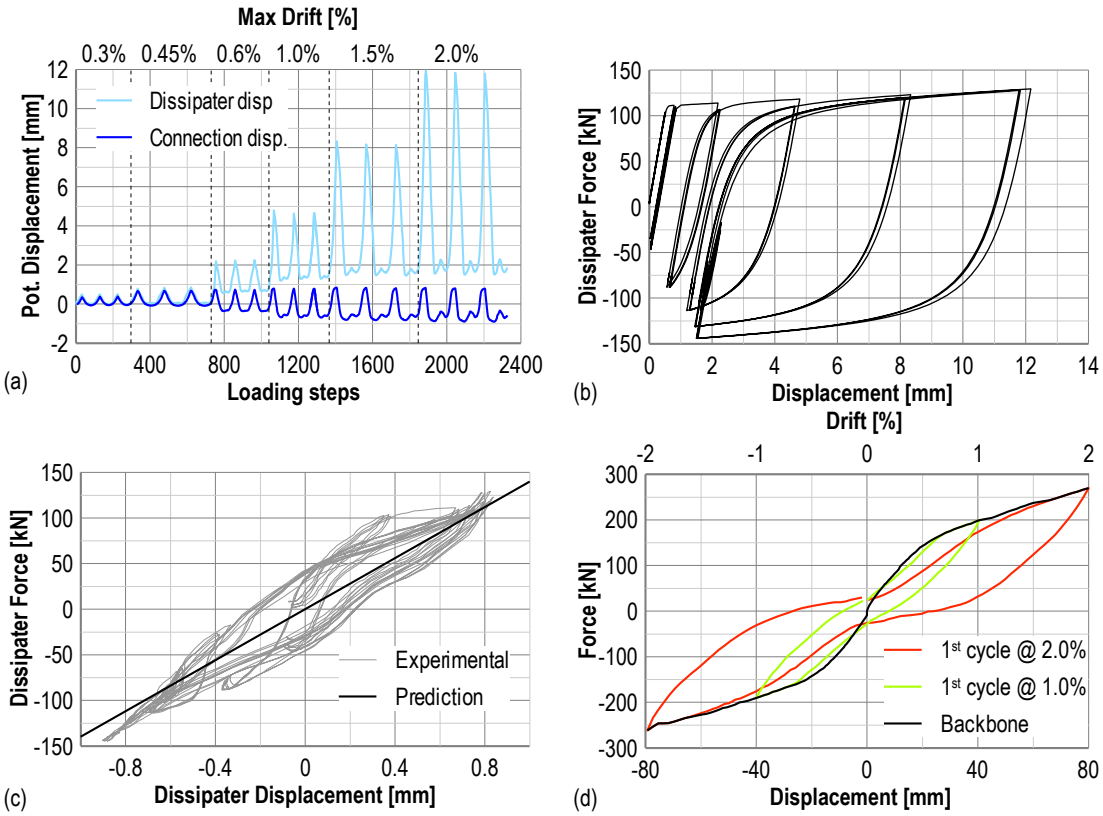

Figure 5-16. Dissipater connection behaviour (S400-8). (a) Dissipater and connection displacements, (b) dissipater force-displacement loop (numerical from net displacements); (c) connection force-slip diagram; (d) S400-8 force-displacement loop showing the effect of connection stiffness

Figure 5-16c shows the dissipater force evaluated from the Menegotto-Pinto hysteresis rule (Menegotto *et al.*, 1973) against the measured connection relative displacement. It can be seen that the stiffness evaluated from Equation (5-2), shown in a solid black line in Figure 5-16, is in good agreement with the experimental data.

It can be seen from Figure 5-16b that as soon as the dissipater yields, some residual net displacement of the dissipater occurs. This effect has a direct influence on the overall behaviour of the system, causing some stiffness degradation. This is highlighted by the slightly pinched loop behaviour observed when the specimen is reloaded to the same drift amplitude as shown in Figure 5-16d.

The connection flexibility also causes an increased ratcheting in the tension-compression dissipater, causing the dissipater to develop lower forces for the same displacement when reloaded (see Figure 5-16b).

This issue can be addressed designing either a stiffer riveted connection or using other fastening options (i.e. split-ring, screws).

5.5.4 Damage observations after the testing campaign

As shown in the pure post-tensioned rocking specimen S600, some minor plastic deformation can be expected when the wall was subjected to high drift levels. This resulted in a small hysteresis loop developed in the post-tensioned only solution.

As a consequence of the hysteretic behaviour of a post-tensioned only solution, the damage was localized at the wall base section and some residual deformation of the wall panel was observed after the testing programme as shown in Figure 5-17.

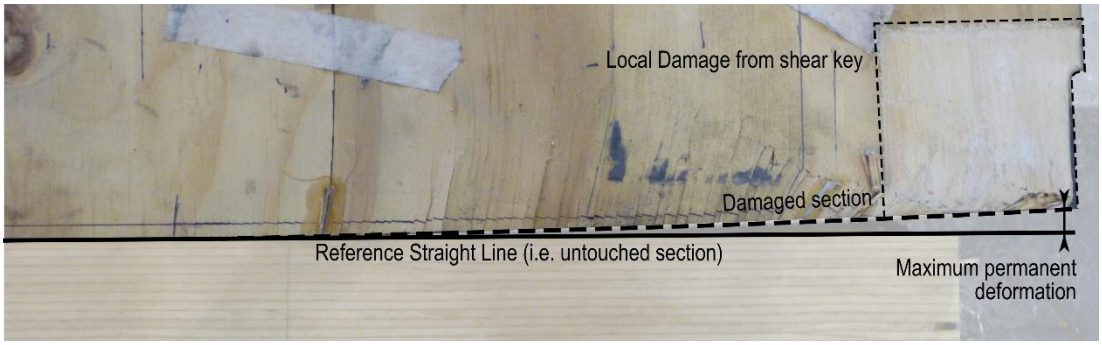

Figure 5-17. Wall base damage observation after testing.

The picture in Figure 5-17 shows a side view of the wall after the test setup was dismantled. To help highlighting the permanent deformation a straight edge was used as a reference point. As highlighted in Figure 5-17, the wall section did not remain plane and some permanent deformation was present.

It is also worth noticing that some minor permanent deformation perpendicular to the grain was present at the wall side. Observations after testing confirmed that this permanent deformation was not significant and did not exceed 4mm after numerous tests at high displacement demands and thus deemed negligible.

5.5.5 Area-based Equivalent viscous damping

The area-based equivalent viscous damping (EVD), ξ_{hyst}, was evaluated from experimental data using Equation (5-3).

$$\xi_{hyst} = \frac{1}{2\pi}\frac{A_h}{F_m \Delta_m} \qquad (5\text{-}3)$$

Where A_h = area within one complete cycle of stabilized force-displacement response
F_m, Δ_m = maximum force and displacement achieved in the stabilized loops

Priestley *et al.* (2007) have proposed analytical equations based on an idealized flag-shaped hysteresis, as shown in Equation (5-4).

$$\xi_{hyst} = \frac{(2-2\beta)(\mu-1)}{\mu\pi\left[1+r(\mu-1)\right]} \qquad (5\text{-}4)$$

Where μ = ductility
β = re-centering ratio (M_{pt}/M_{tot})
r = post-yield stiffness factor

The observed stiffness degradation phenomenon occurred due to the external dissipater connection flexibility. This effect had some influence on the system behaviour in terms of hysteretic damping. To highlight the magnitude of the reduction of the energy dissipated through hysteresis, the area-based viscous damping was evaluated according to Equation (5-4) for each cycle of the experimental tests.

As expected, the stiffness degradation was triggered as soon as the dissipaters activated and developed compressive stresses. Experimental observations on area-based EVD values showed a minor degradation from the first to the subsequent cycle at the same amplitude. The area-based EVD reduction was evaluated with reference to the first cycle area-based EVD values evaluated as shown in Figure 5-18 by the sum of A_0 and A_1.

Figure 5-18a,b also shows the comparison of experimental results with the analytical model of Equation (5-4) for all the systems tested. The analytical area-based EVD prediction is plotted assuming a constant re-centering ratio (design) value and typically showed an increasing trend, decreasing at higher ductility levels. When compared with the experimental observations, it can be seen from Figure 5-18 that the analytical model closely predicts the area-based EVD evaluated at the first loading cycle up to design level (1% drift). However, for higher ductility values Equation (5-4) underestimates the experimental values. This is due to the decreasing of the re-centering ratio at higher drifts caused by isotropic strain hardening in the dissipaters.

Based on the experimental observations of the dissipation degrading behaviour of the system from the first to the third cycles, a damping reduction coefficient was evaluated. The

reduction factor is given as the ratio of the experimentally evaluated area-based EVD averaged over the three cycles of each amplitude and the area-based EVD value evaluated at the first loading cycle. The different values are plotted in Figure 5-18 (bottom right) for the different specimens. For the connection used in the experimental program minimum and maximum reduction factors of 0.4 and 0.85 were observed. It must be noted that for low drifts (i.e. low ductility) the experimentally evaluated area-based EVD is strongly influenced by the slip occurring in the experimental setup. Figure 5-18a,b shows that the minimum and maximum reduction factors for higher drifts (design drift and higher) are approximately 0.55 (S600-4, absolute value 6%) and 0.85 (S400-8, absolute value 14%).

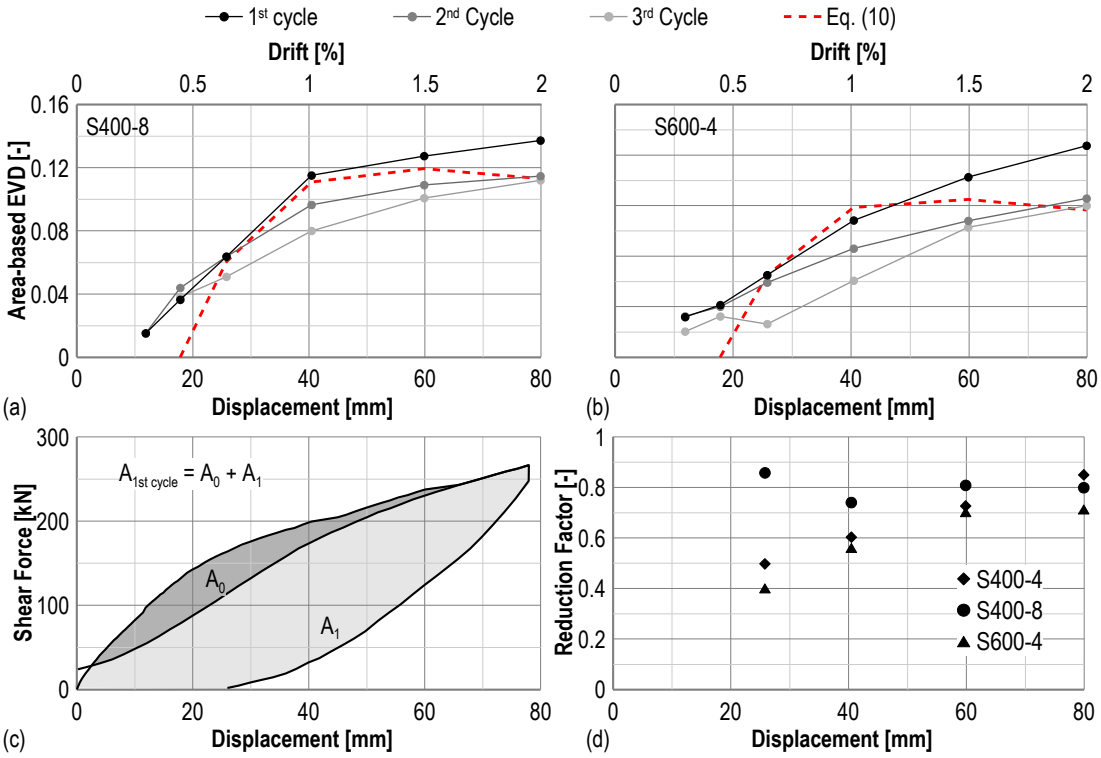

Figure 5-18. Experimental equivalent viscous damping and reduction factor (ratio of EVD evaluated on the backbone curve vs. average of the subsequent cycles).

This reduction factor can have a significant influence on the lateral load design following a displacement-based design methodology (Priestley *et al.*, 2007). Although an experimental evaluation of the area-based EVD reduction factor was provided in the paper, further numerical work is necessary for a more detailed definition of such a factor. The evaluation of the area-based EVD reduction factor can be achieved using advanced numerical models capable of simulating the rocking mechanisms as well as the behaviour of each system component. This will be investigated further in Chapter 8 using a multi-spring model calibrated against the experimental data presented.

5.6 Summary

Table 5-2 reports a summary of the experimental results of significant parameters for several design limit states. The table contains experimental results in terms of timber and post-tensioning stresses as well as of the average strain in the tension-compression yielding dissipaters, for both internal and external configuration.

As mentioned earlier in this chapter, the specimen S600 (i.e. a post-tensioned only solution with 600kN initial post-tensioning force) displayed some plastic behaviour of the timber section due to high compressive stresses. The maximum stress at MCE demand (2% drift) approached the nominal timber compressive strength (45MPa).

As expected, the dissipater elongation in the specimen S400-8 was reduced when compared to the 4 dissipater options (S400-4 and S600-4). This effect was due to an increased number of dissipaters for the same connection (i.e. same connection stiffness). When internal bars were used, an increased unbonded length (300mm) was adopted since no elastic connection contributions were expected and similar strain values as specimen S600-4 were observed.

Table 5-2. Experimental data results, summary of maximum significant performance points values.

ID	*Yield*					*ULS (1% drift)*					*MCE (2% drift)*				
	f_p MPa	γ_p -	f_t MPa	γ_t -	ε_s -	f_p MPa	γ_p -	f_t MPa	γ_t -	ε_s -	f_p MPa	γ_p -	f_t MPa	γ_t -	ε_s -
S200						339	0.40	17	0.39		562	0.67	33	0.73	
S400						437	0.52	20	0.45		646	0.77	35	0.79	
S600						539	0.65	35	0.80		747	0.89	45	1.00	
S400-8	299	0.36	10	0.22	0.0029	399	0.48	16	0.35	0.0190	591	0.71	42	0.92	0.0549
S400-4	292	0.35	8	0.17	0.0032	427	0.51	19	0.42	0.0256	634	0.76	41	0.90	0.0611
S600-4	405	0.49	15	0.33	0.0031	522	0.63	20	0.45	0.0227	715	0.86	35	0.77	0.0579
S600-4i	396	0.47	14	0.31	0.0278	526	0.63	25	0.56	0.0232	755	0.90	44	0.99	n/a*

NOTATION: f_p = maximum post-tensioning stress; f_t =maximum timber stress; ε_s = maximum dissipater average strain;
ξ_{hyst} = area-based hysteretic damping; $\gamma_p = f_p/f_{py}$ (f_{py} post-tensioning steel yield strength); $\gamma_t = f_t/f_{ty}$ (f_{ty} timber yield strength)
* Dissipaters failed at 1.5% drift, hence at MCE drifts the specimen behaved as a post-tensioned only solution

At MCE level, a maximum strain of 6.11% was measured in the dissipaters, which represents a suggested maximum value to avoid premature low cycle fatigue failure based on extensive experimental tests on tension-compression yield dissipaters (Sarti *et al.*, 2013). When subjected to several reversed cycles most of the dissipaters tested in the wall specimens could withstand the entire loading protocol sequence without failure. Internal bars were an exception and prematurely fractured due to insufficient buckling restrain. To avoid this issue a single line of dissipaters positioned at the centreline of the section could be used.

The experimental results summarized in Table 5-2 confirmed material limit state values to be adopted in the design phase. In general, the timber stress at the design level (ULS) shall not exceed 40-50% of the nominal compressive strength and it is expected to reach 70-80% of the nominal strength at MCE demand. The suggested initial post-tensioning stress in the tendons shall not exceed $0.4\text{-}0.5f_{py}$. This upper limit intends to account for the tendon elongation occurring during a seismic event and aims to avoid yielding to the post-tensioning tendons. The dissipaters should be designed to develop a maximum strain at ULS in the range of 2-3%, but should be limited to 6-8% at MCE level. This provides the system with significant ductility and avoids premature low-cycle fatigue failure of the dissipating devices.

5.7 Conclusions

The chapter reported on the experimental response of a series of post-tensioned timber (Laminated Veneer Lumber) walls, using alternative arrangements of dissipaters and post-tensioning level, with particular focus on construction detailing.

The experimental results confirmed the flexibility of the system and all the configurations tested showed excellent performance. Several tests were carried out on the same wall panel and they confirmed that only minor damage occurred to the structural element.

The experimental program showed that the post-tensioning wall system represents a robust solution for resisting seismic actions when properly designed and detailed. This can be achieved by controlling the material stress levels at different performance points. In particular, the post-tensioning bar and timber elements are expected to remain in the elastic range up to MCE levels, while the dissipaters (i.e. the sacrificial elements) are expected to yield and can be expected to fracture for higher demands than ULS.

Testing results highlighted that the connection detailing is crucial to the overall system behaviour. A careful detailing is necessary to minimise the reduction in stiffness resulting from the dissipater's connection displacement. The experimental evaluation of area-based EVD highlighted that this effect caused a reduction of energy dissipation as soon as the dissipaters were activated.

A reduction factor for the area-based EVD has been tentatively proposed based on experimental evidence; further analyses and refinements are required and a more detailed numerical analysis is carried out in Chapter 8 of this dissertation.

5.8 References

ACI 318 Committee. 2011. *Building Code Requirements for Structural Concrete (ACI 318-11) and Commentary*. *American Concrete Institute*. ACI 318 Committee**:** 503.

ACI Innovation Task Group 5 2008. *Acceptance criteria for special unbonded post-tensioned precast structural walls based on validation testing and commentary : an ACI standard*. Farmington Hills, Mich., American Concrete Institute.

Amaris Mesa, A.D. 2010. Developments of Advanced Solutions for Seismic Resisting Precast Concrete Frames *PhD Dissertation*, University of Canterbury, Christchurch, New Zealand.

Buchanan, A.H. 2007. *Timber design guide*. Wellington, New Zealand, New Zealand Timber Industry Federation.

Chopra, A.K., Goel, R.K. 1999. Capacity-Demand-Diagram Methods Based on Inelastic Design Spectrum. *Earthquake Spectra* 15(4): 637-656.

Marriott, D.J., Pampanin, S., Bull, D., Palermo, A. 2008. Dynamic Testing of Precast, Post-Tensioned Rocking Wall Systems with Alternative Dissipating Solutions. *Bulletin of the New Zeland Society for Eartquake Engineering* 41(2): 90-103.

Menegotto, M., Pinto, P.E. 1973. Method of Analysis for Cyclically Loaded Reinforced Concrete Plane Frames Including Changes in Geometry and Non-elastic Behavior of Elements Under Combined Normal Force and Bending. *IABSE Symposium on the Resistance and Ultimate Deformability of Structures Acted on by Well-Defined Repeated Loads, Lisbon*.

Priestley, M.J.N., Calvi, G.M., Kowalsky, M.J. 2007. *Displacement-based seismic design of structures*, IUSS Press.

Sarti, F., Smith, T., Palermo, A., Pampanin, S., Carradine, D.M. 2013. Experimental and analytical study of replaceable Buckling-Restrained Fused-type (BRF) mild steel dissipaters. *New Zealand Society for Earthquake Engineering Annual Conference*, Wellington, New Zealand.

Standards New Zealand. 2006. *NZS 3101: Concrete structures standard*. Standards New Zealand. Wellington, New Zealand, Standards New Zealand.

Zarnani, P., Quenneville, P. 2014. Strength of timber connections under potential failure modes: An improved design procedure. *Construction and Building Materials* 60(0): 81-90.

6 Development and testing of an alternative dissipative post-tensioned rocking timber wall with boundary columns

6.1 Introduction

The objective of this chapter is the development of an alternative Pres-Lam wall configuration aimed to minimize the vertical interaction with the diaphragm system and the investigation of its lateral load response. The research objectives of the experimental program are a) the investigation of the overall seismic behaviour of such system, and b) the development of timber-specific system detailing (Sarti *et al.*, 2015b).

The chapter shows the development of the alternative post-tensioned wall system referred to as Column-Wall-Column (i.e. CWC) system which consists of a single wall coupled with end columns through dissipating devices (U-shaped Flexural Plates). The boundary elements provide the support for the rigid diaphragm with significant reduction of vertical uplifting.

A similar test setup as the experimental testing shown in Chapter 5 was used and briefly discussed in the chapter. Construction detailing was also considered of major importance in the development of this alternative solution, and the chapter shows and discusses the detailing of the system.

To provide a direct comparison with the more "traditional" single wall configuration, several elastic (i.e. post-tensioned only) specimens were tested. Different dissipation arrangements were considered to achieve the equivalent capacity to the single wall specimen, providing a reference comparison for the new system.

A detailed experimental results discussion is provided in the final part of the chapter, which also focused on the influence of the construction detailing on the overall lateral load response of the CWC system.

6.2 Displacement incompatibility in rocking elements

A possible issue with the rocking mechanism is related to vertical displacement incompatibilities between the lateral resisting system and the diaphragm connection. In fact, the uplifting generated at the wall base by the connection rotation is transferred to the drag beams or other similar collector system (see Figure 6-1) and can lead to potential damage to the diaphragm (Henry *et al.*, 2012b). It is worth noting that an analogous issue occurs in monolithic concrete shear walls, where the plastic hinge development and further elongation due to lack of inherent re-centering mechanism result into wall uplifting and consequential diaphragm damage (Fenwick *et al.*, 1993; fib, 2003).

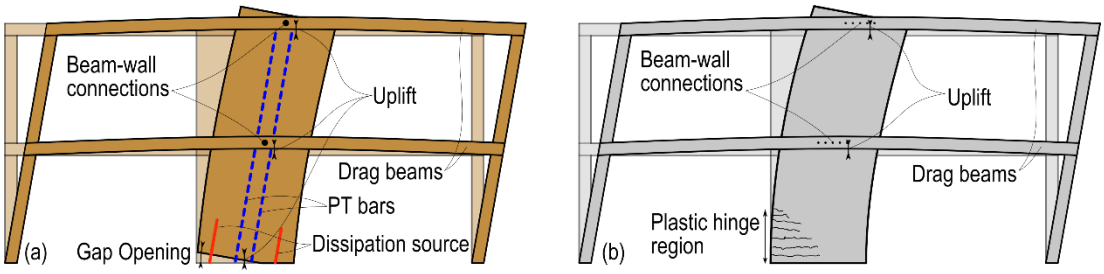

Figure 6-1. Vertical displacement incompatibly between wall and diaphragm. (a) Rocking wall; (b) monolithic concrete wall.

A series of different connection options and construction details to connect the diaphragm drag beams to the rocking wall have been proposed and experimentally validated by Moroder et al. (2014b) who showed that the displacement incompatibility can be addressed by a careful connection detailing in the design phase.

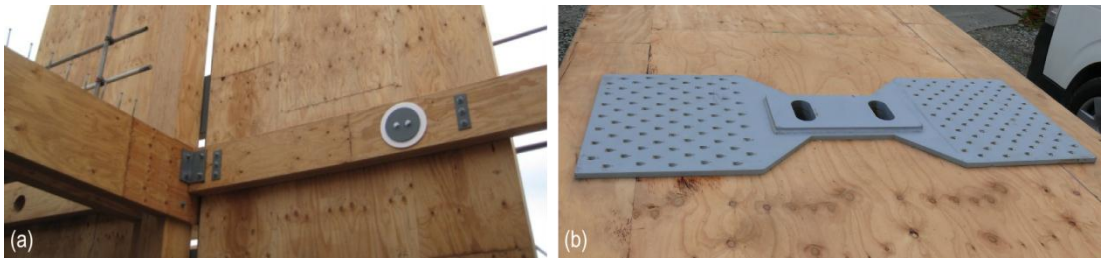

Figure 6-2. Collector beams connection details (modified from Moroder et al. (2014a). (a) NMIT Arts and Media building (Devereux et al., 2011); (b) Trimble Building (Brown et al., 2012)

Recently built Pres-lam buildings provide examples of implementation of the aforementioned connection solutions. The construction detailing of the Nelson and Marlborough Institute of Technology (NMIT) Arts and Media building (Devereux *et al.*, 2011) (Figure 6-2a) adopted 200mm diameter steel pins, located slightly offset from the centre of the (coupled) post-tensioned walls to avoid the central post-tensioning cables. The

absence of continuity of the collector beam and the distance between the pins create little restraint in the case of wall uplift. Furthermore, the pin acts as a hinge so that no rotation is imposed on the beam.

Figure 6-2b shows a different connection detail allowing for the relative vertical displacement between the collector beam and the coupled post-tensioned shear walls in the Trimble Building (Brown *et al.*, 2012). A steel plate with a vertically slotted hole was attached to the timber wall, a steel plate with a round hole was attached to the collector beam and via an interconnecting steel pin, horizontal forces are transferred while allowing for uplift and rotation (Moroder *et al.*, 2014a).

6.3 From coupled walls to a column-wall-column system

Coupled walls are an alternative solution to a single wall configuration, and those consist on two post-tensioned rocking walls which are coupled via yielding devices (Figure 6-3a).

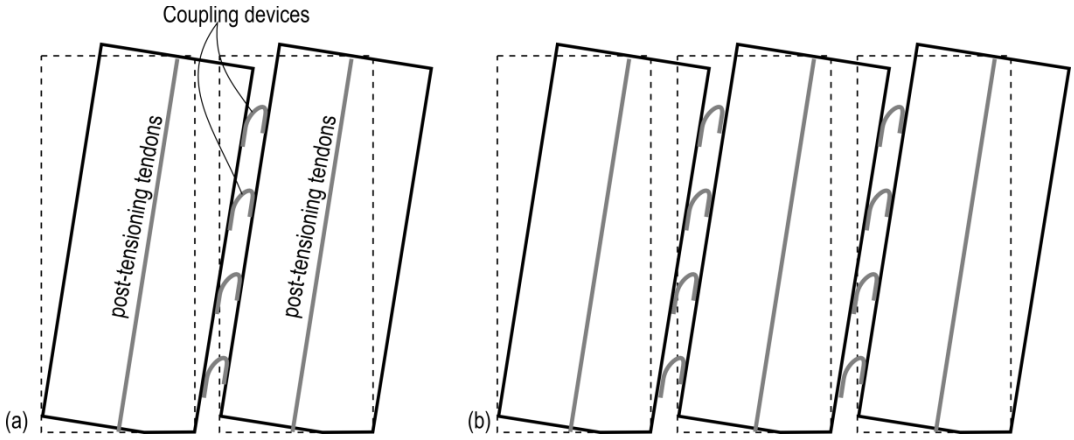

Figure 6-3. (a) Coupled Walls; (b) Multiple coupled walls.

Such system was first tested during the third phase of the PRESSS program (Priestley *et al.*, 1999) and further researched with applications to post-tensioned timber walls (Iqbal *et al.*, 2007). The design principle of the system is to distribute the moment contributions among the two post-tensioned walls, and relying on the dissipaters to connect the two elements and provide damping to the system.

The same concept can be applied to multiple wall elements as shown in Figure 6-3b where three walls can be connected.

The boundary walls can provide the support for the diaphragm, but they are still affected by uplifting due to the gap opening occurring at the wall-foundation (see Figure 6-3b). To avoid

this effect, the boundary elements can be reduced in dimension and effectively become columns, which can still provide the support to the diaphragm while limiting uplifting

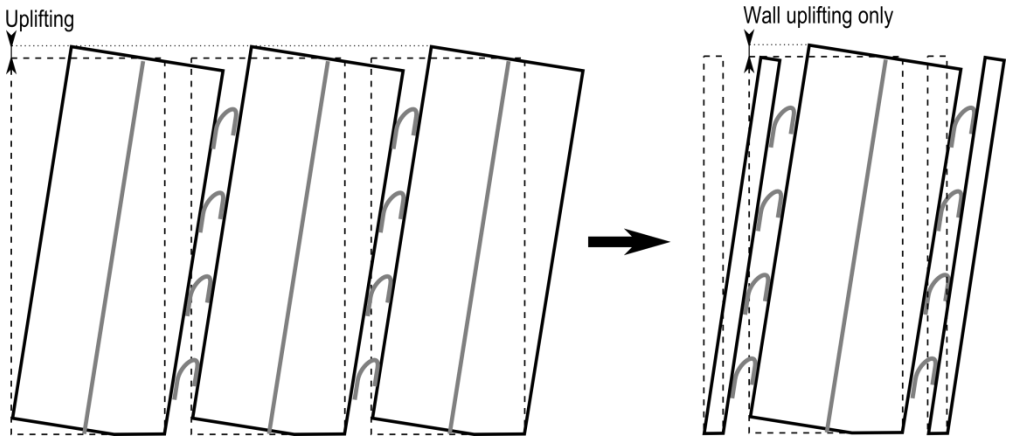

Figure 6-4. Coupled walls to Column-wall-column.

An alternative approach can be the use of a coupled wall configuration capable of limiting the uplifting of the diaphragm supporting elements by reducing the boundary elements dimension (Figure 6-4). This solution was developed for precast concrete and tested by Henry et al. (2012a). The system, referred to as PreWEC system (i.e. Precast Wall with End Columns, see Figure 6-5a), consisted of a precast concrete post-tensioned rocking wall with two steel or concrete end columns that were anchored to the foundation using unbonded post-tensioning (Henry *et al.*, 2012a). Additional dissipation was provided by mild steel devices referred to as O-connectors (Figure 6-5b).

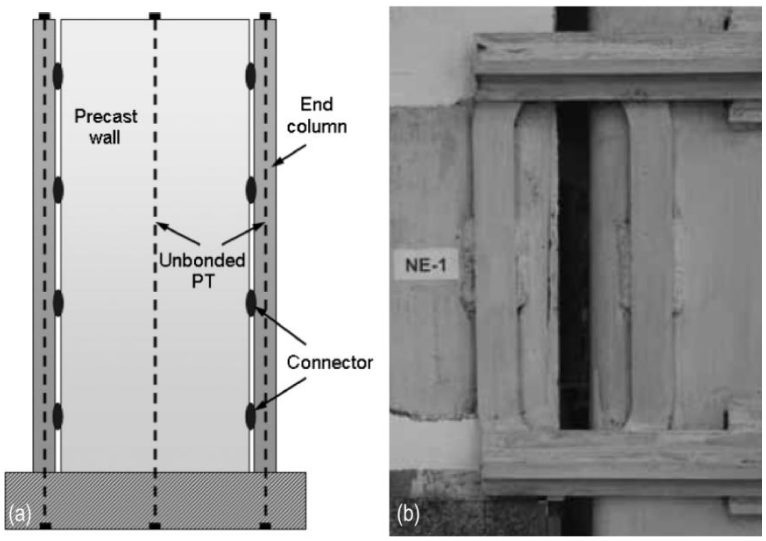

Figure 6-5. (a) PreWEC system; (b) O-connector (modified from Henry et al. (2012a)).

A similar system is proposed in the chapter and extended to timber, and referred to as CWC (Colum-Wall-Column) system. The boundary columns can be connected at the foundation using either post-tensioning or other timber fasteners (i.e. bolts, screws or rivets).

The columns are coupled to the wall system using U-Shaped Flexural Plates (UFPs) (Skinner *et al.*, 1974) or any other dissipative devices, which provide additional overturning moment contribution as well as energy dissipation.

Although the UFPs couple the different components, they do not have the required strength in their out of plane direction to transfer the horizontal shear (e.g. diaphragm inertia forces) between the different elements. To overcome this, horizontal shear transfer devices are used (see Figure 6-6).

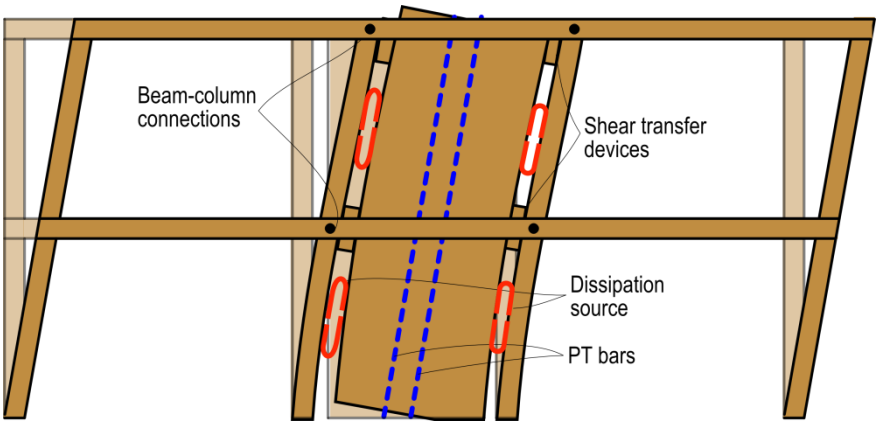

Figure 6-6. Reduced vertical displacement incompatibility in the CWC system.

6.3.1 Design considerations

The design principle of the coupled walls system is to distribute the moment contributions among the two post-tensioned walls, relying on the dissipaters to connect the two elements and provide damping to the system (New Zealand Concrete Society, 2010) as shown in Equation (6-1).

$$OTM = M_{w1} + M_{w2} + \sum V_p L \qquad (6\text{-}1)$$

Where OTM = the overturning moment

M_{w1}, M_{w2} = base moment demands of each wall

ΣV_p = the total shear demand from the coupling elements

L = the centreline-centerline separation between the coupled walls

When three post-tensioned walls are connected, the total overturning moment is given in Equation (6-2).

$$OTM = M_{w1} + M_{w2} + M_{w3} + 2\sum V_p L \quad (6\text{-}2)$$

As the concept of a column-wall-column system if to reduce the uplifting (i.e. the wall section depth), the contributions M_{w1} and M_{w3} tend to decrease significantly, in particular if the columns are pinned, ideally not providing capacity contributions.

For this reason, as well as to provide comparison to the single wall specimens presented in Chapter 5, the following experimental program considers several specimens designed to achieve the same capacity as the specimens in Chapter 5 neglecting the contributions of the columns.

6.4 Design and detailing of the test specimen

6.4.1 Seismic Design of full-scale prototype

The testing specimens were designed as part of a three storey prototype building, implementing an alternative system to the more traditional single post-tensioned single wall. The prototype building was a three storey timber construction with an approximate floor area of 600m^2 (see Appendix A) for more detail on the design of the building).

Due to space constraints in the structural laboratory (i.e. overhead crane clearance), the specimens were tested on a two-thirds scale and the shear and moment demand were scaled according to a constant density approach. The scaled design base shear and moment were 143kN and 475kNm respectively.

The reinforcement layout of the specimens was designed to obtain the same wall capacity as a single wall system (as shown in Chapter 5), so the preliminary design was carried out neglecting any additional contribution due to the boundary columns. This provided direct comparison with the traditional single wall solution (Sarti *et al.*, 2015a).

Table 6-1. Material properties.

Laminated Veneer Lumber		
Modulus of Elasticity	E_t	11000MPa
Compression strength parallel to the grain	f_{ct}	45MPa

Post-tensioning MacAlloy bar steel		
Yield stress	f_{py}	835MPa
Ultimate stress	f_{pu}	1030MPa
Modulus of Elasticity	E_p	170GPa

Mild steel		
Yield stress	f_{ys}	350MPa
Modulus of Elasticity	E_s	200GPa

The reference specimen was designed at a wall re-centering ratio of 0.6. This required an initial post-tensioning force of 400kN to be applied and 8 UFPs (i.e. 4 on each side of the wall) to be connected. The UFPs were 130mm wide flat plates (Mild steel Grade350), 12mm

thick and bent with a radius of 52mm. Table 6-1 contains a summary of the material characteristic values as provided by the manufacturers.

6.4.2 Test specimens detailing

Dissipaters

U-shaped Flexural Plates were used as coupling and dissipation devices. In general, UFPs are connected to the wall edges where the maximum relative displacement between adjacent elements is developed. In order to create a connection that allowed the replacement of the dissipation devices after testing, a steel assembly was fabricated and fastened to the wall and the columns using timber rivets (see Figure 6-7). The rivets were 90mm long and the cross-section dimension was 3.2×6.4mm.

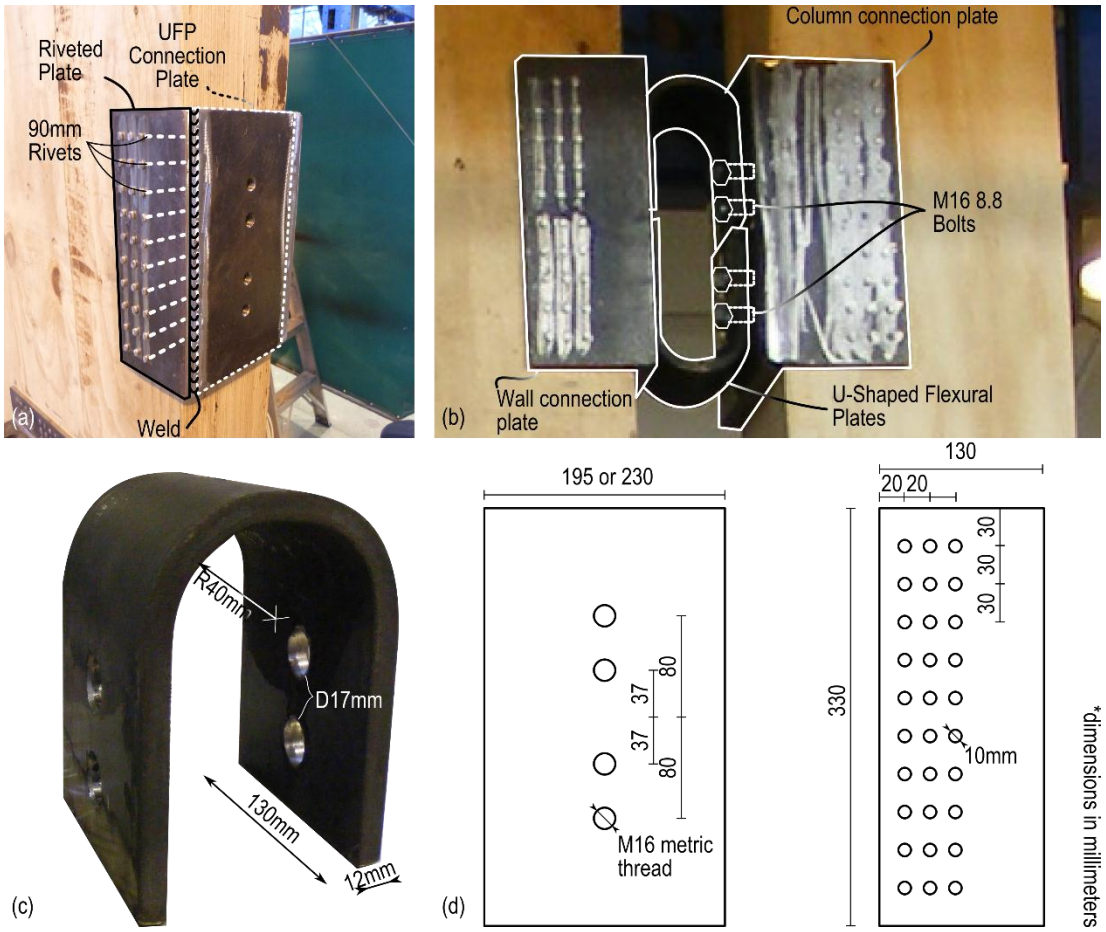

Figure 6-7. UFP connection: (a) detail of the welded connection and riveted plates; (b) detail of the final setup; (c) U-shaped Flexural Plate details; (d) Technical details of the connection plate.

Two 6mm thick steel plates with rows of several 10mm plain holes were welded on the sides of a 20mm thick plate as shown in Figure 6-7. The thicker plate provided the connection

plate for the UFP device via M16 metric threaded holes. Once the wall and columns were positioned, the UFPs could be placed into position and bolted to the coupled elements.

Shear transfer blocks

Whilst UFPs are a suitable way to provide wall coupling as well as dissipation, the low stiffness and strength in the transverse direction of the dissipaters is insufficient to allow using the device to transfer the horizontal shear (i.e. diaphragm forces) between the different components of the system.

Since the relative displacement between the coupled elements is a key feature for the correct functioning of the system, the horizontal forces need to be transferred using sliding devices.

Using such a solution, some friction was expected to develop between the shear transfer device and the wall. Although this friction contribution may increase the dissipative contribution of the system (i.e. higher hysteretic damping), this is not usually easy to evaluate nor should it be relied upon in the design phase unless a specific quality controlled friction device (possibly in combination with, or as an alternative to, the UFP) was used. Moreover, it should be remembered that a significant friction contribution could affect the overall system behaviour, reducing the re-centering capabilities and thus could lead to some residual displacements after testing (or seismic event).

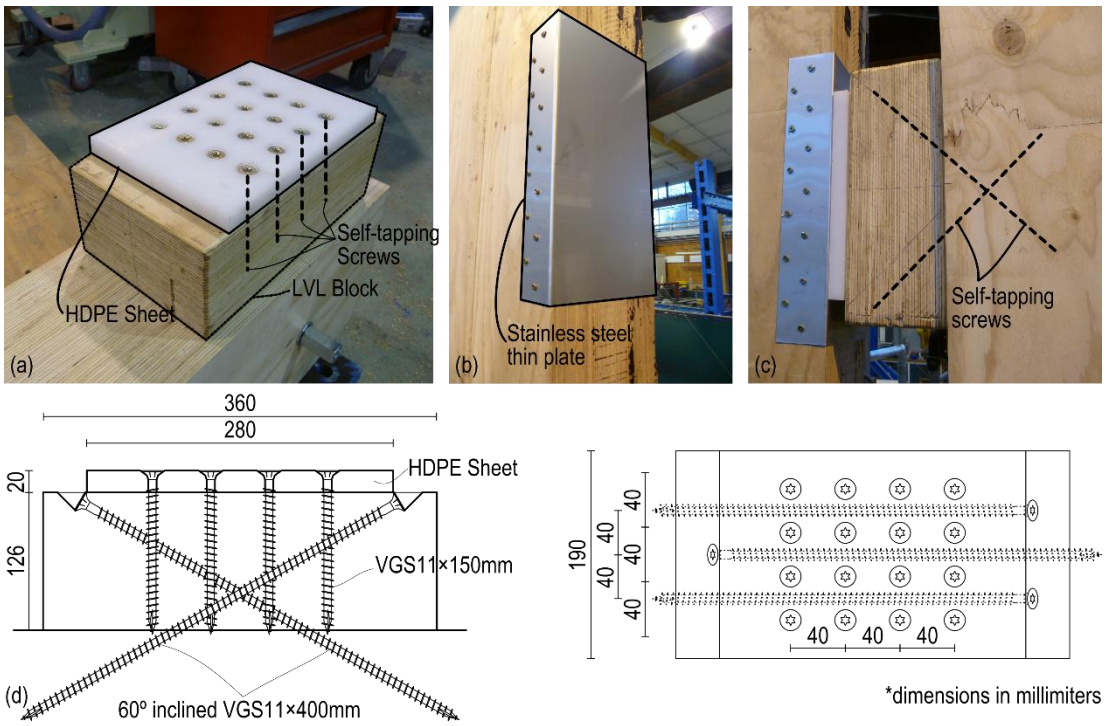

Figure 6-8. Shear transfer device. (a) LVL and HDPE block on the column; (b) Stainless steel sheet on the wall edge; (c) the finished setup; (d) screw layout details.

As a design choice, the shear transfer device was fabricated to minimize the friction force developed by the sliding of the transfer block and the wall panel.

The shear transfer block was a Laminated Veneer Lumber (LVL) element connected to the column through inclined self-tapping screws (see Figure 6-8c,d). A 20mm thick High-Density Polyethylene (HDPE) sheet was screwed to the block's surface and thin stainless steel plates were fixed to the edge of the wall panel as shown in Figure 6-8b. Figure 6-8d shows the screw connection layout.

6.5 Testing methodology

The testing schedule (Table 6-2) consisted of several reinforcing configurations, starting with a number of post-tensioned only specimens (i.e. non-linear elastic behaviour was expected) with 400kN and 600kN initial post-tensioning loads. The main purpose of the post-tensioned only tests was to capture the friction contribution of the shear transfer devices.

Table 6-2.Post-tensioned walls testing schedule.

Test ID	PT Initial	UFPs	Wall Re-centering Ratio, β
CWC400	400kN	n/a	1.00
CWC600	600kN	n/a	1.00
CWC400-8	400kN	8	0.66
CWC400-4	400kN	4	0.80
CWC600-4	600kN	4	0.83

After testing the post-tensioned only specimens, the wall and side column elements were coupled with UFPs and different layouts were implemented to investigate the influence of the re-centering ratio ($\beta = M_{pt}/M_{tot}$).

The specimen representing a structural system with two suspended floors was loaded using a triangular lateral force distribution to simulate the inertia forces associated with a first mode of vibration of the case study. This was achieved using a load distribution beam as shown in Figure 6-9. The load distribution beam had two pins spaced 2m and connected to the specimen with steel plates and threaded rods. The ram was connected using a third pin located at 1.36m from the bottom pin of the distribution (see Figure 6-9).

The ram was connected to the load distribution beam and to the reaction frame through universal joints. The reaction frame was fabricated using a steel column (double 300PFC

profile) and laterally stabilized by two steel struts (SHS100 and SHS200) as shown in Figure 6-9.

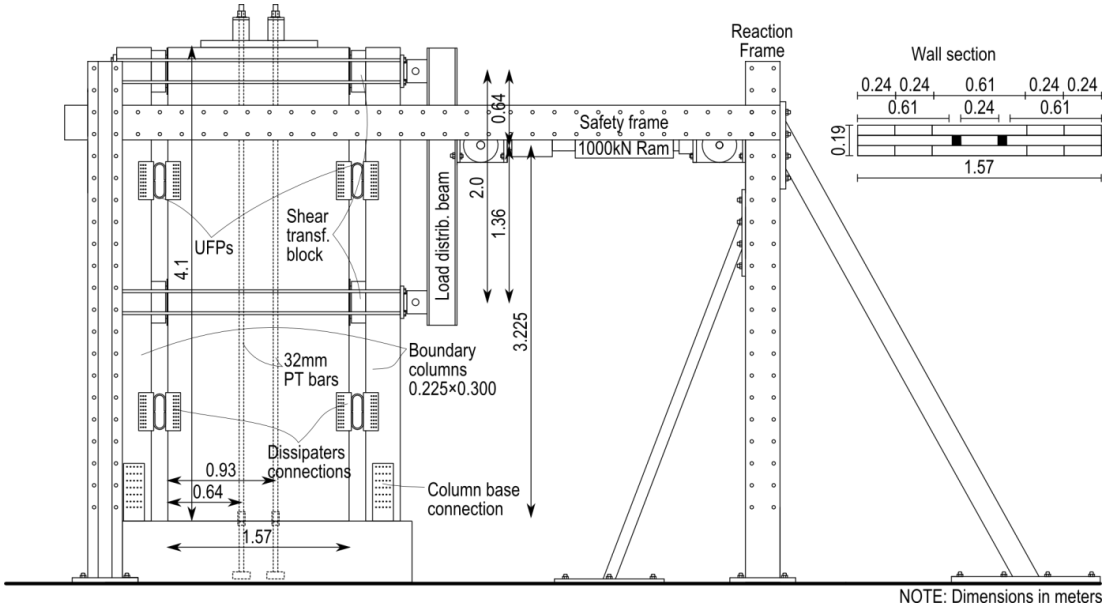

Figure 6-9. Test setup.

The load was applied by a hydraulic actuator with a 1000kN load cell mounted at a height of 3.7m from the strong floor (3.225m from the bottom of the wall).

Since universal joints were used to avoid the development of moment to the hydraulic actuator, the out-of-plane displacement of the specimen was not restrained. Therefore, a safety frame was constructed to avoid displacements in the wall transverse direction.

The quasi-static displacement protocol (Figure 6-11b) consisted of a series of displacement-controlled cycles at increasing levels of amplitude according to the ACI ITG-5.1-07 protocol (ACI Innovation Task Group 5, 2008). The maximum displacement of the first three cycles did not exceed 60% of the design displacement (0.040m or 1%) and the maximum displacement of the subsequent cycles was between 1.25 and 1.5 times the previous maximum displacement. A maximum top drift of 2% was imposed.

6.6 Component testing

As indicated, U-shaped Flexural Plates were used in the CWC system for providing coupling as well as dissipation. The damper was positioned at the sides of the wall element and the uplifting generated by the gap opening allows the activation of the UFP.

A test setup similar to that described in the experimental program in Chapter 3 was used for the testing on the dissipaters. Figure 6-10a shows the test setup consisting of a steel testing

frame manufactured to fit the UFP used in the experimental program. To make the setup symmetric, two side plates were fixed to the base connection plate bolted to the moving head; a central steel plate was then connected to the load cell.

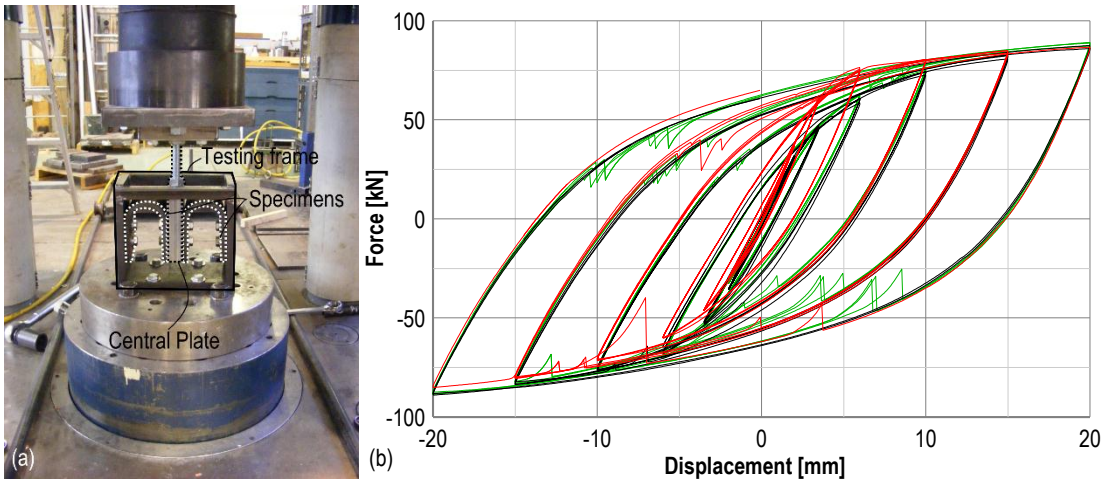

Figure 6-10. (a) Component testing test setup; (b) U-shaped Flexural Plates force-displacement loop.

Although some slip in the setup occurred in the bolted connection, the U-shaped flexural plates showed stable hysteresis throughout the whole test (see Figure 6-10b). Upon repeated testing, the dissipaters did not fail, even after many cycles of up to 20mm displacement. This confirms the improved robustness of this type of device when compared to tension-compression yield dissipaters (see Chapter 3).

6.7 Instrumentation

The displacement at the top of the wall was recorded and at the top of the wall and controlled by feedback from the rotary potentiometer D (see Figure 6-11a). The applied load as well as the post-tensioning forces was recorded using 1000kN load cells, referred to as LC, PT1 and PT2, respectively, and shown in Figure 6-11.

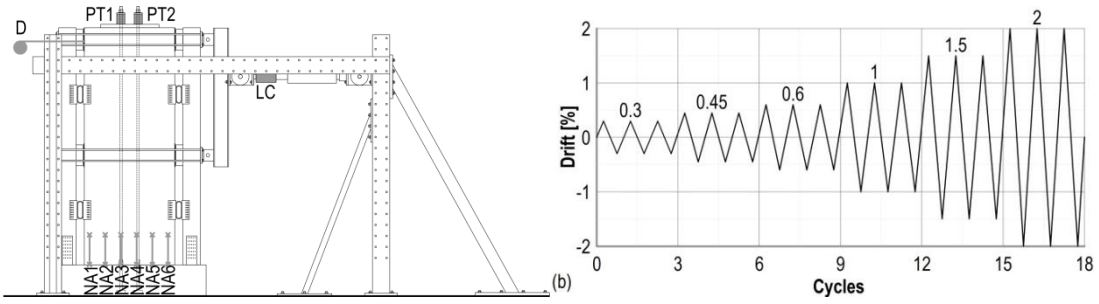

Figure 6-11. (a) Instrumentation setup; (b) testing protocol (ACI Innovation Task Group 5, 2008).

The variation of the compressive region depth was measured by the neutral axis depth. Several spring-loaded potentiometers (NA1 to NA6) were positioned at the wall base at

different spacing to record the uplift of the rocking section along the section depth. This setup also enabled the evaluation of the compressive region (neutral axis) depth and of the connection rotation. The recorded displacement profile was fitted using a linear function, with the slope and zero of such function identifying the connection rotation and neutral axis depth respectively.

6.8 Test results

6.8.1 Pure Post-tensioned specimens

The tests results from pure post-tensioning rocking specimens are shown in Figure 6-12 for two different post-tensioning initial forces (i.e. 400kN and 600kN).

As expected, before the decompression point is reached, the global force-displacement behaviour is that typical of a cantilever system with fixed base.

Although a post-tensioned only rocking solution would be expected to display a non-linear elastic behaviour, an additional contribution from the shear transfer devices between columns and walls occurred. This can be observed in the force-displacement loops of Figure 6-12, where the system shows the development of a small hysteretic area due to the friction force developed.

The sliding friction contribution to the total moment was evaluated in terms of re-centering ratio. Figure 6-13a shows the plots of the re-centering ratio, β, versus the connection rotation as evaluated from the experimental data. In general a decreasing trend is observed for increasing drifts. The experimental values show asymptotic values of about 0.9 and 0.95, which suggests friction contributions of 10% and 5% for CWC400 and CWC600 specimens respectively.

Figure 6-13b-c shows a comparison of the experimental results of CWC system with the post-tensioned single wall option (S400, i.e. post-tensioned only solution at 400kN initial post-tensioning force) reported in Chapter 5. While the moment-rotation chart demonstrates the additional dissipative contribution due to the shear transfer blocks (5 to 10% of the total moment), the neutral axis depth (Figure 6-13c) is not significantly affected by the additional axial contribution developed in the shear transfer device.

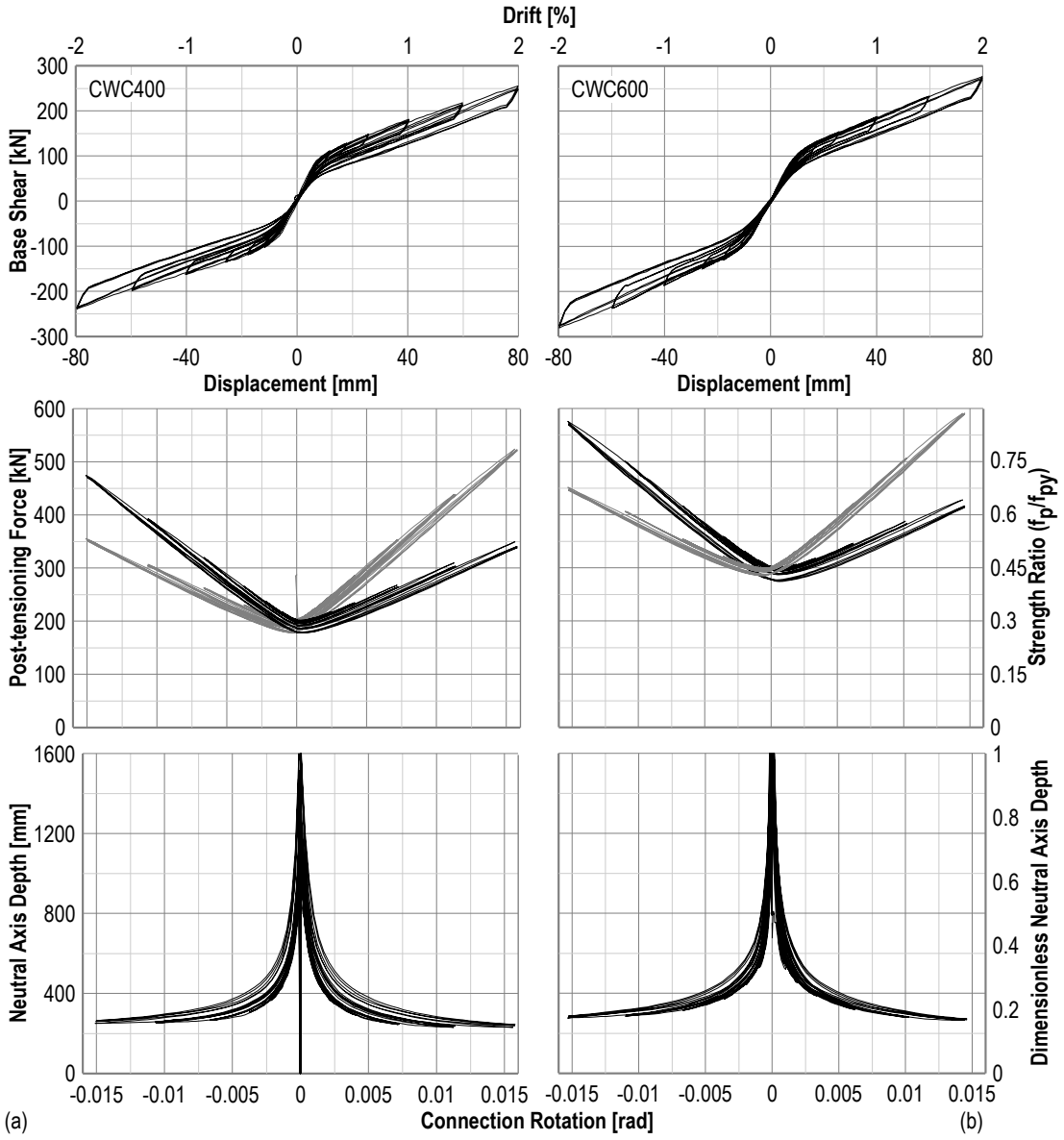

Figure 6-12. Pure post-tensioned rocking experimental results.

The comparison between the alternative system and a more traditional single wall configuration highlights that the two systems can be designed to be equivalent with no apparent major differences in terms of the seismic response. However, the CWC system has the significant advantage of avoiding displacement incompatibility issues thus allowing the diaphragm damage avoidance.

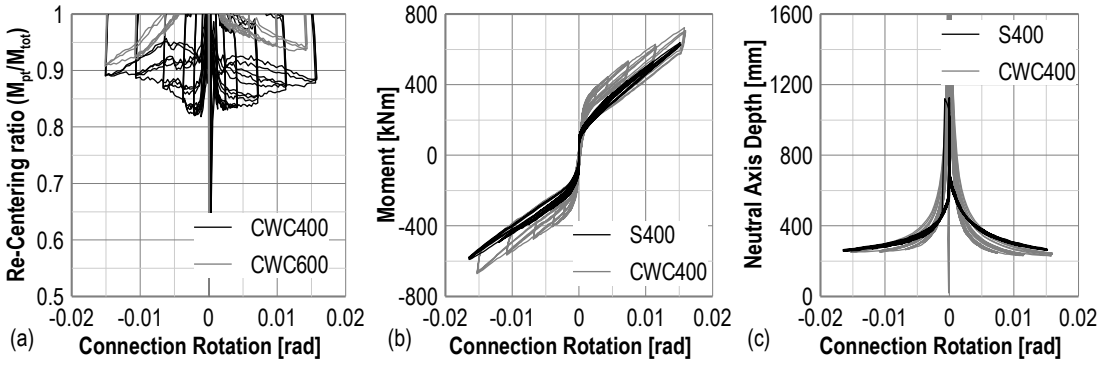

Figure 6-13. Comparison of CWC vs. Single Wall equivalent (a) Re-centering ratio vs. connection rotation. Comparison with single wall options: (b) moment and (c) neutral axis depth versus rotation.

6.8.2 Rocking/Dissipative (hybrid) specimens

After testing the post-tensioned only configuration, U-shaped Flexural plates were added to the system in different configurations.

As highlighted by the experimental results in Figure 6-14, all the specimens displayed a stable hysteresis. Yet, the contribution of the UFPs was not significant in terms of hysteretic area-based damping. The effect of the boundary columns on the shape of the force-displacement loops can be highlighted by distinguishing the elastic contributions of the columns from the overall behaviour as shown in the wall moment-rotation charts of Figure 6-14. The moment-rotation charts of the wall better highlight the difference between the different options showing, as expected, a larger hysteretic area for the specimen CWC400-8 designed with the lowest re-centering ratio.

Unlike tension-compression yield dissipaters (Sarti *et al.*, 2013), U-shaped flexural plates do not show any isotropic strain hardening. This effect is reflected in the experimental results of Figure 6-14 which highlights that no force increase occurred in the unloading branch of the hysteresis where the clamping action from the post-tensioned tendons yields in compression the U-shape flexural plates closing the gap.

Similarly to the single post-tensioned wall configurations the base shear-displacement loops highlight some stiffness degradation. This is assumed to be due to some connection flexibility of the riveted steel anchorage assembly as well as ratcheting in the dissipaters. In fact, as shown in Figure 6-15, while the dissipaters generally undergo significant tension (positive) displacements, they do not deform into net negative displacement. This causes the dissipaters to develop lower forces, for the same level of displacement, during their re-loading.

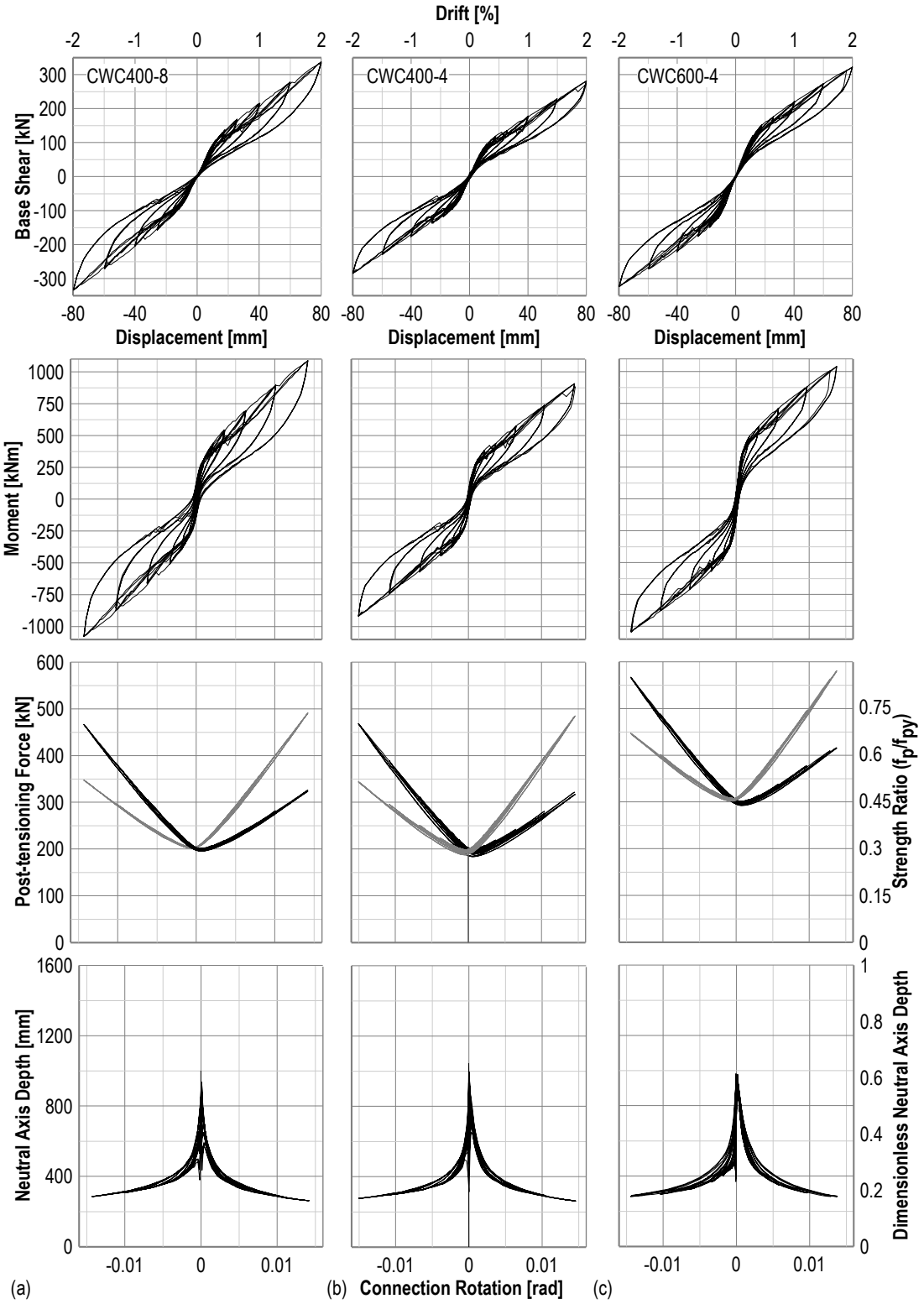

Figure 6-14. Dissipative post-tensioned rocking experimental results.

As an example, Figure 6-15 shows the analytical force-displacement loop of the UFP used in the experimental setup. It can be noted that the force developed at 4mm at first loading is 30kN, while after load reversal and full reloading it is 21kN.

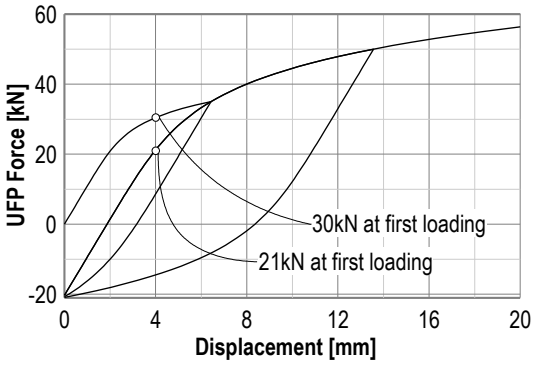

Figure 6-15. Dissipater's ratcheting behaviour.

6.8.3 Area-based Equivalent viscous damping

The equivalent viscous damping (EVD), ξ_{hyst}, for each dissipative rocking specimen tested was calculated using Equation (6-3).

$$\xi_{hyst} = \frac{1}{2\pi}\frac{A_h}{F_m \Delta_m} \qquad (6\text{-}3)$$

Where A_h = area within one complete cycle of stabilized force-displacement response

F_m, Δ_m = maximum force and displacement achieved in the stabilized loops

The results from experimental data were compared to the analytical formula of Equation (6-4), proposed by Priestley et al. (2007) based on an ideal flag-shaped hysteresis.

$$\xi_{hyst} = \frac{(2-2\beta)(\mu-1)}{\mu\pi\left[1+r(\mu-1)\right]} \qquad (6\text{-}4)$$

The formulation reported in Equation (6-4) has been modified from the original nomenclature to include the re-centering ratio β as used in the design of dissipative post-tensioned rocking sections.

The area-based hysteretic viscous damping was evaluated considering the experimental back-bone curve to provide a direct comparison with the analytical model. The area-based EVD was then evaluated for each subsequent cycle in the testing schedule.

The experimental results of the area-based viscous damping show good agreement with the analytical formula proposed by Priestley et al. (2007) up to design level (40mm or 1% drift). For higher level of drift, the model under-predicts the EVD; that is due to a decrease in the re-centering ratio, β.

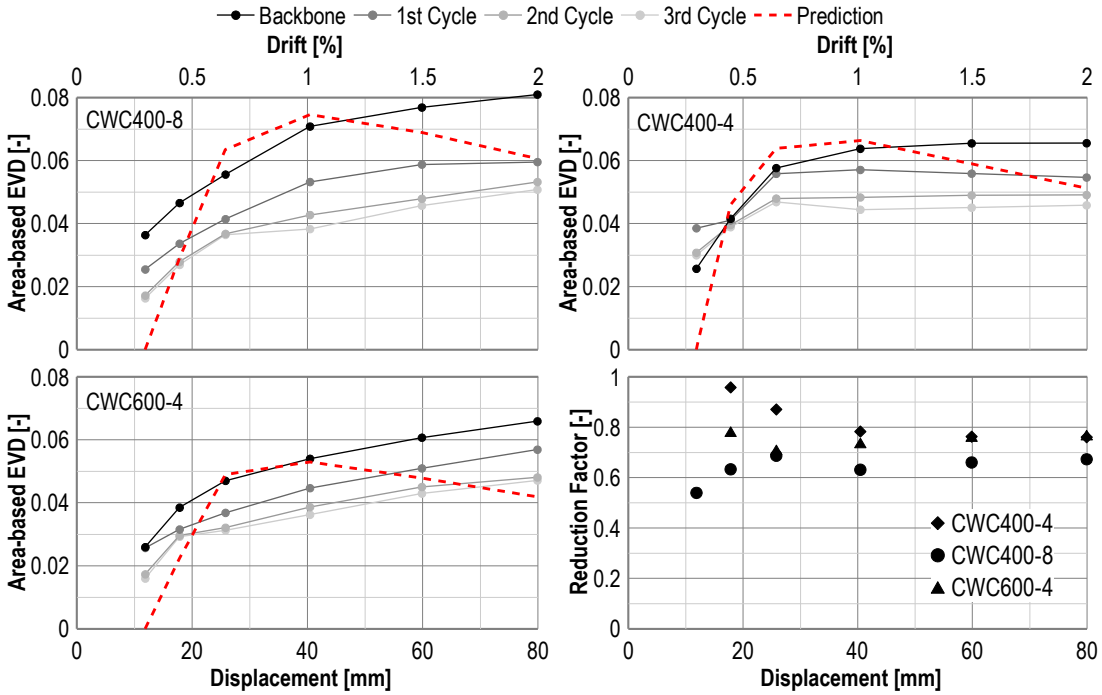

Figure 6-16. Experimental equivalent viscous damping and reduction factor.

The experimental specimens showed an equivalent viscous damping between 5.5% and 7.0% at 1% design drift. Those EVD values are relatively low in comparison to those obtained in a single wall option (in the order 10-12% as discussed in Chapter 5). These reduced values can be justified by the additional elastic contributions from the columns which increase the system's stiffness and strength, yet reducing the hysteretic area of the force-displacement loop.

It can be seen from Figure 6-16 that for drifts in the range of approximately 0.5% to 1.25%, Equation (6-4) is a good prediction of the EVD for the initial (backbone) cycle. For all subsequent cycles Equation (6-4) tends to over-estimate the EVD and this is assumed to be due to the stiffness degradation that occurs as a result of minor displacement in the dissipater fixing devices.

As proposed in Chapter 5, the reduction in EVD that results from dissipater fixture movement can be quantified as a ratio of the EVD obtained during the first (backbone) cycle and the average EVD across all the subsequent cycles. This ratio, as a function of drift, is also shown in Figure 6-16 (bottom right chart). It can be seen that the reduction factor is approximately 0.75.

6.9 Conclusions

While dissipative post-tensioned timber walls are a structurally efficient and robust seismic resisting system for multi-storey buildings, the uplifting coming from the gap opening may cause damage to the floor diaphragm.

The issue can be addressed using either a careful design of the diaphragm connections (Moroder *et al.*, 2014b) or using an alternative wall configuration which minimizes displacement incompatibilities.

The chapter presented the detailing and testing of an alternative Colum-Wall-Column (CWC) system for the mitigation of displacement incompatibilities in the diaphragm.

The experimental program consisted of several wall layouts considering different initial post-tensioning stress levels as well as dissipative devices configurations.

The experimental results on the new alternative system highlighted the flexibility and good performance of the system. All the specimens tested displayed a stable force-displacement response and the development of significant energy dissipation.

Some minor stiffness degradation was observed due to ratcheting in the dissipaters, yet its influence of the overall response (force-displacement) of the system was negligible; however, the stiffness degradation caused a reduction of equivalent viscous damping which was experimentally evaluated. An average value of 0.75 for such reduction factor was found.

6.10 References

ACI Innovation Task Group 5 2008. *Acceptance criteria for special unbonded post-tensioned precast structural walls based on validation testing and commentary : an ACI standard*. Farmington Hills, Mich., American Concrete Institute.

Brown, A., Lester, J., Pampanin, S., Pietra, D. 2012. Pres-Lam in practice - A damage-limiting rebuild project. *New Zealand Society of Structural Engineers Conference*, Auckland, New Zealand.

Devereux, C., Holden, T., Buchanan, A., Pampanin, S. 2011. NMIT Arts & Media Building-Damage Mitigation Using Post-tensioned Timber Walls. *PCEE Conference*, Auckland, New Zealand.

Fenwick, R., Megget, L. 1993. Elongation and load deflection characteristics of reinforced concrete members containing plastic hinges. *Bulletin of the New Zealand National Society for Earthquake Engineering* 26(1): 28-41.

fib 2003. *Seismic design of precast concrete building structures: state-of-art report*. Lausanne, Switzerland, Fédération internationale du béton, Bulletin n. 23 (Chairmen R. Park, F. Watanabe).

Henry, R., Aaleti, S., Sritharan, S., Ingham, J. 2012a. Seismic Analysis of a Low-Damage Precast Wall with End Columns (PreWEC) Including Interaction with Floor Diaphragms. *Journal of the Structural Engineering Society of New Zealand* 25(1): 69-81.

Henry, R., Ingham, J., Sritharan, S. 2012b. Wall-to-floor interaction in concrete buildings with rocking wall systems. *NZSEE Conference*, Christchurch, New Zealand.

Iqbal, A., Pampanin, S., Buchanan, A.H., Palermo, A. 2007. Improved Seismic Performance of LVL Post-tensioned Walls Coupled with UFP devices. *8th Pacific Conference on Earthquake Engineering*, Singapore.

Moroder, D., Sarti, F., Palermo, A., Pampanin, S., Buchanan, A. 2014a. Experimental investigation of wall-to-floor connections in post-tensioned timber buildings. *New Zealand Society for Earthquake Engineering Annual Conference*, Auckland, New Zealand.

Moroder, D., Sarti, F., Palermo, A., Pampanin, S., Buchanan, A. 2014b. Seismic design of floor diaphragms in post-tensioned timber buildings. *World Conference on Timber Engineering*, Quebec City, Canada.

New Zealand Concrete Society 2010. *PRESSS Design Handbook*.

Priestley, M.J.N., Calvi, G.M., Kowalsky, M.J. 2007. *Displacement-based seismic design of structures*, IUSS Press.

Priestley, M.J.N., Sritharan, S., Conley, J.R., Pampanin, S. 1999. Preliminary results and conclusions from the PRESSS five-story precast concrete test building. *Pci Journal* 44(6): 42-67.

Sarti, F., Palermo, A., Pampanin, S. 2015a. Development and Testing of an Alternative Dissipative Posttensioned Rocking Timber Wall with Boundary Columns. *Journal of Structural Engineering*: E4015011.

Sarti, F., Palermo, A., Pampanin, S. 2015b. Quasi-Static Cyclic Testing of Two-Thirds Scale Unbonded Posttensioned Rocking Dissipative Timber Walls. *Journal of Structural Engineering*: E4015005.

Sarti, F., Smith, T., Palermo, A., Pampanin, S., Carradine, D.M. 2013. Experimental and analytical study of replaceable Buckling-Restrained Fused-type (BRF) mild steel dissipaters. *New Zealand Society for Earthquake Engineering Annual Conference*, Wellington, New Zealand.

Skinner, R.I., Kelly, J.M., Heine, A.J. 1974. Hysteretic dampers for earthquake-resistant structures. *Earthquake Engineering & Structural Dynamics* 3(3): 287-296.

7 Structural mechanics of Post-Tensioned Timber Wall systems

7.1 Introduction

The main objective of Chapter 7 is to refine the current analytical models for the design of post-tensioned rocking timber sections, incorporating the design parameters developed in previous experimental chapters and validating its capabilities to predict the wall response.

Firstly, the current moment-rotation procedure is presented, and some refinements are proposed based on experimental and analytical findings on internal and external dissipaters behaviour presented in Chapters 3 and 4 of this dissertation.

Once the moment-rotation response of the connection is evaluated, the general force displacement behaviour of the cantilevered wall can be determined accounting for the flexibility of the wall panel. For a single wall configuration the total displacement is worked out for an assumed triangular distribution of forces, in accordance with the imposed lateral loading scenario (i.e. earthquake). The total displacement of the post-tensioned element is evaluated accounting for the rigid body rotation developed by the gap opening at the base, as well as the elastic bending and shear deformations of the wall.

When a different system such as the column-wall-column option, is used some different considerations must be made. While the wall element takes the most of the inertial forces form earthquake loading, some additional contributions from the boundary elements may be present. A simplified approach for this coupled system is proposed based on simplified assumptions on the displacement profile and the boundary conditions of the system.

7.2 Iterative Moment-rotation analysis

The moment-rotation analysis of post-tensioned rocking sections is carried out following a moment-rotation iterative procedure firstly proposed by Pampanin et al. (2001) and later modified by Palermo et al. (2008) for precast concrete post-tensioned elements. The iterative procedure, referred to as Modified Monolithic Beam Analogy (MMBA), was adapted to post-tensioned timber (Pres-Lam) systems by Newcombe et al. (2008). The MMBA comprises of a step-by-step iterative procedure which is based on global strain compatibility and assumes that the total displacement of the rocking element is equal to that of an analogic monolithic element. The step-by-step procedure is summarized in the flow chart of Figure 7-1.

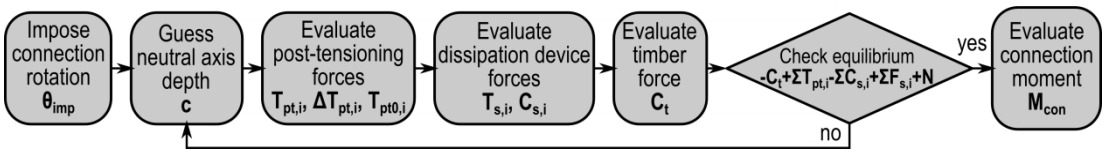

Figure 7-1. Moment-rotation MMBA step-by-step procedure.

Figure 7-2 shows the nomenclature adopted in the following equations.

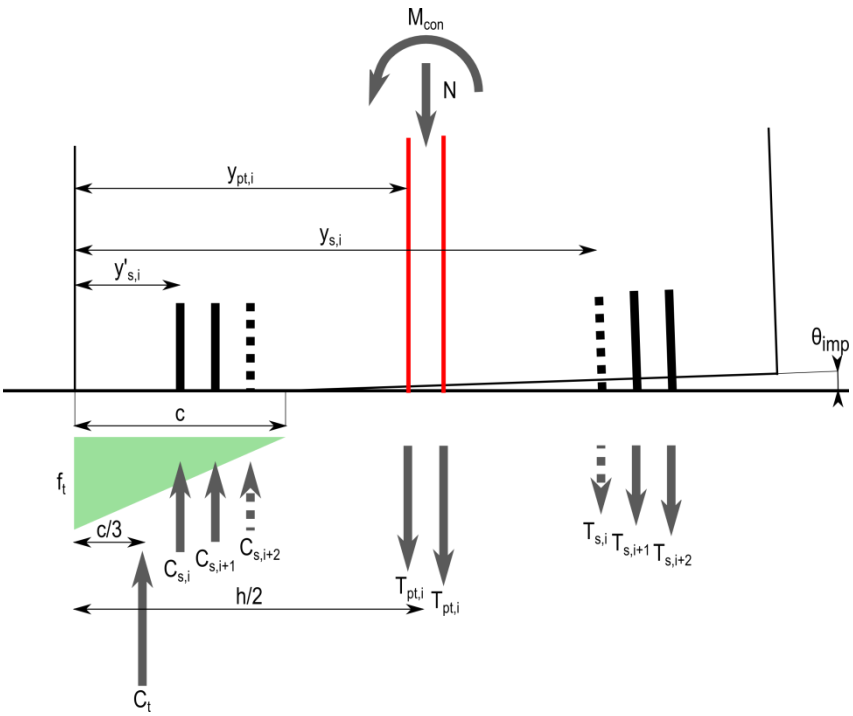

Figure 7-2. Section analysis nomenclature.

The general moment-rotation behaviour of the wall base connection can be broken down into two main areas. When the connection moment is lower than the decompression moment

(Equation (7-1)), M_{dec}, the gap is not expected to open and the wall behaves as a vertical cantilever.

$$M_{dec} = \frac{Z}{A}\left(T_{pt0} + N\right) \quad (7\text{-}1)$$

Where Z = section modulus
A = cross-sectional area
T_{pt0} = initial post-tensioning force
N = axial force from gravity loads

The moment-rotation response past the decompression moment is carried out as follows and as shown in the flowchart of Figure 7-1.

7.2.1 Impose the connection rotation

The base connection rotation, θ_{imp}, is imposed also considering lateral load design and elastic contributions of the cantilevered wall (see section 7.3.1).

7.2.2 Guess the neutral axis depth

As part of the iterative procedure the natural axis depth value, c, must be guessed and later iterated to achieve the vertical force equilibrium of the section.

7.2.3 Evaluate post-tensioning reinforcement forces

For the imposed rotation, θ_{imp}, and guessed neutral axis depth, c, the tendon elongation due to gap opening of the i-th reinforcement layer is worked out as:

$$\Delta_{pt,i} = \theta_{imp}\left(y_{pt,i} - c\right) \quad (7\text{-}2)$$

Where $\Delta_{pt,i}$ = elongation of the i-th post-tensioning reinforcement layer
$y_{pt,i}$ = edge distance of the i-th post-tensioning reinforcement layer

The strain and post-tensioning force increment of the i-th post-tensioning layer is then evaluated as:

$$\Delta\varepsilon_{pt,i} = \frac{\Delta_{pt,i}}{l_{ub,i}} \quad (7\text{-}3)$$

$$\Delta T_{pt,i} = \Delta\varepsilon_{pt,i} E_{pt} A_{pt,i} \quad (7\text{-}4)$$

Where $l_{ub,i}$ = unbonded length of the i-th post-tensioning reinforcement layer

E_{pt} = post-tensioning steel elastic modulus

$A_{pt,i}$ = cross-section area of the i-th post-tensioning reinforcement layer

Finally the total post-tensioning force, $T_{pt,i}$, can be evaluated:

$$T_{pt,i} = T_{pt0,i} + \Delta T_{pt,i} \qquad (7\text{-}5)$$

Where $T_{pt0,i}$ = initial post-tensioning force of the i-th post-tensioning reinforcement layer

7.2.4 Evaluate the dissipation device forces

The displacement due to gap opening of the i-th tension dissipative layer, $\Delta_{s,i}$, and compression dissipative layer, $\Delta_{s,i}$, is given in Equation (7-6):

$$\begin{aligned} \Delta_{s,i} &= \theta_{imp}\left(y_{s,i} - c\right) \\ \Delta'_{s,i} &= \theta_{imp}\left(c - y'_{s,i}\right) \end{aligned} \qquad (7\text{-}6)$$

Where $y_{s,i}$ = edge distance of the i-th mild steel reinforcement tension layer

$y'_{s,i}$ = edge distance of the i-th mild steel reinforcement compressive layer

Tension-compression external dissipaters

Generally, the dissipative system in post-tensioned timber walls consists of internal or external mild steel bars which dissipate energy by axial tension and compression yielding within a fuse area of reduced diameter.

When external fuse-type dissipaters are used, as shown in Chapter 3, the elastic contributions of the different parts of the dissipaters should be considered in the evaluation of the dissipaters elastic deflections; moreover, external dissipaters needs to be connected to the structural element via metallic fasteners which add stiffness contributions to the dissipater system. Using the analytical model shown in Chapter 3 and accounting for the connection's flexibility the dissipater's effective unbonded length, $\overline{l'_{ub}}$, can be evaluated as:

$$\overline{l'_{ub}} = k_a L_{fuse} + \frac{E_s A_{s,i}}{k_{con}} \qquad (7\text{-}7)$$

Where k_a = correction factor as defined in Chapter 3 accounting for the different flexibility contributions

L_{fuse} = dissipater's fuse length

E_s = mild steel modulus of elasticity

$A_{s,i}$ = cross-section area (i.e. fuse area) of the i-th dissipative layer

k_{con} = connection flexibility

Therefore, the strain in the dissipaters, $\varepsilon_{s,i}$ and $\varepsilon'_{s,i}$, is evaluated as:

$$\varepsilon_{s,i} = \frac{\Delta_{s,i}}{\overline{\overline{l'_{ub}}}}$$
$$\varepsilon'_{s,i} = \frac{\Delta'_{s,i}}{\overline{\overline{l'_{ub}}}} \qquad (7\text{-}8)$$

Tension-compression internal dissipaters

Alternatively, internal dissipaters can be used, and the additional displacement for this reinforcement option is given by the tensile strain penetration contribution experimentally calibrated in Chapter 4 for mild steel bars embedded in timber. When the bar is anchored in concrete relying on bond, the contribution proposed by Sritharan (1998) shall be taken into account as well. The strain in the internal dissipater is evaluated below:

$$\varepsilon_{s,i} = \frac{\Delta_{s,i} - \Delta_{sp,i}}{l'_{ub}}$$
$$\varepsilon'_{s,i} = \frac{\Delta'_{s,i}}{l'_{ub}} \qquad (7\text{-}9)$$
$$\Delta_{sp,i} = f_{sy} d_b \left\{ 0.022\left(\frac{2}{3}\varepsilon_{e,i} + \varepsilon_{p,i}\right) + 0.032 \begin{cases} \left(\varepsilon_{e,i} + 0.094\varepsilon_{p,i}\right) & \text{threaded} \\ \left(\varepsilon_{e,i} + 0.031\varepsilon_{p,i}\right) & \text{deformed} \end{cases} \right\}$$

Where f_{sy} = mild steel yield strength

d_b = the bar diameter (i.e. at the start of bond length)

$\varepsilon_{e,i}$ = the elastic strain in the i-th dissipative layer

$\varepsilon_{p,i}$ = the elastic strain in the i-th dissipative layer

As shown in Chapter 3, after the yielding point of the bar is reached, the slip due to tensile strain penetration tends to stabilize having a relatively small slope when compared to the elastic trend; therefore, the following formula can be adopted applying those simplifications and considering the equivalent unbonded length concept as above:

$$\varepsilon_{s,i} = \frac{\Delta_{s,i}}{l'_{ub} + (0.022 + 0.032) f_{sy} d_b} = \frac{\Delta_{s,i}}{\overline{l'_{ub}}} \qquad (7\text{-}10)$$

Once the strain in the mild steel dissipater is evaluated, the stress can be worked out using a bi-linear stress-strain relationship:

$$f_{s,i} = f_{sy}\left[1 + r\left(\frac{\varepsilon_{s,i}}{\varepsilon_{sy}} - 1\right)\right] \qquad (7\text{-}11)$$

Where $f_{s,i}$ = stress of the i-th dissipative layer
f_{sy} = mild steel yield strength
r = post-yielding stiffness ratio (usually taken as 0.8% for mild steel)
$\varepsilon_{s,i}$ = strain of the i-th dissipative layer
ε_{sy} = mild steel yield strain

The steel forces, $T_{s,i}$ and $C_{s,i}$, can now be worked out from Equation (7-12):

$$\begin{aligned} T_{s,i} &= f_{s,i} A_{s,i} \\ C_{s,i} &= f'_{s,i} A'_{s,i} \end{aligned} \qquad (7\text{-}12)$$

U-shaped flexural plates and other devices

U-shaped Flexural Plates (UFPs) (Skinner *et al.*, 1974) can be used in coupled walls and CWC systems as coupling element, but it can also be used connected to the edge of a single wall.

Skinner et al. (1974) first developed the analytical model to predict the yielding behaviour of the devices. The yield force of the UFP device is:

$$F_u = \frac{2M_0}{D_u} \qquad (7\text{-}13)$$

Where M_0 = the yield load moment
D_u = the average bending radius

For rectangular sections, the yield load moment is given by Equation (7-14)

$$M_0 = \frac{1}{4} b_u t_u^2 f_{sy} \qquad (7\text{-}14)$$

Where b_u = the plate width
t_u = the plate thickness
f_{sy} = the mild steel stress.

$$F_u = \frac{b_u t_u^2}{2D_u} f_{sy} \qquad (7\text{-}15)$$

As pointed out by Skinner et al. (1974) the maximum strain developed in the device, ε_{max}, is independent from the stroke and is determined by its geometry:

$$\varepsilon_{max} = \frac{t_u}{D_u} \tag{7-16}$$

Test results showed that the factors contributing to the failure of the device were the stroke and the level of maximum strain. The chart in Figure 7-3 shows experimental-based stroke-strain relationships for different cycles to failure.

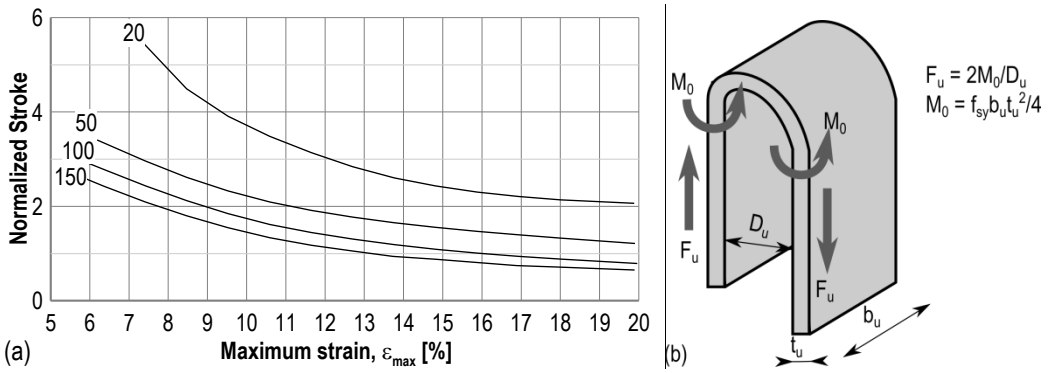

Figure 7-3. (a) Curves of life time of UFPs devices (modified from (Kelly et al., 1974)). (b) UFP device.

Baird et al. (2014) carried out extensive numerical modelling, and using a combination of experimental, analytical and numerical results proposed formulations to determine the key parameters of the force-displacement response of the dissipaters as summarized below.

$$F_u = \frac{f_{sy} b_u t_u^2}{2D_u} \tag{7-17}$$

$$k_0 = \frac{16 E_s b_u}{27\pi}\left(\frac{t_u}{D_u}\right)^3 \tag{7-18}$$

$$R = 7.1 \ln\left(\frac{t_u}{D_u}\right) + 29.5 \tag{7-19}$$

Where F_u = UFP yield force
k_0 = UFP initial stiffness
R = Ramberg-Osgood factor
b_u = width of the UFP plate section
t_u = thickness of the UFP plate section
D_u = diameter of UFP plate bend

E_s = steel elastic modulus

The parameters in Equations (7-17) to (7-19) give the calibration of the Ramberg-Osgood hysteresis in terms of force displacement reported in Equation (7-22).

$$\Delta_{s,i} = \frac{T_{s,i}}{k_0}\left[1+\left(\frac{T_{s,i}}{F_u}\right)^{R-1}\right]$$

$$\Delta'_{s,i} = \frac{C_{s,i}}{k_0}\left[1+\left(\frac{C_{s,i}}{F_u}\right)^{R-1}\right] \qquad (7\text{-}20)$$

Other devices can be used as well and range from mild steel devices such as dissipative angles (Di Cesare *et al.*, 2013), friction devices (Morgen *et al.*, 2007) to velocity-dependant dissipaters (Marriott *et al.*, 2008). The calibration of the force-displacement hysteresis for these devices is not discussed in this document and can be found elsewhere (Morgen *et al.*, 2007; Marriott *et al.*, 2008; Di Cesare *et al.*, 2013).

7.2.5 Evaluate timber force

To evaluate the timber strain, ε_t, the strain compatibility condition is applied, and the displacement of the rocking element is assumed to be the same as that of the analogic monolithic element. This leads to:

$$\varepsilon_t = c\left(\frac{3\theta_{imp}}{L_{cant}} + \phi_{dec}\right) \qquad (7\text{-}21)$$

Where ϕ_{dec} = decompression curvature

$$\phi_{dec} = \frac{M_{dec}}{E_{con} I} \qquad (7\text{-}22)$$

Where E_{con} = connection modulus (equal to $0.7E_t$ for post-tensioned timber walls (STIC, 2013)) This reduced modulus of elasticity accounts for the reduction in stiffness during material testing due to the timber end effects as observed in experimental tests by Newcombe (2007).

E_t = timber modulus of elasticity

I = section second moment of area

L_{cant} = cantilever length

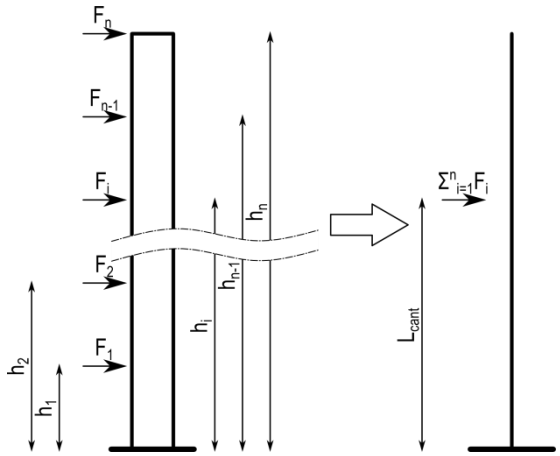

Figure 7-4. Cantilever length.

The effective cantilever length for wall systems depends on the force distribution acting on the structural element, and for wall systems that is the centroid of the force distribution:

$$L_{cant} = \frac{\sum_{i=1}^{n} F_i h_i}{\sum_{i=1}^{n} F_i} \qquad (7\text{-}23)$$

Where F_i = force acting at the i-th storey

h_i = i-th story height

n = total number of storeys

Generally, when designing for earthquake loading the force distribution can be assumed as triangular, and for such distribution the effective cantilever length is equal to 75% of the total building height.

The timber force is then evaluated assuming a triangular stress distribution:

$$C_t = 0.5 E_{con} \varepsilon_t b c \qquad (7\text{-}24)$$

Where b = section width

7.2.6 Check equilibrium and evaluate the connection moment

Once the force contributions are evaluated, the vertical force equilibrium must be assessed.

$$-C_t + \sum_{i=1}^{n_s} T_{s,i} - \sum_{i=1}^{n_s} C_{s,i} + \sum_{i=1}^{n_{pt}} T_{pt,i} + N \qquad (7\text{-}25)$$

If the equilibrium is not satisfied the neutral axis depth value must be iterated, otherwise the connection moment can be evaluated around the timber compression centroid.

$$M_{con} = \sum_{i=1}^{n_{pt}} T_{pt,i}\left(d_{pt,i} - \frac{c}{3}\right) + \sum_{i=1}^{n_s} T_{s,i}\left(d_{s,i} - \frac{c}{3}\right) - \sum_{i=1}^{n_s} C_{s,i}\left(d'_{s,i} - \frac{c}{3}\right) + N\left(\frac{h}{2} - \frac{c}{3}\right) \qquad (7\text{-}26)$$

Where h = section depth

7.3 Force-displacement response

Once the moment-rotation analysis of the connection has been evaluated, the force-displacement response of the post-tensioned rocking wall can be determined. This is generally done considering a known force distribution along the height of the wall element depending on the type of action considered (e.g. triangular force distribution for earthquake loading).

When a single wall system is considered, the displacement contributions depend on the cantilever stiffness of the wall panel (i.e. shear and bending deflections, see Section 7.3.2), whilst when boundary columns are coupled to the wall, the system's behaviour may have additional stiffness contributions (see Section 7.3.3).

7.3.1 Total base shear force

The total base shear force can be evaluated from the connection moment worked out as per moment-rotation procedure. The total shear for the given connection moment will depend on the force distribution. For seismic application a triangular force distribution is generally used to represent a first-mode shape response of the structure. The connection moment and base shear can be written as:

$$M_{con} = \sum_{i=1}^{n} F_i h_i \qquad (7\text{-}27)$$

$$V_{base} = \sum_{i=1}^{n} F_i \qquad (7\text{-}28)$$

Therefore, considering the definition of the cantilever length given in Equation (7-38) the base shear can be written as function of the base moment as:

$$V_{base} = \frac{M_{con}}{L_{cant}} \qquad (7\text{-}29)$$

7.3.2 Cantilever displacement contributions

The total displacement, δ_{tot}, at the top of the wall panel is the combination of the displacement due to gap opening (i.e. rigid body rotation), δ_{gap}, as well as the elastic bending, δ_b, and shear, δ_s, contributions due to the elastic deformation of the wall element.

$$\delta_{tot} = \delta_{gap} + \delta_b + \delta_s \qquad (7\text{-}30)$$

The rigid body rotation of the wall panel results in the displacement contribution, δ_{gap}, given in Equation (7-31).

$$\delta_{gap} = \theta_{imp} h_n \qquad (7\text{-}31)$$

Where θ_{imp} = the base connection rotation

h_n = the top storey height.

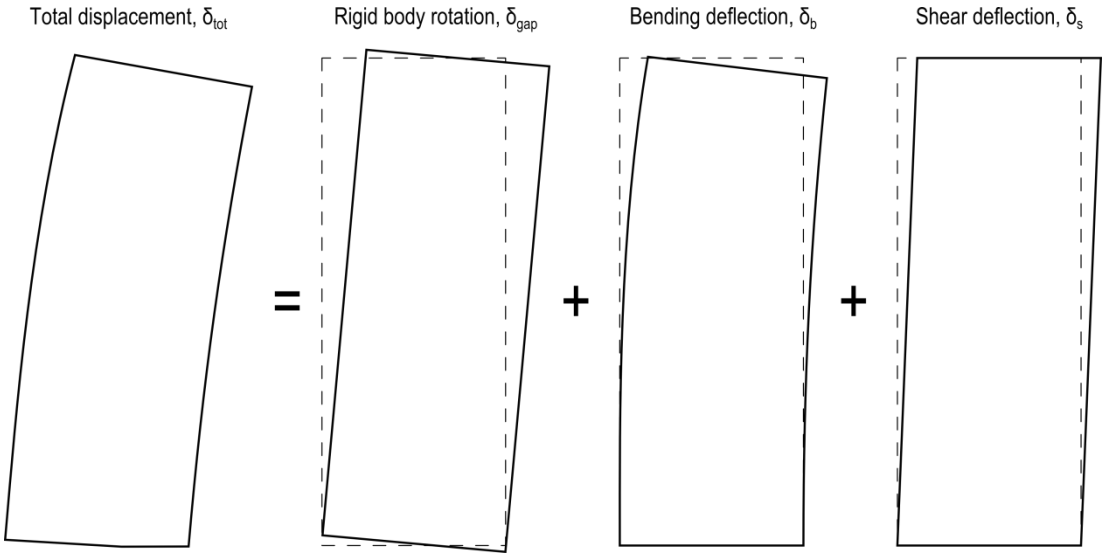

Figure 7-5. Displacement contributions in a post-tensioned rocking wall.

For a general type of loading the bending and shear contributions, δ_b and δ_s, respectively, can be evaluated as:

$$\delta_b = \iint \frac{M(z)}{E_t I} dz \qquad (7\text{-}32)$$

$$\delta_s = \iint \frac{V(z)}{G_t A_{ts}} dz \qquad (7\text{-}33)$$

Where z = height coordinate

M(z) = moment distribution along the cantilever

V(z) = shear distribution along the cantilever

E_t = elastic modulus

G_t = shear modulus

I = second moment of area

A_{ts} = shear area (i.e. 2A/3 for timber rectangular sections)

h_n = height at top level *n*

For seismic applications, the force distribution can be approximated of point loads applied at each storey using a triangular distribution; therefore, the equations above can be written for a general force distribution as:

$$\delta_b = \sum_{i=1}^{n} \frac{F_i h_i^3}{6E_t I}\left(3h_n - h_i\right) \qquad (7\text{-}34)$$

$$\delta_s = \frac{\sum_{i=1}^{n} V_i H_i}{G_t A_{ts}} \qquad (7\text{-}35)$$

Where F_i = applied force at the i-th story

h_i = height at i-th story

H_i = i-th inter-story height

V_i = i-th story shear

In general, an earthquake loading can be approximated as a triangular distribution. For a constant inter-story height, H, Equations (7-34) and (7-35) can be simplified as a function of the base moment, M_{con}, as follows:

$$\delta_b = \frac{M_{con} H^2}{6EI} \frac{n}{\sum_{i=1}^{n} i^2} \sum_{i=1}^{n} i^3 \left(3 - \frac{i}{n}\right) \qquad (7\text{-}36)$$

$$\delta_s = \frac{M_{con}}{G_t A_{ts}} \qquad (7\text{-}37)$$

The total elastic contribution to the drift, θ_w, can be now obtained:

$$\theta_w = \frac{\delta_b + \delta_s}{h_n} = M_{con}\left(\frac{H}{6E_t I}\frac{\sum_{i=1}^{n} i^3\left(3 - \frac{i}{n}\right)}{\sum_{i=i}^{N} i^2} + \frac{1}{G_t A_{ts} H}\frac{1}{n}\right) = M_{con}\left(\frac{H}{6E_t I}k_b + \frac{1}{G_t A_{ts} H}k_s\right) \qquad (7\text{-}38)$$

Where k_b, k_s = bending and shear drift correction factors given in Table 7-1.

Table 7-1. Drift correction factors.

No. of stories	1	2	3	4	5	6	7	8	9	10
k_b	2	26/7	43/8	7	61/7	83/8	12	41/3	46/3	17
k_s	1	0.5	1/3	0.25	0.2	1/6	1/7	0.125	1/9	0.1

7.3.3 Additional contributions of the boundary elements

The evaluation of the force-displacement response of the wall element is valid for single walls, but when other elements are used in the system, such as the boundary columns in the CWC system, an additional contribution may be considered.

The system deflection is governed by the stiffer wall element, and as soon as the gap opens the displacement profile is given by its elastic as well as its base rotation contributions. Although the elastic displacement contributions due to bending and shear of the wall panel can add significant flexibility to the system, in this context the displacement profile can be approximated as triangular and mostly influenced by the connection rotation.

Under this assumption, the boundary columns have to accommodate this triangular displacement profile. If the boundary element is hinged at the base connection (Figure 7-6a), the columns do not significantly contributed to the system's capacity, but, if a different end condition applies (Figure 7-6b), the contribution of the columns must be taken into account.

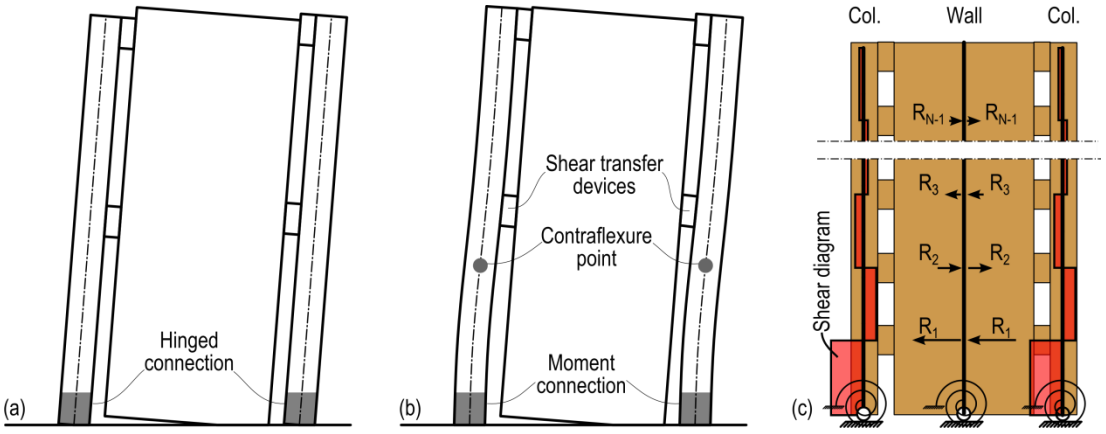

Figure 7-6. Effect of boundary columns with (a) hinge and (b) moment connection. (c) Shear transfer

The issue can be addressed using the approximated approach summarized below for a general case of a multi-storey wall.

The column and the wall can be modelled as a cantilever with a base flexibility k_θ. The structure can be solved by superposition method considering different contributions. For the boundary columns a rigid body rotation is first imposed and the effect of the base joint stiffness is taken into account; finally, a settlement δ_i at each level must be imposed to obtain the imposed displacement profile. The superposition of effects is shown in Figure 7-7 for the column element.

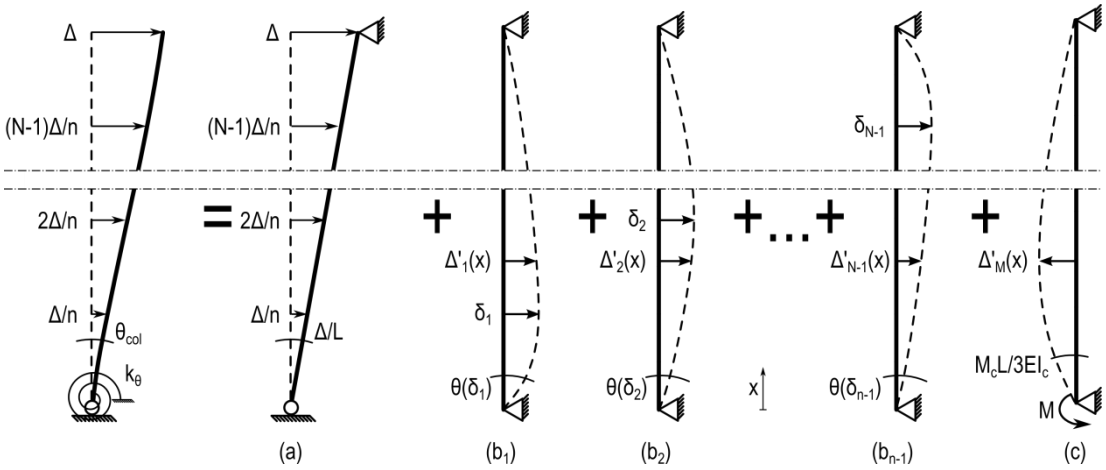

Figure 7-7. Evaluation of boundary column contribution.

Once the base rotation and storey displacement contributions of case (a) to (c) are determined as a function of the geometric and mechanical properties of the columns, the base rotation and storey displacement compatibility can be determined. For sake of brevity, the detailed calculations are not shown in this chapter and shown in Appendix B.

The compatibility equations combine together into a linear system of n-1 equations (being n the total number of storeys) and n unknowns. Following a matrix approach, the solutions of the linear system can be worked out as a function of the top displacement Δ.

The columns transfer some reaction forces to the wall element as shown in Figure 7-6c, and those are given for the general n-th level in Equation (7-39).

$$R_i = \frac{3EI_c}{H^3}\frac{n}{i^2\left(n-i\right)^2}\delta_i \qquad (7\text{-}39)$$

A similar approach can now be adopted for the post-tensioned wall with minor modifications; the cases (b) are now given by the reaction forces as shown in Figure 7-8.

The wall base rotation contributions of cases (b) due to a point load can be evaluated as:

$$\theta_{(bi)} = R_i \frac{H^2}{EI}\frac{\left(n-i\right)\left(n^2-i^2\right)}{6n} \qquad (7\text{-}40)$$

The base rotation compatibility equation on the wall is given in Equation

$$\theta_{con} = \frac{\Delta}{nH} + R_i \frac{H^2}{EI}\frac{\left(n-i\right)\left(n^2-i^2\right)}{6N} - \frac{M_{con}H}{EI}\frac{n}{3} \qquad (7\text{-}41)$$

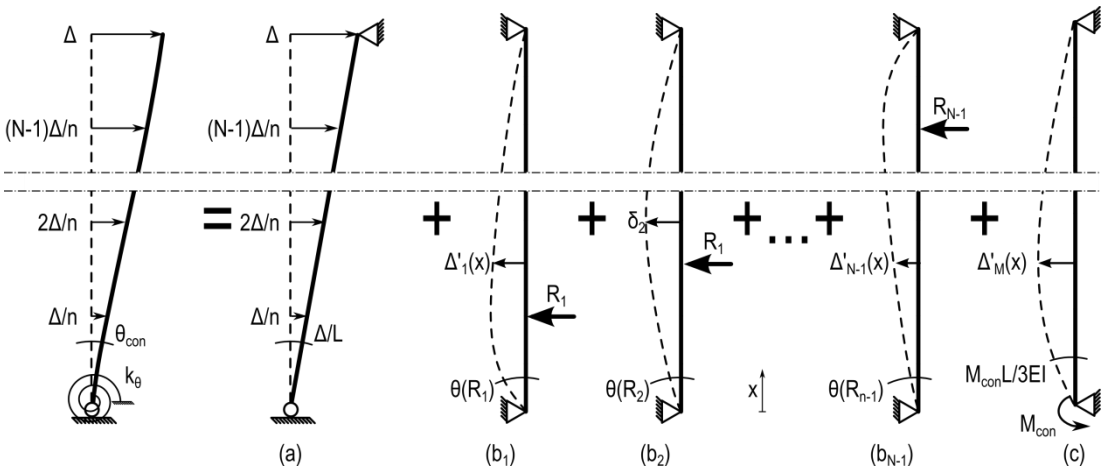

Figure 7-8. Column effects superposition.

Solving for Δ, the top displacement is finally given as:

$$\Delta = \frac{\theta_{imp} + \dfrac{nHM_{con}}{3EI}}{\dfrac{1}{nH} + \dfrac{1}{EI}\left(C_1(n)\dfrac{1}{k_\theta} + C_2(n)\dfrac{1}{EI_c}\right)^{-1}} \qquad (7\text{-}42)$$

Where C_1, C_2 = modification factors (function of n)

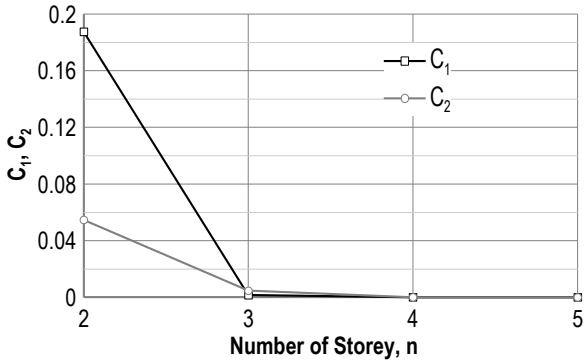

Figure 7-9. Evaluation of wall contribution.

Figure 7-9 shows the two factors C_1 and C_2 plotted versus the total number of storey, and highlights that the column contributions multipliers are significantly decreasing with the total number of storeys.

For practical purposes it is suggested that contributions from boundary columns with moment-resisting base-connections are accounted for when designing small buildings only (i.e. up to three storey), while for taller buildings the contributions can be neglected.

7.4 Experimental comparisons

The analytical model was compared to experimental results shown in Chapters 5 and 6 of the dissertation. The comparison charts below report different parameters significant to design such as the general force-displacement loop accounting for the total base shear and elastic drift contributions as shown in Section 7.3; moreover, the main outputs from the moment-rotation analysis are shown and compared to experimental data. Those include the connection moment, post-tensioning forces and neutral axis depth plotted against the connection rotation.

The moment-rotation analysis above was carried out considering the material properties listed in Table 7-2.

Table 7-2. Material properties.

Post-tensioning steel		
Yield stress	f_{yp}	835MPa
Modulus of Elasticity	E_p	170GPa
Mild steel		
Yield stress	f_{ys}	400MPa
Post-yield stiffness factor	R	0.0
Modulus of Elasticity	E_s	200GPa

Laminated Veneer Lumber		
Modulus of Elasticity	E_t	11000MPa
Connection Modulus	E_{con}	7700MPa
Shear Modulus	G_t	550MPa
Compression strength parallel to the grain	f_{ct}	45MPa
Cantilever length	L_{cant}	3m

7.4.1 Single wall

The single wall specimens were considered first, and Figure 7-10 shows the analytical model results comparison for the post-tensioned only specimens. As shown in the comparison charts, the analytical prediction was capable of accurately predicting the significant design parameters. The neutral axis depth, the post-tensioning forces and the moment analytical results fit the experimental data, but the force-displacement experimental data is, in some cases, over-predicted (see the results for specimen S400).

It is to be clarified that, as shown in Chapter 5 of this dissertation, the timber section after several tests did not remain perfectly plane, and some minor plastic deformations occurred. This effect is deemed responsible of that initial flexibility. This is confirmed by the force-displacement loops of Figure 7-10a,c showing the specimens tested in the first stages of the experimental campaign (i.e. with perfectly plane section).

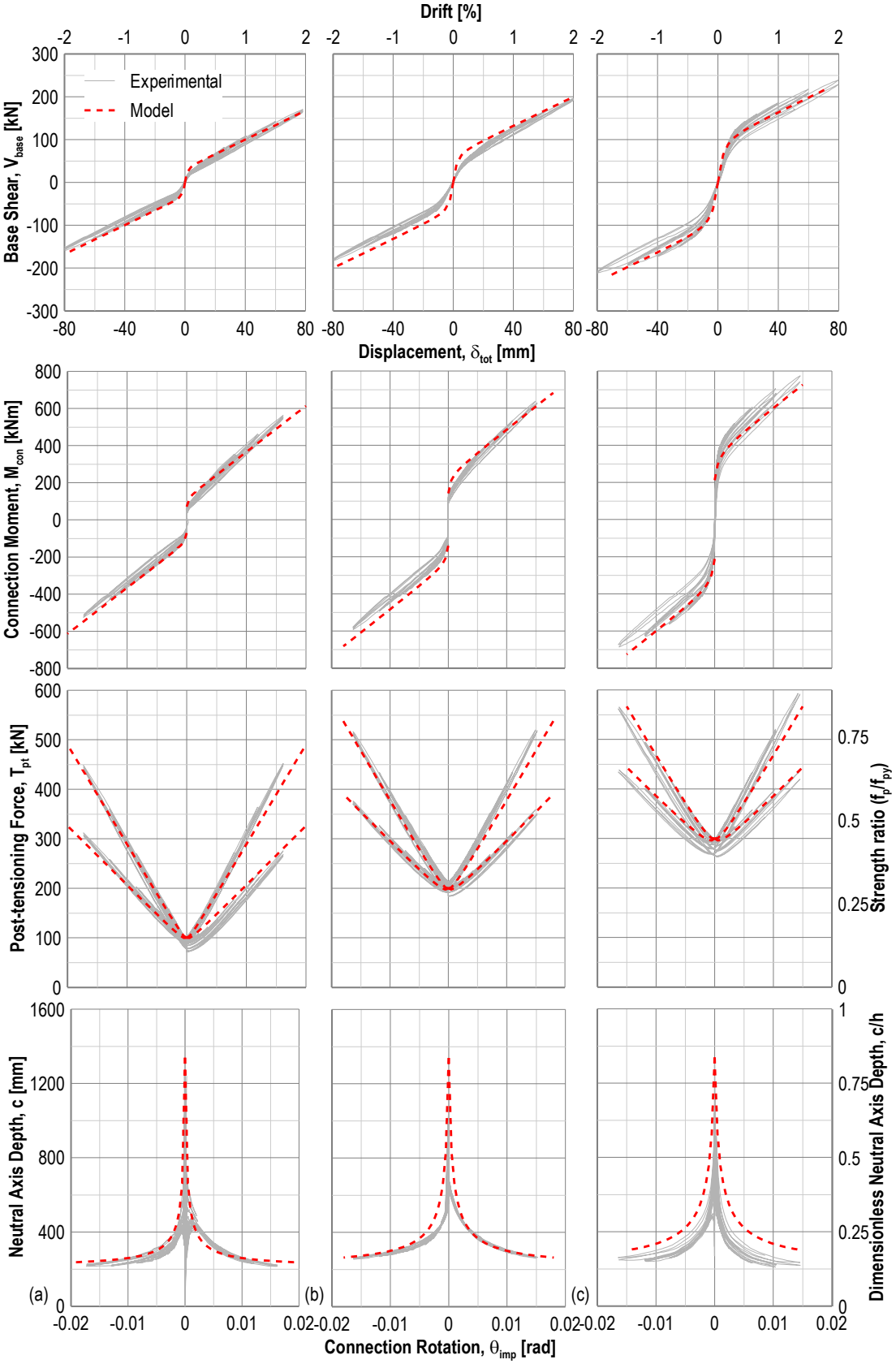

Figure 7-10. Experimental vs. analytical results. (a) S200, (b) S400, (c) S600.

The analytical prediction of the single wall hybrid specimens took into consideration the different dissipater configurations used in the experimental program. As shown in Chapter 5, the predicted stiffness of the dissipaters' connecting plates was found to be 140kN/mm, and that showed good fit with the experimental data (see Chapter 5). The equivalent unbonded length for the specimens with external dissipater must be worked out as per Equation (7-7). The equivalent unbonded lengths for the different specimens are:

- S400-8: $\overline{l'_{ub}} = 1.2 \cdot 250mm + 200GPa \cdot 308mm^2 / 140kN/mm = 740mm$
- S400-4 and S600-4: $\overline{l'_{ub}} = 1.2 \cdot 250mm + 200GPa \cdot 154mm^2 / 140kN/mm = 520mm$

The equations above are for the external dissipaters used, with a fuse length of 250mm, k_a factor of 1.2 (see Chapter 3) and fuse diameter of 14mm.

When internal bars were used the contribution due to strain penetration in timber shall be considered alone, and the concrete contribution is neglected since the bars were threaded to the base plate and not cast into the foundation; therefore, the equivalent unbonded length for the internal dissipater is:

$$\overline{l'_{ub}} = 300mm + 0.031 \cdot 400MPa \cdot 14mm = 474mm$$

The prediction of the hybrid single walls is shown in Figure 7-11 and similar observations as the post-tensioned only solutions can be made.

In particular, the experimental response of the specimens was well predicted, and the implementation of the different flexibility contributions in the dissipaters allows an accurate evaluation of the elastic stiffness of the wall element.

It is worth noticing, as also mentioned above, that although the moment-rotation response of the specimen accurately fit the experimental recorded data, the force-displacement analytical curve over-estimates the experimental response.

It is thought that this under-estimation of the horizontal displacement is due to the minor plastic deformation of the wall base as well as some slip occurring in the wall's longitudinal direction. These effects were not simulated in the analytical model, yet the discrepancy in the prediction of the observed experimental results is minor and therefore deemed negligible.

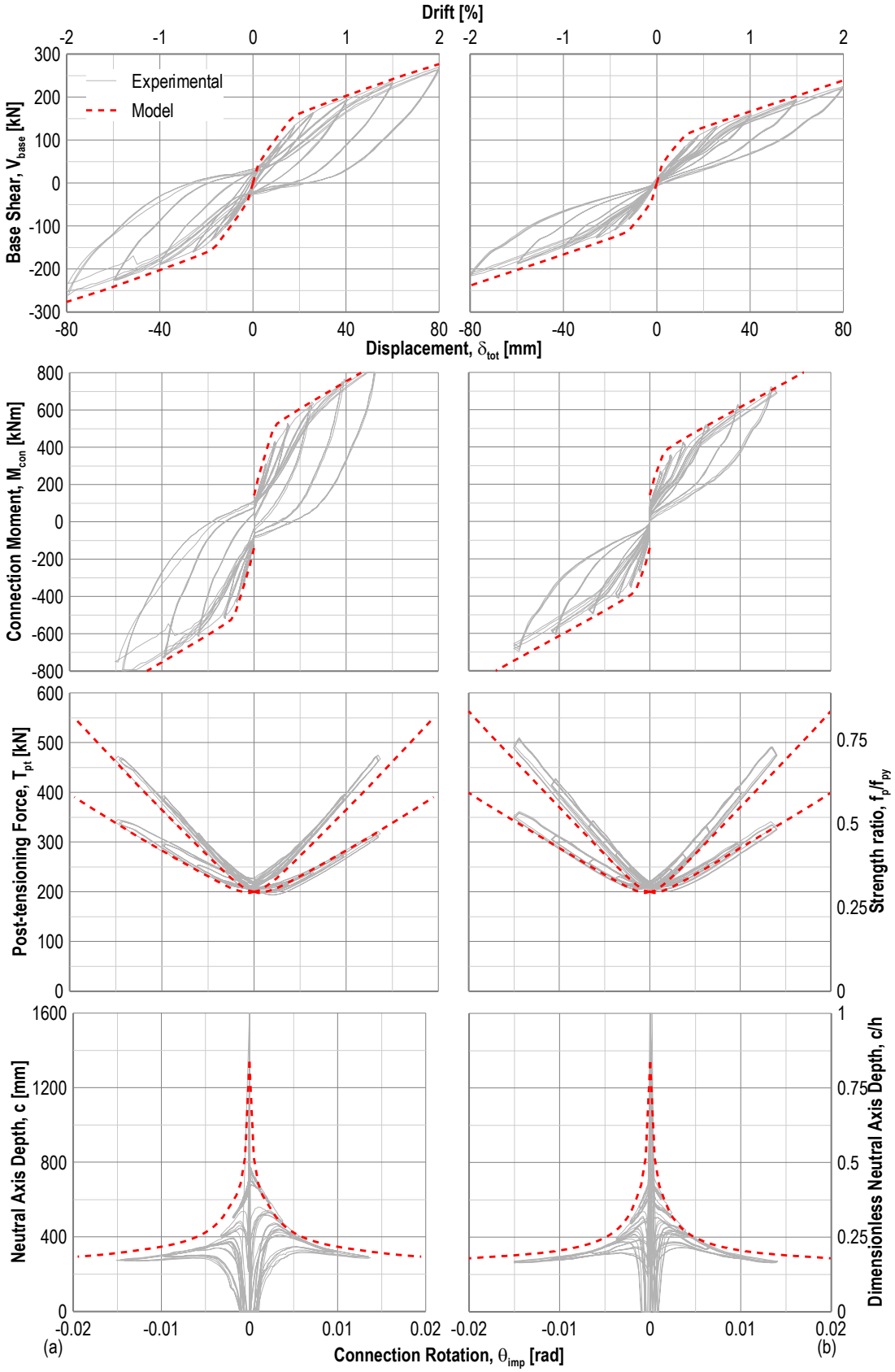

Figure 7-11. Experimental vs. analytical results. (a) S400-8, (b) S400-4.

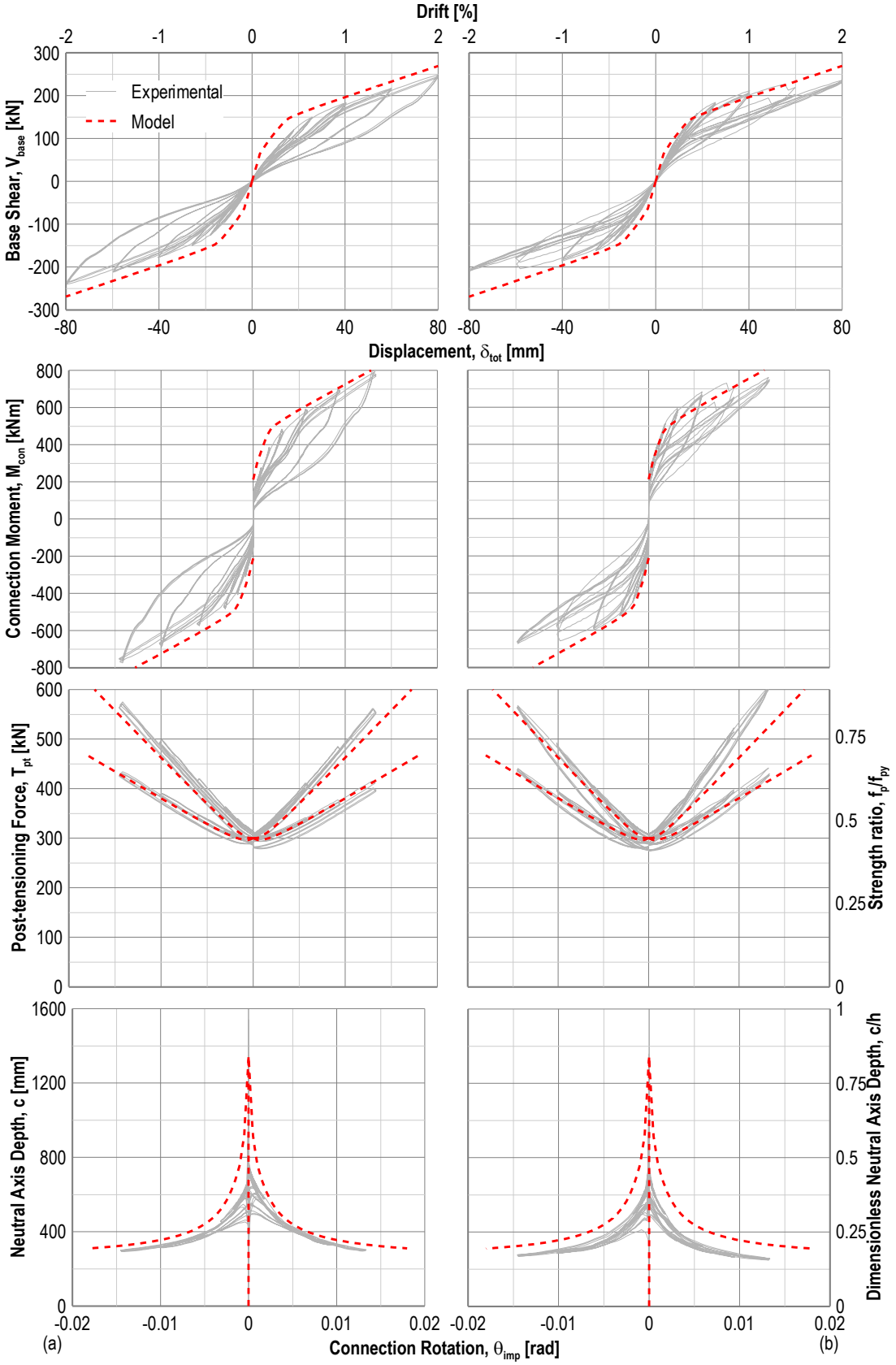

Figure 7-12. Experimental vs. analytical results. (a) S600-4; (b) S600-4i

7.4.2 Column-wall-column system

In the column-wall-column system the dissipation is provided by U-shaped flexural plates which were coupling the boundary elements to the wall panel and yielding by rolling bending developed by the relative displacement between the connected elements.

As shown in Chapter 6, the UFPs used in the experimental campaign were fabricated out of Grade350 mild steel plates. The latter were 130mm wide, 12mm thick and the bend had a radius of 40mm. The hysteresis parameters for the dissipater are summarized as follows:

$$F_u = \frac{350MPa \cdot 0.13m \cdot 0.012^2 mm^2}{2 \cdot 0.092mm} = 35kN$$

$$k_0 = \frac{16 \cdot 200GPa \cdot 0.13m}{27\pi}\left(\frac{0.012m}{0.092m}\right)^3 = 10883kN/m$$

$$R = 7.1\ln\left(\frac{0.012m}{0.092m}\right) + 29.5 = 15.0$$

An additional dissipative contribution was given by the shear transfer blocks. Although those were designed to minimize the frictional contributions to the system, some force was developed at the sliding surface; nevertheless, this friction contribution was neglected when comparing analytical and experimental results in this chapter.

As shown in paragraph 7.3.3, when the system includes boundary column with moment-resisting base connections some additional contributions should be considered. The column connection used in the test setup was a 7×5 10mm diameter coach screw group (for detailed technical drawing of the connection see Appendix D). The stiffness of the connection was evaluated according to Eurocode 5 (European Committee for Standardization, 2004) as follows:

$$k_\theta = K_{ser}\sum r_i^2 \qquad (7\text{-}43)$$

Where k_θ = the connection rotational stiffness

r_i = the fastener's distance from the centroid of the connection group

K_{ser} = total slip modulus given as $K_{ser} = 2\rho^{1.5}D/23$

n = total number of dowels

ρ = timber mean density

d = diameter of the dowel

The total stiffness of the connection resulting from equation (7-43) was 10477kNm/rad.

Figure 7-13 shows the analytical versus experimental results comparisons for the pure post-tensioned rocking CWC specimens.

The charts show that the analytical prediction of the neutral axis depth and post-tensioning force is fitting the experimental results accurately, also confirming that the inclusion of the frictional contribution is not significantly affecting this parameters.

Even though the consideration of the friction forces does not influence the detailed parameters, the moment response was under-predicted as expected.

The comparison of experimental results to the analytical model of the dissipative post-tensioned rocking CWC specimens is shown in Figure 7-14.

The neutral axis and post-tensioning forces were accurately captured using the moment-rotation iterative procedure while neglecting the axial contributions coming from the shear transfer devices (i.e. frictional contribution). The moment rotation loops show that the procedure can closely predict the observed experimental behaviour for low connection rotation values; as expected, for bigger gap opening values, the system display an increased force given by friction developed in the shear transfer blocks.

The force-displacement behaviour of both the dissipative and the pure post-tensioned rocking specimens also shows that the simplified approach proposed for evaluating the general force-displacement behaviour of the system shows good agreement with experimental results. Similarly to the moment-rotation curves, a bigger stiffness was observed in the experimental tests, yet the procedure can predict the behaviour satisfactorily.

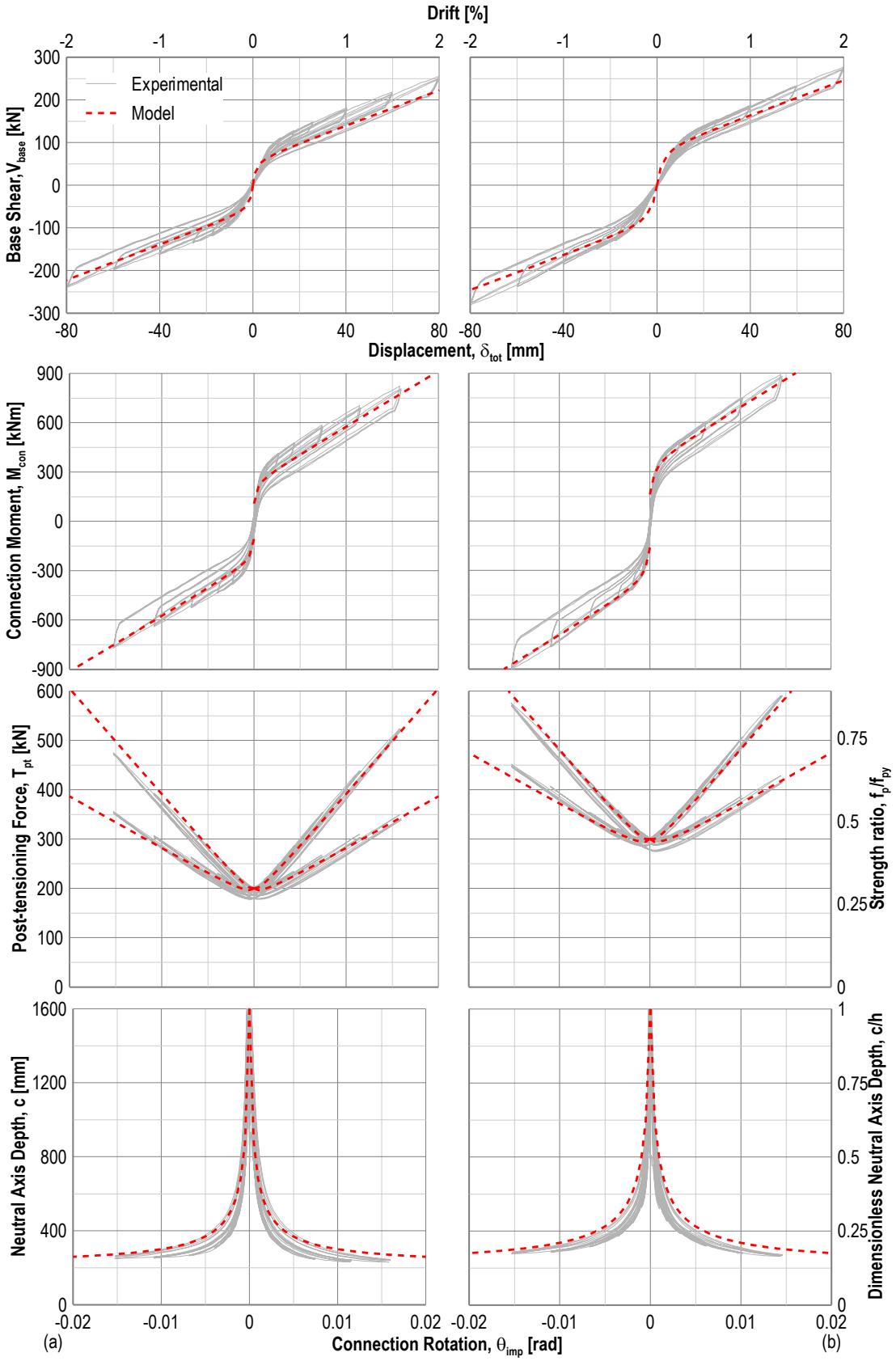

Figure 7-13. Experimental vs. analytical results. (a) CWC400; (b)CWC600.

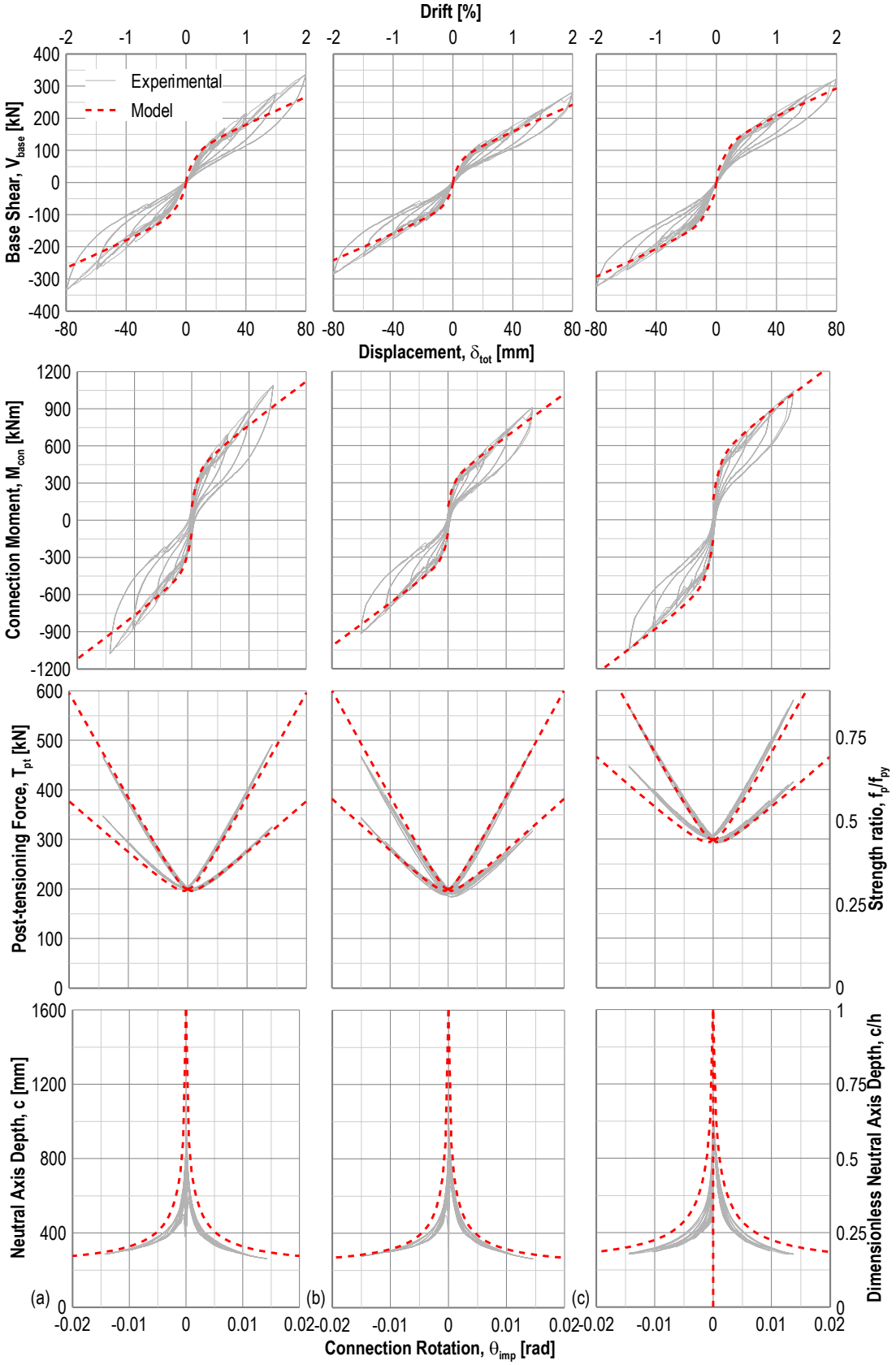

Figure 7-14. Experimental vs. analytical results. (a) CWC400-8; (b)CWC400-4; (c) CWC600-4.

7.5 Conclusions

The chapter presented the analytical modelling of post-tensioned timber wall systems. The current iterative moment-rotation procedure developed first for concrete elements (Pampanin *et al.*, 2001; Palermo *et al.*, 2005) and extended to timber structural members (Newcombe *et al.*, 2008) was presented. The procedure was refined considering experimental and numerical findings on internal (Chapter 4) and external (Chapter 3) dissipaters. The consideration of the different dissipaters' flexibility contributions proved effective in predicting the observed experimental behaviour.

When evaluating the general force-displacement push-over curve of the systems the different elastic contributions to the drift shall be accounted for. Those include the rigid body rotation coming from the gap opening, as well as drift contributions coming from the elastic flexural and shear deformations of the wall panel.

Simplified general formulas were proposed considering a triangular distribution of forces typical of an earthquake loading and a uniform geometry in elevation, and those were compared to experimental results from Chapters 6 and 7, which validated the proposed equations.

The experimental results shown in Chapter 7 showed that the boundary elements can bring some additional stiffness to the system when a moment-resisting connection is adopted. The chapter presented a simplified approach accounting for these contributions, and the analytical simplified approach also showed that the contribution of the boundary columns may be neglected for buildings taller than 3 storeys.

The proposed analytical model for CWC systems, in conjunction with the refined moment-rotation analysis procedure, proved to be capable of predicting the experimental response of CWC specimens. The model confirmed that the frictional contributions of the shear transfer elements can be neglected and does not affect significantly the response evaluation.

7.6 References

Baird, A., Smith, T., Palermo, A., Pampanin, S. 2014. Experimental and Numerical Study of U-Shaped Flexural Plate (UFP) Dissipators. *New Zealand Society for Earthquake Engineering Annual Conference*, Auckland, New Zealand.

Di Cesare, A., Ponzo, F.C., Nigro, D., Simonetti, M., Smith, T., Pampanin, S. 2013. Experimental testing and numerical analysis of steel angles as hysteretic energy

dissipating devices. *Il XV Convegno di Ingegneria Sismica, Associazione Nazionale di Ingegneria Sismica*, Padua, Italy.

European Committee for Standardization. 2004. *Eurocode 5 - Design of timber structures - Part 1-1: General – Common rules and rules for buildings*. *EN 1995-1-1*. European Committee for Standardization. Brussels, Belgium, European Committee for Standardization.

Kelly, J.M., Skinner, R.I., Heine, A.J. 1974. Mechanism of Energy Absorption in Special Devices for Use in Earthquake Resistant Structures. *Bulletin of the New Zealand Society of Earthquake Engineering* 5.

Marriott, D.J., Pampanin, S., Bull, D., Palermo, A. 2008. Dynamic Testing of Precast, Post-Tensioned Rocking Wall Systems with Alternative Dissipating Solutions. *Bulletin of the New Zeland Society for Eartquake Engineering* 41(2): 90-103.

Morgen, B.G., Kurama, Y.C. 2007. Seismic Design of Friction-Damped Precast Concrete Frame Structures. *Journal of Structural Engineering* 133(11): 1501-1511.

Newcombe, M. 2007. Seismic design of multistorey post-tensioned timber buildings. *Master of Engineering. Master thesis*, Università degli Studi di Pavia, Pavia, Italy.

Newcombe, M.P., Pampanin, S., Buchanan, A.H., Palermo, A. 2008. Section Analysis and Cyclic Behavior of Post-Tensioned Jointed Ductile Connections for Multi-Story Timber Buildings. *Journal of Earthquake Engineering* 12(S1): 83-110.

Palermo, A., Pampanin, S. 2008. Analysis and simplified design of precast jointed ductile connections. *World Conference on Earthquake Engineering*, Beijing, China.

Palermo, A., Pampanin, S., Buchanan, A.H., Newcombe, M.P. 2005. Seismic design of multi-storey buildings using laminated veneer lumber (LVL). *New Zealand Society of Earthquake Engineering, Annual Conference*, Wairakei, New Zealand, University of Canterbury. Civil Engineering.

Pampanin, S., Priestley, M.J.N., Sritharan, S. 2001. Analytical modelling of the seicmic behaviour of precast concrete frames designed with ductile connections. *Journal of Earthquake Engineering* 5(3): 329-367.

Skinner, R.I., Kelly, J.M., Heine, A.J. 1974. Hysteretic dampers for earthquake-resistant structures. *Earthquake Engineering & Structural Dynamics* 3(3): 287-296.

Sritharan, S. 1998. *Analysis of concrete bridge joints subjected to seismic actions*, University of California, San Diego.

Structural Timber Innovation Company. 2013. *Design Guide Australia and New Zealand-Post-Tensioned Timber Buildings*. Structural Timber Innovation Company. Christchurch, New Zealand.

8 Non-linear numerical modelling of post-tensioned wall systems

8.1 Introduction

The objective of this chapter is to validate and refine current numerical modelling approaches for the prediction of the seismic response of post-tensioned wall systems as well as simulating the full range of behavioural aspects.

First a more simplified modelling approach, the rotational spring model, is presented and compared to the experimental results. The model consists of a series of rotational springs which concentrate the system's behaviour at the base of the wall element. While this approach is computationally efficient and capable of capturing the force-displacement response of post-tensioned wall system, detailed parameters such as the neutral axis depth and reinforcement elongation are not simulated.

When a more detailed modelling approach is required, the system can be simulated using a multi-spring model. It consists of a more complex model where the gap opening is simulated using a compression-only multi-spring element. Since the rocking mechanism is fully simulated, the post-tensioning reinforcement and the dissipation devices can be modelled using either truss or spring elements. The model is capable of capturing detailed parameters such as the neutral axis depth and the forces in the post-tensioning tendons as well as in the dissipation devices.

The chapter shows the calibration of those models, and focuses in particular on the refinement of the multi-spring model which is developed for use in OpenSEES. The multi-spring model is then used in the final part of the chapter to calibrate a modification factor for the area-based hysteretic viscous damping to be used in a Displacement-Based Design approach.

8.2 Modelling approaches and tools

When modelling post-tensioned rocking elements two main approaches can be used. The most convenient in terms of calibration as well as computational efficiency is to concentrate the system behaviour at the base connection via two rotational springs in parallel. The post-tensioning (re-centering) moment contribution is modelled using a multi-linear elastic hysteresis, while the dissipative contribution can be modelled using a bi-linear moment-rotation relationship. While this modelling approach represents a simplified and very convenient modelling technique, that cannot provide detailed information of the system since the system is not capable of simulating the gap opening (and consequent uplifting), and it is not modelling the actual elongation of the post-tensioning and mild steel reinforcements.

When a more detailed analysis is needed, a different approach can be used. The detailed modelling approach makes use of a base contact element (multi-spring element) simulating the gap opening and neutral axis variation. This allows to physically simulating the system behaviour using truss (or spring) elements to model the post-tensioning and mild steel dissipaters.

The multi-spring model was first developed for precast concrete rocking section by Spieth et al. (2004a). The element was implemented in the modelling software RUAUMOKO (Carr, 2004) which has been widely used in past research on post-tensioned rocking elements (Palermo *et al.*, 2005; Marriott, 2009; Newcombe, 2012).

In more recent years, an open source simulation software, OpenSees, was developed at the University of California, Berkeley (McKenna, 2011), the analyses in this dissertation were carried out using this software. Although OpenSees does not have an implemented multi-spring element, that can be developed within the code.

The chapter presents an the overview and calibration of post-tensioning rocking walls models, using either the rotational spring approach of a more detailed multi-spring modelling approach.

8.3 Rotational spring model

When modelling post-tensioned walls a simplified modelling approach consists of concentrating the system behaviour using a couple of rotational springs calibrated on the moment-rotation analysis presented in Chapter 7.

The re-centering and dissipative contributions are provided by the post-tensioning and mild steel reinforcements respectively. Those two contributions can be modelled using a multi-

linear elastic hysteresis for the re-centering rotational spring and an elastic-plastic relationship for the dissipative contributions.

A similar approach can be adopted when dealing with coupled systems, be it coupled walls or column-wall-columns systems. When coupling boundary columns to the post-tensioned wall, two additional elastic elements are placed at each side of the wall at half-section depth distance from the centreline. The storey nodal points are then connected to the corresponding nodes of the wall elastic elements through rigid trusses, thus coupling the horizontal displacement of those nodes (i.e. no relative horizontal displacement is allowed). To account for the column base connection flexibility an additional rotational spring can be used and calibrated considering the connection type used.

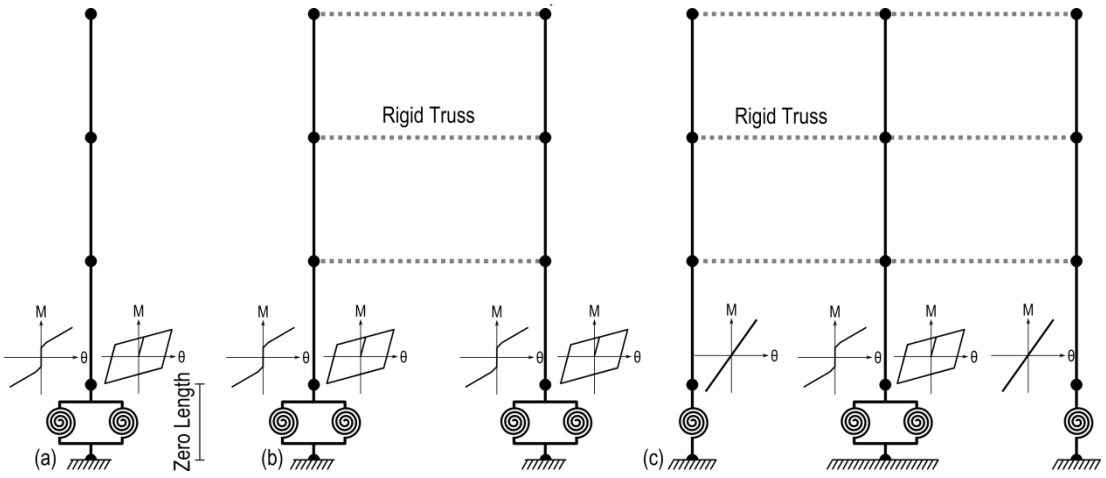

Figure 8-1. Rotational spring models overview.(a) Single wall; (b) coupled walls; (c) column-wall-column system.

8.3.1 Model Calibration

When using rotational springs, the calibration simply consists of matching the analytical moment-rotation results (see Chapter 7). The combination of hysteresis required is a multi-linear elastic relationship for the re-centering ratio, and an elastic-plastic rule for the dissipative contribution.

The multi-linear elastic behaviour of a post-tensioned only solution is usually characterized by a curved transition from the decompression moment, and a linear trend after the moment M_0 has been reached (see Figure 8-2a). For practical purposes the curved transition can be approximated using a secant branch from the decompression moment, which is identified by the coordinates M_0 and θ_0.

The decompression moment, M_{dec}, is defined as:

$$M_{dec} = \frac{Z_t}{A_t}\left(T_{pt0} + N\right) \qquad (8\text{-}1)$$

Where Z_t = section moment of area

A_t = cross-sectional area

T_{pt0} = total initial post-tensioning force

N = axial force form gravity loads (if present)

Although the decompression point should be defined at zero connection rotation, to ensure the numerical stability of the model a non-zero rotation must be defined. In general, a value equal to 1/10 of the rotation θ_0 gives stable and satisfactory results.

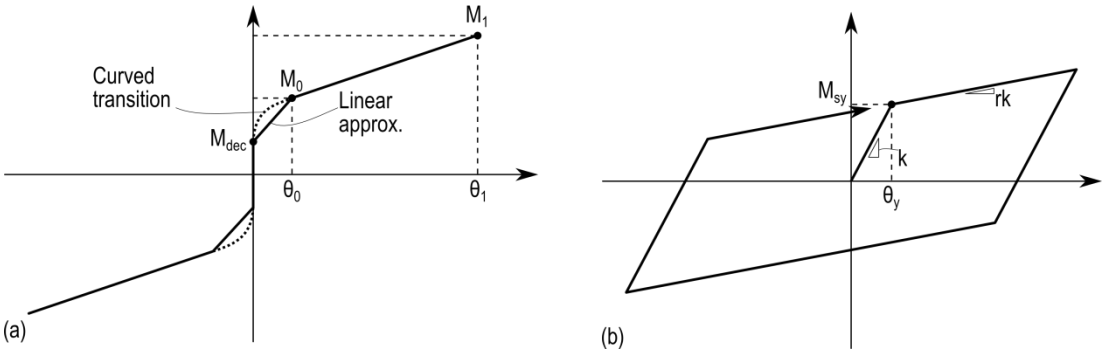

Figure 8-2. Rotational spring model calibration. (a) multi-linear elastic; (b) elastic-plastic.

The dissipative contribution (see Figure 8-2b) is defined by the yielding coordinates (i.e. rotation and moment) resulting from the analytical moment-rotation. A post-yield stiffness ratio must also be provided.

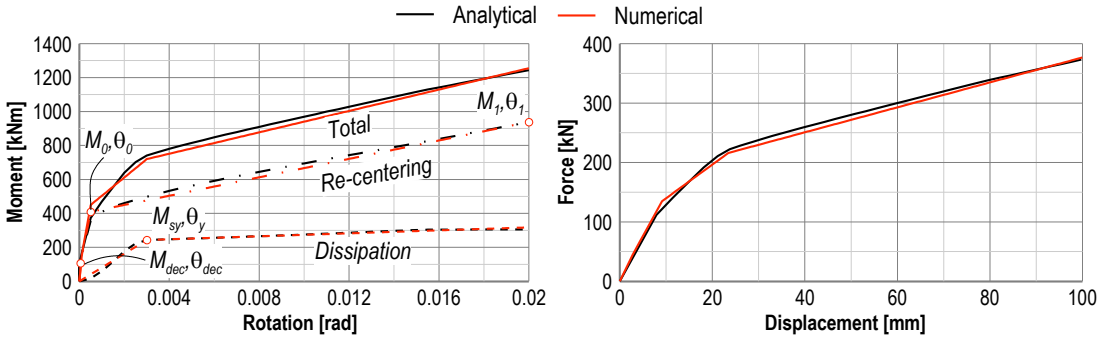

Figure 8-3. S400-8 rotational spring model calibration. (a) moment-rotation; (b) force-displacement.

When defining the wall elements, elastic elements are usually input by defining the elastic material and assigning the section cross-sectional area, A_t, shear area, A_{st}, and second moment of area, I_t.

The results from the analytical moment-rotation analysis of the specimen S400-8 are shown in Figure 8-3 and compared with the numerical model; the calibration parameters are also highlighted in the moment rotation chart for the different moment contributions.

When a coupled system is used, the base connection shall be calibrated in accordance with the moment-rotation analysis of each wall as shown by Iqbal (2011).

In Column-Wall-Column systems the coupled elements are boundary columns which can have several end conditions (i.e. moment connection or pin). If some connection stiffness is provided that shall be taken into account as also shown in Chapter 6 of this dissertation, and this can be done by using an elastic rotational spring at the base of the column element calibrated accounting for the particular fastening method used.

8.3.2 Experimental results comparison and discussion

The results of the rotational spring numerical model were compared with experimental results presented in Chapters 5 and 6. Both single wall and Column-Wall-Column systems were accounted for and the rotational spring models were calibrated using moment-rotation analysis results evaluated as shown in Chapter 7 of the dissertation. For the Column-Wall-Column system, similarly to the analytical models, the additional contribution due to the friction elements was neglected.

Table 8-1 reports the summary of the calibrated parameters of the re-centering and dissipative springs (for nomenclature refer to Figure 8-2).

The wall and column elements were defined as non-linear beam-column elements. For the definition of such element type the elastic section properties were defined as follows.

- Elastic modulus, E_t = 11GPa
- Shear Modulus, G = 550MPa
- Wall properties
    - cross-sectional areas, A = 0.30m^2
    - shear area, A_{ts} = 0.20m^2
    - second moment of area, I = 0.0613m^3
- Column properties
    - cross-sectional areas, A = 0.0675m^2
    - shear area, A_{ts} = 0.045m^2
    - second moment of area, I = 0.000506m^3

Table 8-1. Summary of rotational spring model result calibration parameters

	Re-centering						*Dissipative*		
Test ID	**θ_{dec}**	**M_{dec}**	**θ_0**	**M_0**	**θ_1**	**M_1**	**θ_v**	**M_{sv}**	**r**
S200	0.00005	53	0.0005	117	0.02	613	n/a	n/a	n/a
S400	0.00015	107	0.0015	255	0.02	732	n/a	n/a	n/a
S600	0.00020	160	0.0020	374	0.02	849	n/a	n/a	n/a
S400-8	0.00010	107	0.0010	230	0.02	696	0.0025	253	0.036
S400-4	0.00005	107	0.0005	204	0.02	702	0.0015	110	0.047
S600-4	0.00005	160	0.0005	282	0.02	822	0.0020	119	0.046
CWC400	0.00005	107	0.0005	204	0.02	752	n/a	n/a	n/a
CWC600	0.00005	160	0.0005	280	0.02	869	n/a	n/a	n/a
CWC400-8	0.00005	107	0.0005	200	0.02	733	0.0024	186	0.0306
CWC400-4	0.00005	107	0.0005	202	0.02	742	0.0024	95	0.0273
CWC600-4	0.00005	160	0.0005	276	0.02	851	0.0026	176	0.0461

The force-displacement loops comparison chart of the single wall configurations are shown in Figure 8-4.

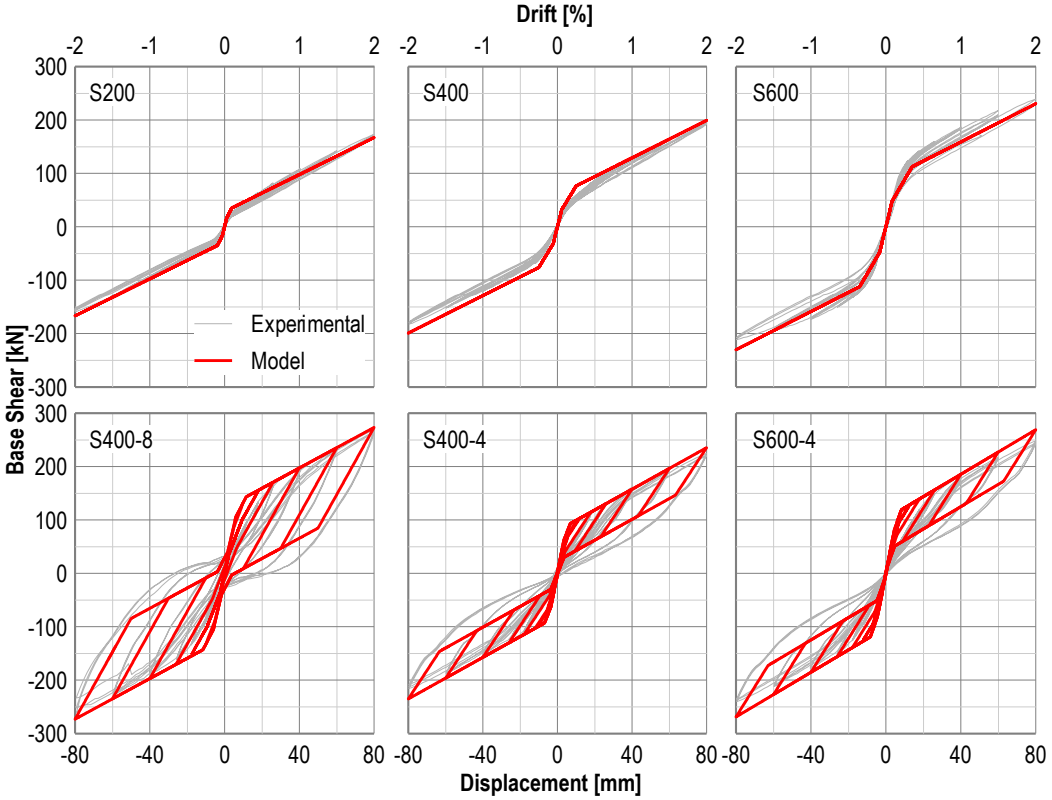

Figure 8-4. Experimental vs. rotational spring model results, single wall system.

As shown in the charts above, the rotational spring post-tensioned only specimens S200, S400 and S600 shows a good fit with experimental results. Similarly to the analytical model, the model slightly underestimates the force-displacement loop of the specimen S600; moreover, the degrading behaviour cannot be captured by this simplified modelling approach.

The dissipative reinforcement options (S400-8 and S600-4) are also shown in Figure 8-4. The models can predict the cyclic behaviour, including the effect of dissipative reinforcement, with relative accuracy. In fact, while the back-bone curve closely fits the experimental results, the model does not account for isotropic strain hardening effects in the mild steel dissipaters. That brings to an underestimation of the energy dissipated by the connection.

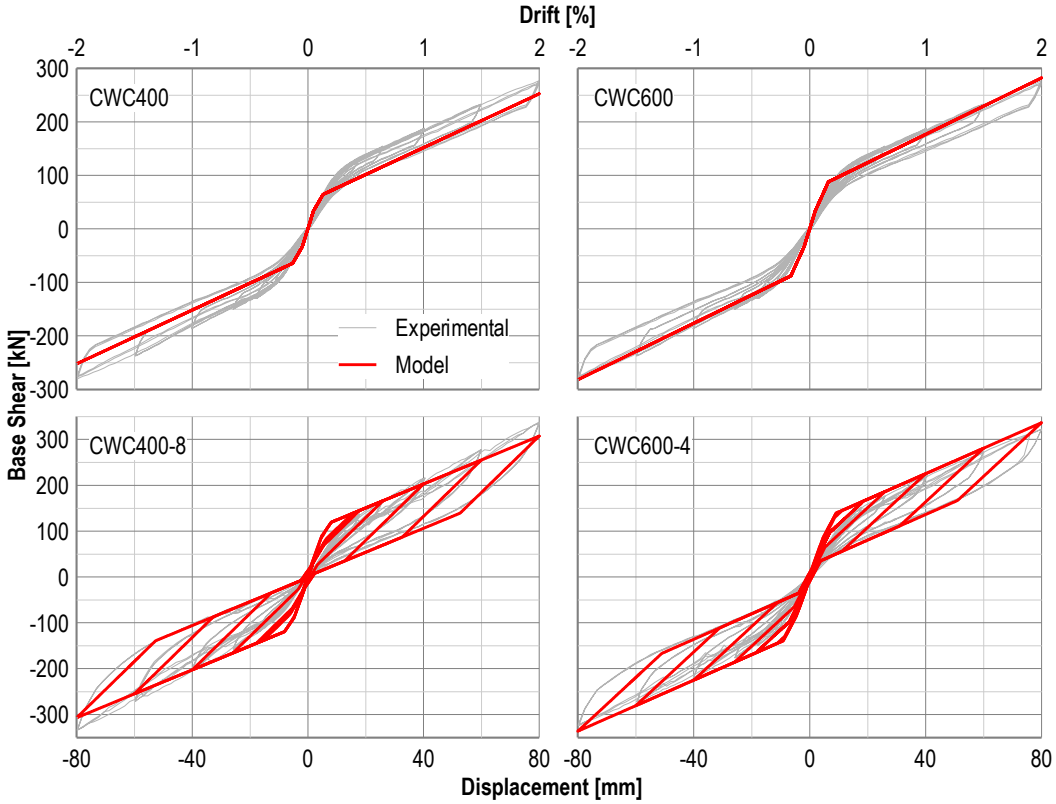

Figure 8-5. Experimental vs. rotational spring model results, CWC system.

The numerical versus experimental comparison of the specimen S600-4 shows a slight over-estimation (approximately 10%) force recorded in the experimental testing. It is thought that this effect is due to the minor damage of the wall section occurred after several tests at MCE demand drift levels.

In the Column-Wall-Column model the two columns were connected to the post-tensioned wall, and the friction contributions were neglected (as also assumed in Chapter 5). As shown in Figure 8-5a this last assumption brings to a minor underestimation of the total shear force developed in the system and it is thus considered satisfactory.

Figure 8-5b,c shows that the model can predict accurately the cyclic behaviour of the hybrid specimens. Since no isotropic strain hardening was observed in the UFP devices (as shown

by component testing in Chapter 6), the model can predict the unloading behaviour of the connection more accurately if compared to the single wall models above.

8.4 Multi-spring model

The main advantage of the multi-spring model is to simulate the base connection via a contact element at the base nodes to uplift and also rotate. Since the gap opening is modelled, the reinforcement is modelled using spring or truss elements.

To account for shear deformations, the wall elastic elements were modelled using non-linear beam-column elements. The non-linear element was modelled as an elastic section and the shear behaviour was incorporated using a section aggregator (McKenna, 2011).

The base multi-spring element consists of several parallel springs connected to the master nodes via rigid link elements. Compression-only material was used to allow the gap opening.

Finally, the post-tensioning reinforcement was modelled through truss elements which were connected at the wall element using rigid links at the anchorage height, allowing for the unbonded length of the post-tensioning tendons.

When a single wall option was considered, the dissipation was concentrated at the wall-foundation interface. The dissipative reinforcement can be modelled using either zero-length spring elements or trusses. For the truss elements the node distance from the base must account for the unbonded length of the dissipater. When using zero-length spring elements, the connection nodes must be at zero distance and the axial stiffness is given as input.

When modelling coupled systems the wall was either coupled to another wall or to boundary columns. The model used a multi-spring unit and post-tensioning springs/trusses, as per a single wall option, and the dissipaters are distributed along the height of the element. This was done by creating a set of nodes at half-section depth distance from the multi-spring centreline, connected via rigid links to the elastic wall elements. The nodes were then connected to the dissipaters' springs.

Figure 8-6 shows the sketch of the multi-spring model for different post-tensioned wall systems.

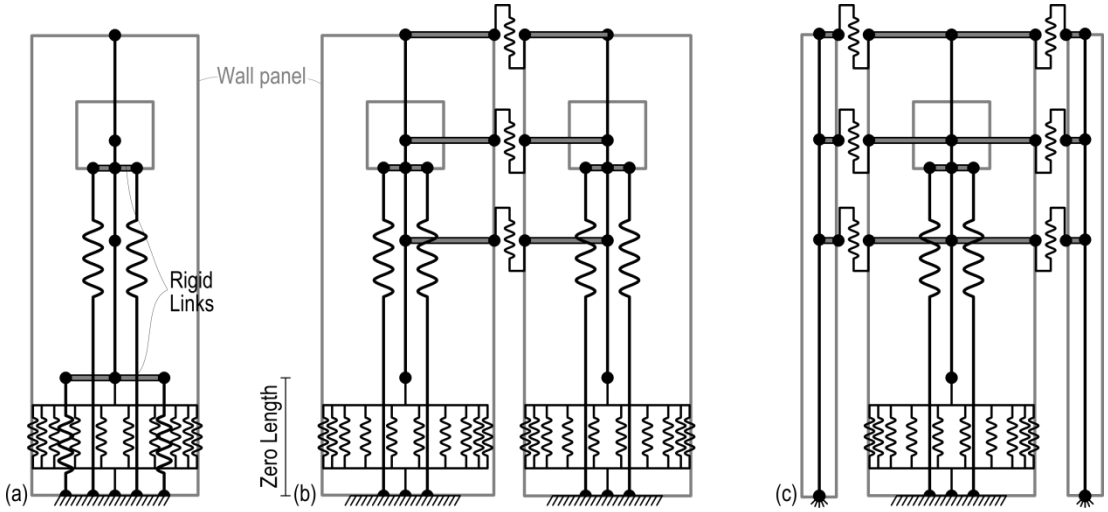

Figure 8-6. Multi-spring models overview.(a) Single wall; (b) coupled walls; (c) column-wall-column system.

8.4.1 Development of a degrading gap multi-spring element

A multi-spring element was developed by Spieth et al. (2004a) and implemented in the analysis software RUAUMOKO (Carr, 2004) with the main objective of the developing an element which simulates the contact area between members allowing gap opening (Spieth *et al.*, 2004b).

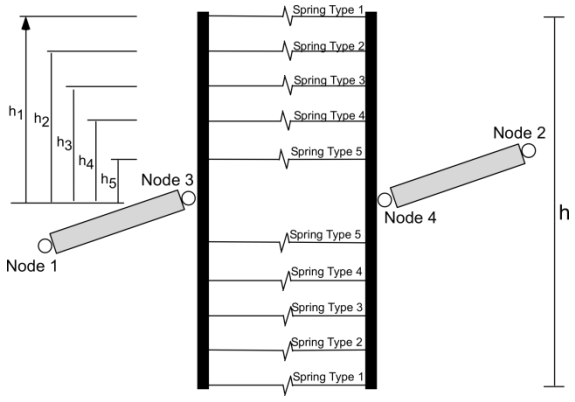

Figure 8-7. Setting of multi-spring contact element with 10 contact springs (Spieth et al., 2004b).

Two different integration schemes were used in the development of the element. Firstly, a Gauss integration distribution was used. This is a common integration scheme in Finite Element Modelling, but has the main disadvantage that the extreme spring are not placed at the edge. Alternatively, a Lobatto integration was used and that allowed to position the first and last springs at the edge of the element.

As anticipated, the numerical analyses were carried out throughout this dissertation using the analysis software OpenSEES (McKenna, 2011) where the multi-spring element was not

available. A multi-spring model based on the research by Spieth et al. (2004a) was then developed for use in OpenSees. The model was composed of multiple longitudinal zero-length springs in parallel, connected to the master nodes using rigid elements (see Figure 8-8).

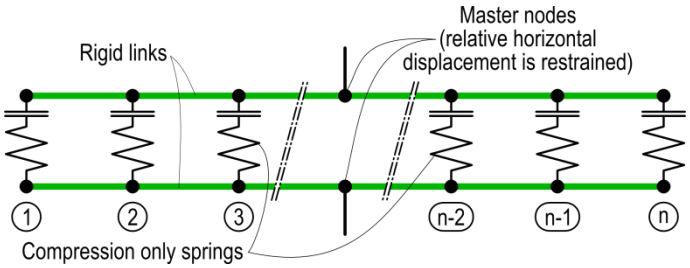

Figure 8-8. Multi-spring model.

In order to simulate the gap opening at the wall base a compression only hysteresis was considered. Based on experimental observations on post-tensioned timber walls shown in Chapter 5, some plastic deformation of the timber section can be expected at MCE demand drifts; consequently, a minor residual gap is developing at the wall base connection. This effect can be simulated using a Popovics stress-strain relationship (uniaxial material Concrete01 in Opensees) calibrated versus material tests (van Beerschoten *et al.*, 2013).

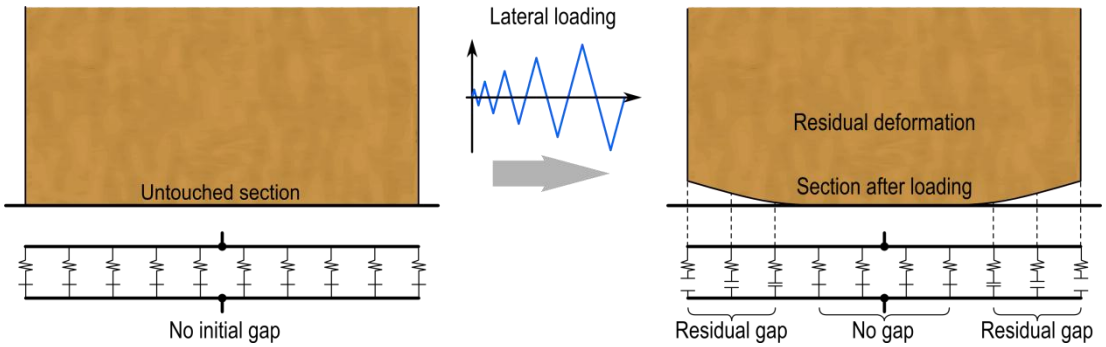

Figure 8-9. Multi-spring with degrading gap.

8.4.2 Model calibration

Similarly to the rotational spring model, the model must be calibrated versus analytical results presented in Chapter 7. The calibration of the model started from the multi-spring axial stiffness calibration using a simplified model; the model was then constructed defining the nodes and connection the contact element at the wall base as well as the post-tensioning springs or trusses.

The initial preload of the springs must be input considering the elastic losses of the model.

Once the preload were applied and shortening of the wall elements and multi-spring unit were evaluated, the dissipating elements were connected avoiding initial compressive stresses.

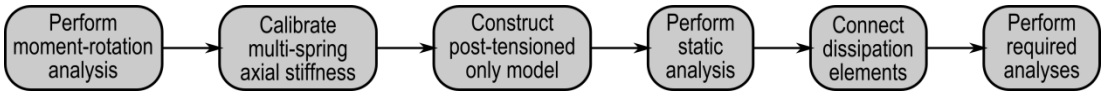

Figure 8-10. Multi-spring model framework.

Multi-spring axial stiffness and strength calibration

Although the multi-spring model can physically model the post-tensioning and mild steel reinforcements, some calibration of the total stiffness of the contact element must be performed. The calibration is carried out fitting the numerical results to the analytical model to calibrate the multi-spring, as shown by Marriott (2009). The calibration model consisted of a zero-length multi-spring element, whose master nodes were connected with zero-length elements simulating the post-tensioning tendons. The model was subjected to the same monotonically increasing rotation as the analytical model, and the significant design parameters were checked (neutral axis, moment and post-tensioning force versus base rotation).

The neutral axis, c, of the multi-spring element was evaluated as:

$$\frac{c}{h} = \frac{\Delta_1}{\Delta_n + \Delta_1} \qquad (8\text{-}2)$$

Where Δ_1, Δ_n = elongation of the end springs

The total moment of the simplified model can be evaluated by summing the moment in the multi-spring, $M_{mspring}$, and the contributions of the post-tensioning forces as:

$$M = M_{mspring} + \sum T_{pt,i} d_{pt,i} \qquad (8\text{-}3)$$

Where $T_{pt,i}$ = force in the i-th spring

$d_{pt,i}$ = distance of the i-th spring from the centreline

Generally a first guess value which gives acceptable fit to the analytical model results is:

$$k_{mspring} = 3.0 \frac{E_{con} A_t}{L_{cant}} \qquad (8\text{-}4)$$

The Concrete01 material for the multi-spring elements was calibrated according to the material testing performed by Van Beerschoten et al. (2013). The input parameters for the material model are summarized in Figure 8-11b and are:

- Maximum material strength, f_t = 45MPa
- Material strain at maximum strength, ε_{t0} = 0.0055
- Timber crushing strength, f_{tu} = 35MPa
- Material strain at crushing strength, ε_{tu} = 0.01

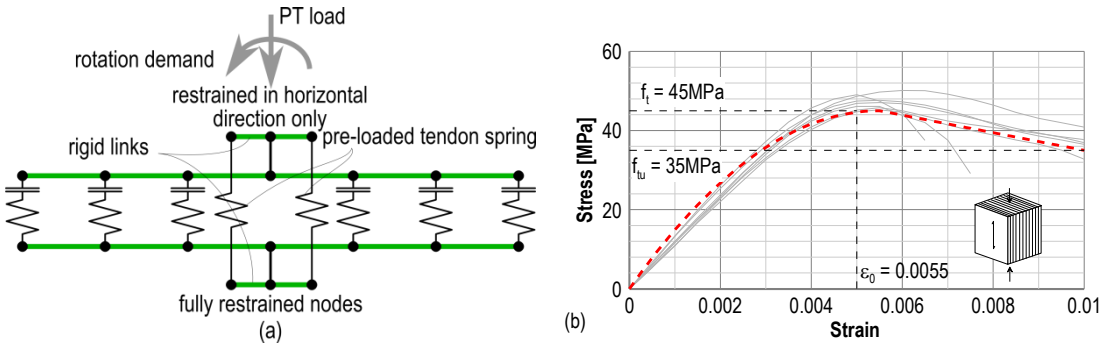

Figure 8-11.(a) Simplified model to be used in the calibration (modified from Marriott (2009); (b) strength calibration (modified from Van Beerschoten et al. (2013)).

The calibrated multi-spring was used and compared against experimental results on the post-tensioned only specimen S600 presented in Chapter 5. The specimen showed a small degradation due to minor timber crushing. The numerical results using the multi-spring unit is shown in Figure 8-12 and they show good fit with the experimental results.

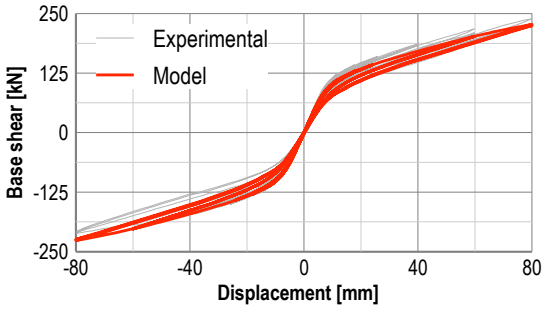

Figure 8-12. Post-tensioned only wall model comparison.

Figure 8-13 shows the multi-spring axial stiffness calibration results for the post-tensioned only test S400. The total initial post-tensioning force was 400kN, and the calibrated axial stiffness of the multi-spring unit was 5.852×10^6kN/m.

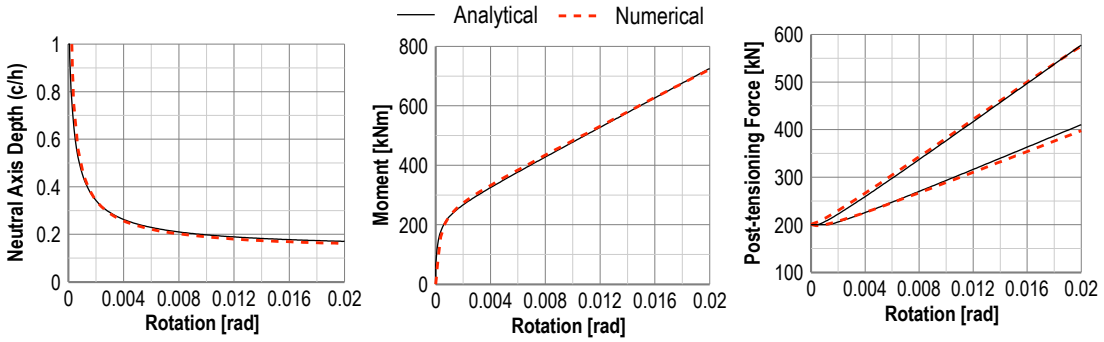

Figure 8-13. Example of multi-spring axial stiffness calibration for specimen S400.

Post-tensioning reinforcement material and initial force calibration

For the post-tensioning and dissipative springs modelling the additional reinforcement, the material calibration was based on the materials' stress-strain relationships.

The post-tensioning reinforcement can be modelled using either an elastic-plastic or Menegotto-Pinto (Menegotto *et al.*, 1973) relationship depending on the type of post-tensioning device used. An elastic-plastic hysteresis is suitable for post-tensioning strands. If post-tensioning bars are used, a Menegotto-Pinto rule is more appropriate. In fact, the hysteresis can model the transition curve typical of hardened steel and can be calibrated to fit the post-tensioning steel stress-strain relationship.

The Menegotto-Pinto parameters were calibrated according to the manufacturer's technical approval (Macalloy, 2007) and are listed below:

- Modulus of elasticity: E_{pt} = 182GPa
- Yield strength (0.1% proof stress): f_{pt} = 835MPa
- Curvature Factor, R = 10
- Post-yield stiffness: r = 0.09

An issue with the multi-spring approach is that some post-tensioning elastic losses are present and those are the result of the axial flexibility of the wall elements as well as the axial stiffness of the multi-spring unit. Once the initial pre-load in the post-tensioning springs/trusses was input and the static analysis was performed, the elastic shortening of the wall and of the multi-spring induced a force loss.

This issue can be addressed by considering the different stiffness contributions involved. The system can be represented by a spring system as shown in Figure 8-14b.

The shortening of the system, $\delta_{initial}$, due to the preload force in the spring, T^*_{pt0}, can be evaluated as:

$$\delta_{initial} = \frac{T^*_{pt0} - \Delta T_{pt}\left(\delta_{initial}\right)}{k_{pt} + \left(1/k_{mspring} + 1/k_{wall}\right)^{-1}} \quad (8\text{-}5)$$

Where k_{pt} = post-tensioning spring stiffness

$k_{mspring}$ = total stiffness of the multi-spring element

The loss of pre-load in the spring is also depending on the initial shortening:

$$\Delta T_{pt}\left(\delta_{initial}\right) = k_{pt}\delta_{initial} \quad (8\text{-}6)$$

Substituting and rearranging, the initial preload in the spring, T^*_{pt0}, to achieve the required initial post-tensioning force T_{pt0}, initial is:

$$T^*_{pt0} = \frac{T_{pt0}}{1 - \frac{k_{pt}}{2k_{pt} + \left(1/k_{mspring} + 1/k_{wall}\right)^{-1}}} \quad (8\text{-}7)$$

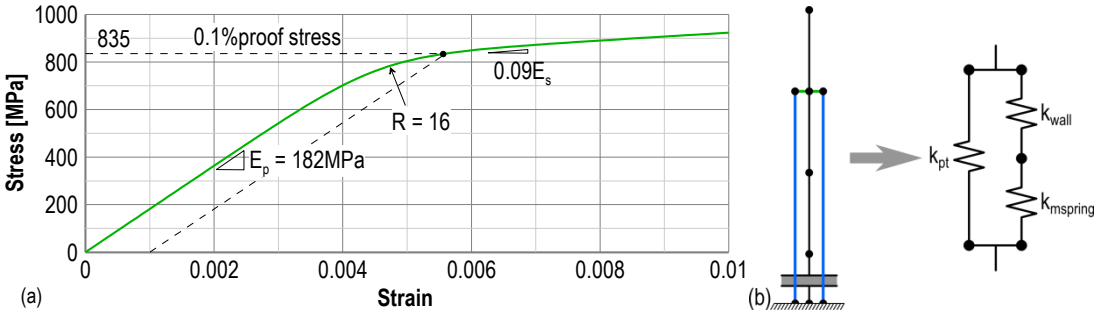

Figure 8-14. Post-tensioning reinforcement calibration. (a) stress-strain relationship; (b) Spring system for initial force calibration.

Dissipative reinforcement calibration and connection stiffness

For modelling dissipative reinforcement a zero-length spring was used, and that must be calibrated considering the particular material used for fabricating the specimen. Generally, for tension-compression yield dissipaters either a Menegotto-Pinto (Menegotto *et al.*, 1973) or a Dodd-Restrepo (Dodd *et al.*, 1995) rule can be used for the dissipaters (see Chapter 3).

The component testing on tension-compression yield dissipaters did not show the yielding plateau; therefore, a Menegotto-Pinto hysteresis (Steel02 in Opensees) was considered more appropriate. The hysteresis parameters are listed below and the comparison with experimental results is shown in Figure 8-15a:

- Modulus of elasticity: E_{pt} = 200GPa
- Yield strength: f_{pt} = 400MPa

- Curvature Factor, R = 20
- Post-yield stiffness: r = 0.08
- Isotropic hardening parameters: $a_1 = 0.05$; $a_2 = 1.0$; $a_3 = 0.0$; $a_4 = 1.0$

U-shaped Flexural Plates were modelled with Ramberg-Osgood hysteresis which was calibrated according to the analytical and experimental work performed by Baird et al. (2014) and summarized in Chapter 7. From experimental component testing a reduced Ramberg-Osgood factor best fitted the experimental results. The following material properties were used (see Figure 8-15b for comparison with experimental results):

- UFP yield force, $F_u = 35$kN
- UFP stiffness, 10883kN/m
- Ramberg-osgood factor, R = 7

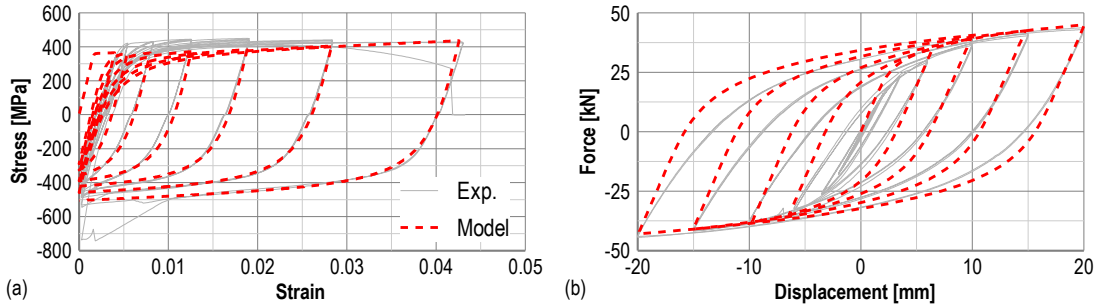

Figure 8-15.Components material calibration. (a) tension-compression yield dissipater; (b) UFP.

As shown in Chapter 5, the dissipaters' connection elastic stiffness can have a significant influence on the overall behaviour of the system. This issue was addressed in the analytical model (see Chapter 7) by considering the effective unbonded length of the dissipater. Although that approach was acceptable for push-over analyses, when the model is subjected to cyclic loading this assumption does not allow a correct prediction of the dissipater's behaviour. When the dissipater is simulated using a single spring calibrated using the effective unbonded length, the dissipater is pushed back to zero displacement. As observed during experimental testing in Chapter 5, this was not a realistic assumption. Due to the compressive stresses in the dissipater, the connection was pushed in the opposite direction causing the dissipater not to go to zero displacement after cyclic yielding (see Figure 8-16). To account for this mechanism the dissipater was connected in series with an additional elastic spring.

As discussed in Chapter 5, the application of an initial post-tensioning force brings to a shortening of the multi-spring unit. This led the dissipaters to compressive stresses before any lateral load was applied. Depending on the geometric characteristics of the dissipaters, this could also result in compressive yielding before any gap opens.

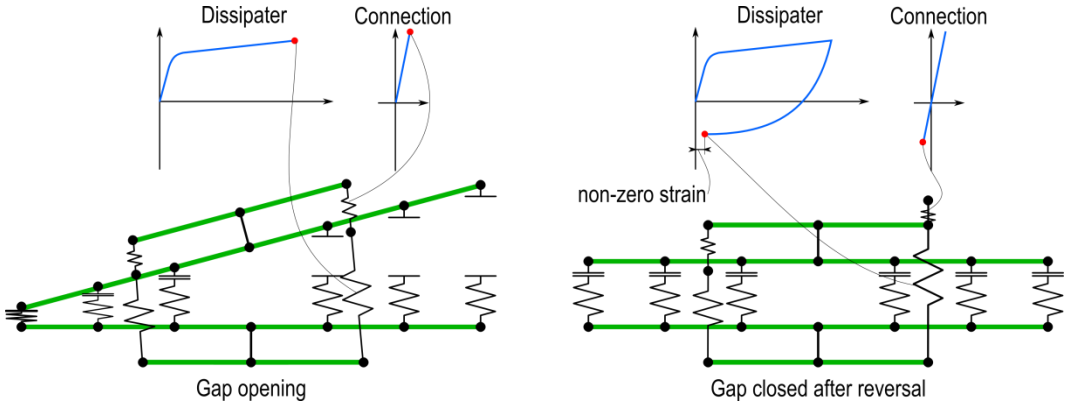

Figure 8-16. Dissipaters behaviour accounting for connection stiffness.

To solve the issue the model was constructed first by defining the structure nodes (including the ones connecting the dissipaters) and connecting the base contact element, the rigid links and post-tensioning springs/trusses into a post-tensioned only solution; a static analysis was then performed and that applied the compressive forces from the post-tensioning springs to the model. Once the static analysis was performed the dissipaters and connection springs were connected. This allowed avoiding of initial compressive stresses in the dissipaters.

8.4.3 Experimental results comparison

Single wall

The comparison of numerical against experimental results is shown in Figure 8-17 for the post-tensioned only specimens. The multi-spring model was capable of predicting the force-displacement behaviour of the specimens.

Figure 8-17 shows that the post-tensioning force and neutral axis depth were well predicted for the specimens.

The post-tensioning force was well predicted for the three specimens, and the consideration of a Menegotto-Pinto hysteresis for the post-tensioning bars allowed the simulation of the post-tensioning loss due to small plasticization of the post-tensioning bars, confirming the observation of the experimental response in Chapter 5.

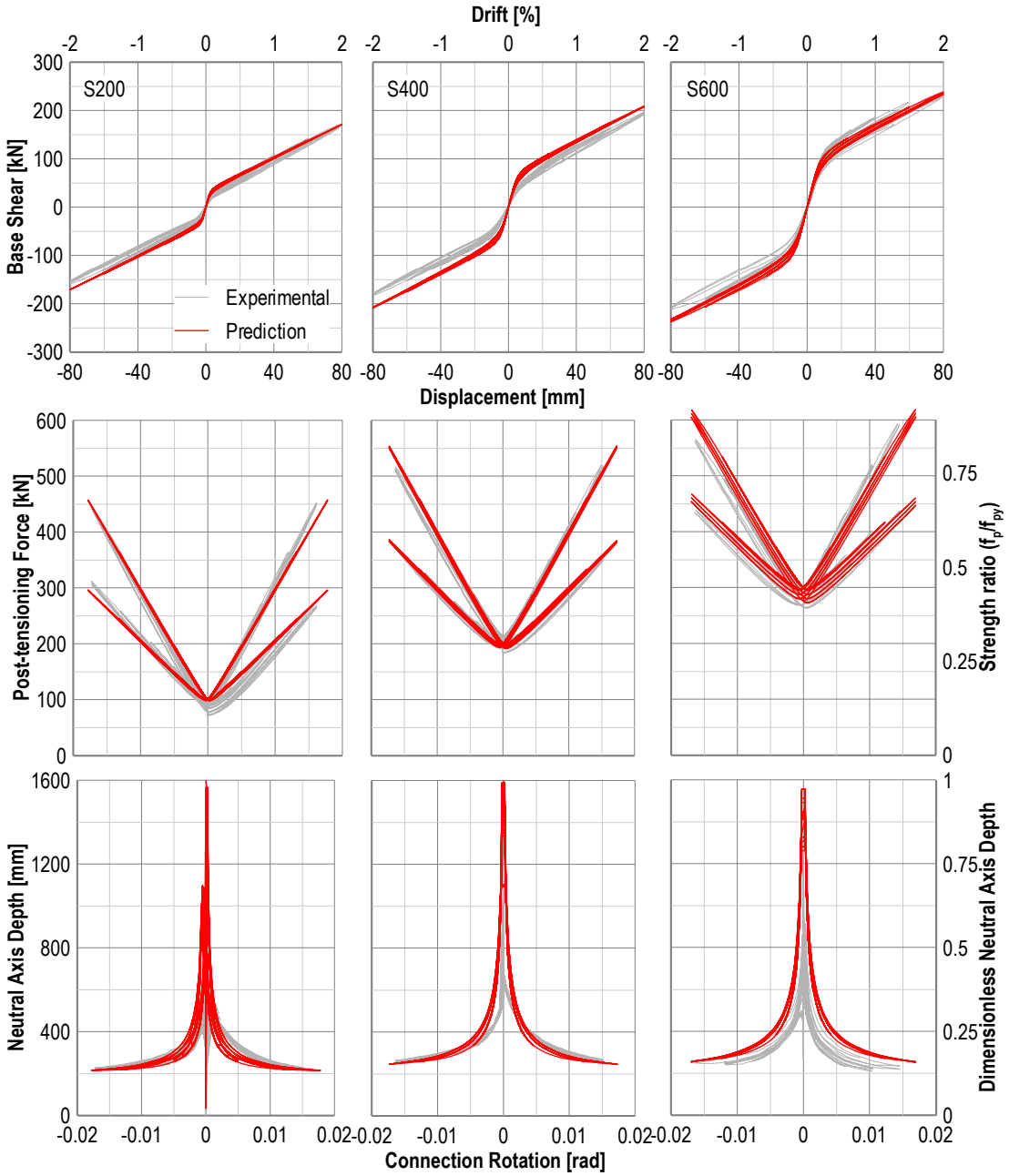

Figure 8-17. Multi-spring model comparisons, pure post-tensioned rocking specimens.

The comparison of numerical results of the dissipative post-tensioned specimens in Figure 8-18 shows the multi-spring model could accurately predict the system response.

A minor over-estimation of the force-displacement response was observed for the specimens S400-4, and that can also be observed in the force-displacement results of specimen S600-4. This is thought to be due to the minor damage to the timber section observed after throughout the testing campaign.

The incorporation of an elastic spring simulating the connection flexibility (as shown in Section 8.4.2) allowed an accurate prediction of the dissipaters' net displacement recorded during experimental tests. This allowed to accurately simulating the stiffness degradation observed in the experimental results.

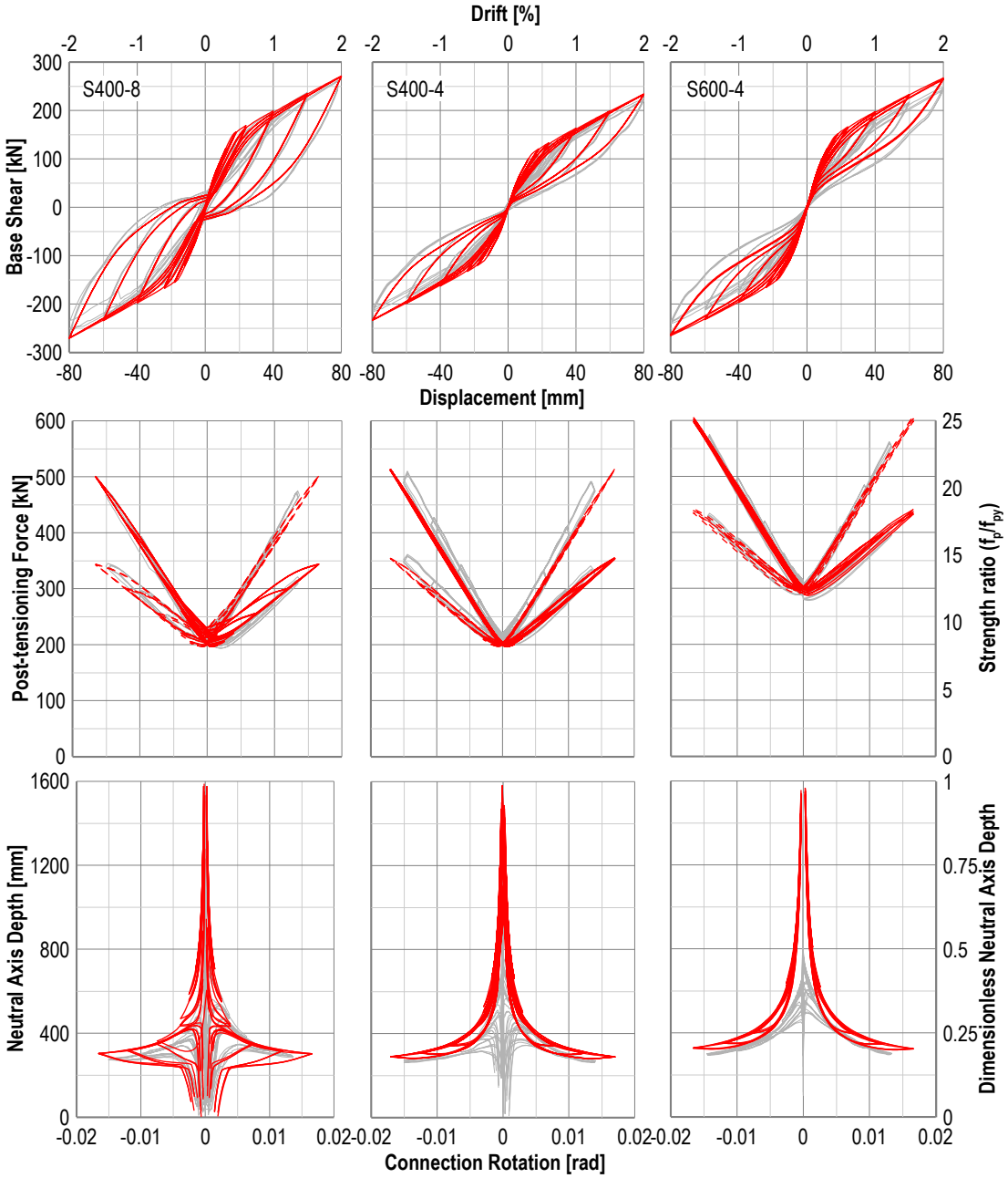

Figure 8-18. Multi-spring model comparisons, dissipative post-tensioned rocking specimens.

Column-wall-column

Similarly to the analytical models comparison (Chapter 7), the friction contribution was neglected. The results of the post-tensioned only specimens in Figure 8-19 highlights that approximation does not influence significantly the accuracy of the results.

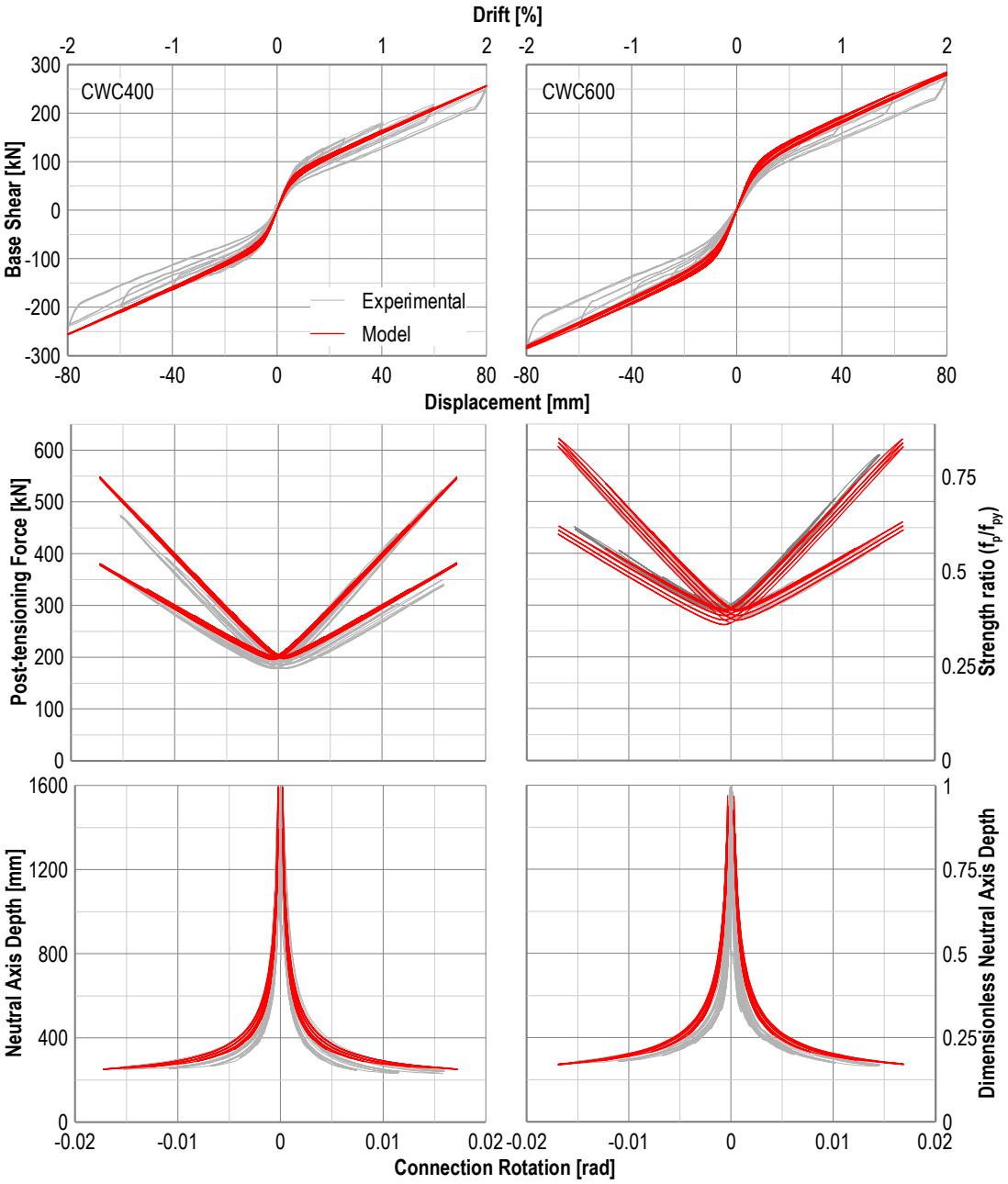

Figure 8-19. Multi-spring model comparisons, pure post-tensioned rocking CWC specimens.

Similarly to the single wall models, the neutral axis depth was well predicted as well as the post-tensioning force. When subjected to higher post-tensioning forces the model was capable of simulating the post-tensioning loss, similarly to the single wall specimens.

The dissipative post-tensioned rocking specimens' experimental results were compared to the numerical results in Figure 8-20.

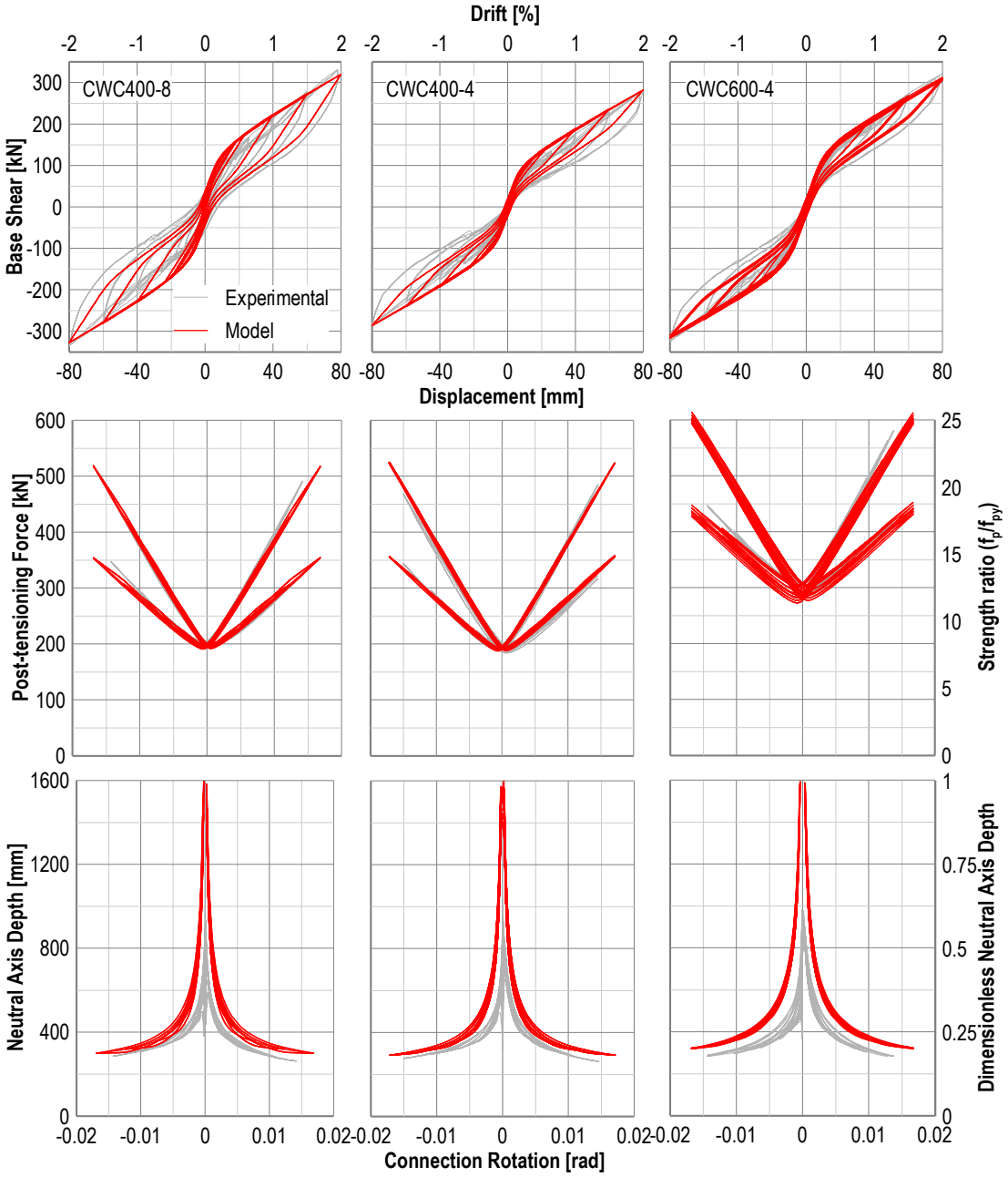

Figure 8-20. Multi-spring model comparisons, dissipative post-tensioned rocking CWC specimens.

In general, the numerical results captured the observed experimental data, but the neutral axis was slightly over-predicted. This did not affect the model prediction of the post-tensioning force, and the force-displacement loops fit the experimental backbone curves.

As shown in the force-displacement loops, while the loading branch of the protocol was well predicted, when unloaded the model slightly over-estimated the force-displacement

experimental curve. This causes a thinner hysteresis resulting in the under-estimation of the hysteretic damping.

8.5 Evaluation of the Equivalent Viscous Damping modification factors

As shown in Chapter 5, the connection flexibility can have a significant influence on the overall system behaviour. Although the effect of the connection stiffness on the equivalent viscous damping of the system was experimentally assessed, more detailed analyses were required to provide modification factors for use in a Displacement-Based Design approach (Priestley *et al.*, 2007).

The multi-spring model was developed and calibrated versus experimental tests on post-tensioned timber walls and it proved to be capable of predicting the general force-displacement behaviour of the post-tensioned walls, including the stiffness degradation due to the connection flexibility.

The model was used for the assessment of the area-based viscous damping in order to define modification factors for the most commonly used analytical model proposed by Priestley et al. (2007) and shown in Equation (8-8) below and plotted in Figure 8-21 for different ductility values, μ, and re-centering ratios, β.

$$\xi_{hyst} = \frac{(2-2\beta)(\mu-1)}{\mu\pi\left[1+r(\mu-1)\right]} \qquad (8\text{-}8)$$

Where μ = ductility

β = re-centering ratio (M_{pt}/M_{tot})

r = post-yield stiffness factor

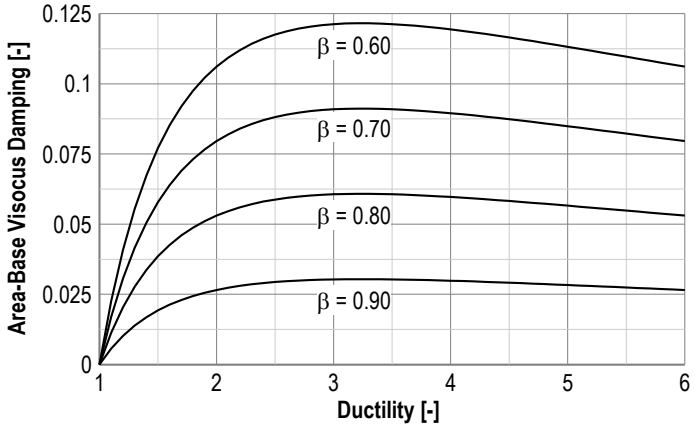

Figure 8-21. Area-based viscous damping variation with the re-centering ratio, β.

The model was based on an ideal flag-shaped hysteresis and that does not account for some behavioural aspects observed in the experimental results. Those showed that the analytical prediction could accurately capture the EVD evaluated at the first loading cycle, whilst underestimating its value for higher ductility levels due to isotropic strain hardening in the steel. When the analytical results were compared to EVD values evaluated for subsequent loading cycles, the stiffness degradation due to the dissipater's connection flexibility resulted in a reduction of EVD.

8.5.1 Analysis methodology

The parametric study aimed at the determination of the modification factors to be applied to Equation (8-8) and comprised of quasi-static analysis on different wall configurations.

First, push-over analyses were carried out to determine the significant parameters such as the yielding point and the post-yielding stiffness ratio; push-pull analyses were then carried out imposing multiple cycles at different drift levels to evaluate the area-based equivalent viscous damping accounting for the connection flexibility effects. The area-based equivalent viscous damping was evaluated using Equation (8-9) below.

$$\xi_{hyst} = \frac{1}{2\pi}\frac{A_h}{F_m \Delta_m} \qquad (8\text{-}9)$$

Where A_h = area within one complete cycle of stabilized force-displacement response

F_m, Δ_m = maximum force and displacement achieved in the stabilized loops

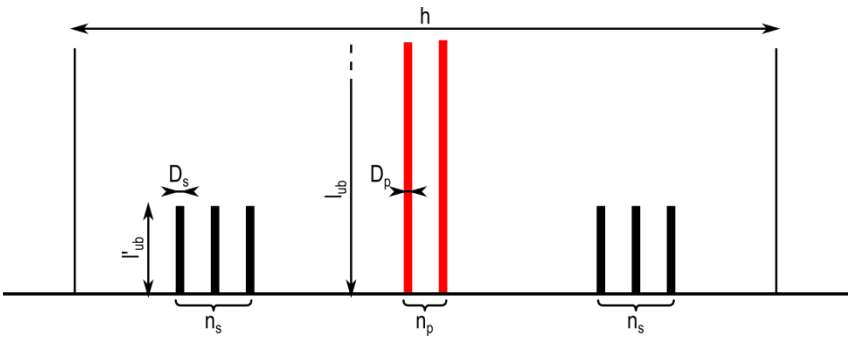

Figure 8-22. Geometric parameters of the case study wall.

The parametric analysis considered a set of case study walls with different cross-sectional dimensions (0.24m×2.4m and 0.36m×3.6m) and three elements heights (3, 6 and 8 storeys, 3m inter-storey height) were accounted for. The design base moment shear for each height was 2300kN, 3000kNm and 4700kNm respectively.

To assess the influence of different re-centering ratios, β, each wall was designed using values of 0.6, 0.7 and 0.8.

Table 8-2. Parametric schedule for EVD modification factor (α_{con} = 0.5, …, 2.0)

ID	N_{storv}	β	b *[m]*	h *[m]*	d_s *[m]*	D_s *[m]*	n_s	l'_{ub} *[m]*	D_p *[m]*	n_p	l_{ub} *[m]*	$T_{pt,initial}$ *[kN]*	Design Shear *[kN]*
W1	3	0.6	0.24	2.4	0.4	0.013	8	0.42	0.032	2	6	760	
W2	3	0.7	0.24	2.4	0.4	0.012	8	0.42	0.025	4	6	880	2300kN
W3	3	0.8	0.24	2.4	0.4	0.011	6	0.42	0.04	2	6	960	
W4	6	0.6	0.36	3.6	0.6	0.02	6	0.65	0.032	4	15	1420	
W5	6	0.7	0.36	3.6	0.6	0.018	6	0.65	0.032	4	15	1700	3000kN
W6	6	0.8	0.36	3.6	0.6	0.014	6	0.65	0.04	4	15	1840	
W7	8	0.6	0.36	3.6	0.6	0.022	6	0.61	0.032	4	21	1680	
W8	8	0.7	0.36	3.6	0.6	0.019	6	0.61	0.04	4	21	2020	4700kN
W9	8	0.8	0.36	3.6	0.6	0.016	6	0.61	0.04	4	21	2340	

A key parameter in the analyses was the dissipaters' connection stiffness. To have a consistent approach within different case study walls, the connection stiffness to dissipater stiffness ratio, α_{con}, was considered.

$$\alpha_{con} = \frac{l'_{ub}}{E_s A_{fuse}} k_{con} \qquad (8\text{-}10)$$

Where l'_{ub} = unbonded length of the dissipater

E_s = steel modulus of elasticity

A_{fuse} = fuse area

k_{con} = dissipaters' connection stiffness

Four values were considered in the analysis (i.e. 0.5, 1.0, 1.5 and 2.0).

8.5.2 Analysis results and modification factors

The push-over curves for each case study wall were used for the determination of the bi-linear approximation providing the key parameters to be used in Equation (8-8) for comparison with the push-pull numerical results. Figure 8-23 shows the results of the case study wall W1 in terms of push-over curve and the comparison of the assumed flag-shape versus the model push-pull curve.

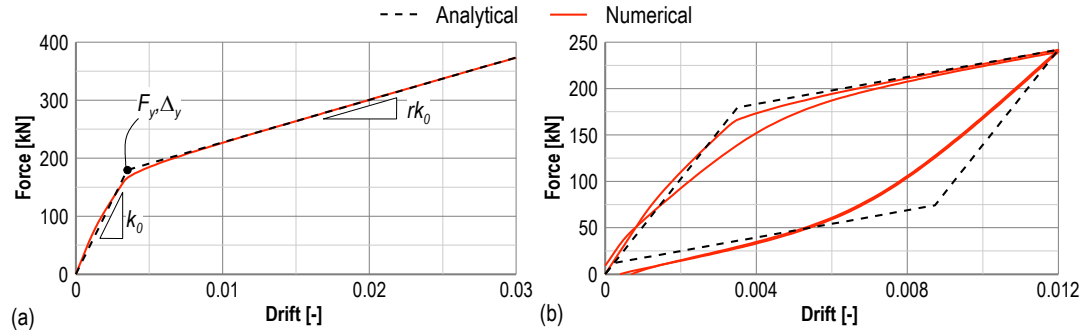

Figure 8-23. (a) Idealized flag shape calibration on push-over curve; (b) comparison versus push-pull analysis.

Figure 8-24a plots the evaluated EVD values versus the ductility for the case study wall W1 and stiffness ratio α_{con} = 0.5. The dashed black line in the chart shows the EVD resulting from Equation (8-8).

The reduction factor was evaluated for each ductility value considering the ratio between the equivalent viscous damping evaluated using Equation (8-8) ($A_{analytical}$ in Figure 8-24b) and the area-based EVD calculated for each reloading cycle of the model ($A_{numerical}$ in Figure 8-24b).

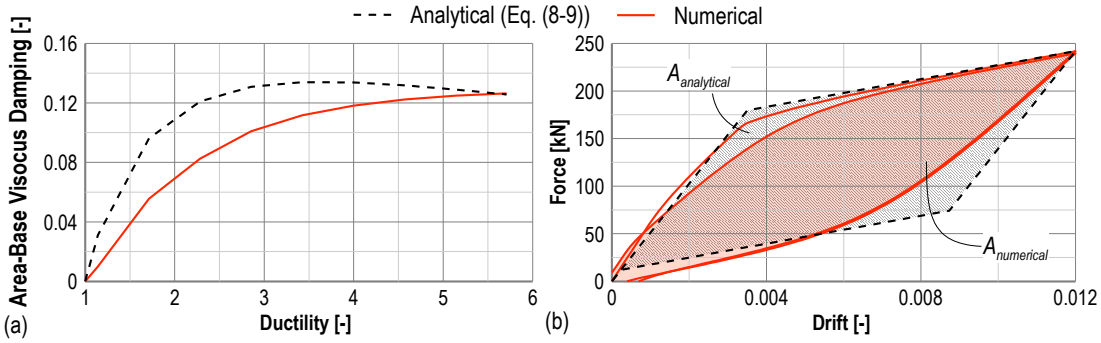

Figure 8-24. (a) EVD for wall W1;(b) Evaluation of hysteretic areas.

While several parameters were accounted for in the parametric study, the influence of each parameter was discussed with reference to the general trend of the modification factor. As expected, the connection stiffness ratio had the most significant influence on the variation of the modification factor. As shown in Figure 8-25a, for a connection stiffness ratio of 1.0 and above, no significant difference in modification factor was observed.

For increased re-centering ratio values (i.e. decreasing the dissipative reinforcement) the reduction factor increased as expected. In fact, for a smaller contribution of the dissipative forces on the system's capacity the reduction is also less significant.

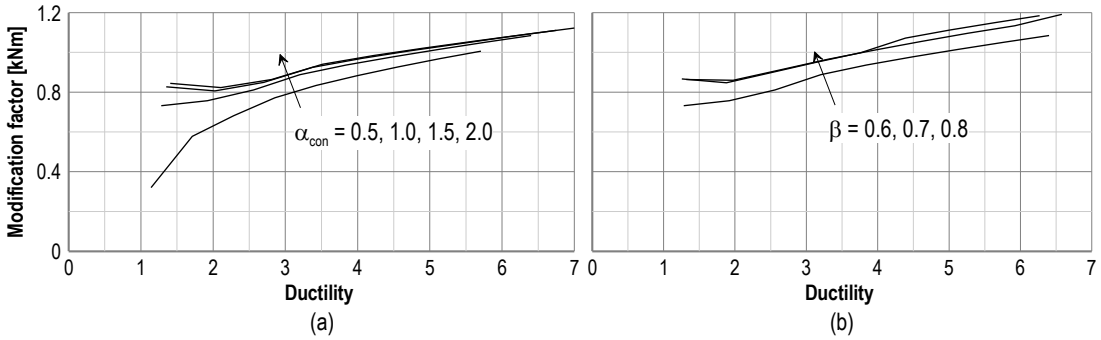

Figure 8-25. Modification factor. (a) Influence of the stiffness ratio (wall W1) (b) Influence of the re-centering ratio (walls W1, W2 and W3).

Since the area-based viscous damping is a design parameter to be used in initial stage of the seismic design of a dissipative post-tensioned timber wall, it was not practical to provide guidelines on such parameter which are stiffness dependant. Therefore, the definition of the general equation of the modification factor did not consider the influence of the above parameters and focused on the average results.

As shown in Chapters 5 and 6 the use of either tension-compression yield device or U-shaped flexural plates for energy dissipation was mainly differentiated by the cyclic behaviour of such dissipaters. In fact, tension compression dissipaters, as also shown in Chapter 3, have a significant isotropic strain hardening effect which effectively increases the amount of energy dissipation. On the other hand, devices such as UFPs do not show strain hardening effects. To account for this fundamental difference in the cyclic behaviour, the analyses were carried out considering dissipaters with and without isotropic strain hardening effects.

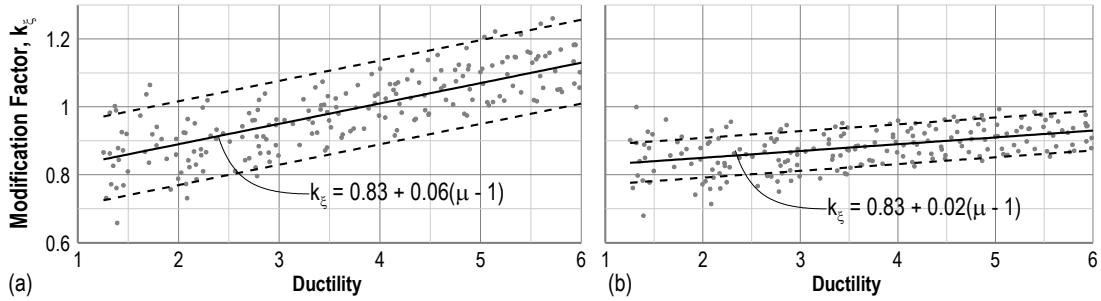

Figure 8-26. EVD modification factors (a) with and (b) without isotropic strain hardening effects.

Figure 8-26 shows a summary of the numerical results which were fitted using linear functions reported in Equation (8-11).

$$k_\xi = 0.83 + (\mu - 1) \cdot \begin{cases} 0.06 \ \textit{with isotropic strain hardening} \\ 0.02 \ \textit{without isotropic strain hardening} \end{cases} \qquad (8\text{-}11)$$

The proposed area-based hysteretic viscous damping design formula is therefore given in Equation (8-12).

$$\xi_{hyst} = k_{\xi} \frac{(2-2\beta)(\mu-1)}{\mu\pi\left[1+r(\mu-1)\right]} \qquad (8\text{-}12)$$

8.6 Comparison between modelling approaches

Two modelling approaches were showed in this chapter and both proved to be effective in the prediction of the observed experimental results. Some differences in the two models have been discusses throughout the chapter and are summarized in this section.

As anticipated, the rotational spring model represents the most convenient modelling approach in term of computational load since the non-linear behaviour is lumped at the base connection and is given by a few elements.

The greatest disadvantage of this modelling approach is that, although showing good accuracy (see Section 8.3.2), it can output only overall response parameters such as force-displacement or moment-rotation.

As discussed in Section 8.4, the multi-spring model, although more computationally demanding, represents a more detailed approach which allows to output more detailed parameters such as the reinforcement elongation as well as the variation of the neutral axis depth.

Figure 8-27 shows the comparison of the two modelling approaches for the wall specimens S400-8 and CWC400-8.

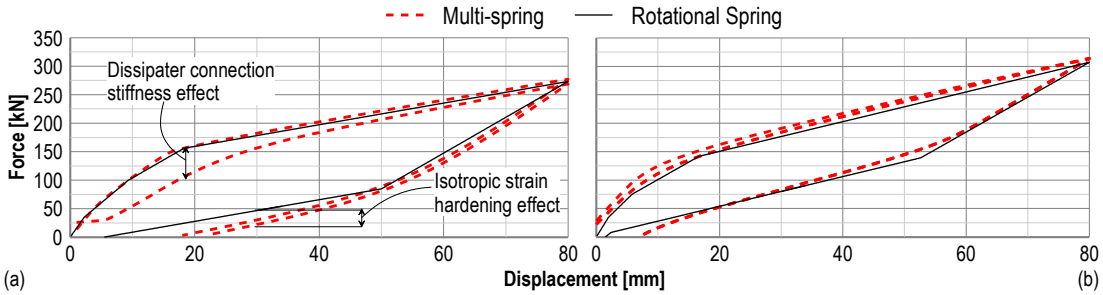

Figure 8-27. Modelling approach comparison. Post-tensioned wall S400-8 (with isotropic strain hardening effects) and (b) CWC400-8 (without isotropic hardening effects).

From the comparison of the two models it is clear that, in terms of cyclic response prediction, the rotational spring model is not capable of accounting for isotropic strain hardening effects, thus underestimating the hysteretic damping of the system (Figure 8-27a).

It can also be noted that the multi-spring model allows the simulation of the dissipater connection flexibility, which is observed from the stiffness degradation shown in Figure 8-27.

When isotropic strain hardening effects are not to be considered and the connection flexibility has a minor influence on the wall response (e.g. when UFPs are used) the two models show very similar results (see Figure 8-27b).

8.7 Conclusions

The modelling approaches presented in the chapter proved effective in the prediction of the observed experimental response of dissipative post-tensioned rocking wall systems.

While the rotational spring model represents a computationally light and efficient modelling approach, it was capable of providing general response parameters such as the force-displacement or moment-rotation behaviour of the system; nevertheless, the rotational spring model was not capable of simulating the isotropic strain hardening of the mild steel dissipaters.

The multi-spring model was used as a more refined tool to capture detailed parameters. While a multi-spring element is implemented in Ruaumoko (Carr, 2004), the chapter presented the development of a multi-spring element in OpenSEES (McKenna, 2011).

The multi-spring was developed and refined to account for the particular behavioural aspects observed during the experimental campaign showed in chapters 5. In particular, the multi-spring unit allowed the use of a degrading gap material, and that enabled the model to simulate the incremental damage occurring at the timber section for high drift levels.

The multi-spring model proved efficient in the prediction of the system behaviour and its detailed parameters. The neutral axis depth as well as post-tensioning forces numerical results accurately fitted the experimental data.

8.8 References

Baird, A., Smith, T., Palermo, A., Pampanin, S. 2014. Experimental and Numerical Study of U-Shaped Flexural Plate (UFP) Dissipators. *New Zealand Society for Earthquake Engineering Annual Conference*, Auckland, New Zealand.

A. Carr. 2004. *Ruaumoko Programme for Inelastic Dynamic Analysis - User Manual*. A. Carr, Department of Civil Engineering, University of Canterbury.

Dodd, L., Restrepo-Posada, J. 1995. Model for predicting cyclic behavior of reinforcing steel. *Journal of Structural Engineering* 121(3): 433-445.

Iqbal, M.A. 2011. Seismic response and design of subassemblies for multi-storey prestressed timber buildings *PhD Dissertation*, University of Canterbury, Christchurch, New Zealand.

Macalloy. 2007. *European Technical Approval ETA-07/0046*. European Organization for Technical Approvals. Charlottenlund, Denmark.

Marriott, D.J. 2009. The Development of High-Performance Post-Tensioned Rocking Systems for the Seismic Design of Structures *PhD Dissertation*, Universtiy of Canterbury, Christchurch, New Zealand.

McKenna, F. 2011. OpenSees: A Framework for Earthquake Engineering Simulation. *Computing in Science and Engg.* 13(4): 58-66.

Menegotto, M., Pinto, P.E. 1973. Method of Analysis for Cyclically Loaded Reinforced Concrete Plane Frames Including Changes in Geometry and Non-elastic Behavior of Elements Under Combined Normal Force and Bending. *IABSE Symposium on the Resistance and Ultimate Deformability of Structures Acted on by Well-Defined Repeated Loads, Lisbon*.

Newcombe, M. 2012. Seismic design of post-tensioned timber frame and wall buildings *PhD Dissertation*, University of Canterbury, Christchurch, New Zealand.

Palermo, A., Pampanin, S., Carr, A. 2005. Efficiency of Simplified Alternative Modeling Approaches to predict the Seismic Response of Precast Concrete Hybrid Systems. *fib Symposium: Keep Concrete Attractive*, Budapest, Hungary.

Priestley, M.J.N., Calvi, G.M., Kowalsky, M.J. 2007. *Displacement-based seismic design of structures*. Pavia, Italy, IUSS Press.

Spieth, H.A., Carr, A.J., Pampanin, S., Murahidy, A.G., Mander, J.B. 2004a. *Modelling of Precast Prestressed Concrete Frame Structures with Rocking Beam-Column Connections.* Technical report Report 2004-01. Christchurch, New Zealand, University of Canterbury.

Spieth, H.A., Carr, A.J., Pampanin, S., Murahidy, A.G., Mander, J.B. 2004b. Modelling of Precast Prestressed Concrete Frame Structures with Rocking Beam-Column Connections. *NZSEE Conference*, Rotorua, New Zealand.

van Beerschoten, W.A., Carradine, D.M., Palermo, A. 2013. Compressive strength and stiffness of Radiata Pine laminated veneer lumber. *European Journal of Wood and Wood Products* 71(6): 795-804.

Part 4:

Wall system performance

9 Determination of the Force-Based Design parameters of Post-tensioned timber wall systems

9.1 Introduction

The objectives of this chapter are the determination of the collapse probability of multi-storey buildings adopting post-tensioned timber walls systems, and to propose Force-Based Design parameters such as the seismic reduction factor, over-strength factor, and deflection amplification factor.

To achieve the research objectives, the research work presented in the chapter shows the determination of the seismic performance factors in accordance with the FEMA P-695 procedure (ATC, 2009). The procedure is a standard methodology for the determination of the seismic design parameters to be used in the evaluation of the lateral load demand in accordance with ASCE/SEI 7-10 (2010) and following a Force-Based Design approach.

The chapter discussed the details of the procedure which consists of extensive numerical analyses to determine the collapse probability of multi-story post-tensioned timber wall building systems. The methodology was applied to perform analysis on several lateral load resisting systems, such as single wall as well as Column-Wall-Colum systems which were discussed in previous chapters. To provide a comprehensive study of multi-storey timber buildings adopting dissipative post-tensioned rocking timber walls, also coupled wall systems (Iqbal *et al.*, 2007; Iqbal, 2011) were considered in the analysis.

While providing a standard and comprehensive procedure for the determination of significant Force-Based Design (FBD) parameters in accordance with ASCE 7-10 (2010), the final part of this chapter discusses the extension of the numerical results in terms of the seismic reduction factor to different standards such as NZS1170.5 (Standards New Zealand, 2004) and EN 1998-1 (2004) (Eurocode 8).

9.2 Overview of the FEMA P-695 procedure

The FEMA P-695 procedure utilizes nonlinear analysis techniques, and explicitly considers uncertainties in ground motion, modelling, design, and test data. The technical approach is a combination of traditional code concepts, advanced nonlinear dynamic analyses, and risk-based assessment techniques (ATC, 2009).

The flow chart in Figure 9-1 summarizes the general framework of the procedure. After the first concept development, required detailed information must be retrieved, including detailed design requirements, and experimental results (material, component and system testing).

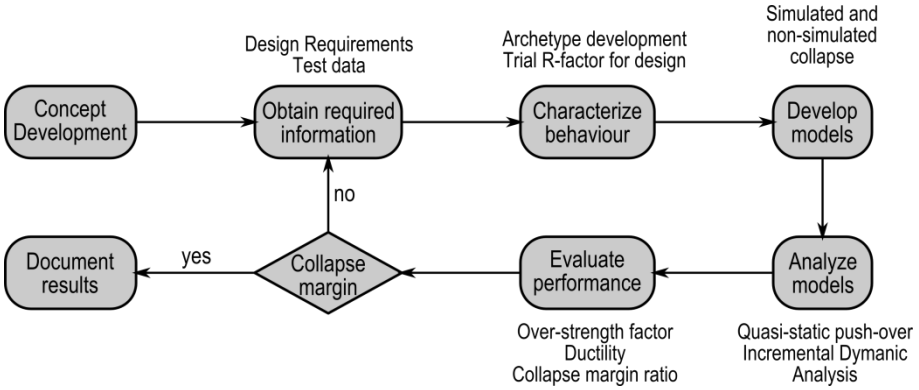

Figure 9-1. FEMA P-695 Methodology framework (modified from (ATC, 2009)).

The system behaviour is then characterized by defining structural system archetypes defined as prototypical representations of a seismic resisting system, which are intended to reflect the range of design parameters and system attributes that are judged to be reasonable representations of the feasible design space and have a measurable impact on system response (ATC, 2009). The range of parameters which should be taken into account in the definition of the system archetypes includes (i) the building height, (ii) the fundamental period, (iii) the structural framing configurations, (iv) the framing bay size or wall lengths, (v) the magnitude of the gravity loads and (vi) member and connection design and detailing requirements.

The system archetypes provide the design basis of a finite number of buildings, which are represented by numerical models, which should provide the most basic idealization of the building, while capturing the main behavioural aspects of the system investigated. Model should include the explicit simulation of the significant collapse and degradation mechanisms of the system where possible, but non-simulated mechanisms can be also considered and usually trigger an earlier collapse.

The developed models are analysed using non-linear quasi-static and dynamic analyses. Static push-over analyses aim at the determination of the system over-strength factor and ductility. Non-linear time-history analyses are carried out to provide statistical information of the median collapse capacity of the archetypes. A set of 22 ground motions (2 components each) are used applying the Incremental Dynamic Analysis (IDA) concept similarly to Vamvatsikos et al. (2002).

The evaluation of the system performance is assessed by evaluating a Collapse Margin Ratio (CMR) defined as the ratio of the median collapse and MCE spectral accelerations (see Figure 9-2b).

The adjusted CMR values are checked against acceptable values determined by design requirements, test data, modelling and record-to-record uncertainties. If collapse margin is acceptable the trial response modification factor used in the design phase is confirmed, and the seismic performance factors can be evaluated.

The seismic performance factors determined in accordance with the FEMA P-695 procedure are the response modification factor, R, the deflection amplification factor, C_d, and the system over-strength factor, Ω_0, defined as shown in Figure 9-2

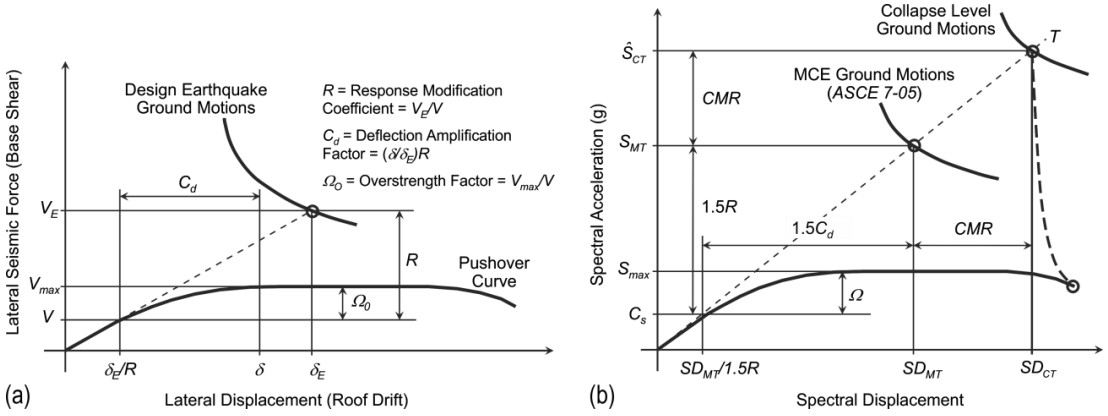

Figure 9-2. Illustration of seismic performance factors (R, Ω_O, and C_d) as defined by (a) NEHRP Recommended Provisions (FEMA, 2004) and (b) FEMA P-695 (ATC, 2009).

9.3 System concept and required information

9.3.1 Design requirements

The design requirements in accordance with ASCE 7-10 (2010) were adopted for the design of the lateral load resisting systems considered in the analyses presented in this chapter. In addition to the code-related seismic design requirements, some system requirements were suggested, also according to the STIC Design Guidelines (STIC, 2013).

The general performance-based design philosophy of post-tensioned timber systems can be qualitatively summarized by Figure 9-3. The general hierarchy of strength and sequence of events would be (STIC, 2013):

1. Yield of the non-prestressed reinforcement (or dissipaters)
2. Yield of the timber at the rocking interface either in the column or the beam
3. Finally yielding of the post-tensioning reinforcement.

Such design philosophy allows the system to:

1. withstand small and frequent events with no significant damage
2. provide the required hysteretic damping under a design level earthquake
3. prevent structural collapse when subjected to a Maximum Credible Event (MCE)

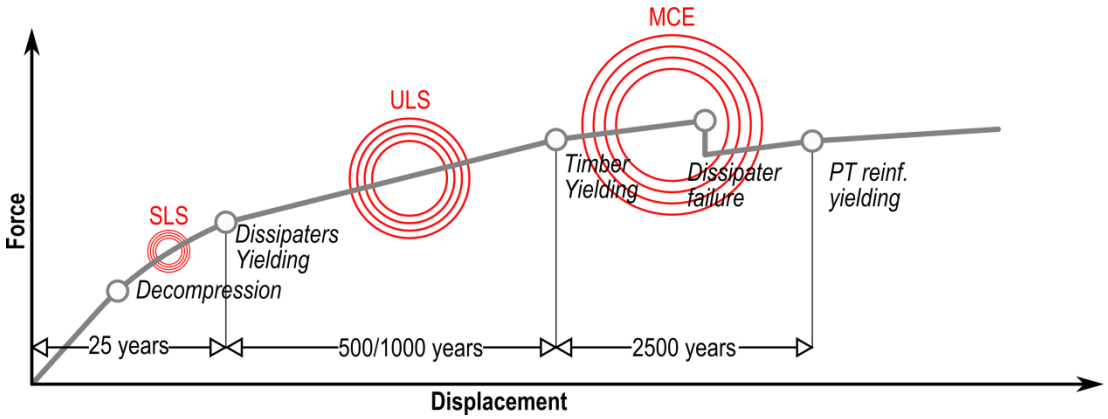

Figure 9-3. Qualitative push-over curve and performance limits.

The proposed system design requirements include suggested values of re-centering ratio, strain limits in the dissipaters at Ultimate Limit State (ULS) and Maximum Credible Event (MCE) level and initial timber stress:

1. Initial timber stress (proportional to the initial post-tensioning force) should not exceed 10% of the timber compressive strength. This stress limit is set to allow the section to develop the gap opening and neutral axis depth necessary to the efficient activation of the dissipaters. For greater initial post-tensioning forces, the decompression point (i.e. the opening of the gap) happens at greater displacements. This effect is due to the elastic deformations of the structural element and can bring to low levels of hysteretic damping.
2. The maximum strain in the tension-compression yield dissipaters shall be in the range of 3-4% at DBE level and 6% at MCE level. The strain range suggested allows the system to develop the necessary damping while providing the dissipater with some failure margin. When using different devices such as UFPs, low-cycle fatigue

analysis considerations from Kelly et al. (1974) applies; therefore, a maximum strain of 10% is proposed.

3. Values of re-centering ratio, β, at design level should not be less than 0.55 (55% re-centering contribution and 45% dissipative contribution) in accordance with Appendix B of NZS3101 (2006). The re-centering ratio value is a key parameter in the hysteretic response of the section. For low values, the structural element exploits a significantly higher amount of dissipation, but residual displacements occur; instead, the post-tensioned connection provides small hysteretic damping for excessive values of β.

9.3.2 Experimental data

A procedure for the analytical modelling of post-tensioned rocking connections and systems was firstly proposed by Pampanin (2000), modified by Palermo (2004) and adapted to post-tensioned timber elements (Newcombe *et al.*, 2008). The model relies on an iterative moment-rotation analysis procedure based on the analogy to an equivalent monolithic solution. The analogy is required when dealing with post-tensioning rocking sections since the use of post-tensioning unbonded reinforcement does not allow the consideration of the Euler-Bernoulli assumption of plane sections (Pampanin *et al.*, 2001). The model is capable of accurately predicting the monotonic behaviour of the system (as shown in Chapter 7) and is used in the design phase; however, for predicting and modelling the cyclic response of the system, comprehensive experimental data is required to calibrate the numerical models. A detailed overview and refinement of the analytical moment-rotation analysis was presented previously in Chapter 7 of the dissertation.

Experimental tests on single walls and the Column-Wall-Column systems were showed and discussed in Chapters 5 and 6 of this dissertation (Sarti *et al.*, 2014; Sarti *et al.*, 2015b; Sarti *et al.*, 2015a); moreover, Iqbal et al. (2007) carried out experimental investigations on coupled wall systems. For each system, several elastic tests with increasing post-tensioning loads were performed and different dissipation options were taken into account.

For the single wall configuration tension-compression yielding mild steel devices (fuse-type dissipaters) were used. The device is made of a mild steel bar machined down to a reduced diameter to concentrate yielding in the central part of the dissipater. Threaded ends provide the dissipater connection to the structural element. To avoid buckling, the fuse area is encased in a steel tube which is filled with either grout or epoxy.

A comprehensive experimental program was presented in Chapter 2 and provided the necessary information for analytical models development used in the calibration of the structural behaviour of the dissipater as well as its low-cycle fatigue behaviour (Sarti *et al.*, 2013).

In Column-Wall-Column and coupled walls systems the structural elements are connected with U-shaped flexural plates. Those devices make use of the rolling (bending) of flat mild steel plates. The dissipater operates between adjacent surfaces whose relative motion is directed parallel to each other (Skinner *et al.*, 1974).

An extensive experimental campaign was carried out by Skinner et al. (1974), and further component testing was performed by Iqbal (2011) and Baird et al. (2014). Analytical models were developed by Skinner et al. (1974), and refined by Baird et al. (2014).

9.4 Archetype development and design

The basic plan view configuration of the archetype buildings is shown in Figure 9-4. The building has an approximate plan of 32m in the longitudinal direction and 18m in the transverse direction with a floor area of approximately 600m^2 per floor. The standard building configuration has post-tensioned timber walls providing lateral load resistance in both the longitudinal and the transversal direction (STIC, 2013). Five three-bay frames spanning 6m in the transverse direction support gravity loads.

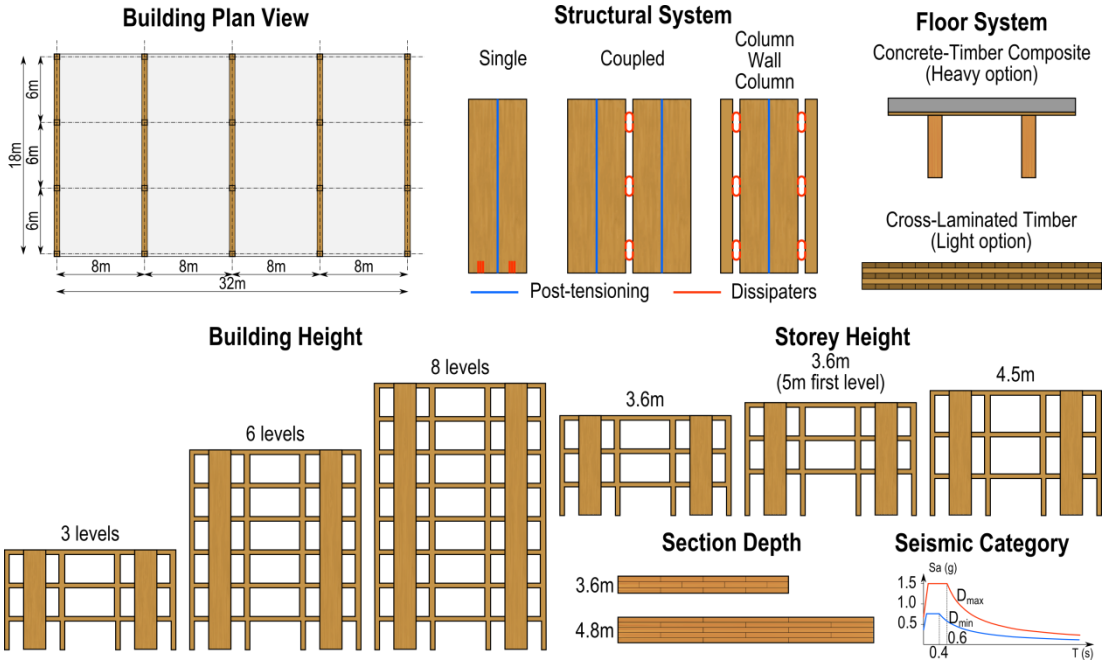

Figure 9-4. Archetype development overview.

Several parameters affecting the structural behaviour of the case study building were accounted for in accordance with the FEMA P-695 procedure (ATC, 2009), and those are summarized below.

- ***Seismic resisting system***. Three different wall systems may be used in multi-storey timber buildings. The single wall solution has concentrated plasticity at the base connection. An alternative solution is coupling two different walls and distributing the dissipaters (U-shaped Flexural Plates) over the building height. A variation of the coupled walls system is the CWC (Column-Wall-Column) system where two boundary columns are used and connected to the wall element with U-shaped Flexural Plates (UFPs).
- ***Building and storey height***. Building heights of 3, 6 and 8 storeys were taken into account with several storey heights. For most archetypes a constant storey height of 3.6m and 4.5m was adopted. A variation of the 3.6m option was also considered and it was representative of an office building with commercial spaces at the ground floor. This last option was considered to account for the influence of a softer ground floor.
- ***Wall depth***. To maintain standard sections according to the available standard profiles dimensions provided by manufacturers and to limit the range of geometries, two main wall dimensions of 3.6m and 4.8m were assumed.
- ***Gravity loads***. The building designs were carried out considering two different floor systems. The "High gravity" solution is a Timber-Concrete Composite (TCC) floor, which consists of timber joists supporting a 0.09m thick concrete topping with a plywood panel providing the permanent formwork. The "Low gravity" option is a full Cross-Laminated Timber (CLT) floor.

The Archetypes were divided for each resisting system into performance groups as shown in Table 9-1. Four main performance groups (PG-1, PG-2, PG-5 and PG-6) were considered in the Seismic Design Category (SDC) D_{max} and fewer archetypes in the lower SDC were analysed.

The archetype buildings were designed in accordance with ASCE/SEI 7-10 (2010) by defining the fundamental period of the structure, the seismic response coefficient and the base shear force. It is worth noticing that the archetype designs were carried out using trial values of the response modification factor, R = 7, and the deflection amplification factor, C_d = 7.5.

Table 9-1. System archetypes.

Group	SDC	Period	Gravity	*ID*	*No. storeys*	*Storey height (m)*	*Wall depth (m)*
PG-1	D_{max}	Short	High (TCC)	1	3	3.6	2.4
				2	3	4.5	2.4
				3	6	3.6	3.6
				4	6	5G,3.6	3.6
PG-2	D_{max}	Long	High (TCC)	5	6	4.5	3.6
				6	8	3.6	3.6
				7	8	4.5	3.6
				8	8	5G,3.6	3.6
PG-3	D_{min}	Short	High (TCC)	9	3	3.6	2.4
PG-4	D_{min}	Long	High (TCC)	10	6	3.6	2.4
				11	8	3.6	3.6
PG-5	D_{max}	Short	Low (CLT)	12	3	3.6	2.4
				13	3	4.5	2.4
				14	6	3.6	3.6
				15	6	5G,3.6	3.6
PG-6	D_{max}	Long	Low	16	6	4.5	3.6
				17	8	3.6	3.6
				18	8	4.5	3.6
				19	8	5G,3.6	3.6
PG-7	D_{min}	Short	Low (CLT)	20	3	3.6	2.4
PG-8	D_{min}	Long	Low (CLT)	21	6	3.6	2.4
				22	8	3.6	3.6

9.5 Model development

Chapter 8 of the dissertation gave a comprehensive and detailed overview of the modelling approaches to simulate the response of dissipative post-tensioned rocking wall systems.

As the numerical models used in the numerical analyses carried out in this chapter were required to be capable of simulating all the behavioural aspects of the response of post-tensioned timber wall, the multi-spring model represented the best approach as discussed in Chapter 8.

Figure 9-5 shows the overview sketches of the different models used in the numerical analysis for (a) single walls, (b) Column-Wall-Colum and (c) coupled walls.

The FEMA P-695 procedure required the numerical models to directly simulate all the significant deterioration modes to the extent possible. The significant mechanisms are summarized below and further discussed in the following sub-section.

1. Compressive failure of the timber at 1% strain
2. Low-cycle fatigue failure of the dissipaters
3. Post-tensioning bars failure at 2% strain

The procedure allows the consideration of non-simulated collapse mechanisms as well, and the non-simulated collapse mechanism considered was a maximum roof drift of 5% as further discussed in Section 9.5.2.

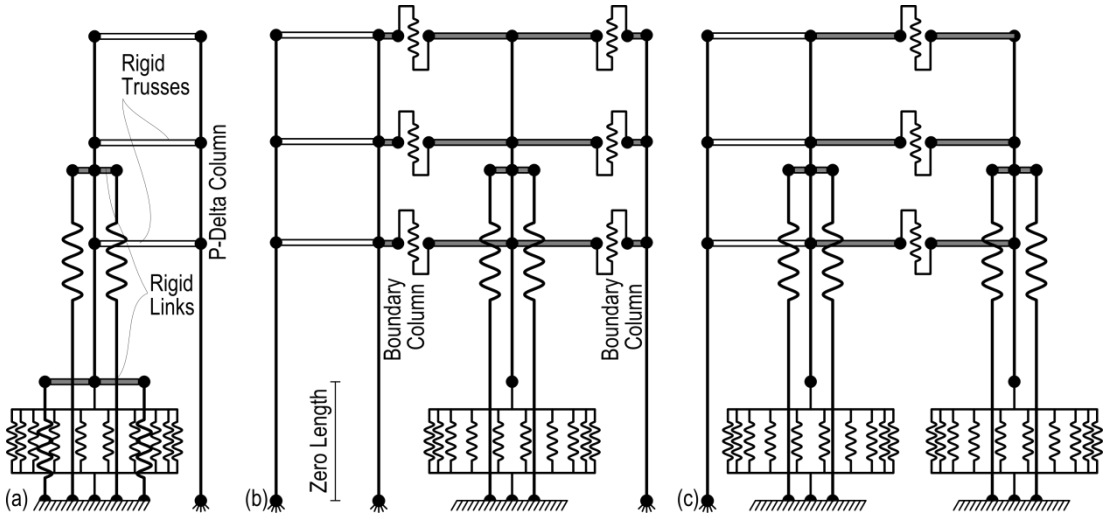

Figure 9-5. Multi-spring models. (a) Single wall; (b) Column-Wall-Colum; (c) coupled walls.

9.5.1 Model calibration accounting for simulated collapse mechanisms

Among the different failure mechanisms listed above, the zero-length springs modelling the tension-compression yield dissipaters and UFPs were calibrated to simulate the low-cycle fatigue failure of the devices.

The low-cycle fatigue model, proposed by Uriz et al. (2008) and implemented in OpenSees (McKenna, 2011), was used to predict low-cycle fatigue failure of the dissipaters tested. This formulation assumes a logarithmic relationship between the number of cycles to failure, N_f, at a constant strain amplitude, ε_i, adopting the Coffin-Manson formula as reported in Equation (9-1):

$$\varepsilon_i = \varepsilon_0 \left(N_f \right)^m \qquad (9\text{-}1)$$

Where ε_i = the strain amplitude which the dissipater undergoes in each cycle i

ε_0 = a material parameter roughly equal to the monotonic failure strain of the material

N_f = the number of cycles to failure

m = an empirical parameter.

The damage accumulation index, DI, is given in equation (9-2) and varies from 0 (undamaged state) to 1 (failure):

$$DI = \sum \frac{n_i}{N_{fi}} = \sum \frac{n_i}{10^{m^{-1}\log(\varepsilon_i/\varepsilon_0)}} \qquad (9\text{-}2)$$

The model proved to be capable of predicting the low-cycle fatigue failure and using m = -0.458 and ε_0 = 0.191 (see Chapter 3).

Experimental material testing on Laminated Veneer Lumber was carried out by van Beerschoten et al. (2013) and a summary of the stress-strain plots of the different specimens tested is shown in Figure 9-6. The experimental results show that a maximum strain limit of 1% can adopted considering the average failure strain value of 1.12% shown in Figure 9-6a (dashed line).

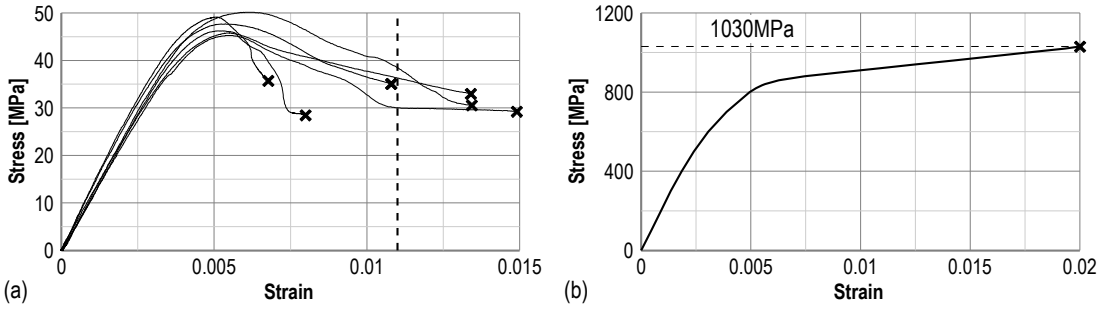

Figure 9-6. (a) LVL material test results (modified from van Beerschoten et al. (2013));(b) Macalloy bars manufacturer's specification (Macalloy, 2007)

A maximum strain in the post-tensioning bars ε_{ptu} = 2% was considered in the model calibration and inferred from the manufacturer's European Technical Approval (Macalloy, 2007). That was taken as the strain corresponding to f_{ptu} = 1030MPa stress in the post-tensioning bar (see Figure 9-6b).

Of the three main failure mechanisms detailed above, the model was considered collapsed only when the maximum strain in either the timber section or the post-tensioning bar was reached. In fact, although the low-cycle fatigue failure mechanism was included in the numerical model, its triggering was not considered directly related to the collapse of the building.

This particular aspect of the system response is due to the design philosophy adopted as discussed in Section 9.3.1. In fact, the total demand is generally carried by two different contributions which are the re-centering and dissipative contributions. In case the dissipaters fail, although strength degradation occurs, the wall still possesses significant capacity as well as stiffness. Nevertheless, the failure of the dissipater may have some influence and eventually trigger a different collapse mechanism since the system has reduced damping capabilities.

9.5.2 Discussion on the maximum lateral drift capacity of the gravity system

Whilst the multi-spring model was used to simulate the post-tensioned rocking wall systems under investigation, the gravity frame system was not explicitly modelled in the analyses. The lateral drift capacity of the gravity timber frame was considered as a non-simulated collapse mechanism.

A parametric analysis was carried out to evaluate the drift capacity of the gravity framing. Since the post-tensioned walls are providing the lateral stability to the building, the gravity frame was modelled with hinged continuous columns and simply supported beams (see Figure 9-7a). In accordance with the archetype buildings geometry, 3, 6 and 8 levels frames were considered, with a story-height of 3.6m and 4.5m. The model was subjected to push-over analysis using a triangular distribution of forces, and the column moment and shear distribution was output from the analysis. As the qualitative internal action distributions in Figure 9-7a show, the column internal actions moment distribution has a maximum moment at the second level, and maximum shear at ground floor. The collapse drift criteria were set as corresponding to either the achievement of the column bending or shear strength.

Figure 9-7b shows the drift capacity resulting from the parametric analysis and shows an inverse proportionality with the column dimension. In accordance with those results a drift limit of 5% was then selected as a non-simulated collapse criterion. Although this value exceeds the drift capacity of shorter building with bigger columns, it is not deemed likely for those buildings to be designed with wider columns.

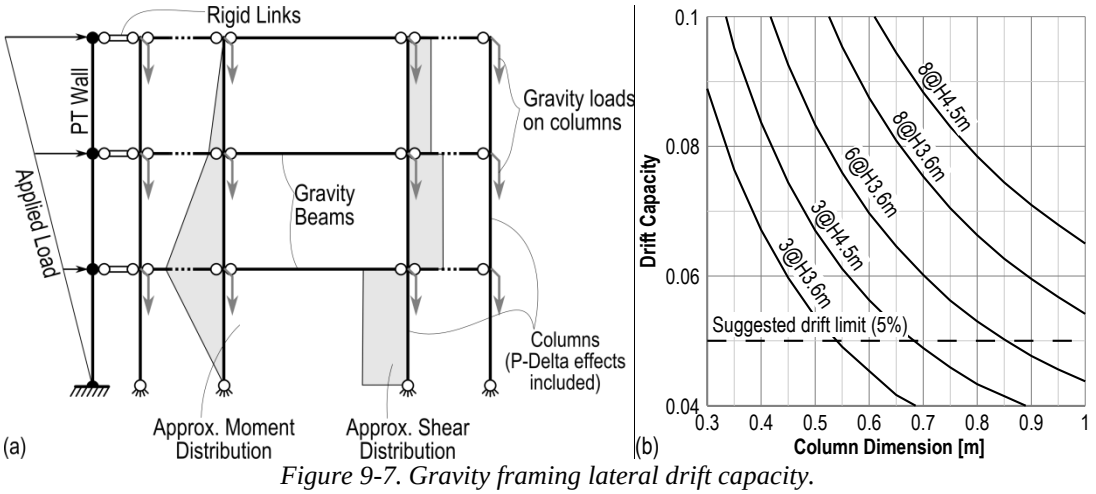

Figure 9-7. Gravity framing lateral drift capacity.

9.5.3 Experimental comparison

Figure 9-8 shows the comparison between experimental and numerical results in terms of force-displacement behaviour.

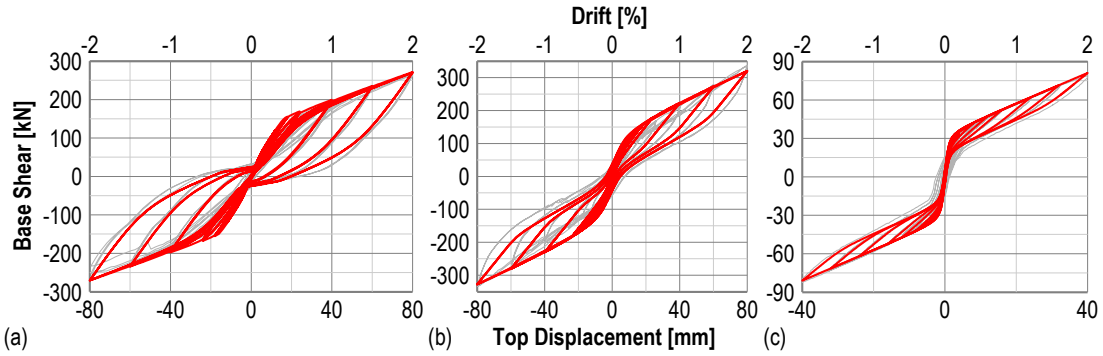

Figure 9-8. Numerical-experimental results comparison. (a) Single wall. (b) Column-Wall-Colum system; (c) Couple walls (experimental data from Iqbal (2011)).

Figure 9-8a,b shows the numerical model comparison of the single wall and Column-Wall-Column systems as also shown in Chapter 8 of the dissertation. As mentioned earlier, Iqbal et al. (2007) performed several tests on coupled wall systems, and experimental data was used to calibrate the model as shown in Figure 9-8c.

The comparison charts of Figure 9-8 show that the models were capable of accurately capturing the systems' response, as also discussed in further detail in Chapter 8 of this dissertation.

9.5.4 Damping model

A tangent stiffness proportional Rayleigh damping model was used in the analyses, and as shown in past research on the dynamic behaviour of post-tensioned timber systems (Marriott, 2009; Smith, 2014), a critical damping of 3% was used for the systems under study.

The calibrated damping model assigned critical damping values to either the first and third for 3-and 6-story buildings or the first and the fourth mode for 8-story buildings. Based on modal analysis results most of the participating modal mass (i.e. approximately 95% or more) was within the first four modes of the structure; therefore, it was considered an acceptable assumption to have some over-damping in the higher modes (5th and higher).

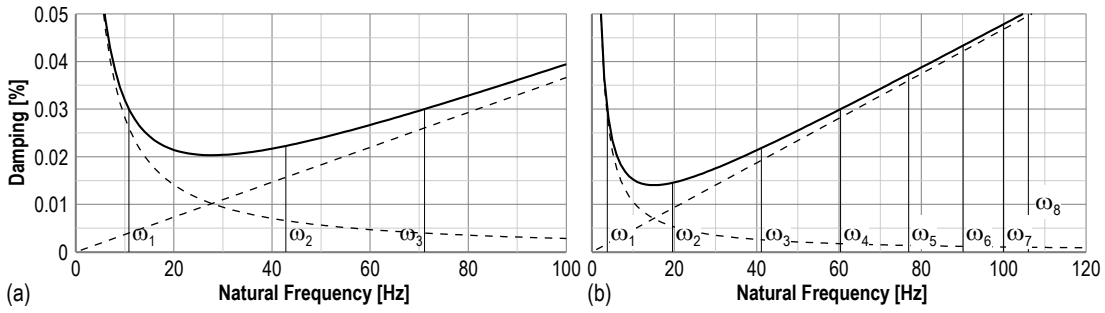

Figure 9-9. Rayleigh damping model calibration. (a) 3-story and (b) 8-story buildings.

9.6 Non-linear quasi-static analysis

The pushover analyses were carried out adopting the lateral force distribution in accordance with ASCE/SEI 7-10 and summarized below.

$$F_i = C_{vi} V \tag{9-3}$$

$$C_{vi} = \frac{W_i h_i^k}{\sum_{j=1}^{n} W_j h_j^k} \tag{9-4}$$

Where F_i = applied force at i-th storey

C_{vi} = vertical distribution factor

V = design base shear

W_i = storey weight

h_i = storey height

k = exponent related to the structure period as follows:

for structures having a period of 0.5s or less, k = 1

for structures having a period of 2.5s or more, k = 2

for structures having a period between 0.5s and 2.5s k shall be 2 or shall be determined by linear interpolation

Quasi-static pushover curves for each archetype provide information on the over-strength factors and the ductility of the system. In particular, the over-strength factor was defined in the Methodology as:

$$\Omega = \frac{V_{max}}{V} \tag{9-5}$$

Where V_{max} = the maximum base shear capacity

The period-based ductility of a given index archetype model is defined as:

$$\mu_T = \frac{\delta_u}{\delta_{y,eff}} \tag{9-6}$$

Where δ_u = the ultimate roof drift displacement

$\delta_{y,eff}$ = the effective yield roof drift displacement.

The ultimate displacement was taken at the abscissa corresponding to a strength degradation of 20% or more (ATC, 2009), or when either of the collapse mechanisms listed in paragraph 9.5 occurred.

Figure 9-10 reports the pushover curves for the Archetype 1 with the three lateral resisting systems (respectively single wall, Column-Wall-Colum and coupled walls). The main difference in the systems behaviour was the degradation occurring due to the dissipaters' failure which was triggering the strength loss. The phenomenon did not occur when using U-shape Flexural Plates, which had a very high failure displacement. This allowed a more redundant system.

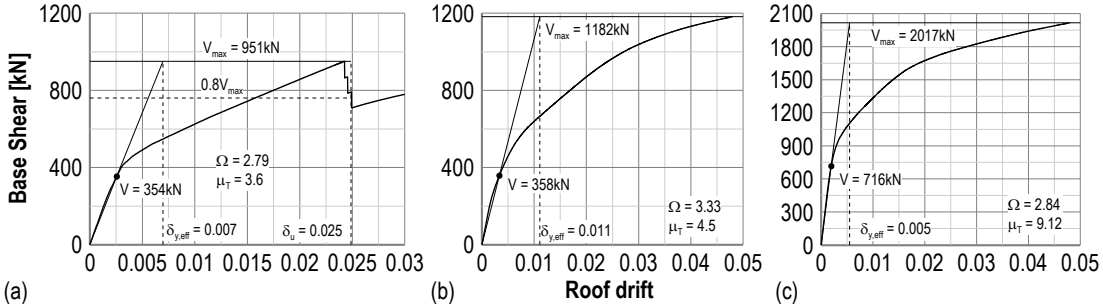

Figure 9-10. Static push-over analysis results (Index Archetype 1). (a) Single wall. (b) Column-Wall-Column. (c) Coupled walls.

9.7 Dynamic analyses

Dynamic analyses were performed using the Incremental Dynamic Analysis (IDA) concept, in which the individual ground motions are scaled to increasing intensities until the structure collapses (Vamvatsikos *et al.*, 2002).

Dynamic analyses were carried out using a set of 22 earthquake records (2 components each). The record set included strong-motion records from all large-magnitude (M > 6.5) events in the Pacific Earthquake Engineering Research Center (PEER) Next-Generation Attenuation (NGA) database (Chiou *et al.*, 2008). Large-magnitude events dominate collapse risk and generally have longer durations of shaking. The set included records from soft rock and stiff soil sites (predominantly Site Class C and D conditions), and from shallow crustal sources (predominantly strike-slip and thrust mechanisms).

The scaling of the records in accordance with the FEMA P-695 procedure (ATC, 2009) involved two steps. To remove variability between records due to inherent differences in magnitude, distance to source, source type and site conditions, the records were "normalized" by their respective peak ground velocities. The records were then scaled to match the spectral acceleration to the MCE spectral acceleration at the fundamental period.

Table 9-2 gives the summary of the record set as well as the normalization factors.

Table 9-2. List of selected recrods from PEER NGA Database and normalization factors (ATC, 2009)

	Earthquake				Site data		Normal.	Normalized motions	
ID	**M**	**Year**	**Name**	**Station**	**PGA_{max} (g)**	**PGV_{max} (cm/s)**	**Factors**	**PGA_{max} (g)**	**PGV_{max} (cm/s)**
1	6.7	1994	Northridge	Beverly Hill – Mulhol	0.52	63	0.65	0.34	41
2	6.7	1994	Northridge	Canyon Country – WLC	0.48	45	0.83	0.4	38
3	7.1	1999	Duzce, Turkey	Bolu	0.82	62	0.63	0.52	39
4	7.1	1999	Hector Mine	Hector	0.34	42	1.09	0.37	46
5	6.5	1979	Imperial Valley	Delta	0.35	33	1.31	0.46	43
6	6.5	1979	Imperial Valley	El Centro Arrya #11	0.38	42	1.01	0.39	43
7	6.9	1995	Kobe, Japan	Nishi-Akashi	0.51	37	1.03	0.53	39
8	6.9	1995	Kobe, Japan	Shin-Osaka	0.24	38	1.10	0.26	42
9	7.5	1999	Kocaeli, Turkey	Duzce	0.36	59	0.69	0.25	41
10	7.5	1999	Kocaeli, Turkey	Arcelik	0.22	40	1.36	0.3	54
11	7.3	1992	Landers	Yermo Fire Station	0.24	52	0.99	0.24	51
12	7.3	1992	Landers	Collwater	0.42	42	1.15	0.48	49
13	6.9	1989	Loma Prieta	Capitola	0.53	35	1.09	0.58	38
14	6.9	1989	Loma Prieta	Gilroy Array #3	0.56	45	0.88	0.49	39
15	7.4	1990	Manjil, Iran	Abbar	0.51	54	0.79	0.4	43
16	6.5	1987	Superstition Hills	El Centro Imp. Co.	0.36	46	0.87	0.31	40
17	6.5	1987	Superstition Hills	Poe Road (temp)	0.45	36	1.17	0.53	42
18	7.0	1992	Cape Mendocino	Rio Dell Overpass	0.55	44	0.82	0.45	36
19	7.6	1999	Chi-Chi, Taiwan	CHY101	0.44	115	0.41	0.18	47
20	7.6	1999	Chi-Chi, Taiwan	TCU045	0.51	39	0.96	0.49	38
21	6.6	1971	San Fernando	LA - Hollywood Stor	0.21	19	2.10	0.44	40
22	6.5	1976	Friuli, Italy	Tolmezzo	0.35	31	1.44	0.5	44

The records were normalized with respect of the value of the peak ground velocity computed in the PEER NGA database (PGV_{PEER}), which is the geometric mean of PGV of the two horizontal components considering different record orientations.

The following formulas define the normalization factors:

$$NM_i = Median\left(PGV_{PEER}\right) / PGV_{PEER,i} \tag{9-7}$$

$$NTH_{1,i} = NM_i \times TH_{1,i} \tag{9-8}$$

$$NTH_{2,i} = NM_i \times TH_{2,i} \tag{9-9}$$

Where NM_i = normalization factor of both horizontal component of the i-th record

$PGV_{PEER,i}$ = the peak ground velocity of the i-th record

$NTH_{1,i}$ = the normalized i-th record, horizontal component 1

$NTH_{2,i}$ = the normalized i-th record, horizontal component 2

$TH_{1,i}$ = the record i, horizontal component 1

$TH_{2,i}$ = the record i, horizontal component 2

For the determination of the seismic performance factors in accordance with the FEMA P-695 procedure the aim of the analysis was the evaluation of the median collapse intensity of

each archetype building; therefore, the scaling method of ASCE 7-10 applies, with the notable exception that the median value of the scaled record set needed only match the MCE demand at the fundamental period, T, rather than over the range of periods required by ASCE/SEI 7-10 (2010)(ATC, 2009).

Non-linear Time History analyses were carried out with the main objective of characterizing the behaviour of each archetype building in terms of Collapse Margin Ratio, CMR. The CMR was defined as the ratio between the median collapse spectral acceleration, S_{CT}, and the MCE intensity as reported in Equation (9-10).

$$CMR = \frac{S_{CT}}{S_{MT}} \tag{9-10}$$

The system behaviour can be significantly influenced by the spectral shape of the ground motion record set, and to account for this aspect the collapse margin ratio was modified using a Spectral Shape Factor, SSF.

$$ACMR = SSF \cdot CMR \tag{9-11}$$

The Spectral Shape Factor depends on the Seismic Design Category of the structure as well as its fundamental period and period-based ductility. The spectral shape factor values for the seismic design category D_{max} are listed in Table 9-3.

Table 9-3. Spectral shape factor values for SDC D_{max}

T	**Period-based ductility, μ_T**							
	1	*1.1*	*1.5*	*2*	*3*	*4*	*6*	*≥8*
≤0.5	1	1.02	1.04	1.06	1.08	1.09	1.12	1.14
0.6	1	1.02	1.05	1.07	1.09	1.11	1.13	1.16
0.7	1	1.03	1.06	1.08	1.1	1.12	1.15	1.18
0.8	1	1.03	1.06	1.08	1.11	1.14	1.17	1.2
0.9	1	1.03	1.07	1.09	1.13	1.15	1.19	1.22
1	1	1.04	1.08	1.1	1.14	1.17	1.21	1.25
1.1	1	1.04	1.08	1.11	1.15	1.18	1.23	1.27
1.2	1	1.04	1.09	1.12	1.17	1.2	1.25	1.3
1.3	1	1.05	1.1	1.13	1.18	1.22	1.27	1.32
1.4	1	1.05	1.1	1.14	1.19	1.23	1.3	1.35
≥1.5	1	1.05	1.11	1.15	1.21	1.25	1.32	1.37

The parameters determining the CMR can be visualized in Figure 9-11(a) in terms of spectral acceleration and the maximum drift. Each plot connects the result of the same ground motion record for increasing intensities.

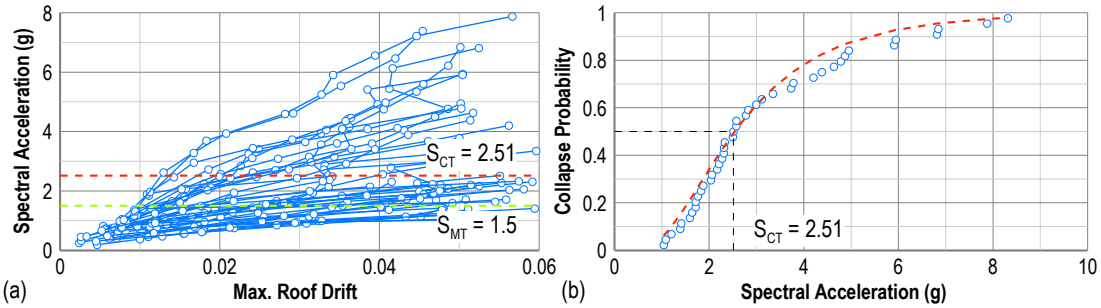

Figure 9-11. Incremental dynamic Analysis results (Index Archetype 1).

The data from IDA analysis can be used for the definition of the index archetype fragility curve in Figure 9-11b. The curve was defined as a cumulative distribution function of the collapse spectral acceleration, and it was fitted with a lognormal function. The slope of the lognormal fitting corresponded to the record-to-record uncertainty value (ATC, 2009).

The collapse spectral acceleration for each ground motion record was assessed considering the simulated and non-simulated collapse mechanisms as stated in paragraph 9.5.

Non-linear time-history analyses were carried out using a set of far-field records from the NGA strong motion database (Chiou *et al.*, 2008). Further details of the record set as well as the scaling methodology can be found in Chapter 9.

9.8 Performance evaluation

9.8.1 System uncertainties

Several sources of uncertainty must be considered for determining the total system collapse uncertainty.

The record-to-record uncertainty, β_{RTR}, is due to variability in the response of the index archetypes to different ground motion records. Variability in response is the result of the combined effects of: (a) variation in frequency content and dynamic characteristics of the various records; and (b) variability in the hazard characterization. A maximum value of 0.40 was assumed, yet for systems that have little or no period elongation that value can be significantly less (ATC, 2009). The value of the record-to-record uncertainty was defined as:

$$0.20 \le \beta_{RTR} = 0.1 + 0.1\mu_T \le 0.40 \qquad (9\text{-}12)$$

Where μ_T = period-based ductility

The design requirements uncertainty, β_{DR}, is related to the completeness and robustness of the design requirements, and the extent to which they provide safeguards against unanticipated failure modes.

The test data uncertainty, β_{TD}, is related to the completeness and robustness of the test data used to define the system.

The modelling uncertainty, β_{MDL}, is related to how well the index archetype models represent the full range of structural response characteristics of the archetype buildings, and how well the analysis models capture structural collapse behaviour through direct simulation or non-simulated component checks (ATC, 2009).

Table 9-4 gives an overview of the quality rating of the design requirements, test data, and modelling. The quantitative values of the different uncertainties were defined as: (A) Superior $\beta = 0.10$; (B) Good $\beta = 0.20$: (C) Fair $\beta = 0.35$: and (D) Poor = $\beta = 0.50$.

Once the different uncertainties sources had been defined, the total system uncertainty was evaluated as reported in Equation (9-13).

$$\beta_{TOT} = \sqrt{\beta_{RTR}^2 + \beta_{DR}^2 + \beta_{TD}^2 + \beta_{MDL}^2} \qquad (9\text{-}13)$$

Where β_{DR} = the design requirements
β_{TD} = test data uncertainty
β_{MDL} = archetype models uncertainty
β_{RTR} = record-to-record uncertainty

For the systems under consideration two assumptions on the total uncertainty were considered. Firstly, a conservative "Fair" system quality rating was chosen (i.e. $\beta_{TOT} = 0.35$). This represents the lower bound value for the performance evaluation of the system.

Another total uncertainty value was also proposed based on the proposed quality rating of the system. The following uncertainties values were proposed:

1. $\beta_{RTR} = 0.40$
2. $\beta_{DR} = 0.20$
3. $\beta_{TD} = 0.35$
4. $\beta_{MDL} = 0.20$

Those values are giving a total uncertainty $\beta_{TOT} = 0.60$.

Table 9-4. Quality rating (modified from ATC (2009)

	Completeness and robustness			**Confidence in basis of design requirements, test results or modelling**		
	Design Requirements	*Test Data*	*Modelling*	*High*	*Medium*	*Low*
High	High. Extensive safeguards against unanticipated failure modes. All important design and quality assurance issues are addressed.	Material, component, connection, assembly, and system behaviour well understood and accounted for. All, or nearly all, important testing issues addressed.	Index models capture the full range of the archetype design space and structural behavioural effects that contribute to collapse.	(A) Superior $\beta = 0.10$	(B) Good $\beta = 0.20$	(C) Fair $\beta = 0.35$
Medium	Medium. Reasonable safeguards against unanticipated failure modes. Most of the important design and quality assurance issues are addressed.	Material, component, connection, assembly, and system behaviour generally understood and accounted for. Most important testing issues addressed.	Index models are generally comprehensive and representative of the design space and behavioural effects that contribute to collapse.	(B) Good $\beta = 0.20$	(C) Fair $\beta = 0.35$	(D) Poor $\beta = 0.50$
Low	Questionable safeguards against unanticipated failure modes. Many important design and quality assurance issues are not addressed.	Material, component, connection, assembly, and system behaviour fairly understood and accounted for. Several important testing issues not addressed.	Significant aspects of the design space and/or collapse behaviour are not captured in the index models.	(C) Fair $\beta = 0.35$	(D) Poor $\beta = 0.50$	-

9.8.2 Evaluation of the seismic performance factors

The seismic performance of the system was defined in terms of response modification factor, R, deflection amplitude factor, C_d, and system over-strength factor, Ω_0.

The trial response modification factor was guessed in the archetype design phase on the basis of R values suggested in ASCE/SEI 7-10 for timber lateral resisting systems. Based on the total system uncertainty values, the acceptable values of the Adjusted Collapse Margin Ratio were taken as 10% and 20% acceptable collapse probability. The trial R-factor assumed in the archetype design phase was confirmed whether the Adjusted Collapse Margin Ratio values satisfy the following conditions:

- The collapse probability for each performance group shall not exceed 10%. This condition was satisfied when the average ACMR value across the performance group was greater or equal to the acceptable value at 10%, $ACMR_{10\%}$.

$$\overline{ACMR} \geq ACMR_{10\%}$$

- The collapse probability for each index archetype building shall not exceed 20%; therefore, the ACMR value for each archetype shall be greater or equal to $ACMR_{20\%}$.

For most of the index archetypes the acceptable values at 10% and 20% probability of collapse were (see Table 9-5):

- "Fair" rating: $ACMR_{10\%} = 2.53$, $ACMR_{20\%} = 1.84$
- Proposed rating: $ACMR_{10\%} = 2.16$, $ACMR_{20\%} = 1.66$

Table 9-5. Acceptable values of ACMR (modified from ATC (2009)

Total system collapse uncertainty	**Collapse probability**				
	5%	***10% ($ACMR_{10\%}$)***	***15%***	***20% ($ACMR_{20\%}$)***	***25%***
⋮	⋮	⋮	⋮	⋮	⋮
0.35	1.78	1.57	1.44	1.34	1.27
0.375	1.85	1.62	1.48	1.37	1.29
0.4	1.93	1.67	1.51	1.4	1.31
0.425	2.01	1.72	1.55	1.43	1.33
0.45	2.1	1.78	1.59	1.46	1.35
0.475	2.18	1.84	1.64	1.49	1.38
0.5	2.28	1.9	1.68	1.52	1.4
0.525	2.37	1.96	1.72	1.56	1.42
0.55	2.47	2.02	1.77	1.59	1.45
0.575	2.57	2.09	1.81	1.62	1.47
0.6	2.68	2.16	1.86	1.66	1.5
⋮	⋮	⋮	⋮	⋮	⋮
0.95	4.77	3.38	2.68	2.22	1.9

The Methodology required the system over-strength factor, Ω_0, to be less than the largest average value of the calculated over-strength for each performance group, Ω. The system over-strength factor should be conservatively increased to account for variation in over-strength results of individual index archetypes, and judgmentally rounded to half unit intervals (e.g., 1.5, 2.0, 2.5, and 3.0) (ATC, 2009).

The deflection amplification factor, C_d, was evaluated as:

$$C_d = \frac{R}{B_I} \qquad (9\text{-}14)$$

Where B_I = numerical coefficient from ASCE/SEI 7-10 (2010) depending on the critical damping of the system and the fundamental period.

Table 9-6 reports the quasi-static and dynamic analyses results for the archetype buildings compared to the acceptable values for every lateral resisting system considered.

Table 9-6. Summary of the performance evaluation

	Group No.	ID	*Over-strength factor* Ω	*System over-strength factor* Ω_0	*Collapse Margin Ratio* CMR	*Adjusted Collapse Margin Ratio* ACMR	*Avg. Adjusted Collapse Margin Ratio* ACMR	*"Fair" rating* Check	*Proposed rating* Check
Single wall system	PG-1	1	2.54	2.61	1.67	2.19	2.55	pass	pass
		2	2.66		1.99	2.45		pass	pass
		3	2.62		2.20	2.74		pass	pass
		4	2.64		2.23	2.83		pass	pass
	PG-2	5	2.50	2.65	2.42	3.02	3.04	pass	pass
		6	2.64		2.19	2.77		pass	pass
		7	2.67		2.62	3.45		pass	pass
		8	2.79		2.29	2.91		pass	pass
	PG-3	9	2.41	2.41	2.73	2.96	2.96	pass	pass
	PG-4	10	2.66	2.77	5.05	4.73	5.20	pass	pass
		11	2.87		4.78	5.67		pass	pass
	PG-5	12	2.61	2.57	1.77	2.35	2.53	pass	pass
		13	2.40		1.86	2.22		pass	pass
		14	2.65		2.12	2.65		pass	pass
		15	2.61		2.33	2.91		pass	pass
	PG-6	16	2.55	2.62	2.27	2.93	3.18	pass	pass
		17	2.60		2.40	3.08		pass	pass
		18	2.61		2.70	3.59		pass	pass
		19	2.72		2.39	3.11		pass	pass
	PG-7	20	2.57	2.57	3.17	3.61	3.61	pass	pass
	PG-8	21	2.64	2.76	4.79	5.34	5.71	pass	pass
		22	2.88		5.02	6.09		pass	pass
Column-Wall-Colum system	PG-1	1	2.92	3.01	2.10	2.74	3.19	pass	pass
		2	3.33		2.41	2.98		pass	pass
		3	2.86		2.53	3.38		pass	pass
		4	2.91		2.75	3.66		pass	pass
	PG-2	5	2.74	3.05	2.70	3.57	3.98	pass	pass
		6	3.20		3.04	4.03		pass	pass
		7	2.98		3.19	4.30		pass	pass
		8	3.30		2.93	4.01		pass	pass
	PG-3	9	2.81	2.81	3.34	3.80	3.80	pass	pass
	PG-4	10	2.69	2.92	5.79	6.77	7.34	pass	pass
		11	3.15		6.50	7.91		pass	pass
	PG-5	12	2.61	2.76	2.00	2.57	3.19	pass	pass
		13	2.71		2.41	3.14		pass	pass
		14	2.84		2.51	3.37		pass	pass
		15	2.89		2.75	3.67		pass	pass
	PG-6	16	3.63	3.13	2.70	3.49	4.00	pass	pass
		17	3.14		3.04	4.17		pass	pass
		18	3.11		3.18	4.32		pass	pass
		19	2.63		2.81	4.02		pass	pass
	PG-7	20	3.06	3.06	3.62	4.13	4.13	pass	pass
	PG-8	21	2.36	2.89	5.79	6.87	6.93	pass	pass
		22	3.42		5.86	7.00		pass	pass
Coupled Walls system	PG-1	1	3.32	3.13	2.16	2.77	3.27	pass	pass
		2	2.84		2.48	3.19		pass	pass
		3	3.15		2.53	3.34		pass	pass
		4	3.20		2.82	3.76		pass	pass
	PG-2	5	3.13	3.19	2.70	3.67	4.04	pass	pass
		6	3.18		2.89	3.95		pass	pass
		7	3.12		3.19	4.46		pass	pass
		8	3.33		2.98	4.10		pass	pass
	PG-3	9	3.58	3.58	3.64	4.09	4.09	pass	pass
	PG-4	10	3.26	3.61	5.95	6.90	6.95	pass	pass

Group No.	ID	*Over-strength factor* **Ω**	*System over-strength factor* **Ω_0**	*Collapse Margin Ratio* **CMR**	*Adjusted Collapse Margin Ratio* **ACMR**	*Avg. Adjusted Collapse Margin Ratio* **ACMR**	*"Fair" rating* **Check**	*Proposed rating* **Check**
	11	3.95		5.86	7.00		pass	pass
PG-5	12	3.55	3.50	2.16	2.77	3.32	pass	pass
	13	3.09		2.47	3.18		pass	pass
	14	3.69		2.71	3.58		pass	pass
	15	3.66		2.82	3.76		pass	pass
PG-6	16	3.06	3.16	2.84	3.86	4.08	pass	pass
	17	3.07		2.76	3.78		pass	pass
	18	3.24		3.27	4.57		pass	pass
	19	3.28		2.98	4.10		pass	pass
PG-7	20	3.37	3.37	3.86	4.33	4.33	pass	pass
PG-8	21	3.21	3.41	5.79	6.71	6.86	pass	pass
	22	3.61		5.86	7.00		pass	pass

In general, higher over-strength factor values were observed for the coupled walls and Column-Wall-Colum systems. As anticipated, this was mainly due to the use of a different type of dissipater when compared to a single wall solution. In fact, tension-compression dissipaters fail at approximately 13% strain resulting in strength degradation; instead, UFPs have a high ultimate displacement. This resulted in no strength degradation in the pushover curve, bringing to higher values of the over-strength factor.

Among the different collapse modes simulated in the model the most commonly occurring mechanism was the exceedance of maximum drift capacity of the gravity frame. This highlighted the high robustness of the lateral load resisting system.

The results of Table 9-6 show that all the archetype buildings satisfied the minimum requirements of the acceptable adjusted collapse margin ratio of the more conservative "Fair" rating. The resulting CMR values from numerical analyses were lowest the performance groups PG-1 (i.e. the stiffest buildings).

Finally, based on the numerical results discussed above, the trial seismic modification factor was confirmed to be R = 7.

To determine the deflection amplification factor, a critical damping of 3% was assumed and based on previous research by Marriott (2009) and Smith (2014); therefore, according to Equation (9-14), a deflection amplification factor $C_d = 7.5$ was proposed.

According to quasi static results, the system over-strength factor to be adopted in design is $\Omega_0 = 3.5$.

9.9 Extension of numerical results to relevant standards

The result of the extensive numerical study presented in the previous sections in accordance with the FEMA P-695 procedure are further discussed in this section and extended to other significant standards such as EN 1998-1 (2004) or NZS 1170.5 (2004).

The major difference in terms of seismic design methodology is in the definition of the design point. As shown in Figure 9-12 seismic design in accordance with ASCE 7-10 (2010) requires that the ductile seismic resisting system is designed elastically for the reduced forces at yielding point. On the other hand, the design point of the lateral resisting system in accordance NZS 1170.5 (2004) or EN 1998-1 (2004) is designed to fulfil some ductility and the equivalent elastic-perfectly plastic approximation is secant to the ULS demand rather than the yield point.

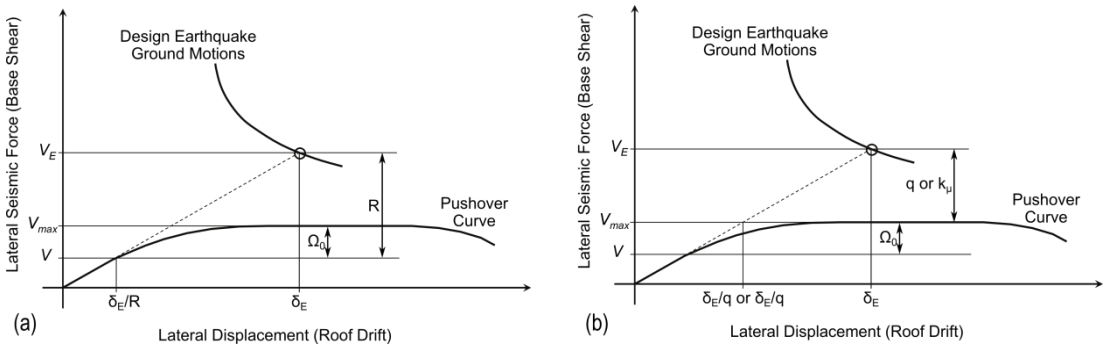

Figure 9-12. Definition of the seismic reduction factors in accordance with (a) ASCE 7-10 and (b) EC8 or NZS1170.5.

Therefore, the seismic reduction factor, R, determined in the numerical study can be modified to account for this different design approach giving either the suggested behaviour factor (EC8), q, or the inelastic spectrum scaling factor (NZS 1170.5), k_μ, as defined by Equation (9-15):

$$q, k_\mu = \frac{R}{\Omega_0} = \frac{7.0}{3.5} = 2.0 \qquad (9\text{-}15)$$

This estimated reduction factor based on the FEMA P-695 procedure and the assumption considered above can be verified and checked through an Acceleration-Displacement Response Spectrum (ADRS) method (Chopra *et al.*, 1999) for the different systems using the ULS spectrum.

For brevity, the charts of Figure 9-13 show the ADRS curves of the three systems investigated for the archetypes 1, 3 and 6. Those buildings were 3, 6 and 8 storey tall and had a storey height of 3.6m.

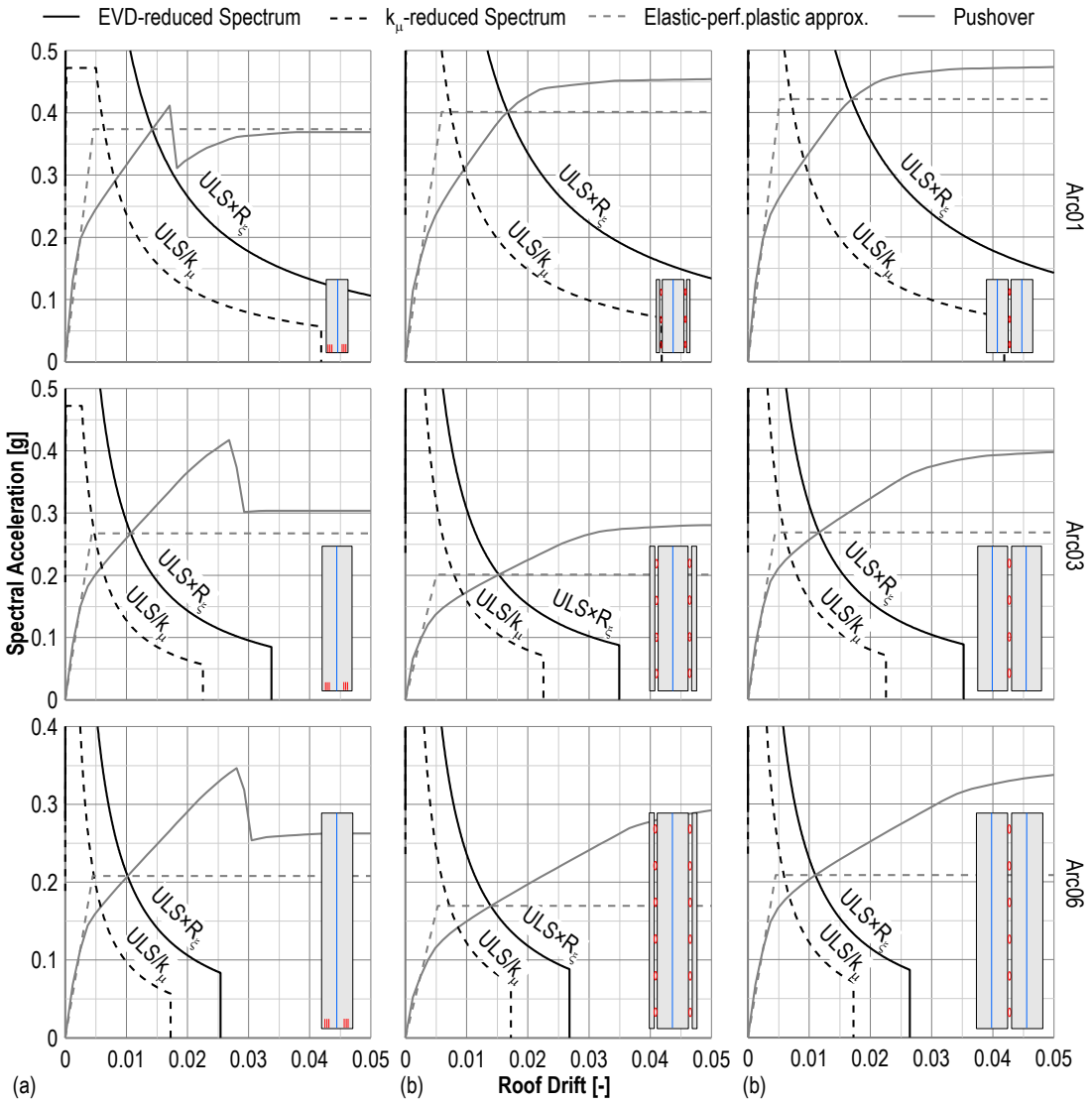

Figure 9-13. ADRS curves for the different wall systems (a) Single wall; (b) Column-Wall-Colum; (c) Coupled walls.

The DBE spectrum was reduced by the hysteretic viscous damping (solid line) and intersected with the pushover curve to give the design point in terms of spectral acceleration and top displacement. The charts also show the DBE spectrum reduced by the seismic reduction factor of Equation (9-15) (dashed line).

The charts shown in Figure 9-13 confirmed that the seismic reduction factor of 2.0 was suitable for the systems analysed and represented a conservative assumption in all the considered cases.

9.10 Considerations on the estimation of the period of vibration

Another key point in the force-based design of a multi-storey building is the estimation of the natural period of vibration.

Seismic design standards have several definitions for such period based on the type of lateral load resisting system. In this chapter the evaluation of the natural period in accordance with ASCE 7-10 (ASCE/SEI) was used and this section compares and discusses the results also in accordance with different standards.

In general, the period estimation in accordance with seismic design standards can be performed using either the empirical method or the Rayleigh method. In both cases the period of vibration is generally underestimated.

Usually the empirical formulas (Equations (9-16) and (9-17)) are calibrated for steel or concrete structures, and the period in the archetype design in Section 9.3.1 was estimated using "other structures" equations.

$$T = C_u C_t h_n^x \qquad \text{(ASCE/SEI, 2010)} \qquad (9\text{-}16)$$

$$T = 1.25 k_t h_n^{0.75} \qquad \text{(Standards New Zealand, 2004)} \qquad (9\text{-}17)$$

Where C_u = Coefficient for Upper Limit on Calculated Period

C_t, x = coefficients determined in accordance with Table 12.8-2 (ASCE/SEI, 2010)

k_t = coefficient determined in accordance with Clause C4.1.2.2 (Standards New Zealand, 2004)

h_n = height from the base of the structure to the uppermost seismic mass

From a comparison of the numerical results this assumption was deemed over-conservative and different coefficients were used. In particular, among the coefficients reported in the standards, those showing a better fit to the numerical results were the ones for moment-resisting concrete frame structures.

Figure 9-14a shows that the moment-resisting concrete frames empirical formulas provide a good estimation of the period of the structure up to 1.5s, while for higher periods the values were still under-estimated. The suggested values for the estimation of the natural period using empirical methods are summarized in Equations (9-18) and (9-19).

$$T = C_u 0.0466 h_n^{0.9} \qquad \text{(ASCE/SEI, 2010)} \qquad (9\text{-}18)$$

$$T = 1.25 \cdot 0.075 h_n^{0.75}$$ (Standards New Zealand, 2004) *(9-19)*

The Rayleigh method provided a better and more reliable estimation of the natural period, yet a modification shall be applied. The elastic stiffness of a seismic resisting system shall be defined as yield-secant stiffness rather than initial. Adopting the initial flexural stiffness would again result in an under-estimation of the natural period of vibration of the structure.

Unlike concrete structures, the yield point of a post-tensioned rocking system is not of easy evaluation from a preliminary design point of view; therefore, it is suggested to evaluate the period considering the stiffness at decompression point and apply a magnification factor of 1.4 which was proposed in this section based on numerical results.

$$T_1 = 1.4 \cdot 2\pi \sqrt{\frac{\sum_{i=1}^{n} W_i d_i^2}{g \sum_{i=1}^{n} F_i d_i}}$$ *(9-20)*

Where d_i = the horizontal displacement of the centre of mass at level *i*, ignoring the effects of torsion

F_i = the displacing force acting at level *i*

i = the level under consideration of structure

n = number of levels in a structure

W_i = the seismic weight at level *i*

The chart in Figure 9-14b reports the comparison of the numerical values against the value evaluated from Equations (9-18) to (9-20).

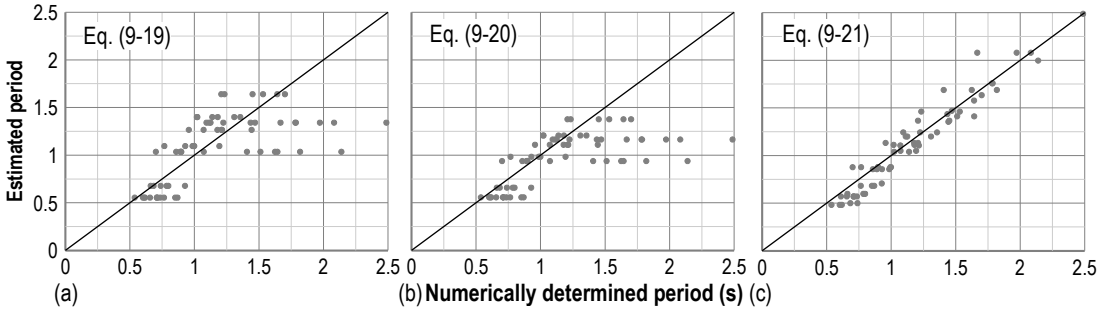

Figure 9-14. Natural period of vibration estimation methods. (a-b) Empirical methods; (c) modified Rayleigh method.

9.11 Conclusion

The chapter showed the application of the FEMA P-695 procedure (ATC, 2009) to determine the seismic performance factors of post-tensioned timber wall systems to be used in ASCE/SEI 7-10 (2010).

Several archetype buildings were taken into account considering several parameters significant to design, such as the seismic resisting system, the building and storey height, the wall depth, the gravity loads magnitude and the seismic design category.

The archetypes were simulated using non-linear models accounting for the full range of behavioural aspects of the system. The drift capacity of the gravity system was also included as a non-simulated collapse mechanism.

Both non-linear static and dynamic analysis were performed to determine the performance factor of the system consisting of the system's ductility, over-strength factor and collapse margin ratio.

The adjusted collapse margin ratio resulting from the dynamic analyses proved to be within the acceptable values and confirmed the trial value of the response modification factor; therefore, the seismic performance factors resulting from the extensive numerical analyses shown in the chapter are summarize below.

- Response modification factor, R = 7.0
- Deflection amplification factor, C_d = 7.5
- System over-strength factor, Ω_0 = 3.5

The seismic performance factors above were determined with the procedure to be applied in accordance with ASCE 7-10 (2010). When different design codes are used a modification of the response modification factor was proposed to work out the behaviour factor, q (EN 1998-1 (2004)), or the inelastic spectrum modification factor, k_μ (NZS 1170.5 (2004)). Based on a different definition of such factors the values proposed was:

$$q, k_\mu = 2.0$$

In accordance with NZS1170.5 (Standards New Zealand, 2004) or EC8 (European Committee for Standardization, 2004) and assuming an equivalent displacement rule, the elastic deflection shall be multiplied by the seismic reduction factor.

In the final part of the chapter some discussion on the estimation of the natural period of vibration was provided. Design codes usually consider traditional concrete or steel structures and the general case coefficients generally significantly under-estimate the first mode period of the structure. Based on numerical results the most suitable coefficients for the evaluation of the natural period of the structure are the ones related to concrete frame structures, as summarized below for different standards.

ASCE 7-10: $T = C_u 0.0466 h_n^{0.9}$

NZS 1170.5: $T = 1.25 \cdot 0.075 h_n^{0.75}$

Finally when considering the Rayleigh method an amplification factor of 1.4 was suggested to account for the reduced stiffness occurring after the rocking element decompressed.

$$T_1 = 1.4 \cdot 2\pi \sqrt{\frac{\sum_{i=1}^{n} W_i d_i^2}{g \sum_{i=1}^{n} F_i d_i}}$$

9.12 References

American Society of Civil Engineers and S. E. Institute. 2010. *Minimum design loads for buildings and other structures*. American Society of Civil Engineers and S. E. Institute. Reston, (VA), American Society of Civil Engineers, Structural Engineering Institute.

Applied Technology Council for the Federal Emergency Management Agency (ATC). 2009. *Quantification of building seismic performance factors*. Applied Technology Council for the Federal Emergency Management Agency (ATC). Washington, D.C., Washington, D.C. : U.S. Dept. of Homeland Security, FEMA.

Baird, A., Smith, T., Palermo, A., Pampanin, S. 2014. Experimental and Numerical Study of U-Shaped Flexural Plate (UFP) Dissipators. *New Zealand Society for Earthquake Engineering Annual Conference*, Auckland, New Zealand.

Chiou, B., Darragh, R., Gregor, N., Silva, W. 2008. NGA project strong-motion database. *Earthquake Spectra* 24(1): 23-44.

Chopra, A.K., Goel, R.K. 1999. Capacity-Demand-Diagram Methods Based on Inelastic Design Spectrum. *Earthquake Spectra* 15(4): 637-656.

Eurocode 8 - Design of structures for earthquake resistance - Part 1: General rules, seismic actions and rules for buildings. European Committee for Standardization. 2004. Brussels, Belgium, European Committee for Standardization.

Federal Emergency Management Agency. 2004. *NEHRP Recommended Provisions for Seismic Regulations for New Buildings and Other Structures*. Federal Emergency Management Agency. Washington, DC.

Iqbal, A., Pampanin, S., Buchanan, A.H., Palermo, A. 2007. Improved Seismic Performance of LVL Post-tensioned Walls Coupled with UFP devices. *8th Pacific Conference on Earthquake Engineering*, Singapore.

Iqbal, M.A. 2011. Seismic response and design of subassemblies for multi-storey prestressed timber buildings *PhD Dissertation*, University of Canterbury, Christchurch, New Zealand.

Kelly, J.M., Skinner, R.I., Heine, A.J. 1974. Mechanism of Energy Absorption in Special Devices for Use in Earthquake Resistant Structures. *Bulletin of the New Zealand Society of Earthquake Engineering* 5(3): 63-88.

Macalloy. 2007. *European Technical Approval ETA-07/0046*. European Organization for Technical Approvals. Charlottenlund, Denmark.

Marriott, D.J. 2009. The Development of High-Performance Post-Tensioned Rocking Systems for the Seismic Design of Structures *PhD Dissertation*, Universtiy of Canterbury, Christchurch, New Zealand.

McKenna, F. 2011. OpenSees: A Framework for Earthquake Engineering Simulation. *Computing in Science and Engg.* 13(4): 58-66.

Newcombe, M.P., Pampanin, S., Buchanan, A.H., Palermo, A. 2008. Section Analysis and Cyclic Behavior of Post-Tensioned Jointed Ductile Connections for Multi-Story Timber Buildings. *Journal of Earthquake Engineering* 12(S1): 83-110.

Palermo, A. 2004. The use of controlled rocking in the seismic design of bridges *PhD Dissertation*, Politecnico di Milano, Milan, Italy.

Pampanin, S. 2000. Alternative design philosophies and seismic response of precast concrete buildings *PhD Dissertation*, Politecnico di Milano, Milan, Italy.

Pampanin, S., Priestley, M.J.N., Sritharan, S. 2001. Analytical modelling of the seicmic behaviour of precast concrete frames designed with ductile connections. *Journal of Earthquake Engineering* 5(3): 329-367.

Sarti, F., Palermo, A., Pampanin, S. 2014. Quasi static cyclic test of 2/3 scale timber single wall and column-wall-column post-tensioned systems. *New Zealand Society for Earthquake Engineering Annual Conference*, Auckland, New Zealand.

Sarti, F., Palermo, A., Pampanin, S. 2015a. Development and testing of an alternative dissipative post-tensioned rocking timber wall with boundary columns *Journal of Structural Engineering*.

Sarti, F., Palermo, A., Pampanin, S. 2015b. Quasi-Static Cyclic Testing of Two-Thirds Scale Unbonded Posttensioned Rocking Dissipative Timber Walls. *Journal of Structural Engineering*.

Sarti, F., Smith, T., Palermo, A., Pampanin, S., Carradine, D.M. 2013. Experimental and analytical study of replaceable Buckling-Restrained Fused-type (BRF) mild steel

dissipaters. *New Zealand Society for Earthquake Engineering Annual Conference*, Wellington, New Zealand.

Skinner, R.I., Kelly, J.M., Heine, A.J. 1974. Hysteretic dampers for earthquake-resistant structures. *Earthquake Engineering & Structural Dynamics* 3(3): 287-296.

Smith, T. 2014. Post-tensioned Timber Frames with Supplemental Damping Devices *PhD Dissertation*, University of Canterbury, Christchurch, New Zealand.

NZS 1170.5: Structural Design Actions - Part 5: Earthquake actions. Standards New Zealand. 2004.

Standards New Zealand. 2006. *NZS 3101: Concrete structures standard*. Standards New Zealand. Wellington, New Zealand, Standards New Zealand.

Structural Timber Innovation Company. 2013. *Design Guide Australia and New Zealand-Post-Tensioned Timber Buildings*. Structural Timber Innovation Company. Christchurch, New Zealand.

Uriz, P. 2008. *Toward earthquake-resistant design of concentrically braced steel-frame structures*, Pacific Earthquake Engineering Research Center.

Vamvatsikos, D., Cornell, C.A. 2002. Incremental dynamic analysis. *Earthquake Engineering & Structural Dynamics* 31(3): 491-514.

van Beerschoten, W.A., Carradine, D.M., Palermo, A. 2013. Compressive strength and stiffness of Radiata Pine laminated veneer lumber. *European Journal of Wood and Wood Products* 71(6): 795-804.

10 Displacement-Based Design of post-tensioned rocking dissipative wall systems

10.1 Introduction

The objective of this chapter is the validation and refinement of the current Displacement-Based Design procedure for post-tensioned rocking timber walls.

In the first part of the chapter, a set of case study buildings are designed in accordance with the current Displacement-Design Procedure and a detailed discussion on the design results is provided with reference to significant design parameters.

The designed buildings provided the basis for the calibration of numerical models, presented and discussed in Chapter 8 of this dissertation, which were used to perform non-linear time-history analyses. The numerical results in terms of average peak displacements, shear and moment envelopes are discussed and compared to the current design assumptions.

Since some of the current design equation proved inaccurate in the prediction of the observed dynamic response of case study buildings, revised equation are developed in the chapter and compared to the numerical results.

The proposed equations are used in the last part of the chapter to design a new set of case study buildings, which are then subjected to further non-linear time-history analyses to validate the proposed design equations.

10.2 Case study buildings parameters and design requirements

Several case study buildings were accounted for in the parametric study presented in this chapter. A set of case study buildings was selected from the archetypes building shown in Chapter 9, and the buidlings main characteristics are listed below:

- seismic resisting system: single wall, CWC, coupled walls
- building height: 3, 6 and 8 storeys with inter-storey heights of 3.6m and 4.5m. A first storey height of 5m was also considered for the 6 and 8 storeys buildings.
- wall dimensions: 3.6m, 4.8m and 5.2m
- Flooring system: Timber-Concrete Composite floor (storey mass 320t)
- re-centering ratio: $\beta = 0.70, 0.85, 1.00$

The summary of the case-study buildings is reported in Table 10-1.

Table 10-1. Case study buildings summary.

ID	No. Of storeys	H_1 *(m)*	H *(m)*	Storey mass *(t)*
1	3	3.6	3.6	320
2	3	4.5	4.5	320
3	6	3.6	3.6	320
4	6	5	3.6	320
5	6	4.5	4.5	320
6	8	3.6	3.6	320
7	8	4.5	4.5	320
8	8	5	3.6	320

10.3 Displacement-Based Design (DBD)

10.3.1 Overview of Displacement-Based Design of Structures

The Displacement-Based Design procedure (DBD) has been developed with the aim of mitigating the deficiencies in current force-based design. The fundamental difference from force-based design is that DBD characterizes the structure by a single-degree-of-freedom (SDOF) representation of performance at peak displacement response, rather than by its initial elastic characteristics (Priestley *et al.*, 2007).

For multi-degree-of-freedom (MDOF) structures the initial part of the design process requires the determination of the characteristics of the equivalent single-degree-of-freedom (SDOF) substitute structure (Priestley *et al.*, 2007) (see Figure 10-1).

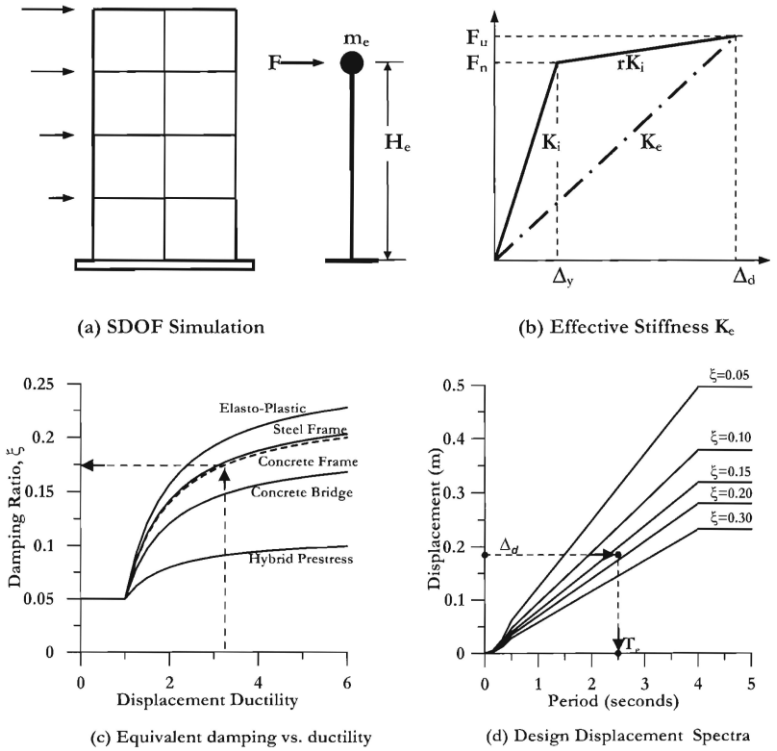

Figure 10-1. Displacement-Based Design fundamentals (Priestley et al., 2007)

The design displacement of the substitute structure depends on the limit state displacement or drift and is given below:

$$\Delta_d = \frac{\sum_{i=1}^{n}\left(m_i \Delta_i^2\right)}{\sum_{i=1}^{n}\left(m_i \Delta_i\right)} \qquad (10\text{-}1)$$

Where m_i = mass of the i-th significant mass location

Δ_i = displacement of the i-th significant mass location

For post-tensioned wall systems the displacement profile can be assumed as linear (Newcombe, 2012); therefore:

$$\Delta_i = \theta_d h_i \qquad (10\text{-}2)$$

Where θ_d = design drift

h_i = height of the i-th level

From consideration of the mass participating in the first inelastic mode of vibration, the effective system mass for the substitute structure is:

$$m_e = \frac{\sum_{i=1}^{n}\left(m_i \Delta_i\right)}{\Delta_d} \qquad (10\text{-}3)$$

Rather than using a ductility-based reduction factor like most of the design standards adopting a force-based design procedure, the design following a DBD approach requires the determination of the equivalent viscous damping, ξ, given by the elastic damping, ξ_{el}, of the structure and the (area-based) hysteretic damping, ξ_{hyst}.

$$\xi = \xi_{el} + \xi_{hyst} \qquad (10\text{-}4)$$

To apply a DBD approach a displacement design spectrum, S_d, must be used, and that is worked out from the 5% damped acceleration spectrum as:

$$S_d\left(T\right) = \frac{C\left(T\right)}{4\pi^2}\frac{T^2}{R_\xi} \qquad (10\text{-}5)$$

Where R_ξ = reduction factor given as a function of the equivalent viscous damping of the structure, ξ.

$$R_\xi = \sqrt{\frac{0.07}{0.02+\xi}} \qquad (10\text{-}6)$$

Once the design displacement spectrum is evaluated, the SDOF substitute structure is characterized by a secant period, T_e, and the secant stiffness, K_e, base shear, V_b, and base moment, M_b, can be determined as follows:

$$K_e = \frac{4\pi^2 m_e}{T_e^2} \qquad (10\text{-}7)$$

$$V_b = K_e \Delta_d \qquad (10\text{-}8)$$

$$M_b = V_b H_e \qquad (10\text{-}9)$$

10.3.2 Discussion on the design Equivalent Viscous Damping

A key parameter in the Displacement-Based Design of structures is the Equivalent Viscous Damping, ξ. This is given by the sum of the elastic damping ratio, ξ_{el}, and hysteretic viscous damping ratio, ξ_{hyst}, of the structural system as shown in Equation (10-10).

$$\xi = \xi_{el} + \xi_{hyst} \tag{10-10}$$

As observed in the dynamic testing results of post-tensioned rocking timber systems by Marriott (2009) and Smith (2014) an elastic damping value of 3% was found for post-tensioned timber systems and it was adopted for the seismic design and numerical modelling carried out in this chapter.

Priestley et al. (2007) proposed an analytical formula for the area-based hysteretic damping, ξ_{hyst}, of a dissipative post-tensioned rocking system and a reduction factor was proposed in Chapter 8 of this dissertation accounting for the observed experimental response of the system and evaluated through numerical simulations. The proposed adjusted formula is shown in Equation (10-11).

$$\xi_{hyst} = k_{\xi} \frac{(2-2\beta)(\mu-1)}{\mu\pi\left[1+r(\mu-1)\right]} \tag{10-11}$$

Where μ = ductility

β = re-centering ratio (M_{pt}/M_{tot})

r = post-yield stiffness factor

k_{ξ} = area-based hysteretic damping modification factor given in Equation (10-12):

$$k_{\xi} = 0.83 + (\mu-1)\cdot\begin{cases}0.06 \; w/\; strain\, hardening\\ 0.02 \;\; w/o\; strain\, hardening\end{cases} \tag{10-12}$$

As suggested by Priestley et al. (2007) the design value of the area-based hysteretic viscous damping, ξ_{hyst}, should be corrected to account for the dynamic behaviour of the system under investigation, and Priestley et al. (2007) suggested correction factors, k_{dyn}, to be applied to the area-based viscous damping ratio and shown in Figure 10-2.

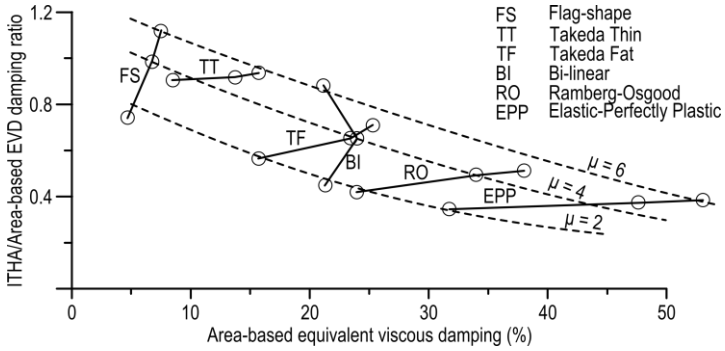

Figure 10-2. Correction factors, k_{dyn}, to be applied to area-based equivalent viscous damping ratio (modified from Priestley et al. (2007)).

Therefore, the hysteretic viscous damping ratio to be adopted in the design is given in Equation (10-13).

$$\xi_{hyst} = k_{dyn} k_{\xi} \frac{(2-2\beta)(\mu-1)}{\mu\pi\left[1+r(\mu-1)\right]} \qquad (10\text{-}13)$$

Where k_{dyn} = correction factor accounting for dynamic reduction of hysteretic viscous damping

10.3.3 Design results and discussion

The set of case study buildings presented in this chapter was designed in accordance with a Displacement-Base Design (Priestley *et al.*, 2007) approach and in accordance with NZS 1170.5 (2004) and accounting for the Equivalent Viscous Damping reduction formulas discussed in Section 10.3.2. This section provides a detailed discussion on the results of the parametric design of the case study buildings accounting for the different design parameters.

For design purposes the following parameters were used:

- Importance level: IL2
- Return period factor: R = 1.0 (500 years return period)
- Location: Christchurch (Z = 0.3)
- Soil Type D
- Structural Performance Factor: $S_p = 1.0$
- Design drift: θ_d = 1.2% (a linear displacement profile was assumed in the design phase as suggested by Newcombe (2012))
- ductility factor: $\mu = 2.5$
- post-yielding stiffness ratio: r = 0.2

These design values resulted in the reduction factors reported in Table 10-2 and Table 10-3. It is worth noticing that for coupled systems, such as the Column-Wall-Column (CWC, see Chapter 6) or coupled walls, U-shaped Flexural Plates (UFPs) were used and no isotropic strain hardening was considered as shown by experimental results by Skinner et al. (1974), Iqbal et al. (2007) and Baird et al. (2014). This resulted in a bigger reduction in area-based hysteretic viscous damping in accordance with Equation (10-12), which was then counter-balanced by a smaller dynamic reduction factor, k_{dyn}, resulting in no major differences in seismic reduction factors, R_{ξ}.

From the results in Table 10-2 it is also worth noticing that the 5% damped spectrum from NZS 1170.5 (2004) was magnified when a post-tensioned only solution was considered. This accounted for the reduced elastic damping assumed for timber systems (ξ_{el} = 3%).

Table 10-2. DBD seismic reduction factors, R_ξ.

Re-centering ratio	**Single walls**					**CWC Coupled walls**				
β	ξ_{hyst}	k_ξ	k_{dyn}	ξ	R_ξ	ξ_{hyst}	k_ξ	k_{dyn}	ξ	R_ξ
0.70	8.81	0.92	0.78	9.32	0.79	8.81	0.86	0.80	9.00	0.80
0.85	4.41	0.92	0.86	6.49	0.91	4.41	0.86	0.88	6.57	0.90
1.00	0.00	0.00	0.00	3.00	1.18	0.00	0.00	0.00	3.00	1.18

As reported in Table 10-3, most of the secant properties of the equivalent SDOF system were not affected by either the re-centering ratio or the wall system adopted. Only the secant period was influenced by those two parameters being dependant on the hysteretic damping of the building.

Table 10-3. Equivalent SDOF secant properties.

ID	**Design Displ.** (m)	**Equiv. Height** (m)	**Equiv. Mass** (t)	*Single wall* **Secant Period** (s)			*CWC Coupled Walls* **Secant Period** (s)		
				β = 0.70	*β = 0.85*	*β = 1.00*	*β = 0.70*	*β = 0.85*	*β = 1.00*
1	0.101	8.4	822	0.911	0.811	0.656	0.902	0.803	0.656
2	0.126	10.5	822	1.085	0.970	0.785	1.075	0.959	0.785
3	0.187	15.6	1549	1.494	1.326	1.074	1.480	1.311	1.074
4	0.200	16.7	1608	1.598	1.403	1.133	1.580	1.387	1.133
5	0.234	19.5	1549	1.866	1.616	1.282	1.845	1.594	1.282
6	0.245	20.4	2031	1.953	1.690	1.330	1.930	1.668	1.330
7	0.306	25.5	2031	2.441	2.113	1.622	2.413	2.084	1.622
8	0.258	21.5	2097	2.055	1.779	1.387	2.031	1.755	1.387

To highlight the influence of the re-centering ratio on the design results, the base shear values (also shown in Table 10-4) were normalized with reference to post-tensioned only solutions (i.e. β = 1.00) and plotted versus the re-centering ratio in Figure 10-3.

Table 10-4. Design base shear results.

ID	*Single wall* (kN)			*CWC Coupled Walls* (kN)		
	β = 0.70	*β = 0.85*	*β = 1.00*	*β = 0.70*	*β = 0.85*	*β = 1.00*
1	3946	4971	7599	4020	5079	7599
2	3475	4349	6641	3538	4445	6641
3	5128	6511	9926	5229	6657	9926
4	4979	6468	9915	5096	6615	9915
5	4108	5482	8707	4205	5633	8707
6	5148	6870	11095	5269	7059	11095
7	4118	5496	9329	4216	5647	9329
8	5051	6741	11086	5170	6926	11086

The influence of the re-centering ratio, β, on the final design and the quantity of seismic resisting elements is rather significant. As shown in Figure 10-3, the relationship between the reduction in base shear and the re-centering ratio is strongly non-linear, meaning that a small reduction in re-centering ratio results in a rather big decrease in design base shear. As shown in Figure 10-3, for a re-centering ratio 0.85 the design base shear was reduced by more than 40%, and approximately 60% at β = 0.70.

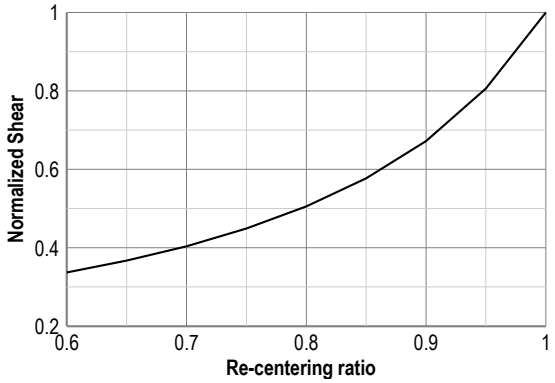

Figure 10-3. DBD normalized design base shear ($V_b(\beta)/ V_b(\beta=1.0)$) results ($\mu = 2.5$).

The implications can also be shown and discussed looking at the final wall design summarized in Table 10-5. The post-tensioned walls were designed accounting for the design requirements discussed in Chapter 9. In the design summary of Table 10-5, the number of seismic resisting elements was mainly governed by the maximum initial timber stress, required to be lower than 10%. As discussed in Chapter 9, this stress value allowed the rocking wall to develop gap opening with a small neutral axis, which results in full and efficient activation of the dissipaters whilst providing a strength margin for more severe events.

Table 10-5. Post-tensioned rocking walls design summary (single walls).

	β = 0.70					***β = 0.85***					***β = 1.00***				
ID	**n_{wall}**	**h**	**A_p**	**T_{pt0}**	**A_s**	**n_{wall}**	**h**	**A_p**	**T_{pt0}**	**A_s**	**n_{wall}**	**h**	**A_p**	**T_{pt0}**	**A_s**
	(-)	**(m)**	**(mm)**	**(kN)**	**(mm)**	**(-)**	**(m)**	**(mm)**	**(kN)**	**(mm)**	**(-)**	**(m)**	**(mm)**	**(kN)**	**(mm)**
1	4	3.6	4D50	2920	16D23	6	3.6	4D50	2920	8D21	4	4.8	6D60	4920	n/a
2	4	3.6	4D50	3600	16D24	6	3.6	4D50	3600	8D22	4	4.8	6D60	7020	n/a
3	4	4.8	6D50	6300	24D25	6	4.8	6D50	6600	12D23	7	5.2	8D60	8800	n/a
4	4	4.8	6D50	7080	24D25	6	4.8	6D60	7140	12D24	7	5.2	8D60	10160	n/a
5	4	4.8	6D50	6600	24D25	6	4.8	6D60	6900	12D24	7	5.2	8D60	10240	n/a
6	6	4.8	6D50	5700	24D24	8	4.8	6D60	6900	12D24	10	5.2	8D60	9600	n/a
7	6	4.8	6D50	5940	24D24	8	4.8	6D60	7140	12D24	10	5.2	8D60	10480	n/a
8	6	4.8	6D50	6300	24D24	8	4.8	6D60	7500	12D24	10	5.2	8D60	10640	n/a

The design data in Table 10-5 highlights not only a significant increase in the number of seismic resisting elements for non-dissipative solutions (β = 1.00), but an increased wall section depth (i.e. 5.2m) was necessary to match the design requirements.

From a comparison of the design data of the dissipative solutions it is clear and expected that a decrease in re-centering ratio (i.e. increase in dissipative reinforcement) results in a decrease in the number of seismic resisting elements in most buildings. On the other hand, a lower re-centering ratio requires a significant increase in dissipative reinforcement and the dissipation connection can become restrictively large. This can result in uneconomical solutions and the designer should evaluate the feasibility of an increased or decreased re-centering ratio on a case-by-case basis.

Table 10-6. Post-tensioned rocking walls design summary (CWC system).

	β = 0.70								***β = 0.85***							
ID	**n_{wall}**	**h**	**A_p**	**T_{pt0}**	**n_u**	**b_u**	**t_u**	**R_u**	**n_{wall}**	**h**	**A_p**	**T_{pt0}**	**n_u**	**b_u**	**t_u**	**R_u**
	(-)	**(m)**	**(mm)**	**(kN)**	**(-)**	**(mm)**	**(mm)**	**(mm)**	**(-)**	**(m)**	**(mm)**	**(kN)**	**(-)**	**(mm)**	**(mm)**	**(mm)**
1	4	3.6	4D50	3060	24	300	12	55	6	3.6	4D50	3020	12	300	12	58
2	4	3.6	4D50	3760	24	300	12	50	6	3.6	4D50	3700	12	300	12	58
3	4	4.8	6D60	6300	30	400	12	50	6	4.8	6D60	6360	12	400	12	48
4	4	4.8	6D60	7110	30	400	12	50	6	4.8	6D60	7320	12	400	12	45
5	4	4.8	6D60	6660	30	400	12	50	6	4.8	6D60	7140	12	400	12	45
6	6	4.8	6D50	6000	32	400	12	65	8	4.8	6D60	7110	16	400	12	60
7	6	4.8	6D50	6180	32	400	12	65	8	4.8	6D60	7350	16	400	12	60
8	6	4.8	6D50	6600	32	400	12	60	8	4.8	6D60	7710	16	400	12	60

Similar results were observed for the CWC (Table 10-6) and coupled walls systems (Table 10-7). In fact, it is worth noticing that although the lower reduction factor in Equation (10-12) for coupled systems, this is counterbalanced by a higher dynamic reduction factor (see Figure 10-2), which leads to very similar design base shear values (see Table 10-4).

Table 10-7. Post-tensioned rocking walls design summary (Coupled walls system).

	β = 0.70								***β = 0.85***							
ID	**n_{wall}**	**h**	**A_p**	**T_{pt0}**	**n_u**	**b_u**	**t_u**	**R_u**	**n_{wall}**	**h**	**A_p**	**T_{pt0}**	**n_u**	**b_u**	**t_u**	**R_u**
	(-)	**(m)**	**(mm)**	**(kN)**	**(-)**	**(mm)**	**(mm)**	**(mm)**	**(-)**	**(m)**	**(mm)**	**(kN)**	**(-)**	**(mm)**	**(mm)**	**(mm)**
1	2	3.6	4D50	2620	21	300	12	48	3	3.6	4D50	2560	9	300	12	48
2	2	3.6	4D50	3360	24	300	12	50	3	3.6	4D50	3280	9	300	12	45
3	2	4.8	4D60	6200	30	400	12	52	3	4.8	4D60	6240	12	400	12	48
4	2	4.8	4D60	6920	30	400	12	50	3	4.8	6D60	6780	12	400	12	45
5	2	4.8	4D60	6520	30	400	12	52	3	4.8	6D60	6600	12	400	12	45
6	3	4.8	4D60	5640	24	400	12	46	4	4.8	6D60	6600	12	400	12	45
7	3	4.8	4D60	5840	24	400	12	46	4	4.8	6D60	6900	12	400	12	45
8	3	4.8	4D60	6120	24	400	12	45	4	4.8	6D60	7260	12	400	12	45

10.4 Modelling approach

A detailed discussion on the different modelling approaches used to simulate post-tensioned dissipative rocking wall systems was presented in Chapter 8 of this dissertation and among the two approaches the multi-spring model was used to perform numerical analyses shown in this chapter.

The same model used to determine the Force-Based Design factors in Chapter 9 was used and is shown in Figure 10-4.

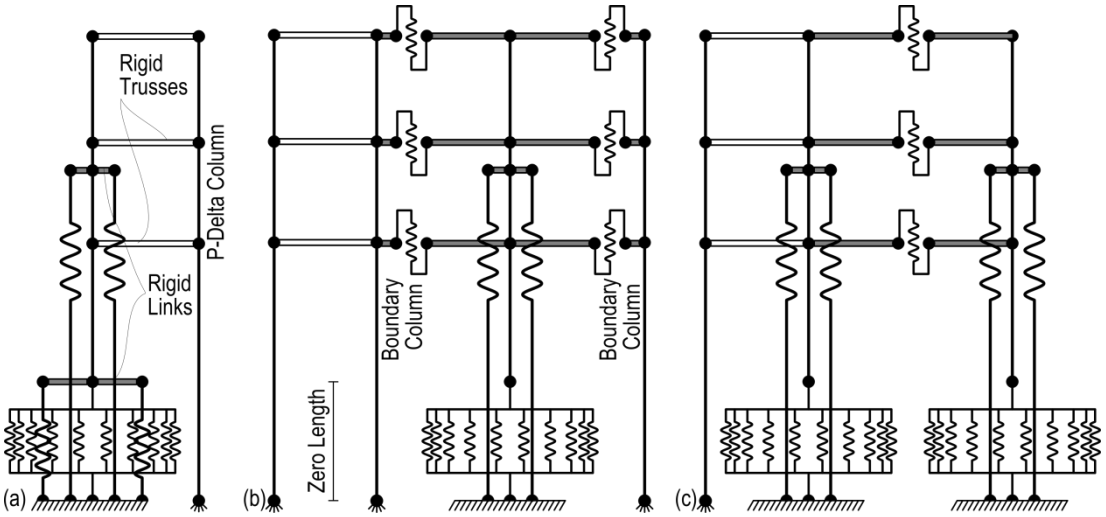

Figure 10-4. Multi-spring models. (a) Single wall; (b) CWC;; (c) coupled walls.

The model simulates the gap opening at the wall-foundation interface with several compression-only gap parallel springs which are connected by rigid links. The post-tensioning bars as well as the dissipaters are modelled via either truss or spring elements.

The development and calibration of the OpenSEES (McKenna, 2011) multi-spring was presented in detail in Chapter 8, and detailed discussion on the use of such model for the modelling of the case study buildings can be found in Chapter 9.

10.5 Non-linear Time History Analyses (NLTHA) results

Several non-linear time history analyses (NLTHA) were carried out on the building designs using the multi-spring models shown in Figure 10-4 and using the ground motion set shown in Chapter 9 of this dissertation, which were scaled in accordance with NZS 1170.5 (2004)

The results are presented and discussed in the following sections with reference to displacement and inter-storey drift profiles, shear and moment envelopes and maximum floor accelerations observed.

The current design formulas adopted in the Displacement-Based Design procedure of post-tensioned timber walls are either validated or refined based on numerical observations.

10.5.1 Displacement profiles and inter-storey drift

The charts in Figure 10-5 show the average peak drift (defined as the storey displacement/building height ratio) profiles for the case study buildings 2, 5 and 7 (refer to Table 10-1) and the three different structural systems, comparing the numerical results to the linear displacement profile assumed in the design phase.

As Figure 10-5 shows, the linear profile assumption does not appear appropriate for predicting the buildings displacement response, and the inter-storey drift is over-predicted by the design assumption. This is mainly due to the displacement shape which assumes a constant inter-storey drift along the height of the building.

It is also noticeable from the charts in Figure 10-5 that the maximum displacement values observed tend to decrease as the hysteretic damping decreases (i.e. higher values of the re-centering ratio β). While this difference in the maximum displacement is rather small for re-centering ratio values of 0.70 and 0.85, this is much more significant for shorter (i.e. lower period) buildings. This reduction in displacement was also observed in numerical analysis on post-tensioned concrete wall systems by Pennucci et al. (2011) and it is thought that the issue is related to inconsistencies in the modelling of MDOF systems. In fact, as pointed out by Grant et al. (2005), the first mode damping according to the Rayleigh model is almost entirely mass proportional, which is constant throughout the NLTHA (Pennucci *et al.*, 2011). This effect is more significant as the hysteretic viscous damping decreases (i.e. increase in re-centering ratio values) as shown in Figure 10-6.

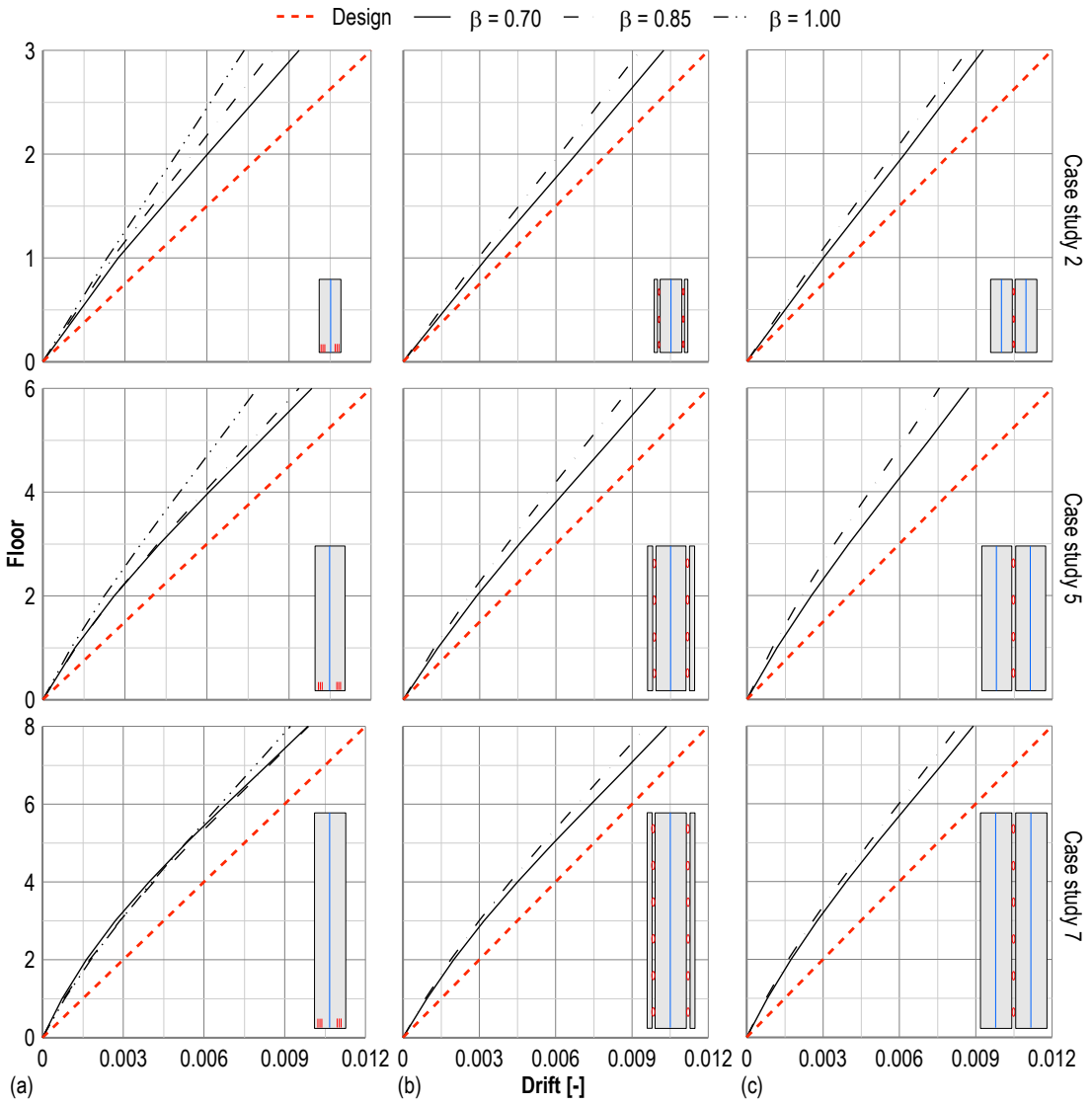

Figure 10-5. Case study buildings 2, 5 and 7 average peak displacement profiles for (a) single wall, (b) CWC and (c) coupled walls systems.

The non-linearity of the displacement profile can be better highlighted by plotting the inter-storey drift, which is generally over-predicted as Figure 10-6 shows. As mentioned above, the linear displacement profile can be a good approximation when considering buildings lower than three storeys, while for taller buildings the inter-storey drift tends to increase with the building height as shown in Figure 10-6 highlighting a cantilever-type of behaviour where the base rotational stiffness results in low drift at low levels. At higher storeys, the influence of elastic deflection (i.e. cantilever behaviour) is more significant.

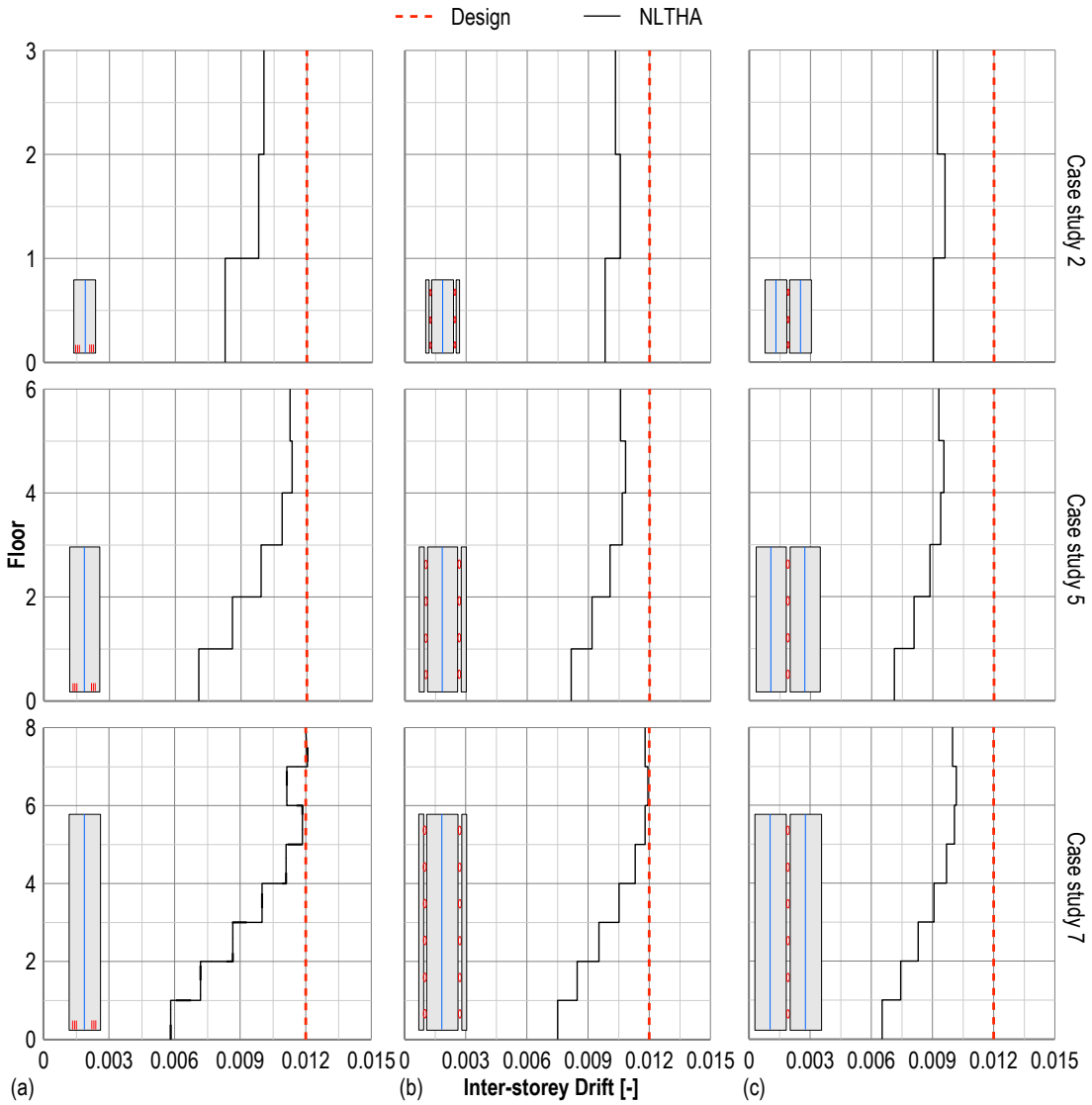

Figure 10-6. Case study buildings 2, 5 and 7 average peak inter-storey drift profiles (β = 0.70) for (a) single wall, (b) CWC and (c) coupled walls systems.

As the results above show, the linear displacement profile was not representative of the observed numerical results, and this resulted in the over-estimation of the building displacements and inter-storey drifts.

To refine the design displacement equations, the elastic contributions of the rocking wall panel were taken into account, and the total displacement of the system can be broken down into two main contributions as shown in Figure 10-7.

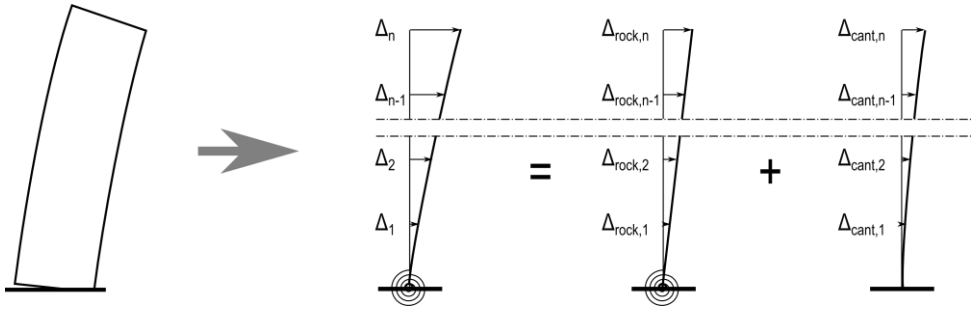

Figure 10-7. Rocking wall displacement contributions.

The rigid body rotation shown in Figure 10-7, results in the linear displacement due to rocking, $\Delta_{gap,i}$, in Equation (10-14)

$$\Delta_{gap,i} \propto \frac{h_i}{h_n} \qquad (10\text{-}14)$$

Where h_i = the height of the i-th storey

h_n = the height of the top storey

The elastic contributions can be approximated as the displacement of a vertical cantilever, $\Delta_{cant,i}$, with a linear curvature distribution approximated as:

$$\Delta_{cant,i} \propto \frac{3}{2}\left(\frac{h_i}{h_n}\right)^2\left(1-\frac{h_i}{3h_n}\right) \qquad (10\text{-}15)$$

The correct definition of the different displacement contributions due to either the rocking mechanism or the elastic displacement contribution should consider the peculiar mechanism of the system (e.g. initial post-tensioning force, dissipaters length and position), but this is not practical from a design perspective since the definition of such displacement would involve some detailed parameters such as the dissipater position and unbonded length as well as initial post-tensioning force (refer to Chapter 7 for more detail). Those parameters are the outcome of the design process and are unknown during the design phase.

A simplified equation for the inelastic displacement shape accounting for the definitions reported in Equations (10-14) and (10-15) was worked out accounting for elastic displacement contributions. In an attempt to provide the most simplified approach, the development of such equation was based on numerous push-over analyses carried out as part of the design phase of this numerical work.

The total displacement shape, δ_i, was then worked out combining Equations (10-14) and (10-15) as follows:

$$\delta_i = (1-k_{el})\frac{h_i}{h_n} + k_{el}\left[\frac{3}{2}\left(\frac{h_i}{h_n}\right)^2\left(1-\frac{h_i}{3h_n}\right)\right] \qquad (10\text{-}16)$$

Where k_{el} = the displacement contribution factor due elastic deflections

The push-over analyses of the designed walls were carried out in accordance with the analytical model shown in Chapter 7 of this dissertation for the case study building designs. Figure 10-8 shows an example of push-over analysis on the case study building 2 highlighting the different contributions due to either the base gap opening (i.e. rigid body rotation, Equation (10-14)) and the elastic contributions (i.e. cantilever elastic displacement, Equation (10-15)).

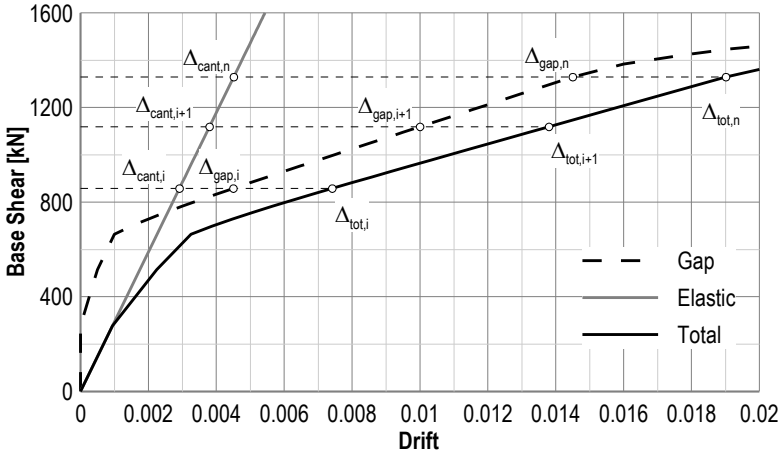

Figure 10-8. Push-over results of the case study building 2

Figure 10-8 plots the push-over curve of the case study building 2 and show the trend of the elastic, $\Delta_{cant,i}$, and rigid body, $\Delta_{gap,i}$, displacement contributions used to calibrate the distplacement contribution factors, which for each push-over step is given by:

$$k_{el,i} = \frac{\Delta_{cant,i}}{\Delta_{cant,i} + \Delta_{gap,i}} = \frac{\Delta_{cant,i}}{\Delta_{tot,i}} \qquad (10\text{-}17)$$

The displacement contribution factor, k_{el}, was plotted versus the ductility, μ, for each designed wall and for several ductility values, and the results for the different systems are shown in Figure 10-9.

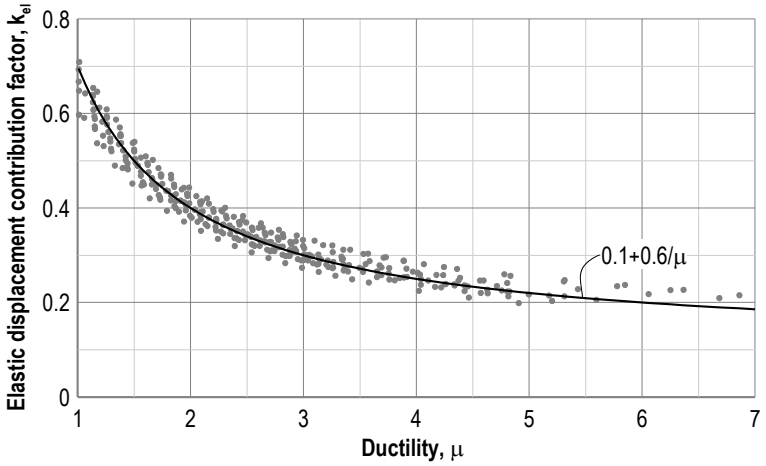

Figure 10-9. Analytical calibration of the displacement contribution factor, k_{el}

The results shown in Figure 10-9 highlight an inverse proportionality with the ductility, μ; therefore, the following equation is proposed:

$$k_{el} = 0.1 + \frac{0.6}{\mu} \qquad (10\text{-}18)$$

In accordance with Displacement-Based Design (Priestley *et al.*, 2007), the design displacement along the height of the structure, Δ_i, must account for the displacement at critical storey as shown in Equation (10-19).

$$\Delta_i = \delta_i \frac{\Delta_c}{\delta_c} \qquad (10\text{-}19)$$

Where Δ_c = the displacement at the critical storey

δ_c = the inelastic mode shape at the critical storey

Unlike frame systems where the first level is the critical storey, the critical storey for a wall system is at the top of the building; therefore, the determination of the design displacement for a wall system needs iteration to match the top inter-storey drift in accordance with Equations (10-16) and (10-19).

For a clearer comparison to NLTHA results, Equation (10-16) was compared to NLTHA results and that was worked out to match the top inter-storey design drift of 1.2%. Figure 10-5 compares the results of Equation (10-16) to the observed NLTHA results and shows that the proposed displacement profile provide a better prediction of the numerical results.

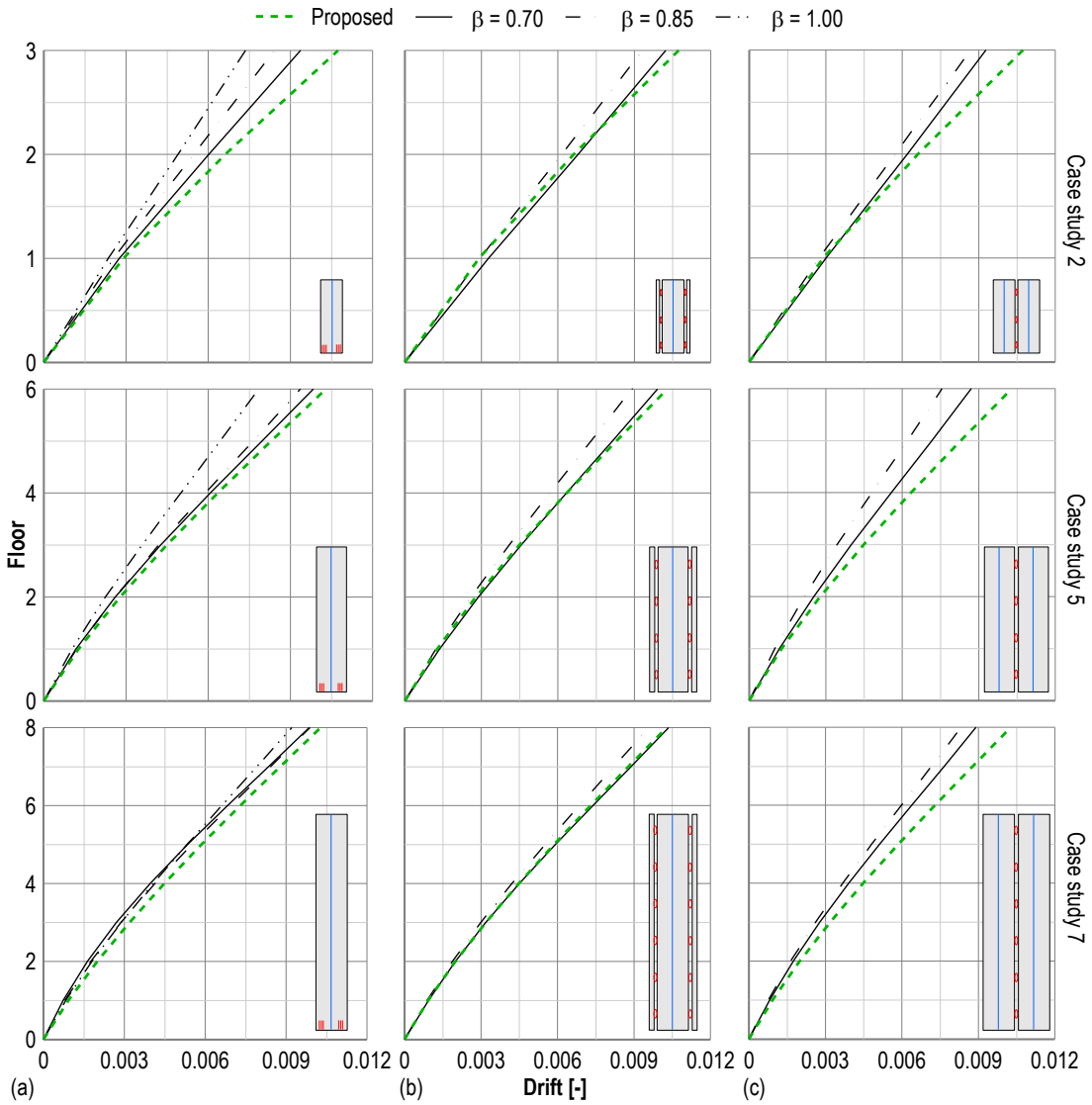

Figure 10-10. Archetypes 1, 3 and 6 average peak inter-storey drift profiles comparison to Eq. (10-19) ($\beta = 0.70$) for (a) single wall, (b) CWC and (c) coupled walls systems.

10.5.2 Shear and bending moment envelopes

The shear envelopes of the case study buildings 2, 5 and 7 are shown in Figure 10-11 and, as expected, dynamic amplification of the shear along the height of the building occurred, particularly for taller buildings. Whilst shorter buildings still display a first-mode shape of the shear distribution along the height of the building, the shear distribution shape is strongly dominated by higher mode effects for buildings taller than 3 storeys (see case study buildings 5 and 7 in Figure 10-11).

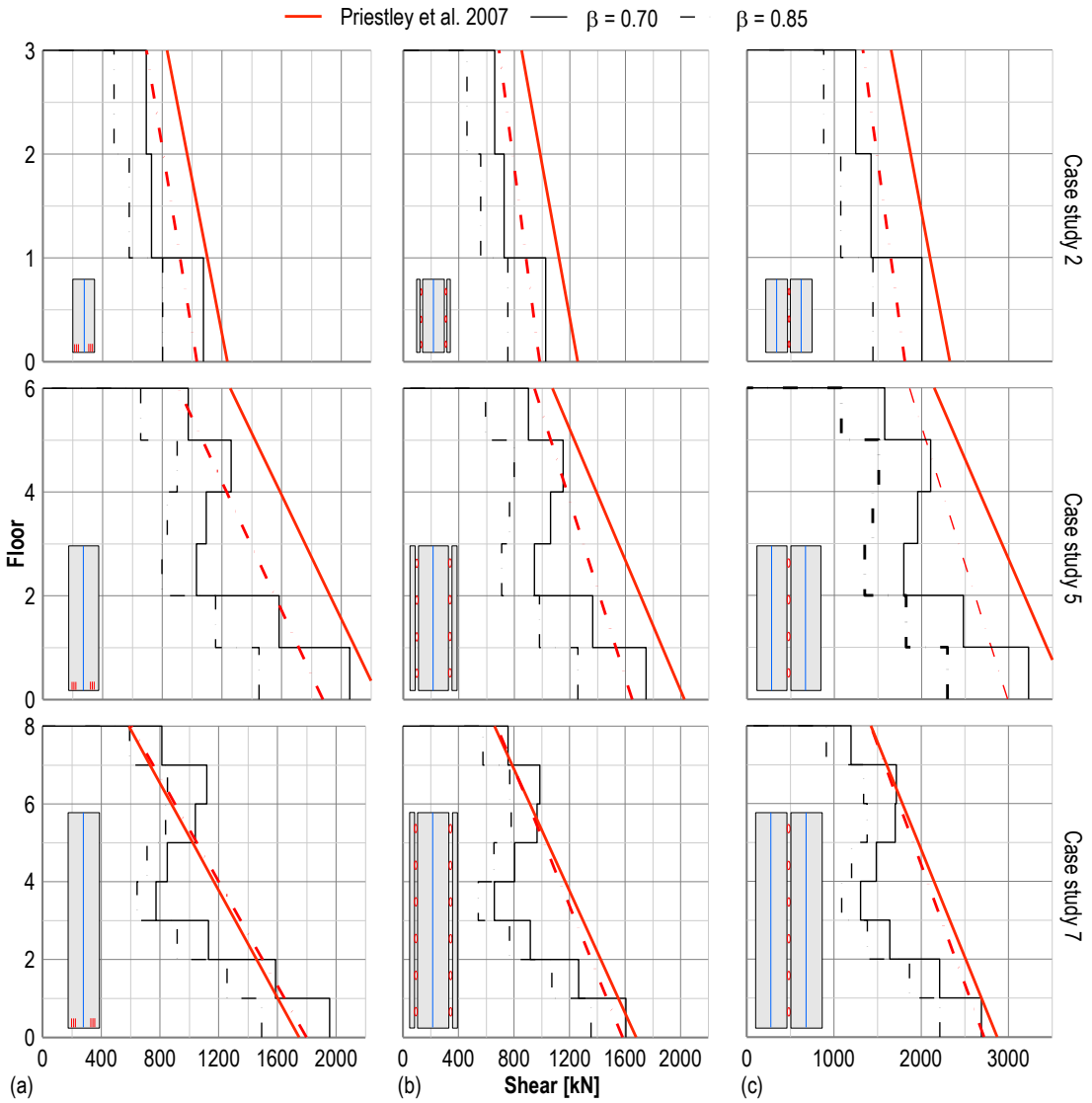

Figure 10-11. Case study buildings 2, 5 and 7 shear envelopes (β = 0.70) for (a) single wall, (b) CWC and (c) coupled walls systems.

According to a capacity design philosophy, this shear amplification must be accounted for and Priestley et al. (2007) suggested simplified shear envelopes to account for higher mode effects. The shear envelope consists of a linear shear distribution defined by the over-strength design base shear, V^o_{Base}, and the over-strength top shear, V^o_n. These two parameters are given in Equations (10-20) and (10-21) and shown in Figure 10-12.

$$V^o_{Base} = \phi^o \omega_V V_b \qquad (10\text{-}20)$$

Where ϕ^o = the over-strength factor relating maximum feasible flexural strength to design strength

ω_V = the dynamic amplification factor given in Equation (10-22)

V_b = the design base shear

$$V_n^o = C_{3,T} V_{Base}^o \quad (10\text{-}21)$$

Where $C_{3,T}$ = seismic coefficients given in Equation (10-24)

$$\omega_V = \frac{\mu}{\phi^o} C_{2,T} + 1.0 \quad (10\text{-}22)$$

Where $C_{2,T}$ = seismic coefficients given in Equations (10-23)

$$C_{2,T} = 0.062 + 0.4(T_i - 0.5) \leq 1.15 \quad (10\text{-}23)$$

$$C_{3,T} = 0.9 - 0.3T_i \geq 0.3 \quad (10\text{-}24)$$

Where T_i = elastic fundamental period of the structure

μ = ductility

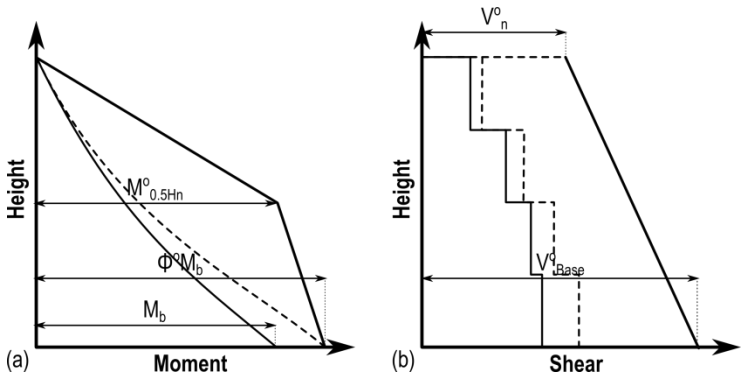

Figure 10-12. Simplified capacity design envelopes (modified after Priestley et al. (2007))

Figure 10-11 reports the comparison of the equations above considering the design ductility μ = 2.5, and over-strength factor ϕ_0 = 1.0. The plots reported below show that the capacity design envelopes by Priestley et al. (2007) are mostly conservative, except for the case study building 7 with single wall system. For this case, the shear force at the wall base as well as above the 6 storey is underestimated by approximately 10% or less. Similarly to Newcombe (2012) this validates the capacity design shear envelopes proposed by Priestley et al. (2007) for dissipative post-tensioned wall systems.

The moment envelopes of the case study buildings 2, 5 and 7 are shown in Figure 10-13 which shows that the bending moment distribution along the height of the building was significantly influenced by higher modes effects. The moment envelopes show that the base moment was not significantly influenced by higher modes effects which instead resulted in a dynamic amplification of the moment at the building mid-height.

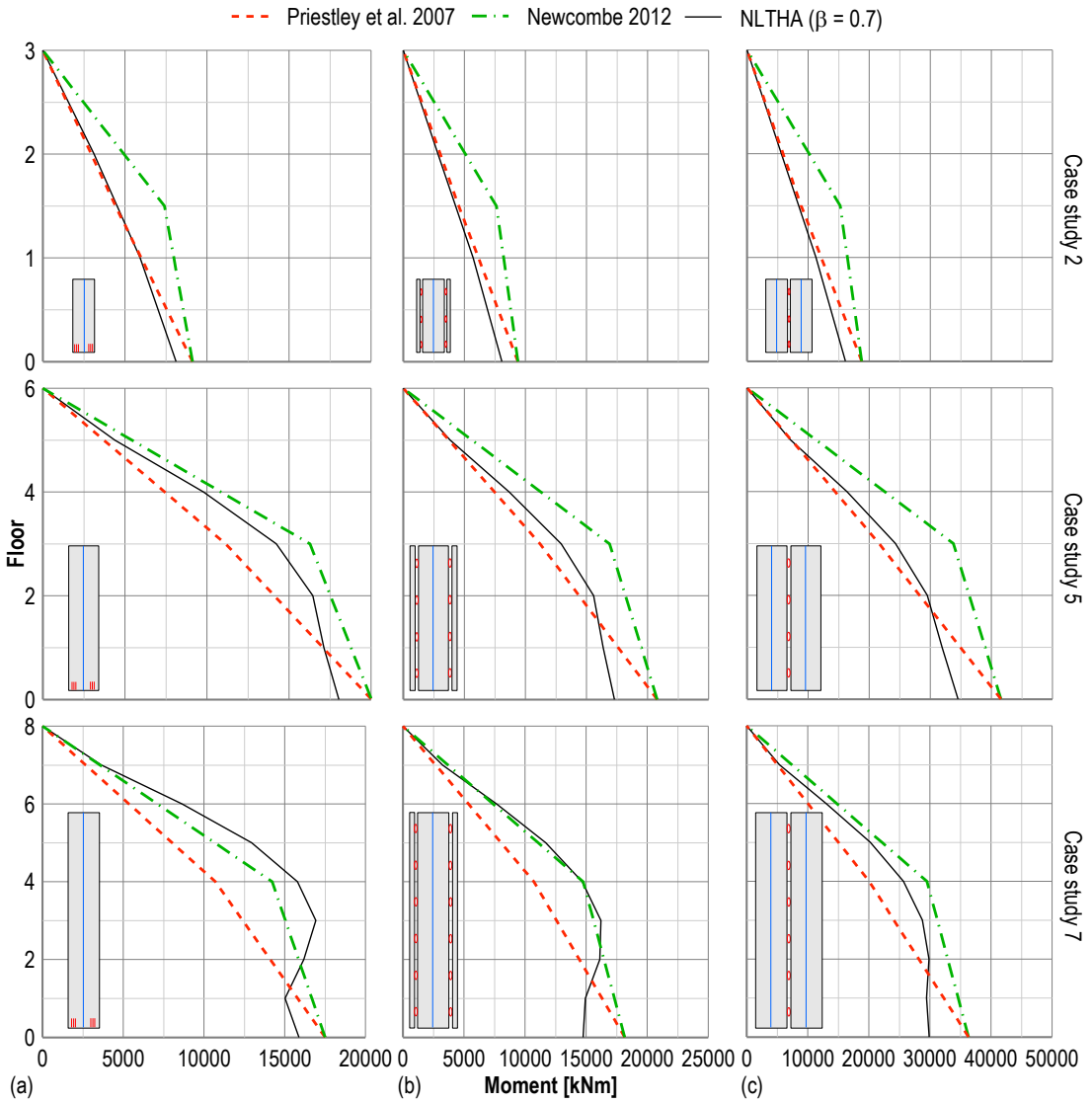

Figure 10-13. Archetypes 1, 3 and 6 moment envelopes (β = 0.70) for (a) single wall, (b) CWC and (c) coupled walls systems.

A bi-linear moment envelope (see Figure 10-12) was suggested by Priestley et al. (2007) and modified for post-tensioned rocking timber walls by Newcombe (2012) and that is defined by the over-strength base moment capacity, $\phi^{o}M_{b}$, and the over-strength moment at mid-height, $M^{o}_{0.5Hn}$, as shown in Figure 10-12 and given in Equations (10-25) and (10-26).

$$M^{o}_{0.5Hn} = C_{1,T}\phi^{o}M_{b} \qquad (10\text{-}25)$$

Where $C_{1,T}$ = seismic coefficients given in Equation (10-28)

$$C_{1,T} = \begin{cases} 0.4 + 0.075 T_i \left(\dfrac{\mu}{\phi_0} - 1 \right) \text{ Priestley } et\ al. \text{ (2007)} \\ 0.7 + 0.1 T_i \left(\dfrac{\mu}{\phi_0} - 1 \right) \text{ Newcombe } et\ al. \text{ (2012)} \end{cases} \qquad \textit{(10-26)}$$

Where T_i = the initial period of the structure

μ/ϕ^o = the ductility demand of the structure

The two envelopes were compared to the numerical results as shown in Figure 10-13, and those proved to be inaccurate in fitting the observed moment envelopes.

The current equations represent two opposites: the equation by Priestley et al. (2007) underestimates the moment at mid-height for most case study building while the equation proposed by Newcombe (2012) provided a better estimate; nevertheless, whilst in a few cases the capacity design envelope underestimated the building response, in general the equation significantly over-estimated the observed moment distribution and thus deemed over-conservative.

Given the inaccuracy of the current capacity design moment envelopes, those were re-calibrated in accordance with the numerical results presented above. Further non-linear time-history analyses were carried out for the case study buildings at different seismic intensities (35, 500, 1000 and 2500 years return period events in accordance with NZS 1170.5 (2004)) to provide more comprehensive data (i.e. a wider range of ductility values).

The factor $C_{1,T}$ was then evaluated based on the numerical results as follows:

$$C_{1,T} = \frac{M_{0.5Hn,NLTHA}}{M_{b,NLTHA}} \qquad \textit{(10-27)}$$

Where $M_{0.5Hn,NLTHA}$ = average maximum moment at mid-height resulting from non-linear time-history analyses

$M_{b,NLTHA}$ = average maximum base moment resulting from non-linear time-history analyses

This was plotted as a function of the ductility factor, μ, in order to re-calibrate Equation (10-26). Figure 10-14 reports the numerical results for the factor $C_{1,T}$ for a selection of case study buildings designed with a single wall solution, and the chart shows a direct proportionality of the mid-height moment factor, $C_{1,T}$, to the ductility, μ, similarly to Equation (10-15). Figure 10-14 also shows that for each case study building the properties of

the linear trend line strongly depends on the initial period of the structre, similarly to current design equations by Priestley et al. (2007) and Newcombe (2012).

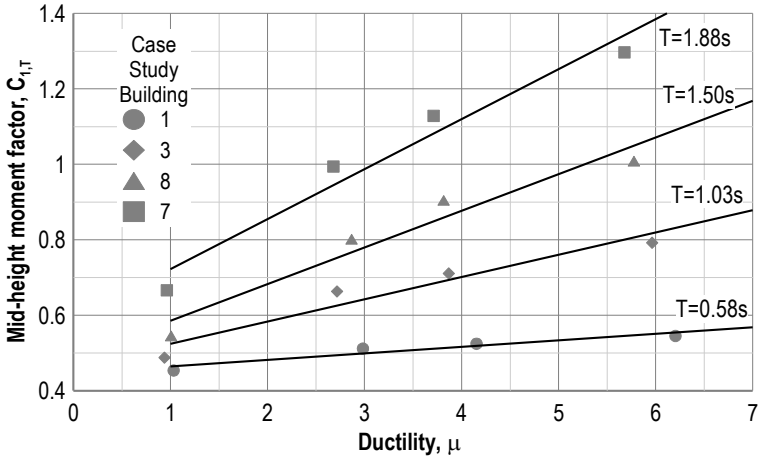

Figure 10-14. Mid-height moment factor, $C_{1,T}$,versus ductility plot (single walls).

In order to re-calibrate Equation (10-26) the trend lines slope and intercept were plotted versus the initial period in order to identify the final calibration of the mid-height moment factor, $C_{1,T}$ (see Figure 10-15).

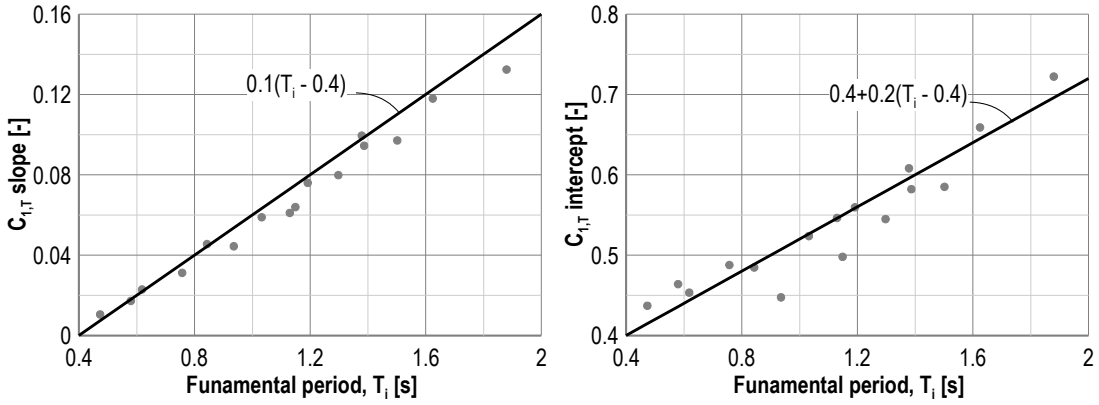

Figure 10-15.Mid-height moment factor, $C_{1,T}$, trend lines (a) slope and (b) intercept.

The slope and intercept of the mid-height moment factor, $C_{1,T}$, as a function of the period show the expected linear trend which provide the proposed Equation (10-28).

$$C_{1,T} = 0.4 + 0.2\left(T_i - 0.4\right) + 0.1\left(T_i - 0.4\right)\left(\frac{\mu}{\phi_0} - 1\right) \qquad \textit{(10-28)}$$

The proposed moment envelope equation is compared to the case study buildings 2, 5 and 7 in Figure 10-16 for the three seismic resisting systems (i.e. single wall, column-wall column and coupled wall systems).

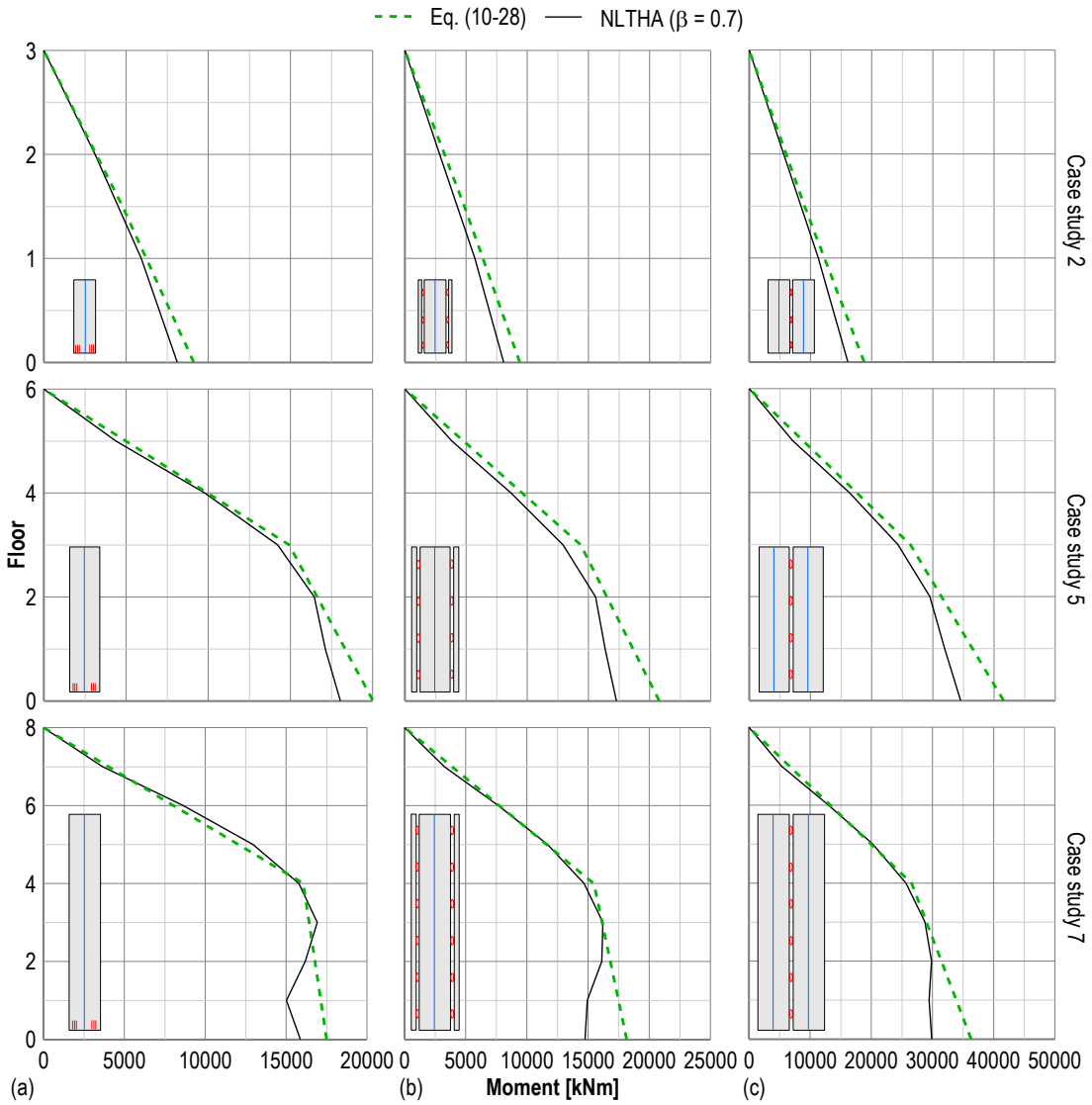

Figure 10-16. Case study buildings 2, 5 and 7 simplified moment envelopes vs. NLTHA results comparison for (a) single wall, (b) CWC and (c) coupled walls systems.

The envelopes, plotted in the green dashed lines, were worked out for each numerical envelope accounting for the design actions (i.e. either shear or moment) and considering the design ductility, $\mu = 2.5$, and over-strength factor, $\phi^o = 1.0$.

10.5.3 Discussion of the over-strength factor of post-tensioned timber walls

As discussed by Priestley et al. (2007) a section being capacity-protected should account for the actual flexural strength which may exceed the design strength for several reasons:

- Material strengths may exceed the nominal or characteristic values used in design.
- Dependable flexural strength may incorporate a strength reduction factor (or partial material factors).

- Strain-hardening of reinforcement or structural steel may not have been considered in determining the flexural capacity of the section (Priestley *et al.*, 2007).

As proposed by Priestley et al. (2007) the recommended values for the over-strength factor is $\phi^o = 1.25$. If strain-hardening is ignored in determining the required section properties $\phi^o = 1.60$ is recommended.

The over-strength factors above were developed for reinforced concrete structures and accounted for the maximum material over-strength (i.e. concrete and steel). These are to be considered conservative values to be adopted in post-tensioned rocking structures in general, since the section capacity in terms of over-strength is dependent on the mild steel dissipater's strength only.

Following a similar section analysis approach as Priestley et al. (2007) more realistic values of the over-strength factors were evaluated for the case study designs.

As suggested by AS/NZS 3404 (Standards New Zealand, 2009) a maximum material variation of 1.30 shall be considered for mild steel elements. This factor was applied in the moment-rotation analysis performed in the design phase.

The section analysis results of the case study building designs showed maximum values of the over-strength factor, ϕ^o, of 1.11 and 1.29 with and without strain hardening effects respectively.

It is therefore suggested that more realistic values of the over-strength factor $\phi^o = 1.15$ shall be adopted. This factor shall be increased to $\phi^o = 1.30$ if strain hardening is ignored in the determination of the section capacity.

10.5.4 Floor accelerations

The maximum floor accelerations are discussed in this section in terms of normalised floor accelerations, which were evaluated as the ratio of the peak floor acceleration to the peak ground acceleration.

The acceleration envelopes consistently show a second mode shape as Figure 10-17 shows (note that the normalised accelerations are reported in their absolute value), and the maximum values were observed at the top storey.

As expected, for each case study building the hysteretic damping had a significant influence on the acceleration response of the buildings, for increasing values of maximum accelerations for increasing values of re-centering ratio.

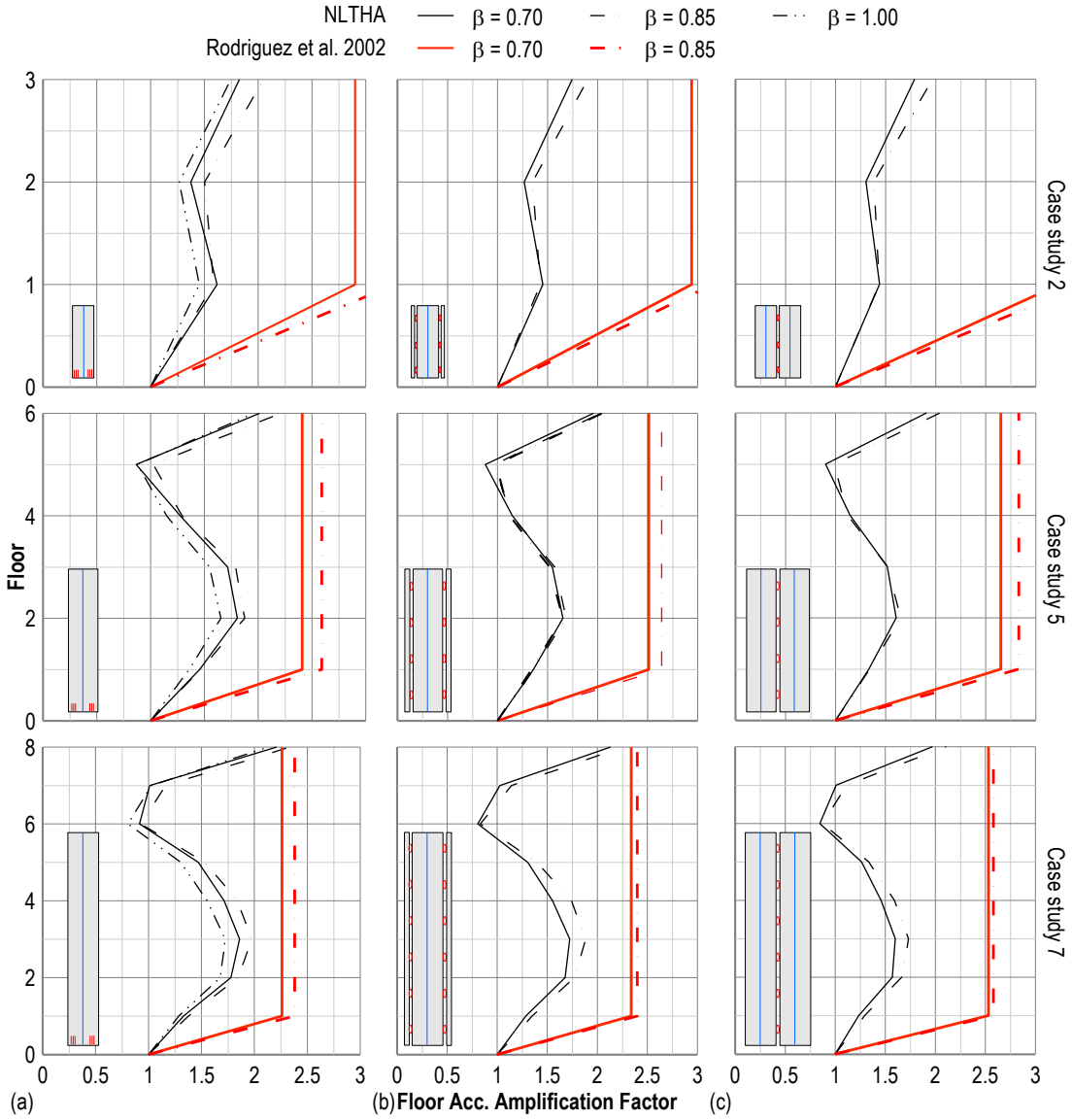

Figure 10-17. Case study buildings 2, 5 and 7 maximum floor acceleration amplification factors for (a) single wall, (b) CWC and (c) coupled walls systems.

Table 10-8 summarizes the maximum floor acceleration amplification factors for the eight case study buildings and the three different wall systems. The maximum values show that no significant difference was observed in terms of maximum acceleration amplification factors between the different systems or for varying re-centering ratios.

Table 10-8. Maximum acceleration amplification factors summary at ULS intensity.

		Maximum acceleration amplification factors							
	ID	**1**	**2**	**3**	**4**	**5**	**6**	**7**	**8**
	No. Storeys	3	3	6	6	6	8	8	8
	h_n *(m)*	10.8	13.5	21.6	23.0	27.0	28.8	36.0	30.2
Single walls	$\beta = 0.70$	1.95	1.83	2.15	2.07	2.01	2.37	2.21	2.22
	$\beta = 0.85$	2.28	2.05	2.35	2.19	2.21	2.51	2.33	2.41
	$\beta = 1.00$	2.67	2.73	2.71	2.55	2.53	2.77	2.68	2.60
CWC	$\beta = 0.70$	1.94	1.75	2.03	1.96	1.96	2.33	2.13	2.11
	$\beta = 0.85$	2.24	1.90	2.16	2.03	2.03	2.37	2.25	2.23
Coupled walls	$\beta = 0.70$	1.95	1.79	2.05	1.99	1.91	2.14	1.97	1.99
	$\beta = 0.85$	2.11	1.97	2.16	2.08	2.04	2.29	2.11	2.20

The acceleration magnification factors in Figure 10-17 were also compared to the floor acceleration prediction method developed by Rodriguez et al. (2002) consisting of a bi-linear relationship defined by the top storey acceleration, C_{pn}, defined in Equation (10-29).

$$C_{pn} = \sqrt{\left[\frac{\eta_1}{R_1} C_h(T_1)\right]^2 + 1.75\ln(n) C_{ho}^2} \qquad (10\text{-}29)$$

Where η_1 = the first mode contribution coefficient

R_1 = reduction factor in the spectral acceleration to account for the effect of structural ductility

C_h = the spectral shape factor in accordance with NZS1170.5 (2004)

T_1 = the fundamental first mode period

n = is the number of storeys

C_{ho} = peak ground acceleration

As the comparison with numerical results shows in Figure 10-17, the current prediction is generally conservative, in particular for shorter buildings and coupled wall systems.

10.6 Validation of the proposed DBD procedure

The outcomes of the numerical analyses carried out as part of the previous section were the basis for the refinement of the current Displacement-Based Design procedure for post-tensioned timber walls. In particular, the parametric analysis showed that the current DBD inelastic displacement shape was inaccurate in the prediction of the observed behaviour of the buildings.

In this section, a new set of case study buildings were designed in accordance with the proposed and revised procedure, and non-linear time-history analyses were carried out to validate the procedure using a new set of ground motions.

The case study buildings were designed considering the following parameters:

- Importance level: IL2
- Return period factor: R = 1.0 (500 years return period)
- Location: Christchurch (Z = 0.3)
- Soil Type D
- Structural Performance Factor: $S_p = 1.0$
- Design drift: $\theta_d = 1.5\%$
- ductility factor: $\mu = 2.5$
- post-yielding stiffness: r = 0.2
- re-centering ratio: $\beta = 0.75$

The set of case study buildings is shown in Table 10-9 and includes 8 buildings of 2 to 9 storeys which were designed using a single wall system solution. The proposed displacement profile (see Equations (10-16) to (10-19)) was adopted in the design of case study buildings taller than two storeys. The results from the Displacement-Based Design procedure for the nine case study building are also summarized in Table 10-9 in terms of initial post-tensioning force and steel reinforcement layout.

Table 10-9. Design validation case study buildings design summary.

ID	**No. Of storeys**	**H**	**h_n**	**Wall depth**	**Storey Mass**	**n_{wall}**	A_p	T_{pt0}	A_s
		(m)	*(m)*	*(m)*	*(t)*	*(-)*	(mm)	(kN)	(mm)
1	2	3.6	7.2	3.6	221.8	2	4D42	1320	6D21
2	3	3.6	10.8	3.6	221.8	2	4D60	3600	8D24
3	4	3.6	14.4	3.6	221.8	3	4D60	4120	8D23.5
4	5	3.6	18.0	3.6	221.8	4	4D60	4480	8D23.5
5	6	3.6	21.6	4.8	221.8	2	6D60	9312	14D26.5
6	7	3.6	25.2	4.8	221.8	3	6D60	6960	12D25
7	8	3.6	28.8	4.8	221.8	4	6D60	6600	12D23
8	9	3.6	32.4	4.8	221.8	5	6D60	6000	12D22
9	10	3.6	36.0	4.8	221.8	6	6D50	5100	10D22

The set of case study buildings was subjected to a set of ground motions selected from the PEER ground motion database (Chiou *et al.*, 2008) and scaled in accordance with NZS 1170.5 (2004) for the soil type D spectrum considered in the design phase. The record set comprised of 10 ground motion records which are summarized in Table 10-10, and their spectra are reported and compared to the design spectrum in Figure 10-18.

Table 10-10. Design validation case study buildings design summary.

ID	Database ID	Event Name	Station	Year	Mw	PGA
1	NGA0006	Imperial Valley-02	El Centro Array #9	1940	6.95	0.26
2	NGA0170	Imperial Valley-06	EC County Center FF	1979	6.53	0.22
3	NGA0178	Imperial Valley-06	El Centro Array #3	1979	6.53	0.26
4	NGA0721	Superstition Hills-02	El Centro Imp. Co. Cent	1987	6.54	0.29
5	NGA1048	Northridge-01	Northridge - 17645 Saticoy St	1994	6.69	0.41
6	NGA1077	Northridge-01	Santa Monica City Hall	1994	6.69	0.59
7	NGA1158	Kocaeli, Turkey	Duzce	1999	7.51	0.33
8	NGA1198	Chi-Chi, Taiwan	CHY029	1999	7.62	0.26
9	NGA1227	Chi-Chi, Taiwan	CHY074	1999	7.62	0.21
10	NGA1521	Chi-Chi, Taiwan	TCU089	1999	7.62	0.29

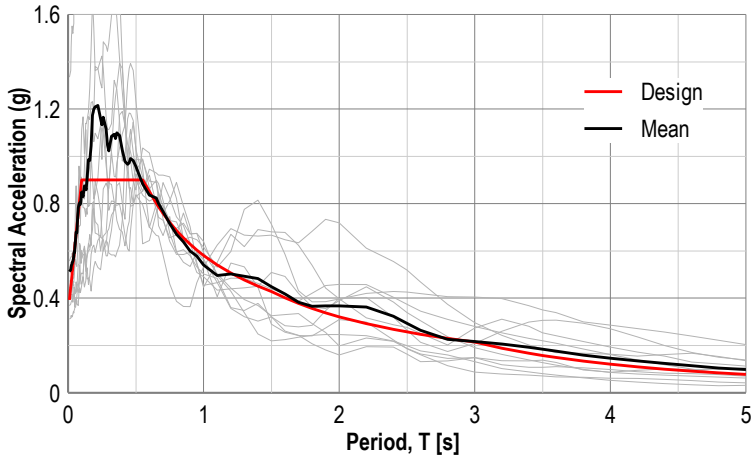

Figure 10-18. Selected record spectra comparison to design spectrum (scaling at T = 1.0s).

The average maximum displacement profiles of the nine case study buildings is shown in Figure 10-19 and the proposed Equation (10-16) shows good agreement with the numerical results. In general, the displacement appears to be slightly overestimated by Equation (10-16), in particular the case study building 1 (2 storeys) and, similarly to previous section, this is thought to be resulting from the damping model adopted in the analyses as pointed out by Grant et al. (2005).

Lastly, the modified capacity design moment envelope was compared to the average moment envelopes observed in the numerical analyses as shown in Figure 10-20 which also confirms that the proposed moment envelopes can be considered appropriate to predict the moment envelopes resulting from dynamic analyses.

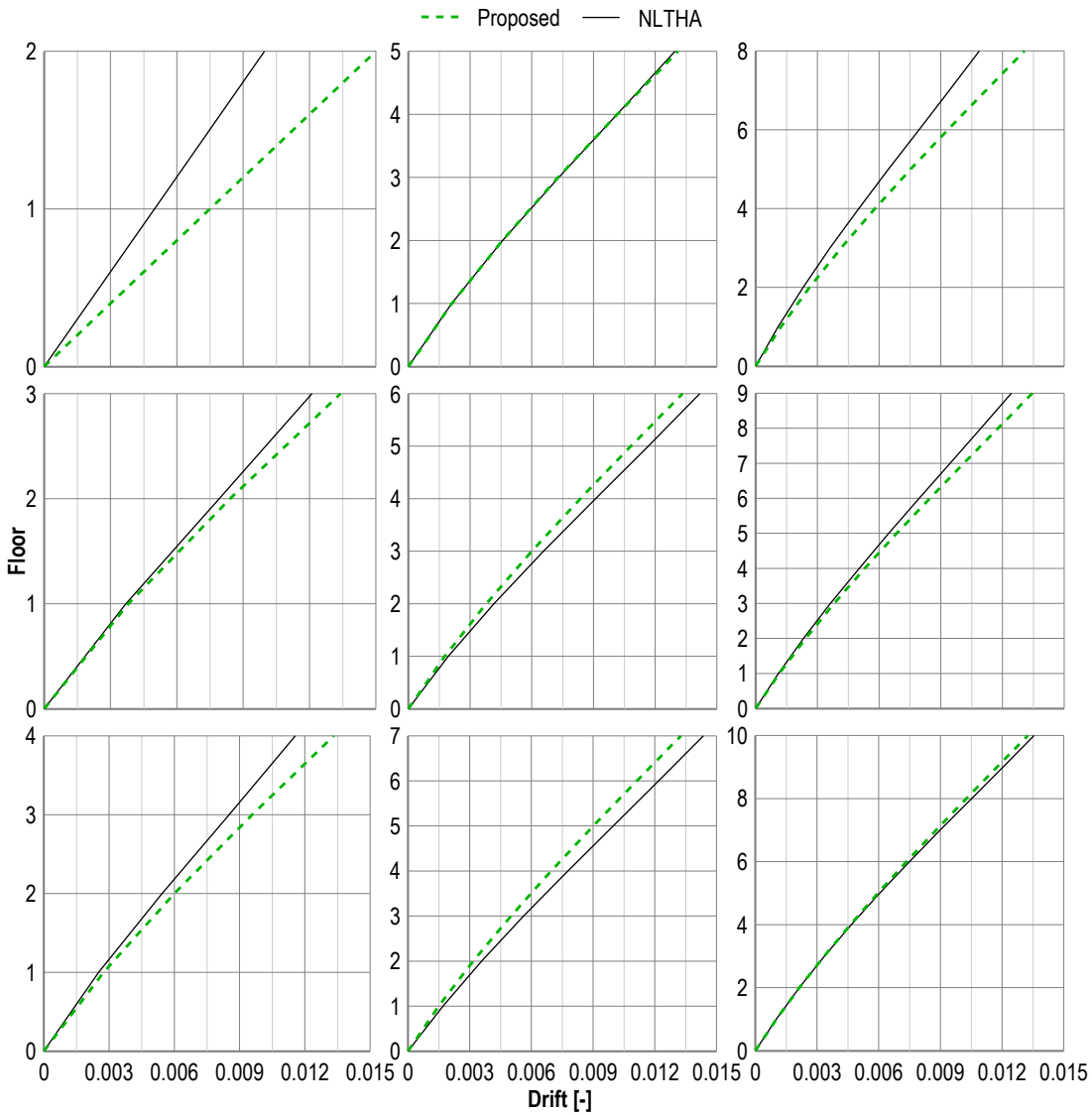

Figure 10-19.NLTHA average peak drift results comparison versus proposed design profile (Equations (10-16) to (10-19)).

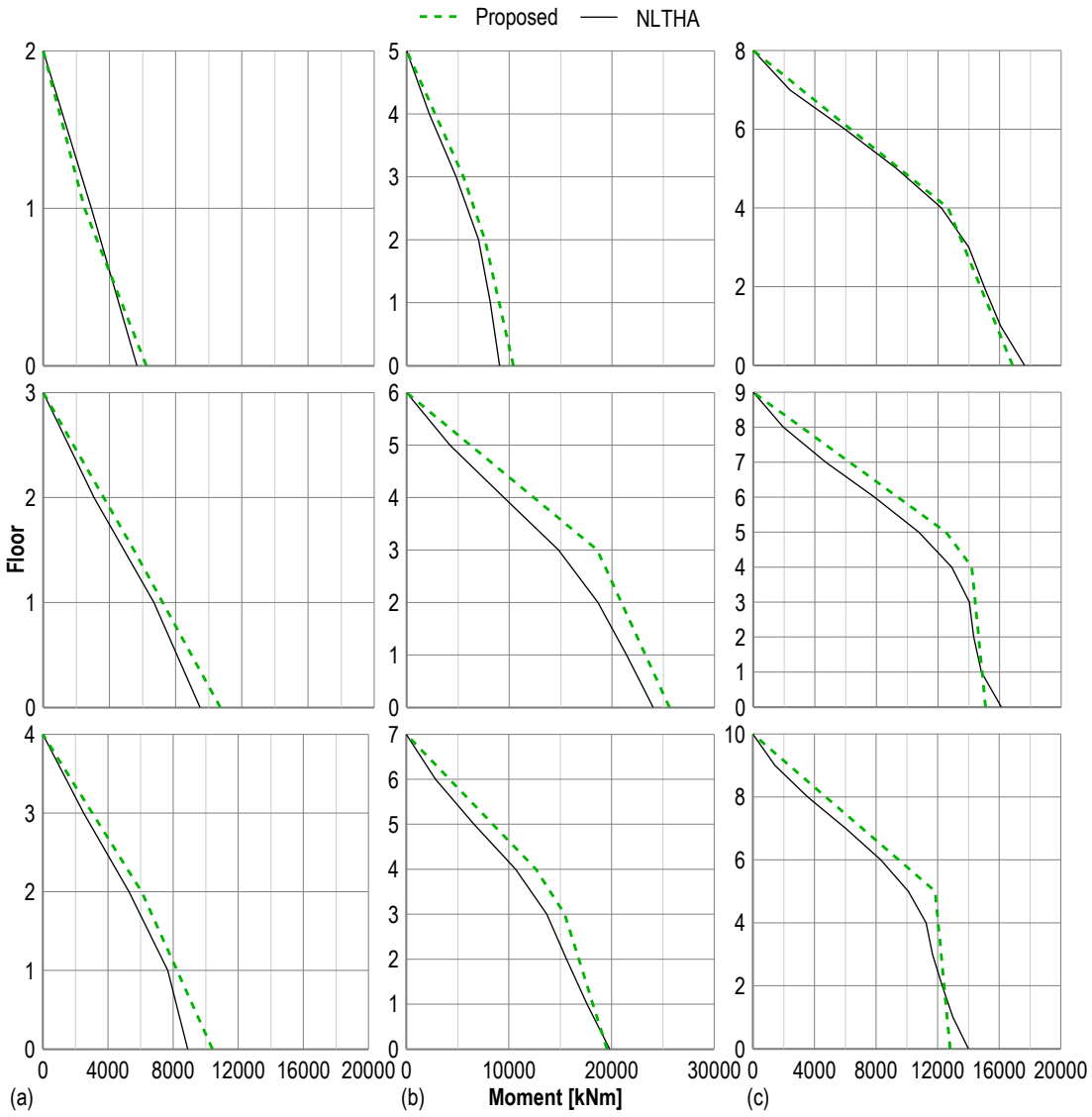

Figure 10-20. NLTHA moment envelopes comparison versus proposed capacity design envelope (Equation (10-28)).

10.7 Conclusions

This chapter presented and discussed the design and results of a comprehensive parametric study with the main objective of validate and refining the current Displacement-Based Design procedure.

In the initial part of the chapter the parametric design of the case study buildings was carried out and its results were discussed. The influence of the re-centering ratio was looked at in terms of total base shear, and the DBD results showed that a minimum decrease of the re-centering ratio (i.e. increase in dissipative contribution) results into a significant reduction of the design base shear. In particular, by distributing 15% of the total moment demand to the dissipative devices, the design base shear is reduced by approximately 40% when compared

to post-tensioned only solutions (i.e. non-dissipative). The parametric design also showed that a fully elastic design (i.e. post-tensioned only) would be impractical.

NLHTA results showed that the linear displacement profile assumed in the design phase was not satisfactory and an alternative design displacement profile was suggested based on analytical moment-rotation analyses and accounting for the wall's elastic deflections.

The numerical results confirmed the accuracy of the shear capacity demand envelope proposed by Priestley et al. (2007), whilst the current moment envelope equations proved inaccurate in capturing the observed response by either under-estimating the building's response (i.e. Priestley et al. (2007)) or significantly over-estimating that (i.e. Newcombe (2012)); therefore, the current capacity design moment envelope was re-calibrated based on the numerical results presented in this chapter.

In the final part of the chapter the proposed equations were validated with the design of a set of case study buildings in accordance with the refined DBD equations, which proved capable of fitting the numerical results of the new set of case study buildings.

10.8 References

Baird, A., Smith, T., Palermo, A., Pampanin, S. 2014. Experimental and Numerical Study of U-Shaped Flexural Plate (UFP) Dissipators. *New Zealand Society for Earthquake Engineering Annual Conference*, Auckland, New Zealand.

Chiou, B., Darragh, R., Gregor, N., Silva, W. 2008. NGA project strong-motion database. *Earthquake Spectra* 24(1): 23-44.

Grant, D.N., Blandon, C.A., priestley, M.J.N. 2005. *Modelling inelastic response in Direct Displacement-Based Design*. Technical report I. Press. Pavia.

Iqbal, A., Pampanin, S., Buchanan, A.H., Palermo, A. 2007. Improved Seismic Performance of LVL Post-tensioned Walls Coupled with UFP devices. *8th Pacific Conference on Earthquake Engineering*, Singapore.

Marriott, D.J. 2009. The Development of High-Performance Post-Tensioned Rocking Systems for the Seismic Design of Structures *PhD Dissertation*, Universtiy of Canterbury, Christchurch, New Zealand.

McKenna, F. 2011. OpenSees: A Framework for Earthquake Engineering Simulation. *Computing in Science and Engg.* 13(4): 58-66.

Newcombe, M. 2012. Seismic design of post-tensioned timber frame and wall buildings *PhD Dissertation*, University of Canterbury, Christchurch, New Zealand.

Pennucci, D., Sullivan, T.J., Calvi, G.M. 2011. *Performance-based seismic design of tall RC wall buildings*. Pavia, Italy, IUSS Press.

Priestley, M.J.N., Calvi, G.M., Kowalsky, M.J. 2007. *Displacement-based seismic design of structures*, IUSS Press.

Rodriguez, M.E., Restrepo, J.I., Carr, A.J. 2002. Earthquake-induced floor horizontal accelerations in buildings. *Earthquake engineering & structural dynamics* 31(3): 693-718.

Skinner, R.I., Kelly, J.M., Heine, A.J. 1974. Hysteretic dampers for earthquake-resistant structures. *Earthquake Engineering & Structural Dynamics* 3(3): 287-296.

Smith, T. 2014. Post-tensioned Timber Frames with Supplemental Damping Devices *PhD Dissertation*, University of Canterbury, Christchurch, New Zealand.

NZS 1170.5: Structural Design Actions - Part 5: Earthquake actions. Standards New Zealand. 2004.

Standards New Zealand 2009. *NZS 3404: Steel Structures Standard*.

11 Summary of the design procedure for dissipative post-tensioned rocking timber walls

11.1 Introduction

The main objective of this chapter is to provide a summary containing the necessary information for designing dissipative post-tensioned timber wall systems.

The chapter firstly discusses the design framework and performance-based design philosophy and then presents the main design parameters and equations developed in Chapters 9 and 10 which are used to determine the seismic demand in accordance with relevant standards and either a Force-Based or Displacement-Based Design procedure.

The capacity of the structural system must be evaluated, the analytical model, referred to as MMBA (Modified Monolithic Beam Analogy) is presented and that incorporates the refinements developed in Chapter 7.

Finally, a brief discussion and suggestion on the construction detailing of the systems is provided.

11.2 Design framework and philosophy

The general performance-based design philosophy of post-tensioned timber systems can be qualitatively summarized by Figure 11-1. The general hierarchy of strength and sequence of events would be (STIC, 2013):

1. Yield of the non-prestressed reinforcement (or dissipaters)
2. Yield of the timber at the rocking interface either in the column or the beam
3. Finally yielding of the post-tensioning reinforcement.

Such design philosophy allows the system to:

1. withstand small and frequent events with no significant damage
2. provide the required hysteretic damping under a design level earthquake
3. prevent structural collapse when subjected to a Maximum Credible Event (MCE)

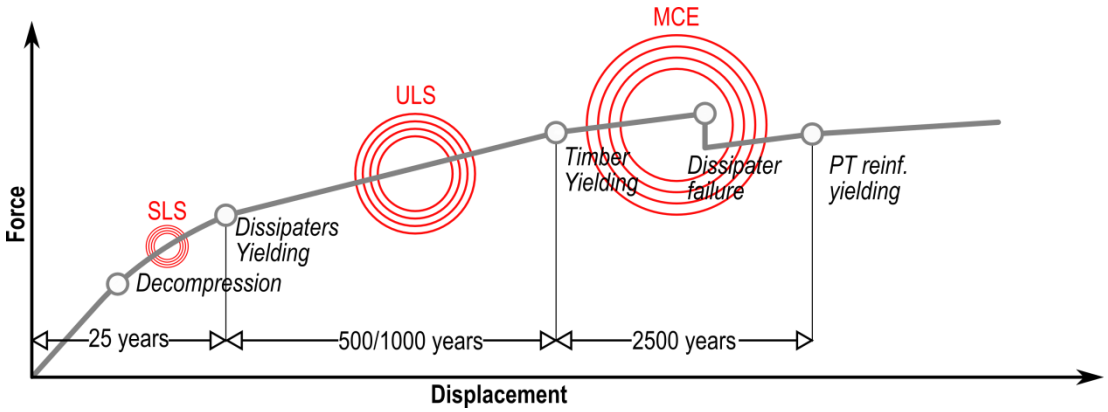

Figure 11-1. Qualitative push-over curve and performance limits.

The proposed system design requirements include suggested values of re-centering ratio, strain limits in the dissipaters at ULS and MCE level and initial timber stress:

- Initial timber stress (proportional to the initial post-tensioning force) shall not exceed 10% of the timber compressive strength.
- The maximum strain in the tension-compression yield dissipaters shall be in the range of 3-4% at Ultimate Limit State Earthquake (ULS) level and 6% at Maximum Credible Earthquake (MCE) level.
- Values of re-centering ratio (β) at design level shall be no less than 0.55 (55% re-centering contribution and 45% dissipative contribution) in accordance with NZS 3101 (2006b).

The design requirements proposed and showed above shall be used in the seismic design of a dissipative post-tensioned rocking wall system and adopting the seismic design procedure summarized by the flowchart in Figure 11-2.

Once the seismic demand has been determined following either a Force-Based Design or a Displacement-Based Design procedure, the section can be preliminarily designed and the post-tensioning and dissipative reinforcements are determined.

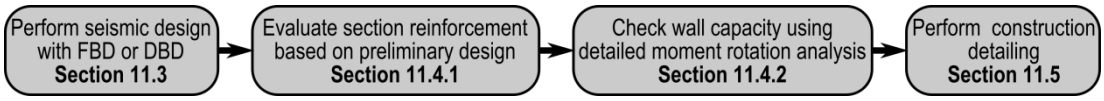

Figure 11-2. Seismic design procedure.

The preliminary design of the section shall then be checked via a more detailed analysis tool as shown in Chapter 7 of the dissertation. A moment-rotation analysis shall be performed to assess that the seismic demand does not exceed the section capacity; moreover, detailed material limit state shall be checked.

Once the section reinforcement has been designed and its capacity checked, the seismic resisting element shall be detailed as shown in section 11.4.4. The construction detailing of a dissipative post-tensioned rocking wall system generally involves the post-tensioning anchorage as well as the dissipaters and their attachment to the timber wall panel.

11.3 Determination of the horizontal actions

Both Force-Based Design (FBD) and Displacement-Based Design (DBD) methods of dissipative post-tensioned rocking timber wall systems have been discussed in the preceding chapters and can be used for the seismic design of post-tensioned timber walls.

In general, the seismic design of a multi-storey building starts from the determination of the building geometry (i.e. number of seismic resisting elements and location) and the total seismic mass. The seismic demand can then be evaluated according to either FBD or DBD procedure. Finally the total base shear resulting from the lateral load design methodology is distributed along the height of the building in accordance with the reference standard.

In particular, Chapter 10 discussed the determination of the seismic performance factors of post-tensioned timber walls to be used in a Force-Based Design procedure in accordance with the FEMA P-695 procedure.

Although not yet extensively adopted in seismic design codes worldwide, Displacement-Based Design (DBD) offers an alternative and reliable method to more traditional FBD

methods as also pointed out in Priestley (2003) and Priestley et al. (2007). Chapter 10 proposed refined DBD formulas for the seismic design of post-tensioned timber wall systems.

The following sections provide a detailed overview of the FBD and DBD procedures incorporating the findings of Chapters 10 and 11.

11.3.1 Force-Based Design (FBD)

The Force-Based seismic Design of a post-tensioned timber wall system shall be performed following the steps below which are also summarized in the flowchart shown in Figure 11-3.

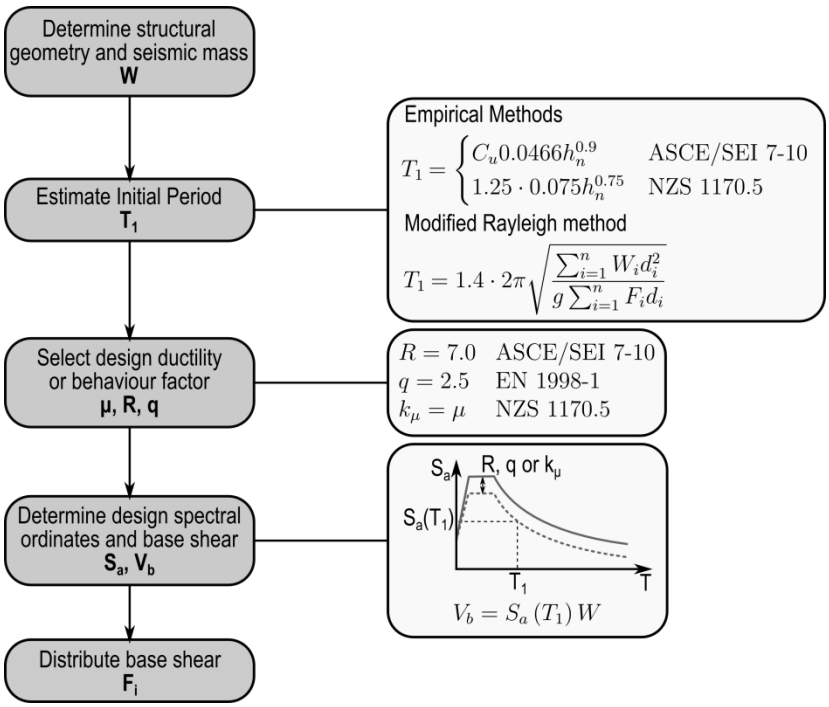

Figure 11-3. Force-Based Design procedure.

1. Determine the structural geometry and evaluate the seismic mass

The structure's geometry is defined and the number and location of the structural elements are determined also in accordance with architectural restraints. The seismic mass of the building is then evaluated based on the preliminary structure geometry.

2. Estimate initial period

The initial period of the structure can be evaluated using either an empirical formula or the Rayleigh method.

As shown in Chapter 9, modal analyses of the numerical models showed that the empirical formulas which fitted better the natural period of the structure were those referring to concrete frame buildings. Those empirical equations are reported in Equation (11-1).

$$T = C_u 0.0466 h_n^{0.9} \quad \text{ASCE 7-10}$$
$$T = 1.25 \cdot 0.075 h_n^{0.75} \quad \text{NZS 1170.5, EN 1998-1} \qquad (11\text{-}1)$$

Where C_u = the Coefficient for Upper Limit on Calculated Period (ASCE/SEI, 2010)
h_n = the height from the base of the structure to the uppermost seismic mass

A better estimation on the initial period can be obtained using the Rayleigh method.

Due to the particular rocking mechanism of the wall system, the yield-secant stiffness is rather different from the initial stiffness of the cantilevered wall; therefore, an amplification of 1.4 should be applied to the Rayleigh formula as shown in Chapter 11.

$$T_1 = 1.4 \cdot 2\pi \sqrt{\frac{\sum_{i=1}^{n} W_i d_i^2}{g \sum_{i=1}^{n} F_i d_i}} \qquad (11\text{-}2)$$

Where d_i = the horizontal displacement of the center of mass at level *i*, ignoring the effects of torsion
F_i = the displacing force acting at level *i*
i = the level of the structure under consideration
n = number of levels in the structure
W_i = the seismic weight at level *i*

3. Select the design ductility or behaviour factor/seismic reduction factor

The parametric seismic design performed in Chapters 9 and 10 on several case study buildings following the design philosophy reported in Section 11.2 showed that a ULS design ductility between 2 and 3 is suitable for dissipative post-tensioned rocking systems.

The resulting reduction factors vary in accordance with the reference standard used in the seismic design of the structure.

If NZS 1170.5 (2004) applies this value can be used to evaluate the inelastic spectrum scaling factor, k_μ, as

$$k_\mu = \begin{cases} \mu & for\, T_1 \geq 0.7s \\ \dfrac{(\mu - 1)T_1}{0.7} + 1 & for\, T_1 < 0.7s \end{cases} \qquad (11\text{-}3)$$

When ASCE/SEI 7-10 (2010) is used a seismic reduction factor R = 7.0 shall be used. This value was confirmed by the numerical results reported in Chapter 10 of this dissertation carried out in accordance with the FEMA P-695 procedure (ATC, 2009).

This value of the seismic performance factor corresponds to a behaviour factor q = 2.5 in accordance with EN 1998-1 (2004b) as shown by ADRS analyses shown in Chapter 9.

4. Determine the design spectral ordinates and the base shear

The 5% damped spectrum of the reference standard is selected for the building location and soil properties. The nominal spectrum is then reduced using either the inelastic spectrum scaling factor, k_μ, the seismic reduction factor, R, or the behaviour factor, q.

The design spectral acceleration is then determined for the estimated natural period of the structure and the base shear can be evaluated as

$$V = S_a(T_1)W \qquad (11\text{-}4)$$

Where W = total seismic weight

5. Distribute the base shear

Once the base shear is evaluated, it is distributed up the height of the building in accordance with the reference code. Equations (11-5) and (11-6) give a summary of the difference force distributions.

$$F_i = C_{vi}V$$
$$C_{vi} = \frac{W_i h_i^k}{\sum_{j=1}^{n} W_j h_j^k} \qquad \text{(ASCE 7-10 (2010))} \qquad (11\text{-}5)$$

$$F_i = F_t + 0.92V_b \frac{W_i h_i}{\sum_{i=1}^{n} W_i h_i} \qquad \text{(NZS 1170.5 (2004))} \qquad (11\text{-}6)$$

Where F_i = applied force at i-th storey

F_t = $0.08V_b$ at the top floor and zero elsewhere

C_{vi} = vertical distribution factor

V = design base shear

W_i = storey seismic weight

h_i = storey height

k = exponent related to the structure period as follows:

for structures having a period of 0.5s or less, k = 1

for structures having a period of 2.5s or more, k = 2

for structures having a period between 0.5s and 2.5s k shall be 2 or shall be determined by linear interpolation

11.3.2 Displacement-Based Design (DBD)

The Displacement-Based Design procedure for dissipative post-tensioned rocking wall systems can be summarized in the following points and as shown in the summary flowchart in Figure 11-4.

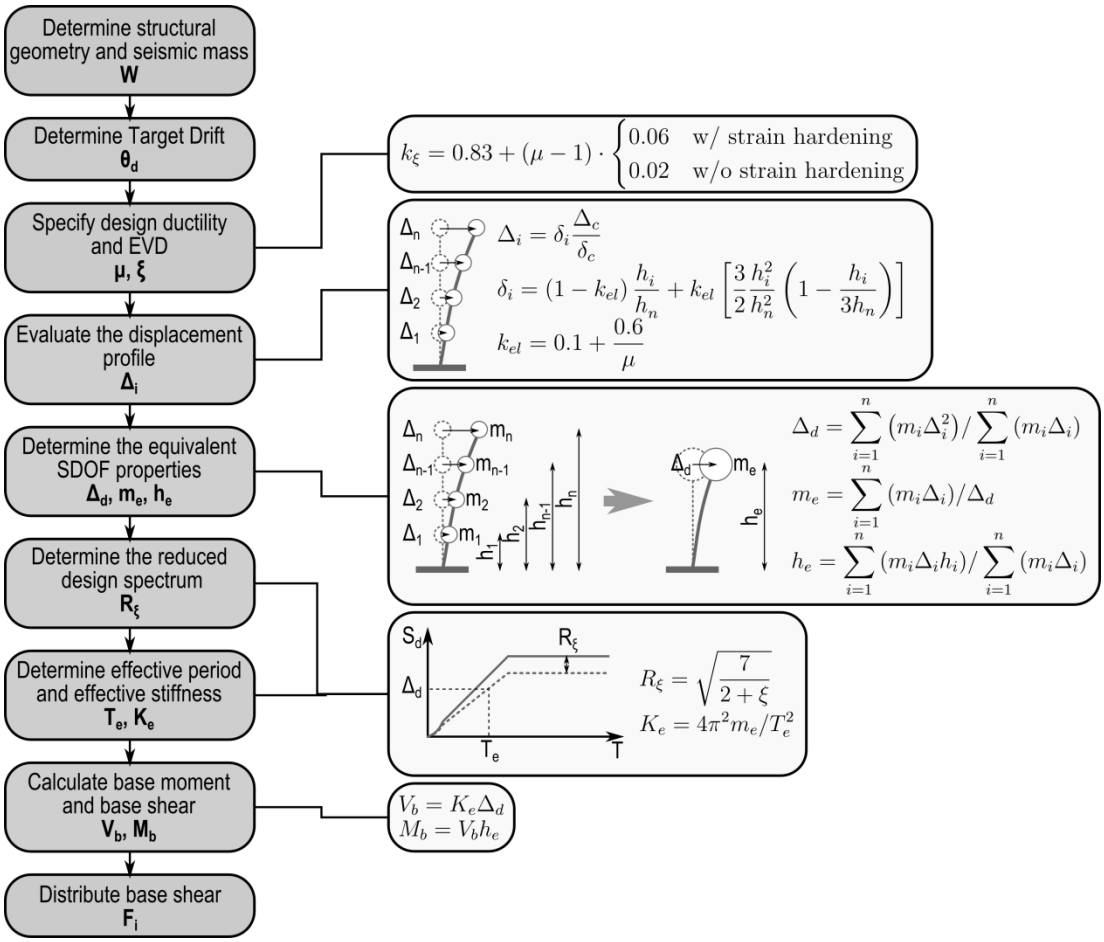

Figure 11-4. Displacement-Based Design procedure.

1. Determine the structural geometry and evaluate the seismic mass

The structure's geometry is defined and the number and location of the structural elements are determined also in accordance with architectural restraints. The seismic mass of the building is then evaluated based on the preliminary structure geometry.

2. Determine the target drift

Although in most design codes a maximum inter-storey drift limit of 2.5% is suggested (EN 1998-1 (2004b), NZS 1170.5 (2004), ASCE 7-10 (2010)), for dissipative post-tensioned rocking wall systems a top design displacement of 1 to 1.5% is suggested.

3. Specify design ductility and evaluate equivalent viscous damping

Design ductility in the range of 2 to 3 is generally suitable for post-tensioned wall systems, and for the selected design ductility, the equivalent viscous damping can be evaluated. That is given by the sum of the elastic damping and the hysteretic damping of the system.

$$\xi = \xi_{el} + \xi_{hyst} \qquad (11\text{-}7)$$

Where ξ_{el} = the elastic damping of the structure

ξ_{hyst} = the hysteretic damping

As pointed out by Marriott (2009) and Smith (2014) an elastic damping of 3% can be used for multi-storey timber buildings.

When evaluating the hysteretic viscous damping of systems characterized by flag-shaped hysteresis rules the analytical formula first proposed by Priestley et al. (2007) can be used. The formula is based on an ideal flag-shaped hysteresis and was refined in Chapter 8 and reported in Equation (11-8).

$$\xi = k_{dyn} k_{\xi} \frac{(2-2\beta)(\mu-1)}{\mu\pi\left[1+r(\mu-1)\right]} \qquad (11\text{-}8)$$

Where μ = ductility

β = re-centering ratio (M_{pt}/M_{tot})

r = post-yield stiffness factor

k_{ξ} = EVD modification factor given in Equation (11-9):

$$k_{\xi} = 0.83 + (\mu - 1) \cdot \begin{cases} 0.06 \ w/ \ strain\,hardening \\ 0.02 \ \ w/o \ strain\,hardening \end{cases} \qquad (11\text{-}9)$$

k_{dyn} = area-based hysteretic viscous damping dynamic reduction factor (Figure 11-5)

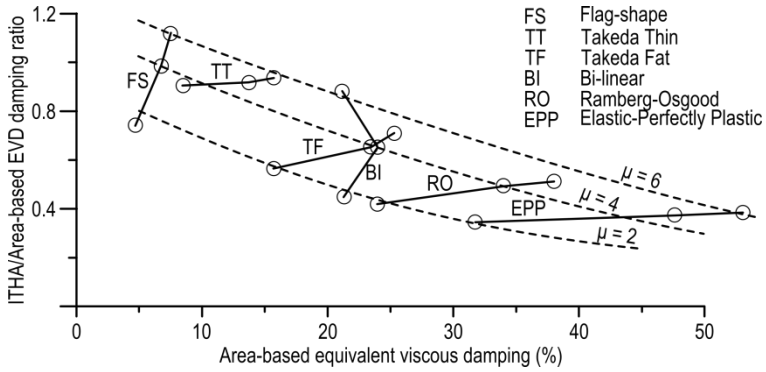

Figure 11-5. Correction factors to be applied to area-based equivalent viscous damping ratio (modified from Priestley et al. (2007)).

4. Evaluate the displacement profile

As shown by the numerical analyses results in Chapter 11 a linear displacement profile is not suitable for buildings taller than three storeys. As shown in Chapter 11 this can be due to more important elastic displacement contributions for tall buildings.

The displacements of the individual masses, Δ_i, are given by

$$\Delta_i = \delta_i \left(\frac{\Delta_c}{\delta_c} \right) \qquad (11\text{-}10)$$

Where Δ_c = the design displacement at the critical mass c

δ_c = the value of the inelastic mode shape at mass c

The inelastic mode shape, δ_i, shall be calculated according to Equation (11-11).

$$\delta_i = \begin{cases} \dfrac{h_i}{h_n} & n < 3 \\ \left(1 - k_{el}\right)\dfrac{h_i}{h_n} + k_{el}\left[\dfrac{3}{2}\left(\dfrac{h_i}{h_n}\right)^2\left(1 - \dfrac{h_i}{3h_n}\right)\right] & n \geq 3 \end{cases} \qquad (11\text{-}11)$$

Where h_i = the height of the i-th storey

h_n = the height of the top storey

k_{el} = an analytical calibrated factor accounting for the ratio of elastic contributions to the total drift given by Equation (11-12).

$$k_{el} = 0.1 + \frac{0.6}{\mu} \quad (11\text{-}12)$$

5. Determine the equivalent SDOF properties

When designing Multi-Degrees-Of-Freedom systems an equivalent Single-Degree-Of-Freedom substitute structure is used to represent the structure. The substitute structure is defined by design displacement, equivalent mass and equivalent height (Priestley *et al.*, 2007).

The design displacement of the equivalent SDOF structure is given by

$$\Delta_d = \frac{\sum_{i=1}^{n}\left(m_i \Delta_i^2\right)}{\sum_{i=1}^{n}\left(m_i \Delta_i\right)} \quad (11\text{-}13)$$

Where m_i = the mass of the i-th significant mass location

The effective height and effective mass given in Equations (11-14) and (11-15).

$$h_e = \frac{\sum_{i=1}^{n}\left(m_i \Delta_i h_i\right)}{\sum_{i=1}^{n}\left(m_i \Delta_i\right)} \quad (11\text{-}14)$$

$$m_e = \frac{\sum_{i=1}^{n}\left(m_i \Delta_i\right)}{\Delta_d} \quad (11\text{-}15)$$

6. Determine the displacement design spectrum

The 5% damped spectrum of the design site as given in the reference design standard is converted into a spectral displacement spectrum, $S_d(T)$, as follows

$$S_d(T) = \frac{S_a(T)}{\omega^2} = \frac{S_a(T)}{4\pi^2} T^2 \quad (11\text{-}16)$$

Where T = period

$S_a(T)$ = spectral acceleration at period T

The 5%-damped design displacement spectrum reduction factor is evaluated using Equation (11-17):

$$R_\xi = \left(\frac{7}{2+\xi} \right)^\alpha \quad (11\text{-}17)$$

Where α = 0.5 and 0.25 for far-field and near-field seismic spectra respectively

ξ = equivalent viscous damping

7. Determine the effective period and the effective stiffness

The effective, T_e, period is evaluated from the intersection of the equivalent SDOF design displacement and the reduced displacement spectrum.

The effective stiffness, K_e, can be then calculated using the effective (secant) period, T_e, and the equivalent mass as:

$$K_e = \frac{4\pi^2 m_e}{T_e^2} \quad (11\text{-}18)$$

8. Calculate the base shear and moment

The base shear and moment are determined using the effective stiffness, equivalent mass and effective height.

$$V_b = K_e \Delta_d \quad (11\text{-}19)$$

$$M_b = V_b H_e \quad (11\text{-}20)$$

9. Distribute the base shear

Once the base shear is evaluated, it is distributed up the height of the building in accordance with the reference code. Equations (11-5) and (11-6) give a summary of the difference force distributions. Alternatively, the force distribution in accordance with the DBD procedure can be used as Equation (11-21).

$$F_i = \frac{m_i \Delta_i}{\sum_{i=1}^{n} m_i \Delta_i} V_b \quad (11\text{-}21)$$

11.4 Section design

11.4.1 Preliminary design

The preliminary design of a dissipative post-tensioned rocking section is summarized in Figure 11-6.

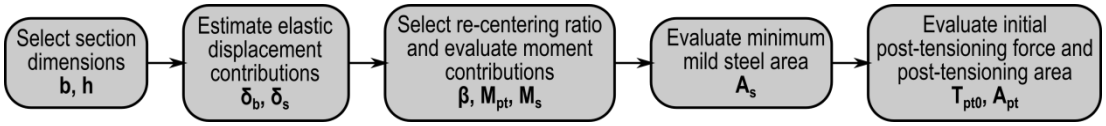

Figure 11-6. Preliminary design procedure.

Once the building seismic demand is determined in accordance with either FBD or DBD as shown in previous sections, the wall section dimensions shall be selected and the elastic bending, θ_b, and shear, θ_s, contributions to the total drift, θ_w, shall be determined in accordance with Equations (11-22) and (11-23).

$$\theta_b = \sum_{i=1}^{n} \frac{F_i h_i^3}{6 E_t I} \left(3 - \frac{h_i}{h_n} \right) \qquad (11\text{-}22)$$

$$\theta_s = \frac{\sum_{i=1}^{n} V_i H_i}{h_n G_t A_{ts}} \qquad (11\text{-}23)$$

Where F_i = the applied force at the i-th story
h_i = the height at i-th story
h_n = the height at top level *N*
H_i = the i-th inter-story height
V_i = the i-th story shear
E_t = the elastic modulus
G_t = the shear modulus
I = the second moment of area
A_{ts} = the shear area (i.e. 2A/3 for timber rectangular sections)

This results in the imposed connection rotation, θ_{imp}, in Equation

$$\theta_{imp} = \theta_w - (\theta_b + \theta_s) \qquad (11\text{-}24)$$

The post-tensioning and dissipative moment demands, M_{pt} and M_s respectively, are determined for a given re-centering ratio, β, as:

$$M_{pt}^{*} = \beta \frac{M_b}{\phi},\ M_s^{*} = (1-\beta)\frac{M_b}{\phi} \qquad (11\text{-}25)$$

Where ϕ = the strength reduction factor (ϕ = 0.9 for LVL in accordance with NZS3603 (1993))

For the preliminary design phase the post-tensioning bars and dissipaters groups are considered concentrated in their centroid (see Figure 11-7).

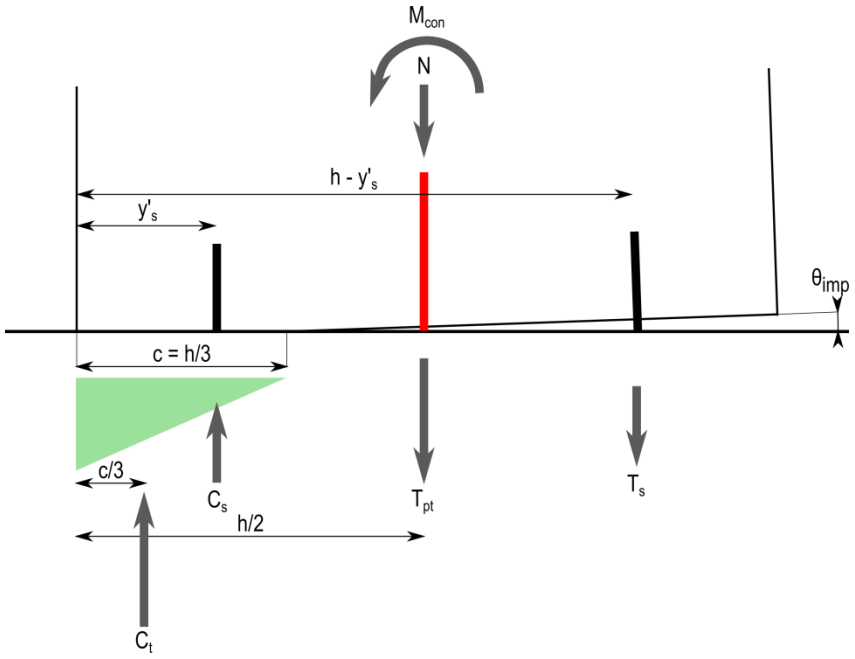

Figure 11-7. Preliminary design nomenclature.

To determine the moment capacity of the section the neutral axis depth must be assumed. This parameter mainly depends on the axial stress of the section, but for a section designed in accordance with the design requirements reported in Section 11.2 that can be assumed as 30% of the wall's section depth.

The required post-tensioning force to achieve the post-tensioning moment demand of Equation (11-25) can then be evaluated in accordance with Equation (11-26).

$$T_{pt} = \frac{M_{pt}^{*}}{h/2 - c/3} = \frac{M_{pt}^{*}}{0.4h}, c = 0.3h \qquad (11\text{-}26)$$

The post-tensioning area can then be evaluated also taking into account the design requirements as reported in Section 11.2. In fact, the post-tensioning bars must not yield under a Maximum Credible Earthquake and that can be achieved considering a maximum

stress at ULS of 70% of the yield strength of the post-tensioning bars. Therefore, the post-tensioned steel area, A_{pt}, is:

$$A_{pt} = \frac{T_{pt}}{0.7 f_{py}} \quad (11\text{-}27)$$

Where f_{py} = the post-tensioning steel yield strength

To evaluate the required initial post-tensioning force required, the post-tensioning bar elongation, Δ_{pt}, and the post-tensioning force increase, ΔT_{pt}, must be evaluated.

$$\Delta_{pt} = \theta_{imp}\left(\frac{h}{2} - c\right) = 0.2h\theta_{imp}, c = 0.3h \quad (11\text{-}28)$$

$$\Delta T_{pt} = \frac{\Delta_{pt}}{l_{ub}} E_{pt} A_{pt} \quad (11\text{-}29)$$

Where l_{ub} = the post-tensioning bars unbonded length

E_{pt} = the post-tensioning steel modulus of elasticity

The initial post-tensioning force must be evaluated by subtracting the post-tensioning force increase, ΔT_{pt}, from the required post-tensioning force, T_{pt}, as follows

$$T_{pt0} = T_{pt} - \Delta T_{pt} \quad (11\text{-}30)$$

The required force in the dissipative devices is evaluated by dividing the dissipative moment demand by the lever arm of each dissipater layer. The preliminary design can be performed by assuming that both the dissipative layers have yielded and considering that both the tension and compression forces are equal.

Considering tension-compression yielding dissipaters the minimum dissipater area is given in Equation (11-31).

$$A_s \geq \frac{M_s^*}{f_s\left(\varepsilon_s = 0.03\right)\left(h - 2y'_s\right)} \quad (11\text{-}31)$$

Where f_s = mild steel stress

y'_s = the compressive dissipater distance from the extreme compression fiber

If other types of dissipation devices are used (e.g. U-shaped Flexural Plates) the design force of the dissipater shall be evaluated instead:

$$T_s \geq \frac{M_s^*}{\left(h - 2y'_s\right)} \qquad (11\text{-}32)$$

11.4.2 Detailed design

The preliminary design shown in the previous section provides simplified equations for the evaluation of the section post-tensioning and dissipative reinforcement bars. Once the required post-tensioning bars and dissipaters have been determined a detailed design should be performed using the iterative moment-rotation analysis discussed in Chapter 7 and shown by the flowchart in Figure 11-8 and with the nomenclature reported in Figure 11-9.

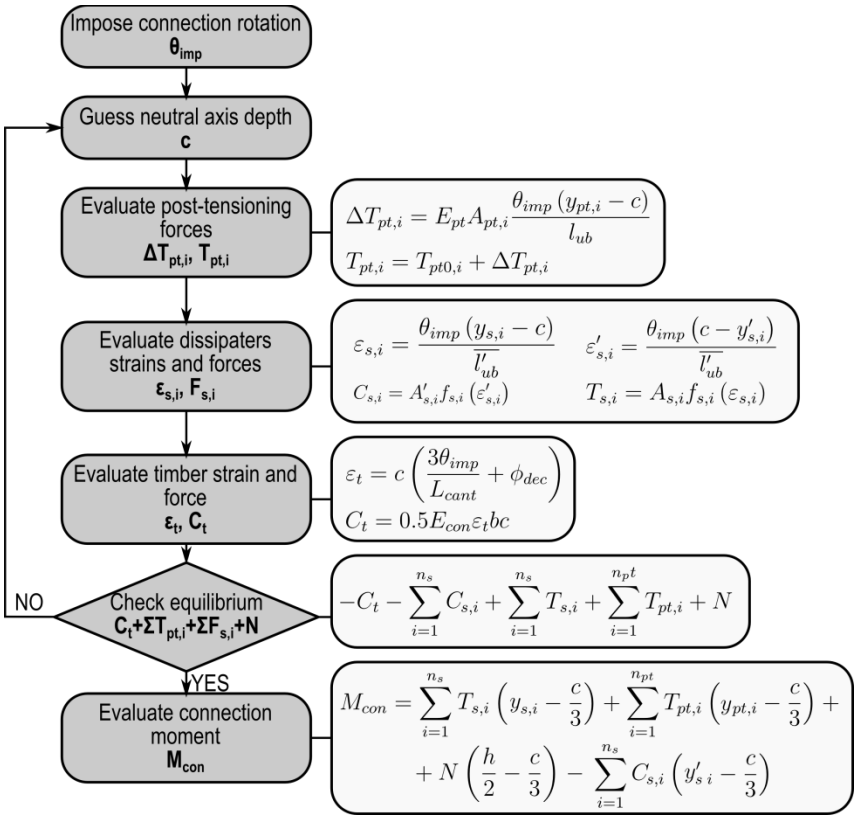

Figure 11-8. Detailed design iterative procedure.

1. Impose connection rotation

The first step in the detailed design of a dissipative post-tensioned rocking section is the determination of the imposed connection rotation, θ_{imp}, accounting for the elastic drift contribution of the cantilevered wall panel as shown in Equations (11-22) to (11-24).

2. Guess neutral axis depth

As part of the procedure the neutral axis, c, must be guessed and several iterations may be required to achieve the force equilibrium.

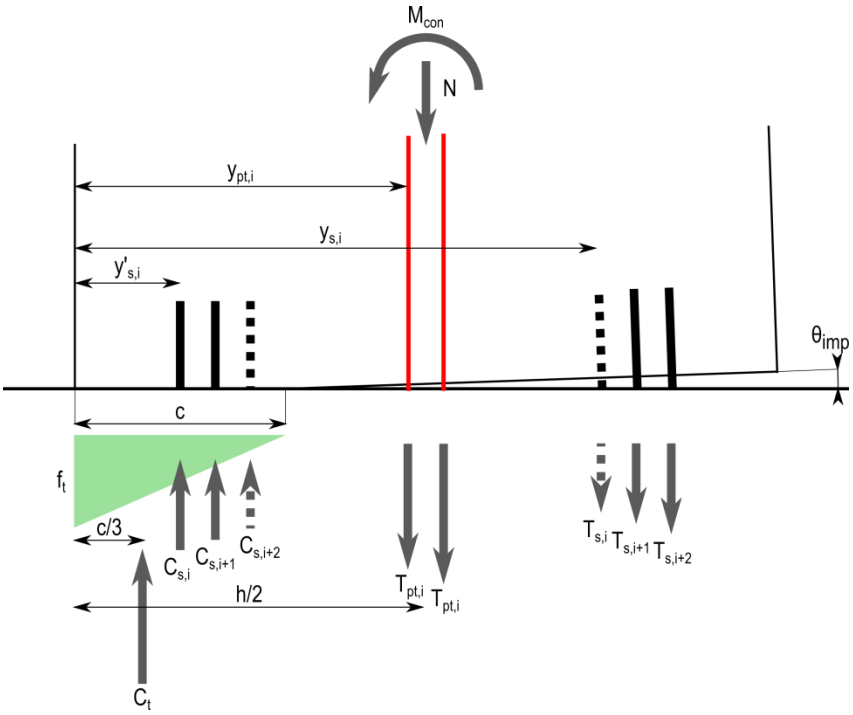

Figure 11-9. Detailed design nomenclature

3. Evaluate post-tensioning forces

The elongation in the i-th post-tensioning bar, $\Delta_{pt,i}$, can be evaluated as

$$\Delta_{pt,i} = \theta_{imp}\left(y_{pt,i} - c\right) \qquad (11\text{-}33)$$

Where $\Delta_{pt,i}$ = elongation of the i-th post-tensioning reinforcement layer

$d_{pt,i}$ = distance of the i-th post-tensioning reinforcement layer from the extreme compression fiber

The resulting strain increment, $\Delta\varepsilon_{pt,i}$, for a given unbonded length, l_{ub}, is

$$\Delta\varepsilon_{pt,i} = \frac{\Delta_{pt,i}}{l_{ub}} \qquad (11\text{-}34)$$

The post-tensioning bar elongation results in a force increment, $\Delta T_{pt,i}$, which is evaluated considering that the bar remains in the elastic range of stresses

$$\Delta T_{pt,i} = \Delta\varepsilon_{pt,i} E_{pt} A_{pt,i} \quad (11\text{-}35)$$

Where E_{pt} = post-tensioning steel elastic modulus

$A_{pt,i}$ = cross-section area of the i-th post-tensioning reinforcement layer

The sum of the force increment and the initial post-tensioning force in each bar, $T_{pt0,i,}$ as evaluated in the preliminary design phase gives the total post-tensioning force, $T_{pt,i}$, in the post-tensioning tendons.

$$T_{pt,i} = T_{pt0,i} + \Delta T_{pt,i} \quad (11\text{-}36)$$

Where $T_{pt0,i}$ = initial post-tensioning force of the i-th post-tensioning reinforcement layer

4. Evaluate dissipaters strain and force

The elongation in the dissipation devices, $\Delta_{s,i}$, can be evaluated similarly to the post-tensioning reinforcement above and is given by Equation (11-37).

$$\begin{aligned} \Delta_{s,i} &= \theta_{imp}\left(y_{s,i} - c\right) \\ \Delta'_{s,i} &= \theta_{imp}\left(c - y'_{s,i}\right) \end{aligned} \quad (11\text{-}37)$$

Where $y_{s,i}$ = distance of the i-th mild steel tension reinforcement layer from the extreme compression fiber

$y'_{s,i}$ = distance of the i-th mild steel compressive reinforcement layer from the extreme compression fiber

The resulting force depends on the type of dissipater used. As Chapter 7 showed either tension-compression yielding dissipaters or U-shaped Flexural Plate (UFP) dissipaters can be used.

Tension-compression yielding dissipaters

When tension-compression yielding dissipaters are used the strain in the bar, $\varepsilon_{s,i}$, is evaluated considering the displacement resulting from Equation (11-37) and the unbonded length of the dissipater, l'_{ub}. This shall account for every elastic contribution coming either from the elastic displacements of the connection in external dissipaters or strain penetration effects in internal bars.

$$\varepsilon_{s,i} = \frac{\Delta_{s,i}}{l'_{ub}} \quad (11\text{-}38)$$

Where $\overline{l_{ub}^{'}}$ is given in Equations (11-39) and (11-40) for external and internal dissipaters respectively.

$$\overline{l_{ub}^{'}} = k_a L_{fuse} + \frac{E_s A_{s,i}}{k_{con}} \qquad (11\text{-}39)$$

Where k_a = is a correction factor as defined in Chapter 4 and accounting for different flexibility contributions

L_{fuse} = dissipater's fuse length

E_s = mild steel modulus of elasticity

$A_{s,i}$ = cross-section area (i.e. fuse area) of the i-th dissipative layer

k_{con} = connection flexibility

$$\overline{l_{ub}^{'}} = l_{ub}^{'} + \left(\frac{2}{3}0.022 + 0.032\right) f_{sy} D_{fuse} \qquad (11\text{-}40)$$

Where $l_{ub}^{'}$ = the unbonded length of the internal dissipater

f_{sy} = the mild steel yielding strength

D_{fuse} = the fuse diameter of the dissipater

Once the strain in the mild steel dissipater is evaluated, the stress, $f_{s,i,}$ can be worked out using a bi-linear stress-strain relationship:

$$f_{s,i} = f_{sy}\left[1 + r\left(\frac{\varepsilon_{s,i}}{\varepsilon_{sy}} - 1\right)\right] \qquad (11\text{-}41)$$

Where r = post-yielding stiffness ratio (usually taken as 0.8% for mild steel)

ε_{sy} = mild steel yield strain

The steel forces, $T_{s,i}$ and $C_{s,i}$, can now be worked out from Equation (11-42):

$$\begin{aligned} T_{s,i} &= f_{s,i} A_{s,i} \\ C_{s,i} &= f'_{s,i}\, A'_{s,i} \end{aligned} \qquad (11\text{-}42)$$

U-shaped Flexural Plates

UFPs can also be used to provide dissipation to the system. Rather than determining the strain in the device, the force-displacement relationship can be modelled using a Ramberg-Osgood hysteretic rule.

$$\Delta_s = \frac{F_u}{k_0}\left[1+\left(\frac{F_s}{F_u}\right)^{R-1}\right] \quad (11\text{-}43)$$

Where F_u = the UFP yielding force (Equation (11-44))

k_0 = the UFP initial stiffness (Equation (11-45))

R = the Ramberg-Osgood factor (Equation (11-46))

The parameters above were calibrated versus experimental and numerical results by Baird et al. (2014)

$$F_u = \frac{f_{sy} b_u t_u^2}{2D_u} \quad (11\text{-}44)$$

$$k_0 = \frac{16E_s b_u}{27\pi}\left(\frac{t_u}{D_u}\right)^3 \quad (11\text{-}45)$$

$$R = 7.1\ln\left(\frac{t_u}{D_u}\right) + 29.5 \quad (11\text{-}46)$$

Where b_u = width of the UFP plate section

t_u = thickness of the UFP plate section

D_u = diameter of UFP plate bend

E_s = steel elastic modulus

5. Evaluate timber strain and force

As indicated in Chapter 7 of this dissertation, the moment-rotation iterative procedure must rely on the global strain compatibility of an equivalent monolithic element (Pampanin *et al.*, 2001) referred to as Modified Monolithic Beam Analogy (Palermo *et al.*, 2005). As shown by Newcombe et al. (2008) and reported in Chapter 7, the elastic portion of the MMBA can be used to model post-tensioned rocking timber sections. The maximum strain, ε_s, is evaluated as

$$\varepsilon_t = c\left(\frac{3\theta_{imp}}{L_{cant}} + \phi_{dec}\right) \quad (11\text{-}47)$$

Where ϕ_{dec} = decompression curvature

$$\phi_{dec} = \frac{M_{dec}}{E_{con} I} \tag{11-48}$$

Where E_{con} = connection modulus (equal to $0.7E_t$ for post-tensioned timber walls)

E_t = timber modulus of elasticity

I = section second moment of area

L_{cant} = cantilever length

The timber force is evaluated assuming a triangular stress distribution:

$$C_t = 0.5 E_{con} \varepsilon_t b c \tag{11-49}$$

Where b = section width

6. Check equilibrium

The force balance can be then evaluated using Equation (11-50)

$$-C_t + \sum_{i=1}^{n_s} T_{s,i} - \sum_{i=1}^{n_s} C_{s,i} + \sum_{i=1}^{n_{pt}} T_{pt,i} + N \tag{11-50}$$

And the neutral axis depth is iterated until balance is reached.

7. Evaluate connection moment

Finally, the connection moment is evaluated and checked versus the moment demand evaluated in the seismic design phase.

$$M_{con} = \sum_{i=1}^{n_{pt}} T_{pt,i} \left(y_{pt,i} - \frac{c}{3} \right) + \sum_{i=1}^{n_s} T_{s,i} \left(y_{s,i} - \frac{c}{3} \right) - \sum_{i=1}^{n_s} C_{s,i} \left(y'_{s,i} - \frac{c}{3} \right) + N \left(\frac{h}{2} - \frac{c}{3} \right) \tag{11-51}$$

Where h = section depth

11.4.3 Strength checks

Once the section reinforcement has been determined, the wall's panel strength checks must be performed in accordance with the relevant material standard. The strength checks shown below are in accordance with NZS3603 (Standards New Zealand, 1993).

As the numerical results presented in Chapter 11 shown, higher modes effects have a major influence in the shear and moment envelopes along the height of the building. Those should be taken into account when checking the Ultimate Limit State strength of the timber panel.

Bending strength

The bending strength of the wall element is checked according to New Zealand Timber Code (Standards New Zealand, 2006a)

$$\phi M_{n,b} \geq \phi^o M_b \qquad (11\text{-}52)$$

Where ϕ^o = the over-strength factor

M_b = the design base moment

ϕ = the strength reduction factor

$M_{n,b}$ = the nominal bending strength of the section given by Equation (11-53).

$$\phi M_{n,b} = \phi k_1 k_4 k_5 k_8 f_b^{'} Z \qquad (11\text{-}53)$$

Where k_1 = the load duration factor for strength

k_4 = the parallel support factor

k_5 = the grid system factor

k_8 = the stability factor

$f^{'}_b$ = the timber bending strength accounting for the size factor given by Equation (11-54))

$$f_b^{'} = f_b \left(\frac{300}{h} \right)^{0.167} \qquad (11\text{-}54)$$

Where f_b = the timber bending strength

h = the section depth in millimetres

When the wall's section has the same dimensions throughout the building height, the base moment only shall be checked. If a reduced section is used at higher storeys, the strength checks shall take into account the simplified moment envelope suggested in Chapter 10 of this dissertation as summarized below.

The simplified moment envelope accounting for higher modes effects is given by a bi-linear curve defined by the over-strength base moment, $\phi^o M_b$, and the over-strength moment at mid-height, $M^o_{0.5Hn}$, given in Equation (11-55).

$$M^o_{0.5Hn} = C_{1,T} \phi^o M_b \qquad (11\text{-}55)$$

Where $C_{1,T}$ = seismic coefficients given in Equation (11-56)

$$C_{1,T} = 0.4 + 0.2(T_i - 0.4) + 0.1(T_i - 0.4)\left(\frac{\mu}{\phi_0} - 1 \right) \qquad (11\text{-}56)$$

Where T_i = the initial period of the structure

μ/ϕ^o = the ductility demand of the structure

Shear Strength

The shear strength of the wall is checked versus the over-strength design base shear, V^o_{Base}, considering dynamic amplification factors defined in Chapter 11.

$$V^o_{Base} = \phi^o \omega_V V_b \quad (11\text{-}57)$$

Where ω_V = the dynamic amplification factor given in Equation (11-58)

V_b = the design base shear

$$\omega_V = \frac{\mu}{\phi^o} C_{2,T} + 1.0 \quad (11\text{-}58)$$

Where $C_{2,T}$ = seismic coefficients given in Equations (11-59)

$$C_{2,T} = 0.062 + 0.4(T_i - 0.5) \le 1.15 \quad (11\text{-}59)$$

The shear strength check in accordance with NZS3603 (1993) is given by Equation

$$\phi V_{n,b} \ge V^o_{Base} \quad (11\text{-}60)$$

Where V_b = the design base shear

ϕ = the strength reduction factor

$V_{n,b}$ = the nominal bending shearof the section given by Equation (11-61).

$$\phi V_{n,b} = \phi k_1 k_4 k_5 f_s A_{s,w} \quad (11\text{-}61)$$

Where f_s = the timber shear strength

$A_{s,w}$ = the shear cross-sectional area of the wall's panel

Like the moment strength checks, when the section dimensions vary over the height of the building the shear envelope shall be considered. The simplified shear envelope is defined by a linear interpolation between the over-strength design base shear, V^o_{Base}, and the over-strength top shear, V^o_n, which is evaluated in Equation

$$V^o_n = C_{3,T} V^o_{Base} \quad (11\text{-}62)$$

Where $C_{3,T}$ = seismic coefficients given in Equation (11-63)

$$C_{3,T} = 0.9 - 0.3T_i \ge 0.3 \quad (11\text{-}63)$$

11.4.4 Over-strength factors

As discussed by Priestley et al. (2007) a section being capacity-protected should account for the actual flexural strength.

As proposed by Priestley et al. (2007) the recommended values for the over-strength factor is $\phi^o = 1.25$. If strain-hardening is ignored in determining the required section properties $\phi^o = 1.60$ is recommended.

As suggested in Chapter 10 of this dissertation, the values above are deemed conservative and an over-strength factor $\phi^o = 1.15$ shall be adopted. This factor shall be increased to $\phi^o = 1.30$ if strain hardening is ignored in the determination of the section capacity.

11.5 Serviceability limit state design

The body of research carried out and shown in this dissertation focused on the seismic behaviour of post-tensioned rocking timber wall systems, and in particular on their behaviour under Ultimate Limit State level demand or higher.

It must be clarified that, although none of the case study buildings was governed by SLS design limits; this may not be true for different cases. The case study buildings considered in this research work were assumed to be located in Christchurch which is a high-seismic area and a ULS governed design is generally expected.

When the building is to be designed in a lower seismicity area SLS design may be governing the design of the structure under either seismic or wind loading, in accordance with the relevant standards.

In such a design scenario the post-tensioned wall is not expected to yield the dissipater or to develop gap opening at the wall-foundation interface. Therefore, the moment demand of the wall shall be evaluated as follows:

$$M^* \le M_{dec} = \left(T_{pt0} + N\right)\frac{Z}{A} \qquad (11\text{-}64)$$

Where M^* = the base moment SLS demand

M_{dec} = the decompression moment

T_{pt0} = the initial post-tensioning force

N = the axial force from gravity loading

Z = the section modulus

A = the section area

Once the condition in Equation (11-64) is satisfied the building deflection can be evaluated the vertical cantilever deflection and checked versus code-based SLS deflection limits.

11.6 Discussion on post-tensioning losses

Due to its structure, timber is subjected to dimensional variations which are caused by thermal and relative humidity variations, as well as creep.

As shown in previous sections, the post-tensioning force is a major design parameter and possible post-tensioning losses shall be accounted for in the initial design phase of the structural element.

The main effect of post-tensioning losses on the behaviour of the system would be a decrease in its capacity which depends on the magnitude of post-tensioning loss as well as on the design re-centering ratio. It is worth noticing in fact that a post-tensioning loss of 10% would result in a capacity loss of 6% to 10% of the section capacity with a re-centering ratio, β, ranging from 0.6 to 1.0.

Experimental test results on post-tensioned LVL beams loaded parallel to the grain (Davies *et al.*, 2011) highlighted losses of 1.4% and 1.5% for respectively pure creep and mechano-sorption creep over a one year period. The total post-tensioning loss of 2.9% was approximately extrapolated of a 50 years period assumed service life and resulted in between 6 and 10% (Davies *et al.*, 2011).

Analytical prediction of post-tensioning losses have been developed base on the experimental data above by Giorgini et al. (2010) and Fragiacomo et al. (2011).

11.7 Construction detailing

As highlighted in the experimental stages of this dissertation, construction detailing can have a major influence on the actual behaviour of the system.

To ensure that the designed solution matches the predicted design response, few construction detailing aspects must be accounted for. This section provides a brief discussion on the main construction details to be addressed.

11.7.1 Post-tensioning anchorage

A correct detailing of the post-tensioning anchorage system is crucial to avoid localized plasticity which can result in a reduction of the post-tensioning forces, thus a decrease in the wall capacity.

A simplified and rather conservative design of the post-tensioning plate is shown in Appendix C. That consists of assuming the post-tensioning anchorage plate as a continuous beam subjected to a uniformly distributed load (timber stress). The supports represent the point loads from the post-tensioning bars.

While this simplified modelling is rather conservative for the evaluation of the thickness of the anchorage plate, it generally underestimates stress concentrations around the post-tensioning voids in the timber section.

Figure 11-10 shows the Finite Element Model (FEM) results of a bearing plate, and as the vertical cross-section shows, the axial stress in the plate is well below the steel strength (i.e. 300MPa).

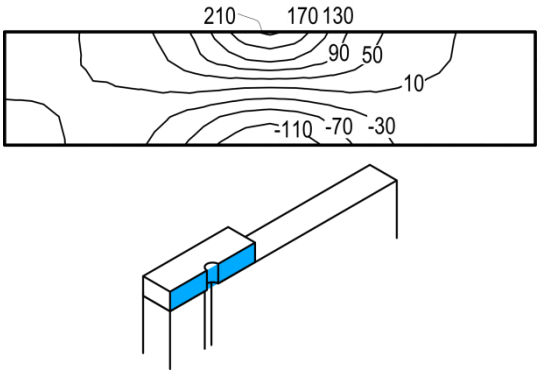

Figure 11-10. Axial stress fields in the post-tensioning anchorage plate.

To avoid significant stress concentrations, it is good practice to design a post-tensioning anchorage bearing on the full wall section width. In this case, concentrated stress values are rather limited and within material strength limits. If this condition does not apply and the plate is bearing on a reduced area, stress concentration can be more significant (see Figure 11-11).

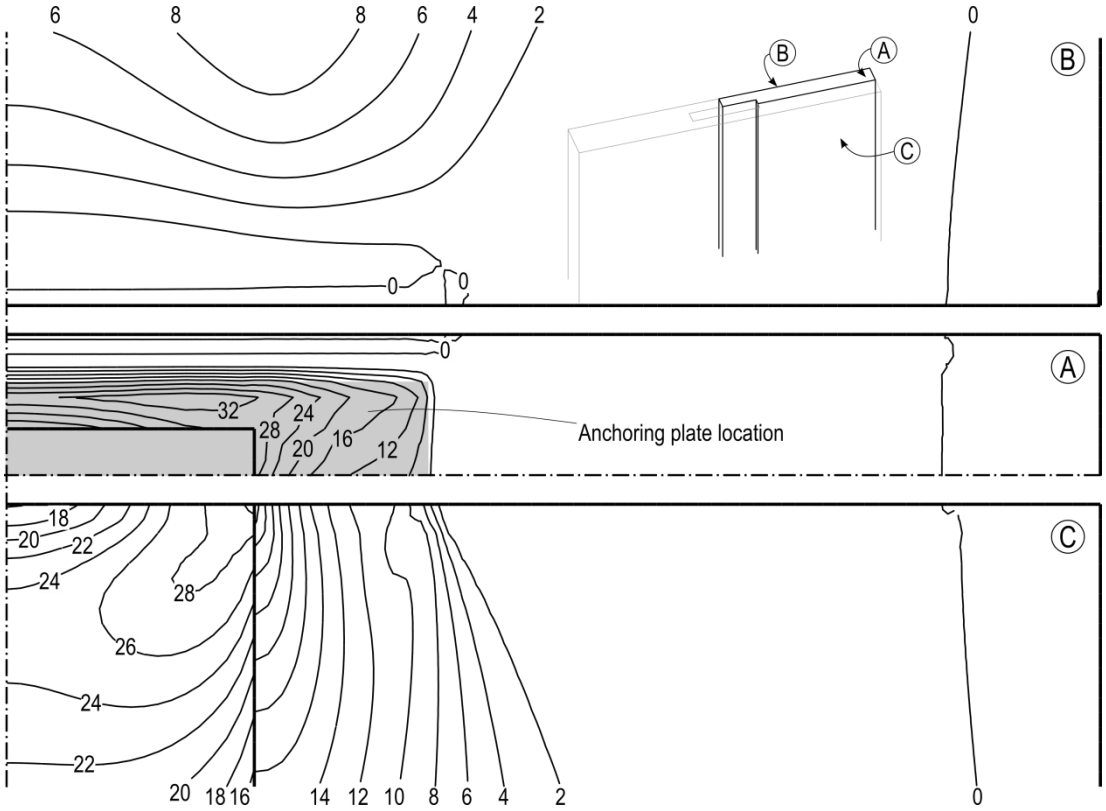

Figure 11-11. Wall parallel-to-grain axial stress fields (in MPa, compression is positive) for the anchorage option 3.

A more detailed discussion on the effects of different construction detailing deficiencies is provided in Appendix C.

11.7.2 Dissipater connections

Experimental results on post-tensioned rocking timber walls in Chapters 5 and 6 showed that some reduction in the area-based hysteretic viscous damping can occur as a result of a flexible dissipater connection.

In the experimental stages presented in Chapters 5 and 6 the dissipater connection was designed using timber rivets (Zarnani *et al.*, 2014). Several fastening options such as screws, nails, bolts or split rings are available.

Numerical analyses discussed in Chapter 8 highlighted the importance of the dissipater's connection stiffness. The results suggested that a connection to dissipater stiffness ratio greater than 1.0 is preferred.

As part of the design process, once the post-tensioned wall reinforcement has been designed, the connection must be detailed accounting for the suggested stiffness ratio of 1.0 (see Chapter 8).

The stiffness of several type of metallic fasteners can be designed in accordance with Table 7.1 of EN 1995-1-1 (2004a)and Equation (11-65).

$$K_{ser} = \begin{cases} 2\dfrac{\rho_m^{1.5} d}{23} & for\ bolt,\ screws\ and\ nails \\ 2\dfrac{1.5\rho_m^{1.5} d_c}{4} & for\ toothed-plate\ connectors \end{cases} \qquad (11\text{-}65)$$

Where K_{ser} = the slip modulus

ρ_m = the timber mean density

d = the fastener diameter

d_c = the split-ring diameter

When timber rivets are used as fastening option, experimentally calibrated Equation (11-66) By Zarnani et al. (2014) shall be used.

$$\delta = 4\left(1-\sqrt{1-\frac{F}{Q}}\right) \qquad (11\text{-}66)$$

Where F = the force in the connection and

Q = the connection capacity

Whilst the experimental and numerical work has shown in this dissertation highlighted the importance of the connection stiffness, the strength of such connection must be checked also considering over-strength factors.

When mild steel dissipaters are used the over-strength modification factor of 1.3 as suggested by NZS 3404 (1997) shall be used. Therefore:

$$1.3S^* \le \phi Q_n \qquad (11\text{-}67)$$

Where S^* = the connection demand given by the characteristic strength of the dissipater group

ϕ = strength reduction factor

Q_n = nominal strength of the connection

11.7.3 Shear keys

In post-tensioned rocking elements high compressive forces are developed by the post-tensioning tendons to provide a moment-resisting connection.

When the element is subjected to horizontal forces, the post-tensioning force acting on the wall element can results in significant friction force developing at the wall-foundation interface.

Despite the friction force developed, Appendix B of NZS3101:2006 (2006b) does not permit resisting of shear by friction, differently from ACI 318-11 (ACI, 2011); therefore, external shear keys needs to be designed to carry the horizontal action and prevent slip in the wall's longitudinal direction.

As shown in Chapter 5 of this dissertation a 40mm thick steel plate was designed for preventing both longitudinal and transverse sliding of the wall panel. This design accounted for the loads expected under a quasi-static type of loading.

Similar solutions can be adopted and detailed to avoid local failure of the timber section, such as perpendicular-to-grain timber crushing.

In particular, it is important to account for higher modes amplifications. As shown in the numerical analyses in Chapter 11 a significant dynamic amplification can occur due to higher mode effects and that amplified shear must be accounted for in the shear key design.

11.8 References

ACI 318 Committee. 2011. *Building Code Requirements for Structural Concrete (ACI 318-11) and Commentary*. *American Concrete Institute*. ACI 318 Committee**:** 503.

American Society of Civil Engineers and S. E. Institute. 2010. *Minimum design loads for buildings and other structures*. American Society of Civil Engineers and S. E. Institute. Reston, (VA), American Society of Civil Engineers, Structural Engineering Institute.

Applied Technology Council for the Federal Emergency Management Agency (ATC). 2009. *Quantification of building seismic performance factors*. Applied Technology Council for the Federal Emergency Management Agency (ATC). Washington, D.C.], Washington, D.C. : U.S. Dept. of Homeland Security, FEMA.

Baird, A., Smith, T., Palermo, A., Pampanin, S. 2014. Experimental and Numerical Study of U-Shaped Flexural Plate (UFP) Dissipators. *New Zealand Society for Earthquake Engineering Annual Conference*, Auckland, New Zealand.

Davies, M., Fragiacomo, M. 2011. Long-term behavior of prestressed LVL members. I: Experimental tests. *Journal of Structural Engineering* 137(12): 1553-1561.

European Committee for Standardization. 2004a. *Eurocode 5 - Design of timber structures - Part 1-1: General – Common rules and rules for buildings*. *EN 1995-1-1*. European

Committee for Standardization. Brussels, Belgium, European Committee for Standardization.

Eurocode 8 - Design of structures for earthquake resistance - Part 1: General rules, seismic actions and rules for buildings. European Committee for Standardization. 2004b. Brussels, Belgium, European Committee for Standardization.

Fragiacomo, M., Davies, M. 2011. Long-Term Behavior of Prestressed LVL Members. II: Analytical Approach. *Journal of Structural Engineering* 137(12): 1562-1572.

Giorgini, S., Neale, A., Palermo, A., Carradine, D., Pampanin, S., Buchanan, A.H. 2010. Predicting Time Dependent Effects in Unbonded Post-tensioned Timber Beams and Frames. *Meeting of the Working Commission W18-Timber Structures, CIB*, Nelson, New Zealand.

Marriott, D.J. 2009. The Development of High-Performance Post-Tensioned Rocking Systems for the Seismic Design of Structures *PhD Dissertation*, Universtiy of Canterbury, Christchurch, New Zealand.

Newcombe, M.P., Pampanin, S., Buchanan, A.H., Palermo, A. 2008. Section Analysis and Cyclic Behavior of Post-Tensioned Jointed Ductile Connections for Multi-Story Timber Buildings. *Journal of Earthquake Engineering* 12(S1): 83-110.

Palermo, A., Pampanin, S., Carr, A. 2005. Efficiency of Simplified Alternative Modeling Approaches to predict the Seismic Response of Precast Concrete Hybrid Systems. *fib Symposium: Keep Concrete Attractive*, Budapest, Hungary.

Pampanin, S., Priestley, M.J.N., Sritharan, S. 2001. Analytical modelling of the seicmic behaviour of precast concrete frames designed with ductile connections. *Journal of Earthquake Engineering* 5(3): 329-367.

Priestley, M.J.N., Calvi, G.M., Kowalsky, M.J. 2007. *Displacement-based seismic design of structures*, IUSS Press.

Priestley, M.N. 2003. *Myths and fallacies in earthquake engineering, revisited*, IUSS press.

Smith, T. 2014. Post-tensioned Timber Frames with Supplemental Damping Devices *PhD Dissertation*, University of Canterbury, Christchurch, New Zealand.

Standards New Zealand 1993. *NZS 3603: Timber structures standard*. Wellington, New Zealand, Standards New Zealand.

Standards New Zealand 1997. *NZS 3404: Steel Structures Standard*.

NZS 1170.5: Structural Design Actions - Part 5: Earthquake actions. Standards New Zealand. 2004.

Standards New Zealand. 2006a. *Concrete structures standard*. Wellington, New Zealand, Standards New Zealand. NZS3061:2006.

Standards New Zealand. 2006b. *NZS 3101: Concrete structures standard*. Standards New Zealand. Wellington, New Zealand, Standards New Zealand.

Structural Timber Innovation Company. 2013. *Design Guide Australia and New Zealand-Post-Tensioned Timber Buildings*. Structural Timber Innovation Company. Christchurch, New Zealand.

Zarnani, P., Quenneville, P. 2014. Strength of timber connections under potential failure modes: An improved design procedure. *Construction and Building Materials* 60(0): 81-90.

Part 5:

Closure

12 Conclusions and recommendations for future research

12.1 Conclusions

The scope of this research was the investigation and prediction of the lateral load response of dissipative post-tensioned rocking timber (Laminated Veneer Lumber) walls. The research focused on the behaviour of single Laminated Veneer Lumber (LVL) post-tensioned wall systems with several reinforcement layouts. Within the scope of this dissertation, an alternative system for diaphragm interaction reduction was developed and its behaviour investigated.

The main objectives of this research were addressed through three experimental stages involving both component testing on dissipaters and post-tensioned rocking wall subassemblies. The experimental data was used throughout this dissertation to calibrate analytical and numerical models used for the refinement of the current design practice.

In Chapter 1 the main objectives of this dissertation were presented and grouped in three main research areas. The conclusions drawn from the experimental and numerical work presented in this dissertation are summarized below with reference to the research objectives.

Dissipation devices

1. *Determine the main failure mechanisms governing the response of external tension-compression yield fuse-type dissipaters*

   Experimental testing on a number of different dissipater geometries has highlighted that the dissipater shows very stable hysteresis loops up to 6% strain, which is considered the maximum design strain at MCE level demand. Beyond this strain value, the dissipaters showed interaction between the yielding bar and the anti-buckling system, resulting in the buckling mechanism of the whole dissipater when subjected to cyclic compressive stresses.

2. *Develop and calibrate a numerical models capable of simulating the key behavioural aspects of the dissipaters in order to determine significant design procedures and parameters*

   The objective was addressed by developing and calibrating a fiber-element model capable of simulating the significant failure mechanisms. The calibrated model proved capable of fitting the experimental results successfully, and was used to calibrate design parameters such as onset average strain and the maximum compressive force in the dissipater. The numerical analyses also showed that a design fuse slenderness ratio of 60 is generally recommended for this dissipaters, and for higher slenderness values the anti-buckling system must be detailed considering interaction of the fused bar and the filler.

3. *Develop and validate simplified analytical models to predict the external dissipaters' response*

   The comparison of such analytical models to the experimental results confirmed the model's capability of predicting the back-bone curve of the dissipaters. The comparison of the model results to a more simplified assumption considering the displacement of the fuse portion only proved that this assumption was unconservative.

   The numerical modelling results were also incorporated in a simplified cyclic analytical force-displacement curve capable of simulating the observed experimental behaviour with good accuracy.

4. *Experimentally determine the response of internal bars in terms of tensile strain penetration effects*

   A comprehensive set of experimental test provided the strain profile along the bond area of the specimens. This experimental data was fitted considering a theoretical approach based on the differential equations governing the bond behaviour.

5. *Determine a simplified formulation for the strain penetration length to be used in design*

   A bilinear relationship was calibrated based on the experimental results and following a theoretical approach as stated above, this approach allowed the estimation of the response of internal dissipaters in terms of strain penetration length, which is the key parameter to be adopted in the design.

Wall connection performance

6. *Experimentally determine the lateral load response of large-scale single post-tensioned timber walls with several reinforcement configurations*

   A number of specimens were tested using both post-tensioned only (i.e. non-dissipative) and dissipative configurations. The experimental tests confirmed the good performance of the wall system at high drift levels (up to 2%) with minor damage to the structural element. Test results on the dissipative configurations showed that the system can provide a significant amount of damping while minimizing the residual displacement after testing, proving the robustness of the system.

7. *Assess the influence on the structural response of construction details such as the dissipaters connection to the structural element*

   As part of the experimental program, the external dissipater connection consisted of a steel plate attached to the wall panel using timber rivets. The differential movement between the connection and the wall panel was measured throughout the tests, and this allowed investigating the influence of the connection stiffness on the wall response. Result on the area-based hysteretic damping showed that the dissipater connection flexibility can significantly affect the energy dissipation capabilities of the system. The tests provided a set of experimental results used to quantify the reduction in damping, and this resulted to be between 0.2 and 0.4. The experimental results provided the basis for a more detailed investigation of his phenomenon using numerical models.

8. *Develop an alternative solution to minimize the vertical interaction with the diaphragm system and investigate its behaviour.*

   To achieve this objective an alternative configuration to the “traditional” single wall system was developed, and referred to as Column-Wall-Column (CWC) system. The system uses boundary columns coupled with the post-tensioned wall to provide the support for the diaphragm minimizing the interaction with the lateral load resisting system. The experimental program accounted for a similar testing schedule to the single wall specimens in order to provide a direct comparison.

The experimental results on the new alternative system highlighted the design flexibility and good performance of the system. All the specimens displayed a stable force-displacement response and the development of significant energy dissipation.

Some minor stiffness degradation was observed due to ratcheting in the dissipaters, but its influence of the overall response (force-displacement) of the system was negligible; however, the stiffness degradation caused a reduction of equivalent viscous damping which was experimentally evaluated. An average value of 0.25 for such reduction factor was found.

9. *Refine the current analytical models incorporating design parameters developed and validated in previous stages and validate its capabilities to predict the wall response*

   Design parameters based on experimental observations of the response of external and internal dissipaters were incorporated in the current analytical models and proved capable of predicting the observed experimental response of the post-tensioned connections tested. For the CWC system a simplified model was also developed to account for the additional contributions of the boundary columns with different base connections to the system. The simplified analytical model showed that the capacity contribution of the boundary columns decreases significantly with increasing heights, thus making the column moment contribution negligible. This implies that the design can be carried out by neglecting these contributions.

10. *Validate and refine current numerical modelling approaches for the prediction the seismic response of post-tensioned wall systems as well as simulating the full range of behavioural aspects*

    Whilst the rotational spring model is a simple and computationally light modelling approach able to give good response prediction, it is a very simplified modelling tool, incapable of providing detail parameters. The multi-spring model is an alternative and more refined tool, and that was further developed to capture the observed response of the system, also considering its degradation mechanisms. The model was capable of closely fitting the experimental results considering the main aspects influencing its response, including the timber plastic behaviour and the dissipater connection stiffness. The model was also used to calibrate simplified analytical equations for the determination of the reduction of area-based hysteretic damping.

Wall system performance

11. *Determine the collapse probability of multi-storey buildings adopting post-tensioned rocking timber wall systems*

    An extensive numerical analysis was performed in accordance with the FEMA P-695 which aims at the determination the seismic performance factors of a structural system accounting for the collapse probability of the building. The numerical analysis was performed on a comprehensive set of case study buildings, and the analysis proved that response modification factor R = 7 may be adopted for the design of dissipative post-tensioned wall systems in accordance with ASCE/SEI 7-10 (2010).

12. *Propose Force-Based Design parameters such as seismic reduction factors, over-strength factors and deflection amplification factors in accordance with current seismic design codes*

    The suggested seismic reduction factor R = 7 determined in accordance with the FEMA P-695 (ATC, 2009) procedure was extended to different significant design codes accounting for a different definition of spectral reduction factor. A reduction factor k_μ = 2.5 in accordance with NZS1170.5 (2004) was proposed based on considerations on the different standard definition of the seismic reduction factor and validated using an Acceleration-Displacement Response Spectrum method.

13. *Validate and refine significant Displacement-Based Design parameters and equations of post-tensioned timber wall systems with particular focus on displacement profile, equivalent viscous damping reduction and higher modes amplification factors*

    Further numerical analyses showed that, whilst a linear displacement shape was used in the case study building design phase, the assumption proved to be inaccurate to capture the peak drift profile along the height of the building. An alternative inelastic displacement shape formulation was calibrated against push-over curves and proved capable of better fitting the numerical results.

    Non-linear time-history analyses result confirmed that higher-mode effects can significantly affect the capacity design of a post-tensioned timber wall system for multi-storey timber buildings. Current design formulas for the capacity design moment envelope proved to be inaccurate to predict the behaviour of the system;

therefore, the bi-linear moment envelop was re-calibrated based on the observed numerical results.

The proposed equations were successfully validated in the last part of Chapter 10 showing good fit with the numerical results.

12.2 Recommendations for future research

1. The experimental and numerical work presented in this dissertation considered the use of Laminated Veneer Lumber (LVL). Whilst LVL has many advantages mainly related to its superior strength, Cross-Laminated Timber (CLT) is being widely used for the construction of multi-storey timber buildings and shows potential to be used in the Pres-Lam system. It is recommended that further experimental research is carried out investigating the response of post-tensioned CLT wall systems.
2. This dissertation showed the experimental and numerical analyses on several post-tensioned rocking systems (single, CWC and coupled). In particular, numerical analyses showed significant higher mode amplification of the shear and moment distribution along the height of the buildings. While the timber panel strength is generally well above the amplified shear and moment demand, as the wall panel is likely to be made out of several segments, the connection between those must be carefully detailed considering the amplified actions.

   Higher mode effects can be reduced adopting a segmental wall system. The system was researched by Wiebe et al. (2009) with application on rocking steel braced frames. The segmental wall system has the potential of being extended to post-tensioned rocking timber walls. Although the body of research presented in this dissertation considered the rocking mechanism occurring at the wall base, numerical and analytical models can be used for a segmental wall system, but further research is required in this field.
3. Pres-Lam frames are also a viable solution to resist lateral loading. Pres-Lam wall and frame systems were investigated in this dissertation and by Smith et al. (2014), respectively. The benefits of the two systems can be combined as a dual system (Abellán *et al.*, 2012), but a further research phase is required to investigate the system.
4. The numerical modelling carried out in this research was focused on the response of the wall subassembly. This is a simplified assumption to easily identify the significant parameters affecting the response of the system, but its validity is limited to regular building (i.e. non-torsional prone buildings). As suggested by the latest

draft revision of NZS1170.5 (2015), the loss of torsional stiffness due to differential yielding of the lateral load resisting systems within a building is limited for self-centering systems; however, further research in this field is still required.

5. As anticipated, although the research presented in this dissertation focused on the seismic behaviour of post-tensioned timber wall systems, lateral load resisting systems must also consider wind loading. The design of tall buildings is likely to be governed by wind loading particularly in low and medium seismic areas, yet seismic action must not be overlooked, in particular due to higher mode amplifications. Further numerical analyses are required to investigate the matter.
6. Due to its peculiar structure, timber is subjected to dimensional variations which can be caused by a number of factors such as thermal and relative humidity variations, as well as creep. As mentioned in this dissertation, these factors can lead to post-tensioning losses which affect the capacity of the structural wall. Limited research was carried out on the long-term behaviour of post-tensioned timber structures and further research needs to be performed and is currently on-going at the University of Canterbury.

12.3 References

Abellán, A.R.R., Sullivan, T.J., Pampanin, S. 2012. Adapting DDBD for the design of Frame-Wall Structures with Hybrid-Rocking Joints. *WCEE*, Lisbon, Portugal.

American Society of Civil Engineers and S. E. Institute. 2010. *Minimum design loads for buildings and other structures*. American Society of Civil Engineers and S. E. Institute. Reston, (VA), American Society of Civil Engineers, Structural Engineering Institute.

Applied Technology Council for the Federal Emergency Management Agency (ATC). 2009. *Quantification of building seismic performance factors*. Applied Technology Council for the Federal Emergency Management Agency (ATC). Washington, D.C.], Washington, D.C. : U.S. Dept. of Homeland Security, FEMA.

Smith, T. 2014. Post-tensioned Timber Frames with Supplemental Damping Devices *PhD Dissertation*, University of Canterbury, Christchurch, New Zealand.

NZS 1170.5: Structural Design Actions - Part 5: Earthquake actions. Standards New Zealand. 2004.

Standards New Zealand 2015. *AS/NZS 1170.5: Structural Design Actions - Part 5: Earthquake actions*.

Wiebe, L., Christopoulos, C. 2009. Mitigation of higher mode effects in base-rocking systems by using multiple rocking sections. *Journal of Earthquake Engineering* 13(S1): 83-108.

Part 6:
Appendices

Appendix A: Experimental specimen design

A.1 Design of the test specimen

A.1.1 Seismic Design of full-scale prototype

The prototype case study building was a three storey building with two suspended floors and a lightweight third floor. The building had an approximate plan of 32m in the longitudinal direction and 18m in the transverse direction with a floor area of approximately 600m^2 per floor. The ground floor level was assumed to be used for retail purposes, level two as office space and level 3 with residential type loadings.

The building was designed using the Christchurch CBD hazard factor (Z = 0.3) and a soil type D according to NZS1170.5 (Standards New Zealand, 2004). For design purposes, the seismic mass of the light-weight top floor was concentrated at the second level, resulting in equal storey seismic weights of 2540kN (635kN per wall).

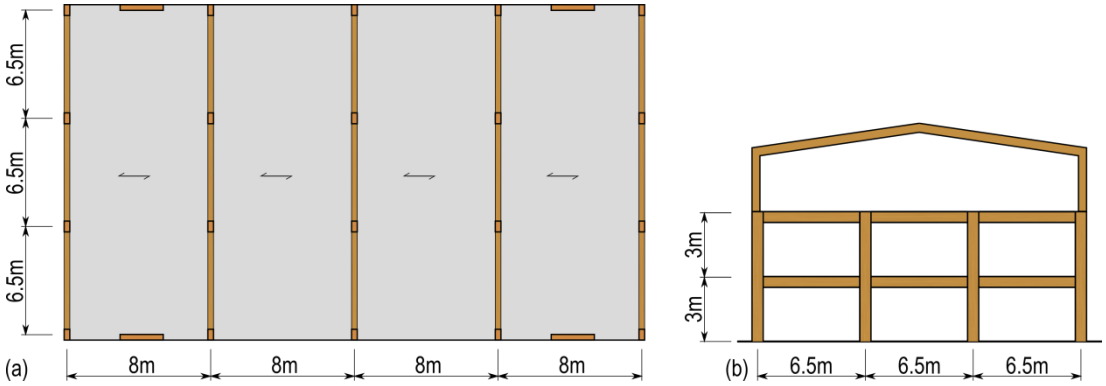

Figure A-1. Typical floor plan, frame elevation and frame sections.

The building structural configuration had 5, 3-bay frames spanning in the transverse direction, supporting gravity loads, and four single post-tensioned timber walls (2.4m×0.45m in section) providing lateral load resistance in both the longitudinal and the transversal directions.

The lateral load demand was evaluated in accordance with a Displacement-Based Design (DBD) approach (Priestley *et al.*, 2007), and the building structure was converted to a single

degree of freedom (SFOD) structure and characterized in terms of secant period and stiffness.

The floor system adopted for the case study building was a full timber solution and consisted of a 7 layer 200mm thick Cross-Laminated Timber (CLT) panel.

The seismic weights (Table A-1) were evaluated considering the full timber flooring option (1.8kPa) and considering an extra dead load of 0.5kPa. As part of the dead load on the structure a distributed weight of 0.3kPa was incorporated to account for the façade and 0.6kPa for the penthouse structure at the top floor.

Different live loads were considered for the different floors given the different use (3kPa for the ground and first floors for office use and 1.5kPa for the residential penthouse at the top floor). For seismic design purposes the top floor mass was concentrated at the second floor.

Table A-1. Summary of Seismic Weights

Level	$W_{i,\,total}$ (kN)	$W_{i,\,wall}$ (kN)
2	2540	635
1	2633	658
Total	12169	3042

For the seismic design of the structure under investigation, a maximum drift at Ultimate Limit State (ULS) of 1% was chosen. The equivalent SDOF structure characteristics were then evaluated according to the DBD procedure (Priestley *et al.*, 2007) as follows.

Table A-2: Equivalent static analysis to determine distribution of seismic shears

Level	h_i (m)	Δ_i (m)	m_i (t)	$m_i\Delta_i$	$m_i\Delta_i h_i$	$m_i\Delta_i^2$
2	6	0.060	65	3.886	23.314	0.233
1	3	0.030	67	2.014	6.043	0.060
∑			132	5.9	29.4	0.294

The design displacement, Δ_d, mass, m_e, and height, h_e, of the equivalent SDOF system are defined in Equations (A-1) through (A-3):

$$\Delta_d = \frac{\sum_{i=1}^{n} m_i \Delta_i^2}{\sum_{i=1}^{n} m_i \Delta_i} = \frac{0.294}{5.9} = 0.050m \qquad \textit{(A-1)}$$

$$m_e = \frac{\sum_{i=1}^{n} m_i \Delta_i}{\Delta_d} = \frac{5.9}{0.050} = 119t \qquad \textit{(A-2)}$$

$$h_e = \frac{\sum_{i=1}^{n} m_i \Delta_i h_i}{\sum_{i=1}^{n} m_i \Delta_i} = \frac{29.4}{5.9} = 5.0m \qquad (A\text{-}3)$$

Where m_i = seismic mass of the i-th storey

Δ_i = design displacement of the i-th storey

h_i =height of the i-th storey

The 5% damping displacement spectrum must be reduced to account for the equivalent viscous damping of the structure. For flag-shaped hysteresis, Priestley et al. (2007) proposed an analytical formula for the hysteretic damping of such systems, based on an idealized flag-shape hysteresis.

The hysteretic damping, ξ_{hyst}, was calculated for a re-centering ratio, β, value of 0.6 and ductility, μ, of 2. The post-yielding stiffness factor, r, of 0.3.

$$\xi_{hyst} = \frac{2(1-\beta)(\mu-1)}{\mu\pi\left[1+r(\mu-1)\right]} = \frac{2(1-0.6)(2-1)}{2\pi\left[1+0.3(2-1)\right]} = 9.9\% \qquad (A\text{-}4)$$

The elastic damping contribution, ξ_{el}, must also be considered giving the total damping, ξ, in Equation (A-5):

$$\xi = \xi_{el} + \xi_{hyst} = 3\% + 9.9\% = 12.9\% \qquad (A\text{-}5)$$

This combines to give a total reduction factor, R_ξ, of:

$$R_\xi = \sqrt{\frac{7}{2+\xi}} = 0.69 \qquad (A\text{-}6)$$

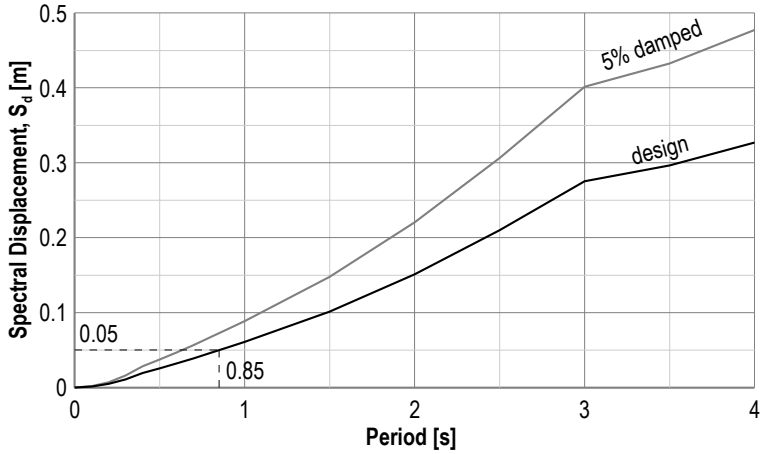

Figure A-2. ULS displacement design spectrum.

Given the effective (SDOF) design drift of Δ_d = 0.050m the effective (secant) period of the SDOF system can be taken from the reduced displacement spectra as, T_e = 0.85s (see Figure A-2). The effective system stiffness can be calculated as:

$$K_e = \frac{4\pi^2 m_e}{T_e^2} = \frac{4\pi^2 \cdot 119t}{0.85^2 s^2} = 6478kN/m \qquad (A\text{-}7)$$

Multiplying this stiffness by the design drift gives the wall base shear:

$$V_b = K_e \Delta_d = 6478kN/m \cdot 0.050m = 322kN \qquad (A\text{-}8)$$

$$M_b = V_b h_e = 1604kN \qquad (A\text{-}9)$$

A.1.2 Design of the wall specimen

Space constraints (maximum crane clearance in the laboratory) did not allow the testing of the full-scale specimen; therefore, the experimental specimen was tested on a two-thirds scale. The scaled Laminated Veneer Lumber specimen was constructed as 1.6m×0.19m in cross-section and 4.1m tall.

The scaled seismic action used for the specimen design and detailing were worked out following a constant density approach:

$$V_{b,2/3} = \frac{V_b}{(2/3)^2} = 143kN, M_{b,2/3} = \frac{M_b}{(2/3)^3} = 475kN \qquad (A\text{-}10)$$

Reinforcement design

The preliminary design of the reinforcement configuration is performed below considering the material properties summarized in Table A-3.

Table A-3: material properties

Post-tensioning steel

Property		Value
Yield stress	f_{yp}	835MPa
Ultimate stress	f_{up}	1,030MPa
Modulus of Elasticity	E_p	170GPa

Mild steel

Property		Value
Yield stress	f_{yp}	320MPa
Ultimate stress	f_{up}	400MPa
Modulus of Elasticity	E_p	200GPa

Laminated Veneer Lumber

Property		Value
Modulus of Elasticity	E_t	11000MPa
Bending strength	f_{bt}	38MPa
Compression strength	f_{ct}	38MPa
Shear strength	f_{st}	5MPa

A re-centering ratio β = 0.6 (or λ = 1.5) was assumed. Therefore the post-tensioning contribution will be 60% of total required base moment.

$$\phi M_{pt} = \phi\left(T_{pt} + N\right) j_d \qquad \textit{(A-11)}$$

Where N = Axial force from gravity loads.

Assuming *c/h = 0.3* and a triangular (linear) stress distribution;

$$j_d = 0.5h - c/3 = 0.4h \qquad \textit{(A-12)}$$

Rearranging and solving for the post-tensioned force at the target drift,

$$T_{pt} = \frac{0.6 \cdot 475kNm}{0.9 \cdot 0.4 \cdot 1.6m} = 495kN \qquad \textit{(A-13)}$$

Therefore, considering 32mm diameter post-tensioning bars, two of them would be sufficient.

The tendon elongation due to gap opening[1]:

$$\Delta_{pt} = \theta_{imp}\left(0.5h - c\right) = 0.008rad \cdot \left(0.5 \cdot 1.6m - 0.30 \cdot 1.6m\right) = 2.6mm \qquad \textit{(A-14)}$$

The tendon force due to gap opening is calculated knowing the additional tendon strain, where l_{ub}[2]is the unbonded length of the tendon, in this example is as follows.

$$\Delta T_{pt} = n_{pt} E_{pt} A_{pt} \frac{n \cdot \Delta_{pt}}{l_{ub}} = 2 \cdot 170GPa \cdot 804mm^2 \frac{1 \cdot 2.6mm}{5m} = 142kN \qquad \textit{(A-15)}$$

Therefore, the initial post-tensioned force is given by the difference between the required force at the target drift and the additional tendon force due to elongation.

$$T_{pt0} = 495kN - 142kN = 353kN \qquad \textit{(A-16)}$$

Which corresponds to approximately 177kN/bar (say 200kN/bar).

The minimum mild steel reinforcement area is:

[1] The connection rotation θ_{imp} = 0.008rad is resulting from the 1% design drift assumed and considering the elastic displacement contribution (approximately 0.2% for the case study wall).

[2] Unbonded length of the post-tensioning bars, L_{ub}, is 5m and accounts for the foundation depth and the load cells setup on the top of the wall as shown in Chapter 5.

$$A_s \geq \frac{M^*}{\phi f_{sy} j_d} = \frac{0.4 \cdot 475kNm}{0.9 \cdot 400MPa \cdot 0.9m} = 586mm^2 \qquad \text{(A-17)}$$

Where j_d = 0.9m, assuming the dissipaters edge distance is 0.525m. Considering D14mm dissipater, 4 mild steel reinforcing bars would be sufficient.

A.2 References

Priestley, M.J.N., Calvi, G.M., Kowalsky, M.J. 2007. *Displacement-based seismic design of structures*, IUSS Press.

NZS 1170.5: Structural Design Actions - Part 5: Earthquake actions. Standards New Zealand. 2004.

Appendix B: A simplified analytical model for Column-Wall-Column systems

B.1 Introduction

As shown by experimental results shown in Chapter 6 of this dissertation, the behaviour of the Column-Wall-Column systems can be significantly affected by the boundary columns In coupled systems, and in particular for column-wall-column systems, it has been proved that the boundary elements can bring some stiffness contributions to the system. A simplified approach was attempted in Chapter 7 of the dissertation and proved capable of predicting the observed experimental behaviour. In order to extend the model to a more general case, the superposition method is applied to a general case of two vertical cantilevers with base flexibility.

B.2 Column contribution

For an imposed triangular displacement contribution, the effects can be superpositioned as shown in Figure B-1.

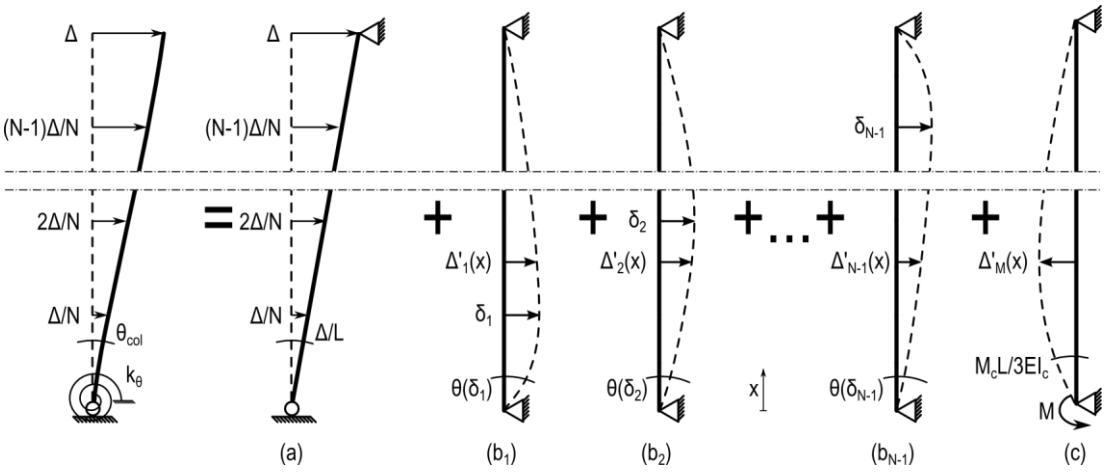

Figure B-1.Column effects superposition.

For case (a) the general equations for the displacement, $\Delta_{n,(a)}$, at the n-th storey and the base rotation can be given for a constant inter-storey height as:

$$\Delta_{n,(a)} = \Delta \frac{n}{N} \tag{B-1}$$

$$\theta_{(a)} = \frac{\Delta}{NH} \tag{B-2}$$

Where Δ = top displacement

N = total number of storey

H = inter-storey height

The load case (a) does not impose any internal actions; therefore, shear and bending moment are zero along the element.

The effect of a settlement δ_i on a simply supported beam is considered in cases (b), and the displacement equation along the element can be evaluated as:

$$\Delta'_{(bn)} = \delta_i \begin{cases} \dfrac{n}{2i^2(N-i)}\left(2Ni - i^2 - n^2\right) & n \le i \\ \dfrac{1}{2i^2(N-i)}\left[\dfrac{N}{N-i}(n-i)^3 + n\left(2Ni - i^2\right) - n^3\right] & i < n \le N \end{cases} = \delta_i \begin{cases} \alpha_{n,i} & n \le i \\ \beta_{n,i} & i < n \le N \end{cases} \tag{B-3}$$

The base rotation:

$$\theta_{(bn)} = \frac{2N - i}{2i(N-i)}\delta_i \tag{B-4}$$

Bending moment and shear:

$$M_{(bn)} = \frac{3EI_c}{i(N-1)H^2}\delta_i \begin{cases} \dfrac{n}{i} & n \le i \\ 1 - \dfrac{n-i}{N-i} & i < n \le N \end{cases} \tag{B-5}$$

$$V_{(bn)} = \frac{3EI_c}{i^2(N-i)^2 H^3}\delta_i \begin{cases} N - i & n \le i \\ i & i < n \le N \end{cases} \tag{B-6}$$

The effect of the moment developed at the column base connection on a simply supported beam can be written as follows.

$$\Delta'_{(c)} = \frac{M_c H^2}{6EI_c}\frac{n}{N}\left(N-n\right)\left(2N-n\right) = M_c\gamma_n \qquad \textit{(B-7)}$$

$$\theta_{(c)} = \frac{M_c}{3EI_c}NH \qquad \textit{(B-8)}$$

$$M_{(bn)} = M_c\left(1-\frac{n}{N}\right) \qquad \textit{(B-9)}$$

$$V_{(bn)} = \frac{M_c}{NH} \qquad \textit{(B-10)}$$

Once the above cases are defined in terms of displacements and base rotation, the following compatibility equations can be defined.

Displacement compatibility at the n-th storey:

$$\begin{aligned}&\Delta_n = \Delta_{n,(a)} + \sum_{i=1}^{N-1}\Delta_{n,(bi)} + \Delta_{n,(c)} \rightarrow \Delta\frac{n}{N} = \Delta\frac{n}{N} + \sum_{i=1}^{N-1}\delta_i\begin{cases}\alpha_{n,i} & n\le i\\ \beta_{n,i} & i<n\le N\end{cases} - \gamma_n M_c\\ &\rightarrow \sum_{i=1}^{N-1}\delta_i\begin{cases}\alpha_{n,i} & n\le i\\ \beta_{n,i} & i<n\le N\end{cases} - \gamma_n M_c = 0\end{aligned} \qquad \textit{(B-11)}$$

Base rotation compatibility:

$$\begin{aligned}&\theta_c = \theta_{(a)} + \sum_{i=1}^{N-1}\theta_{(bi)} + \theta_{(c)} \rightarrow \frac{M_c}{k_\theta} = \Delta\frac{N}{H} + \sum_{i=1}^{N-1}\frac{2N-i}{2i\left(N-i\right)}\frac{\delta_i}{H} - \frac{M_c NH}{3EI_c}\\ &\rightarrow \sum_{i=1}^{N-1}\frac{2N-i}{2i\left(N-i\right)}\delta_i - \frac{M_c H^2}{EI_c}\left(\frac{EI_c}{Hk_\theta}+\frac{N}{3}\right) = -\frac{\Delta}{N}\end{aligned} \qquad \textit{(B-12)}$$

Equations (B-11) and (B-12) represent a linear system in the unknowns δ_1, δ_1 …, δ_{N-1} and M_c, which can be solved as a function of the top displacement Δ in matrix form as shown in Equation (B-13).

$$\left[\begin{array}{ccccc}
\alpha_{1,1} & \alpha_{1,2} & \alpha_{1,3} & \alpha_{1,N-1} & \gamma_1\\
\beta_{2,1} & \alpha_{2,2} & \alpha_{2,3} & \alpha_{2,N-1} & \gamma_2\\
\beta_{3,1} & \beta_{3,2} & \alpha_{3,3} & \alpha_{3,N-1} & \gamma_3\\
\beta_{N-1,1} & \beta_{N-1,2} & \beta_{N-1,3} & \alpha_{N-1,N-1} & \gamma_{N-1}\\
\hline
\frac{2N-1}{2(N-1)} & \frac{2N-2}{4(N-1)} & \frac{2N-3}{9(N-1)} & \frac{N+1}{2(N-1)} & -\frac{H^2}{EI_c}\left(\frac{EI_c}{Hk_\theta}+\frac{N}{3}\right)
\end{array}\right]\left[\begin{array}{c}\delta_1\\ \delta_2\\ \delta_3\\ \\ \frac{\delta_{N-1}}{M_c}\end{array}\right] = \left[\begin{array}{c}0\\0\\0\\ \\ -\frac{\Delta}{N}\end{array}\right] \qquad \textit{(B-13)}$$

Once the unknowns are worked out, the shear profile can be determined; as a result, the column transfers the reaction forces to the wall panel as shown in Figure B-2.

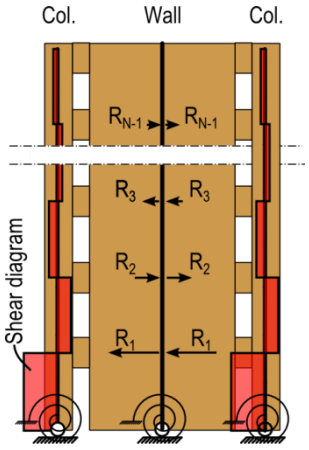

Figure B-2.Shear transfer.

The reaction force R_n is given by the difference of the shear at the bottom and top of the n-th storey height. This reaction is only governed by the imposed settlement at each storey and can be evaluated by Equation (B-14)

$$R_n = \frac{3EI}{H^3}\frac{N}{n^2\left(N-n\right)^2}\delta_n \qquad (B\text{-}14)$$

A similar approach can now be adopted for the post-tensioned wall with minor modifications. The cases (b) are now given by the reaction forces as shown in Figure B-3.

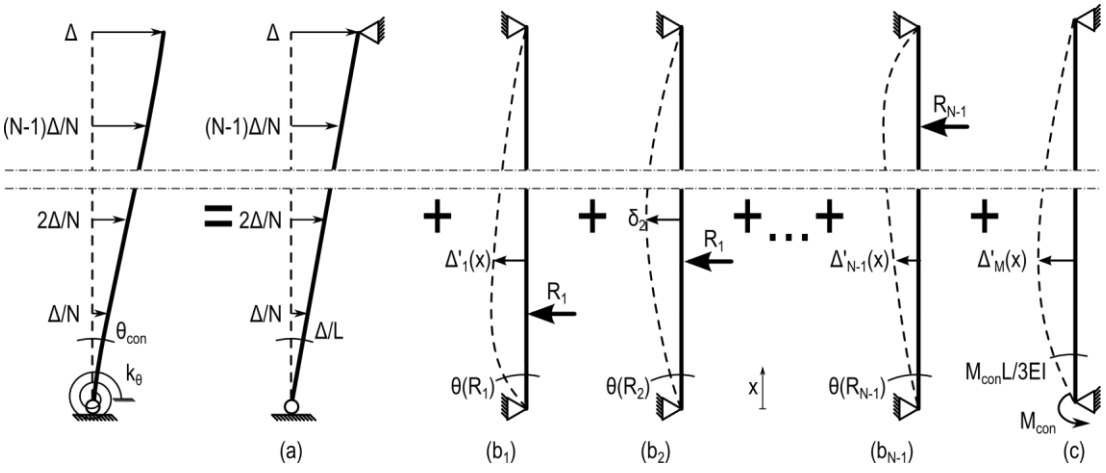

Figure B-3. Column effects superposition.

The wall base rotation contributions of cases (b) due to a point load can be evaluated as:

$$\theta_{(bi)} = R_i \frac{H^2}{EI} \frac{(N-i)\left(N^2-i^2\right)}{6N} \tag{B-15}$$

The base rotation compatibility equation on the wall is given in Equation

$$\theta_{con} = \frac{\Delta}{NH} + R_i \frac{H^2}{EI} \frac{(N-i)\left(N^2-i^2\right)}{6N} - \frac{M_{con}H}{EI} \frac{N}{3} \tag{B-16}$$

Appendix C: Post-tensioning anchorage detailing: design and FEM modelling

The design of the post-tensioning anchorage is a key construction detail in the seismic design of dissipative post-tensioned rocking elements since the stress concentration resulting from a poorly detailed post-tensioning anchorage may result in localized damage.

In this section a simplified design of the post-tensioning bearing plate is carried out assuming that the reaction of the timber section is a uniform pressure over the steel plate's surface.

After the simplified design was carried out on a case study detail, finite element modelling analyses were carried out for the same plate accounting for different wall section layouts.

C.1 Simplified design

Since the post-tensioning bearing plate is generally much stiffer than the timber bearing surface, the stress distribution in the design phase can be approximately assumed as constant, but this approximation can apply only for a well detailed anchorage plate. In particular, it is suggested that the anchoring plate bears on the full width of the wall section; moreover, the bearing area shall be maximized. This can be obtained, as also shown in Chapters 5 and 6, by a careful detailing of the timber section. Standard profiles can be assembled and glued to leave small voids for the post-tensioning bars. When manufacturing does not allow that, a void may be left between bars, but the effective timber bearing area must be considered.

Under those assumptions the anchorage plate can be designed using a simplified approach and considering the plate as a continuous beam on point supports subjected to a uniformly distributed load (UDL). The UDL represents the timber bearing stress, while the reactions at the point supports are the post-tensioning forces as shown in Figure C-1.

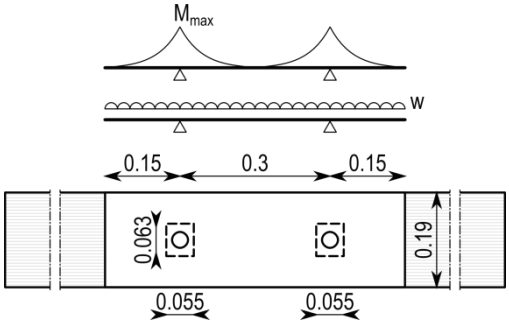

Figure C-1. Simplified design of a post-tensioning anchorage.

As an example the bearing plate of the test specimen reported in Chapter 5 and 6 was re-designed in this section. Possible issues related to poor design detailing of the plate are also discussed with reference to Finite Element Models (FEM) in the following section.

The details of the new anchoring plate are reported in Figure C-1 which shows the geometry of the plate and location of the post-tensioning bars as well as the simplified model used for the evaluation of the plate thickness.

The anchoring plate should be designed assuming a maximum force in each bar equal to the yielding load, $T_{pt,y}$, which for 32mm Macalloy bars is given by:

$$T_{pty} = A_{pt} f_{py} = 804mm^2 \cdot 835MPa = 671kN \qquad (C\text{-}1)$$

Where A_{pt} = the post-tensioning bar area

f_{py} = post-tensioning steel yield strength

Considering a 190mm wide and 600mm long plate as shown in Figure C-1 the timber stress, σ_t, under the maximum load of the two post-tensioning bars would be:

$$\sigma_t = \frac{2T_{pty}}{bh - 2b_h h_h} = \frac{2 \cdot 671Kn}{190mm \cdot 600mm - 2 \cdot 55mm \cdot 65mm} = 12.6MPa < \phi f_t = 34.2MPa \therefore OK \qquad (C\text{-}2)$$

The total load is converted into a UDL considering the plate to be 190mm wide. This result in the uniformly distributed load w = 2237kN/m and a maximum moment at the support M_{max} = 26.3kNm; therefore, the minimum required plate thickness, t_{min}, is given by:

$$t_{min} = \sqrt{\frac{6M_{max}/\phi}{bf_{sy}}} = \sqrt{\frac{6 \cdot 26.3kNm/0.9}{190mm \cdot 350MPa}} = 51mm \rightarrow 60mm \qquad (C\text{-}3)$$

Where b = the plate width

f_{sy} = steel yielding strength

C.2 FEM modelling

Finite Element Modelling (FEM) was carried out using Abaqus (Simulia, 2011) in order to investigate the influence of different section layouts on the stress distribution around the anchoring bearing surface.

Two section options were considered. The first is the optimal layout, as also shown in Chapters 5 and 6, which minimizes the voids in the section (see Figure C-2, option 1 and 3).

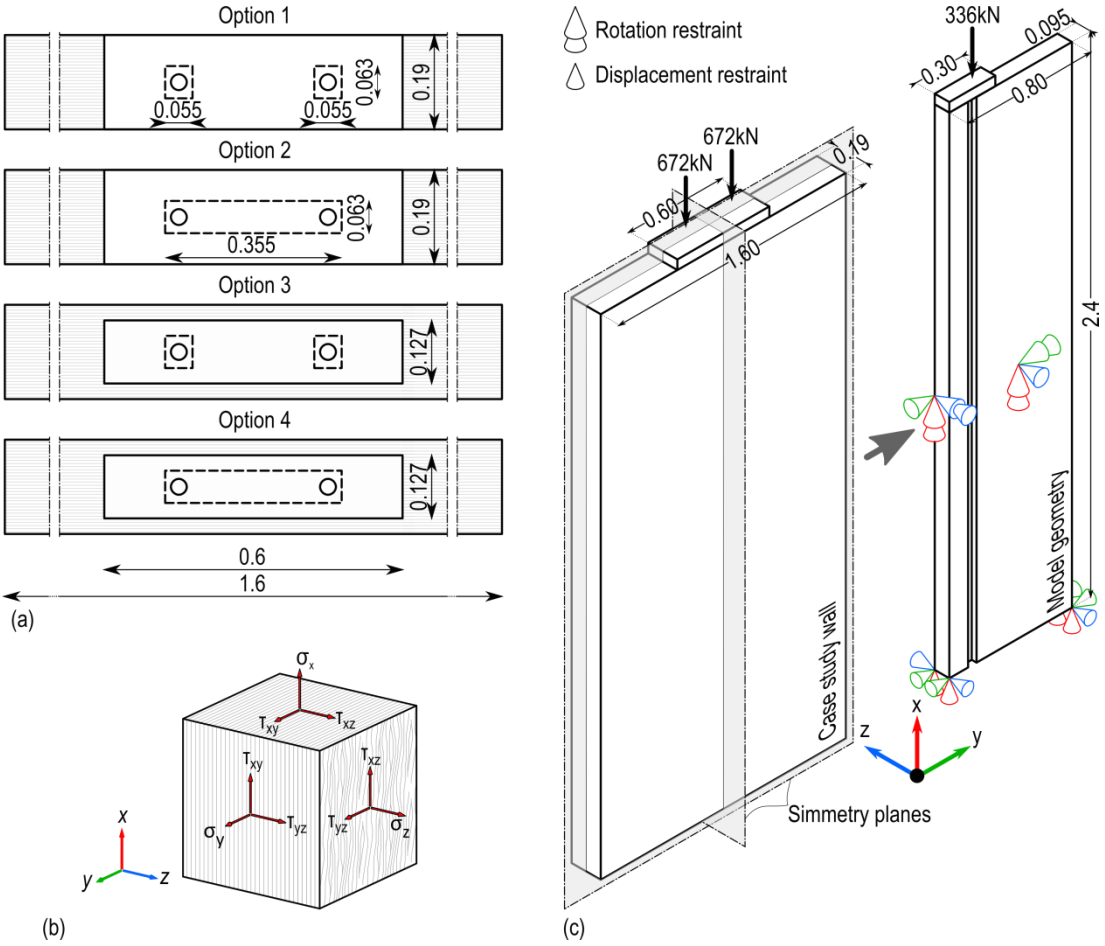

Figure C-2. (a) Post-tensioning anchorage layout options; (b) Definition of LVL stresses; (c) Finite Element Model layout and boundary conditions.

Since the bars are usually positioned in a group at the wall panel's mid-depth, another option was considered and a void was left between the two bars (see Figure C-2, option 2 and 4). This section layout was recently used in few multi-storey post-tensioned timber buildings, such as the Nelson and Marlborough Institute of Technology (Devereux *et al.*, 2011), the Carterton Events Centre (Palermo *et al.*, 2012) and the Trimble Building (Brown *et al.*, 2012).

When designing the post-tensioning anchorage it is suggested to design the steel plate bearing on the entire wall section width as shown in Options 1 and 2. The influence of a narrower plate on the stress distribution in the timber section was further investigated by analysing the finite element models of Option 3 and 4.

In the Abaqus model the timber section was modelled using an anisotropic elastic material. The material was defined using the material properties investigated by Van Beerschoten et al. (2014) and reported in Table C-1. The steel plate was also modelled as an elastic element and modulus of elasticity and Poisson's ratio were 200GPa and 0.3 respectively.

Table C-1. LVL material properties(van Beerschoten et al., 2014)

E_x	E_y	E_z	ν_{xy}	ν_{xz}	ν_{yz}	G_{xy}	G_{xz}	G_{yz}
12000	430	370	0.57	0.66	0.2	1070	909	72

NOTE: x direction is parallel to the grain

The wall element was a 1.6m deep, 0.19m wide and 3.2m tall section. To optimize the finite element analysis the symmetry of the element was considered and the boundary conditions were assigned accordingly. The displacement in the three directions was restrained at the base of the wall. The symmetry of the case study wall was considered and boundary conditions in the xz and xy planes were assigned at the section surfaces as shown in Figure C-2c.

The static analyses were performed imposing the axial load corresponding to the yielding of the two bars as shown in the design phase. Considering the symmetry of the model a point load of 336kN was imposed (i.e. $T_{pty}/2$).

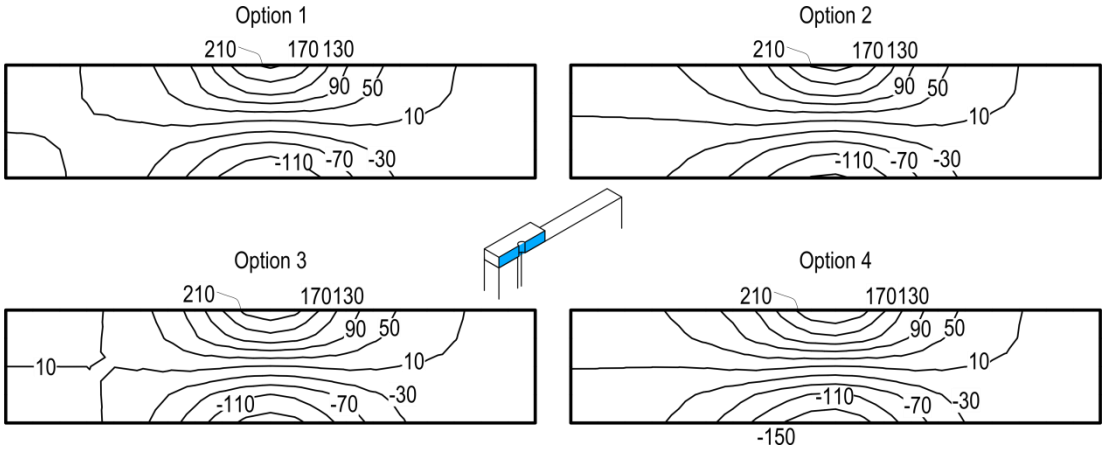

Figure C-3. Axial stress fields in the post-tensioning anchorage plate.

The axial stress results in the post-tensioning anchorage steel plate shown in Figure C-3 confirms that the simplified design proposed above is appropriate. The four different options

show maximum compressive stresses up to approximately 240MPa and maximum tension stresses of approximately 170MPa.

In the following charts the modelling results are shown in terms of timber axial stress fields. The data analysis focussed in particular on the axial stress in the parallel to the grain direction of the wall element (σ_x in Figure C-2b) and also the stress fields in the "weak" perpendicular to the grain direction was considered (σ_z in Figure C-2b). This stress was oriented in the transverse direction of the wall.

The parallel-to-grain axial stress results of the anchorage Option 1 are shown in Figure C-4. As the stress fields show, the small void created to accommodate the post-tensioning bar creates a stress concentration which results in a maximum compressive stress of approximately 21MPa. Although this value is still within the nominal strength values it is approximately twice than the predicted stress considered in the simplified design phase. However, the increased stress is localized in a rather small area and is thus deemed acceptable.

It can also be observed that the stress fields resulting from void does not develop in depth in the longitudinal direction of the wall panel and the stress values are within the average value of 12.6MPa at a distance of approximately 100mm from the bearing surface.

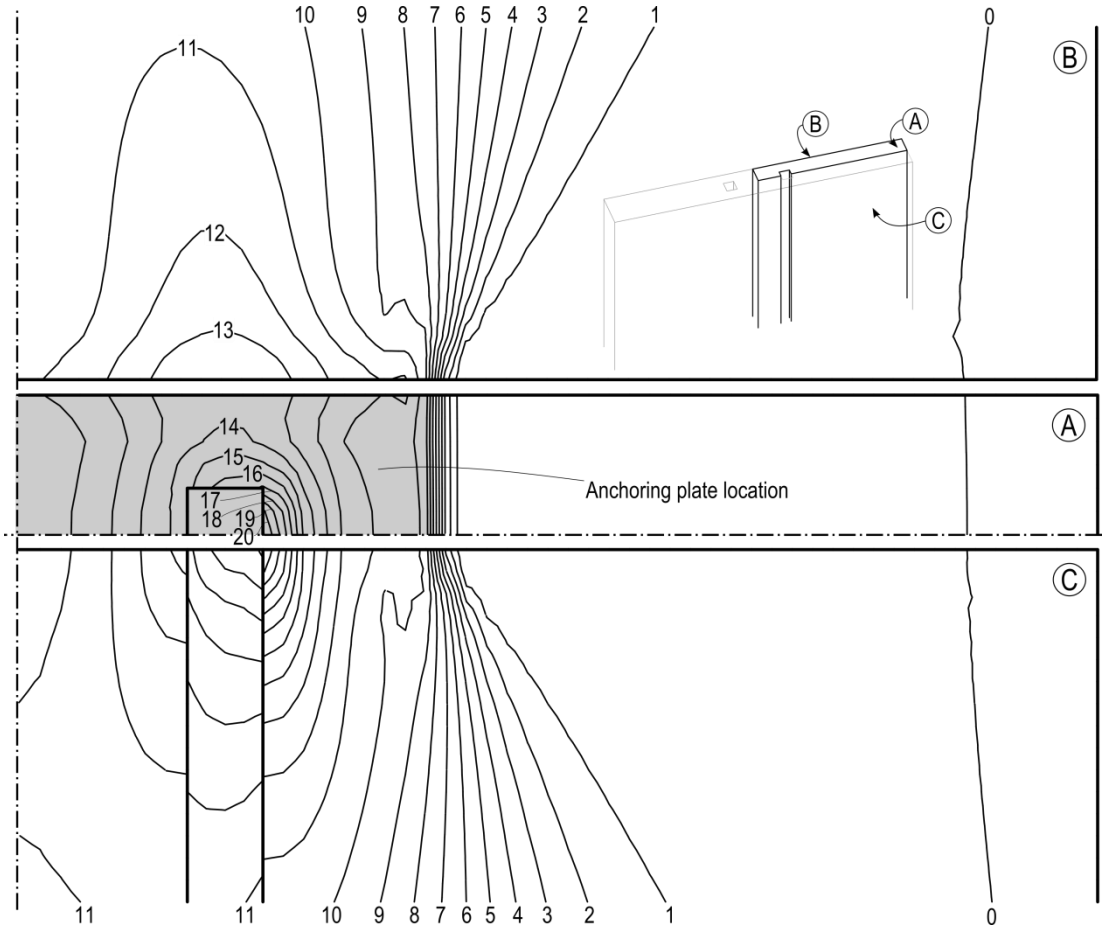

Figure C-4. Wall parallel-to-grain axial stress fields (in MPa) for the anchorage option 1.

Figure C-5 shows that the stress distribution in Option 2 is rather different from the previous case. As expected, an increase in axial stress was observed as a result of the reduced bearing area. The stress concentration in the area surrounding the hole shows a maximum stress of approximately 23MPa.

As expected a stress increase was observed for Option 2 as a result of the reduced bearing surface. In fact, the average timber stress as assumed in the design phase considering for this section option is given in Equation (C-4).

$$\sigma_t = \frac{2T_{pty}}{bh - b_h h_h} = \frac{2 \cdot 671Kn}{190mm \cdot 600mm - 355mm \cdot 63mm} = 14.6MPa < \phi f_t = 34.2MPa \therefore OK \qquad (C\text{-}4)$$

This corresponds to a stress increase of approximately 15% compared to Option 1 values.

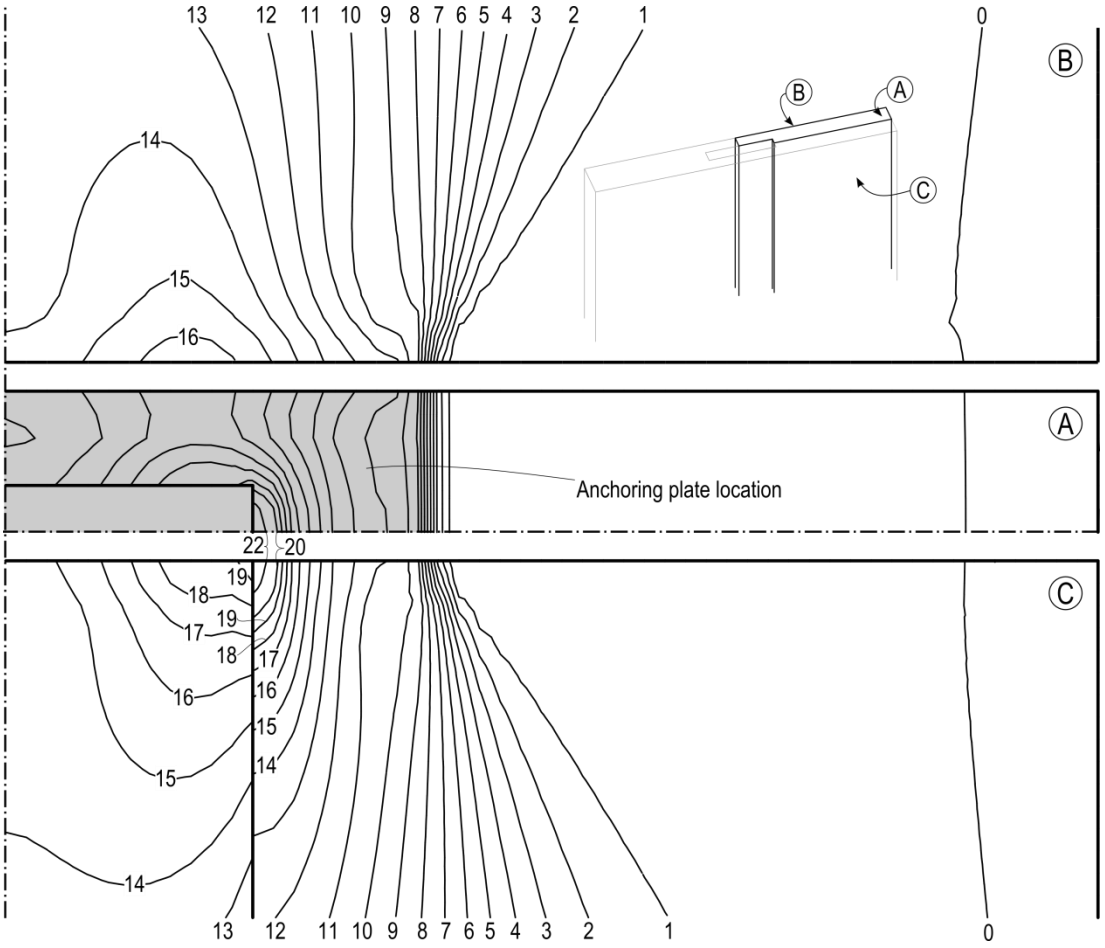

Figure C-5. Wall parallel-to-grain axial stress fields (in MPa) for the anchorage option 2.

Options 3 and 4 were accounted for to assess the influence of a reduced plate width.

The average stresses as measured in the design phase considering a uniform pressure distribution are:

$$\sigma_{t,3} = \frac{2 \cdot 671Kn}{127mm \cdot 600mm - 55mm \cdot 63mm} = 18.5MPa < \phi f_t = 34.2MPa \therefore OK \qquad (C\text{-}5)$$

$$\sigma_{t,4} = \frac{2 \cdot 671Kn}{127mm \cdot 600mm - 355mm \cdot 63mm} = 24.9MPa < \phi f_t = 34.2MPa \therefore OK \qquad (C\text{-}6)$$

Although the average stresses evaluated by Equations (C-5) and (C-6) for the post-tensioning anchorage Options 3 and 4 are within elastic values, FEM results in Figure C-6 and Figure C-7 show significant stress concentrations. In particular, the stress fields of Option 4 show maximum values close to the compressive strength of the material.

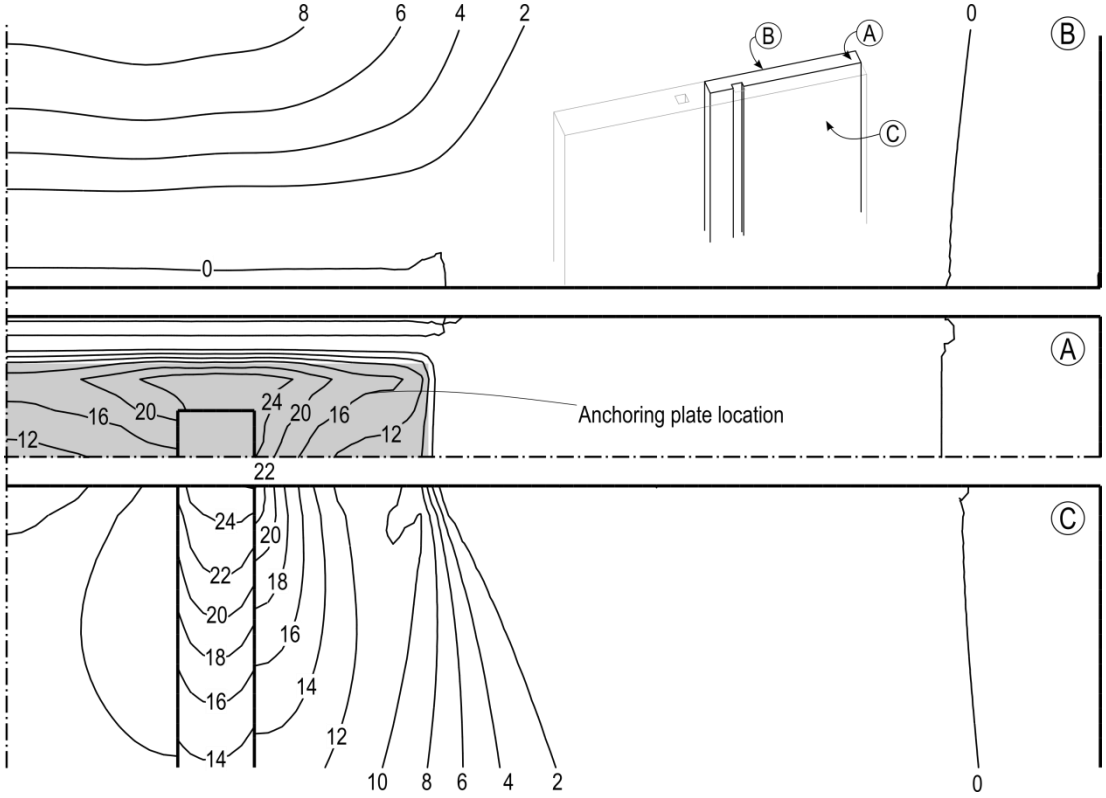

Figure C-6. Wall parallel-to-grain axial stress fields (in MPa) for the anchorage option 3.

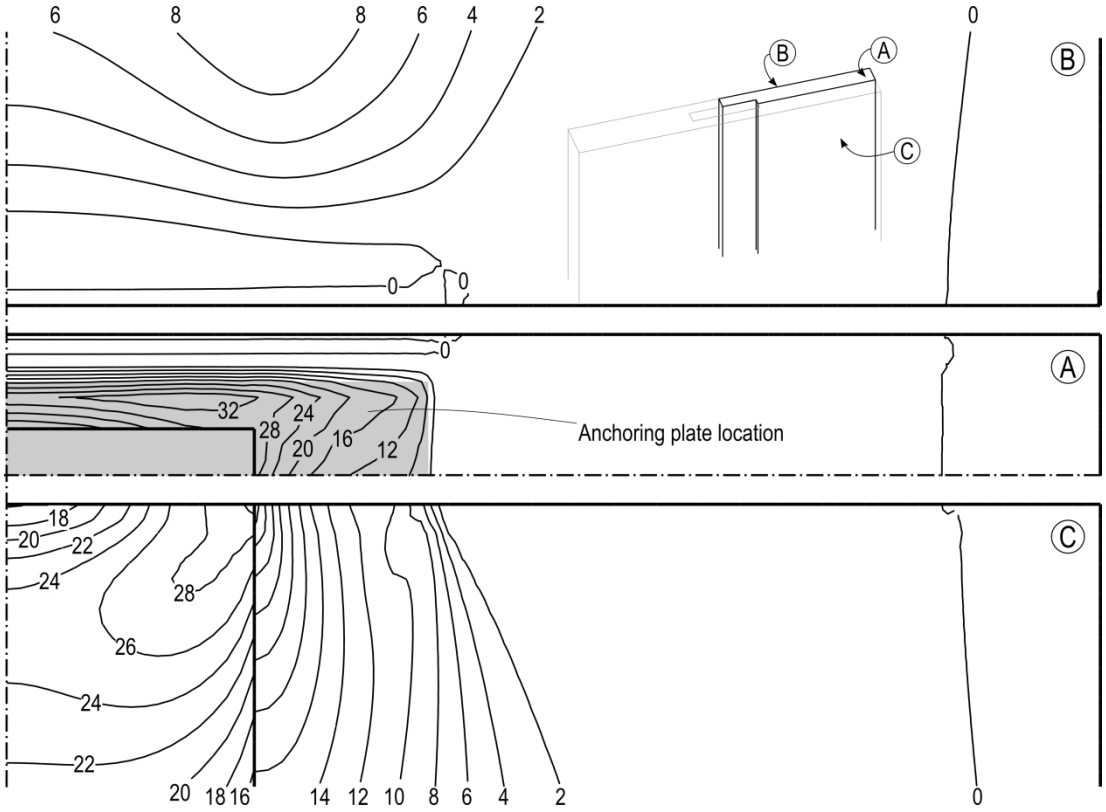

Figure C-7. Wall parallel-to-grain axial stress fields (in MPa) for the anchorage option 4.

It must be noted that this stress concentration is strongly influencing the long-term behaviour of the section by increasing the vertical displacement due to linear and non-linear creep which results in more significant post-tensioning losses. The NMIT building is an example of this design case as highlighted by monitoring results carried out by Morris et al. (2012) who observed a post-tensioning loss of up to 20% over a period of 18 months.

When looking at the compressive stress distribution in the "weak" perpendicular to the grain direction (i.e. Z direction in Figure C-2b,c) Options 1 and 2 show minor compression to the grain stresses.

As shown in Figure C-8c,d some tension perpendicular to the grain develops for Options 3 and 4. This is due to the reduced bearing surface which develops some bending stresses in the external layers of the wall's section. In particular, Figure C-8c,d shows maximum values of 0.51 and 1.1MPa.

Although no perpendicular-to-grain tension strength data is provided by the manufacturers (Nelson Pine Industries Limited, 2012), tension strength in the perpendicular to the grain direction generally ranges from 0.4 to 0.8 in accordance with AS 1720.1 (2010). In particular, for radiata pine the nominal tension perpendicular-to-grain strength is 0.5MPa; therefore, the observed values are above the elastic limit of the material and some local reinforcing is needed.

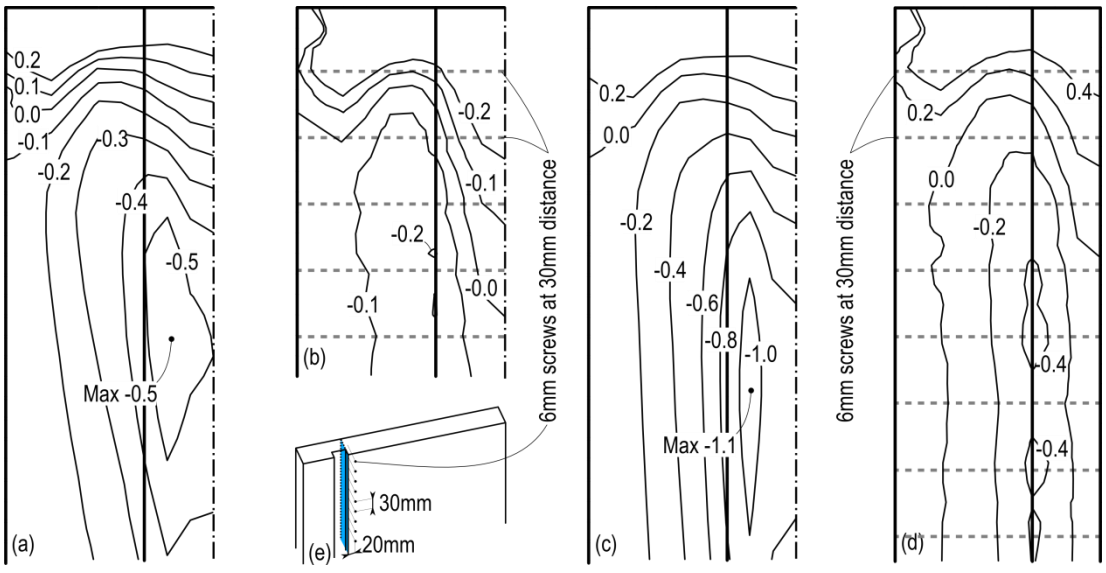

Figure C-8. Perpendicular-to-grain axial stress fields (tension is negative). Option 3 (a) without and (b) with screw reinforcement. Option 4 (c) without and (d) with screw reinforcement. (e) Model sketch indicating the section plane positon and screw reinforcement.

The Finite Element Model analysis was carried out for the anchorage Options 3 and 4 implementing some screw reinforcement as shown in Figure C-8e. To overcome the perpendicular-to-grain tension issue a row of twelve 6mm diameter fully threaded screws were used to reinforce the hole. The screws were spaced 30mm from the top edge and between each other and 20mm from the void.

From the analysis results shown in Figure C-8b,d it can be observed that the screw reinforcement results in a significant decrease in perpendicular to the grain tension stresses. As the stress distributions show, maximum tension stress values of 0.21MPa and 0.45MPa occur at the critical section which are now within the elastic values in accordance to AS 1720.1 (2010).

C.3 Discussion

The simplified design of the post-tensioning anchorage steel plate was presented in this section assuming a uniform pressure over the bearing surface. Finite Element analyses confirmed that this design approach can be used when the plate's bearing area is over the full width of the wall. When a narrower plate is used, some bending stresses in the external layers of the wall section develops and results in tension perpendicular to the grain. This can exceed the material strength and some screw reinforcement is needed as shown in previous sections.

C.4 References

Brown, A., Lester, J., Pampanin, S., Pietra, D. 2012. Pres-Lam in practice - A damage-limiting rebuild project. *New Zealand Society of Structural Engineers Conference*, Auckland, New Zealand.

Devereux, C., Holden, T., Buchanan, A., Pampanin, S. 2011. NMIT Arts & Media Building-Damage Mitigation Using Post-tensioned Timber Walls. *PCEE Conference*, Auckland, New Zealand.

Morris, H., Wang, M., Zhu, X. 2012. Deformation and loads in an LVL building with 3-storey post-tensioned shear walls. *World Conference on Timber Engineering*, Auckland, New Zealand.

Nelson Pine Industries Limited. 2012. *Specific Engineering Design Guide*. Technical report NPIL/LVL 04, Nelson Pine Industries Limited. Richmond, Nelson, New Zealand.

Palermo, A., Sarti, F., Baird, A., Dekker, D. 2012. From theory to practice: design, analysis and construction of dissipative timber rocking post-Tensioning wall system for Carterton

Events Centre, New Zealand. *World Conference on Earthquake Engineering*, Lisbon, Portugal.

Simulia. 2011. *Abaqus 6.11-2*. Simulia. Providence, RI, USA.

Standards Australia 2010. *Timber structures - Part 1: Design methods*, Standards Australia.

van Beerschoten, W.A., Carradine, D.M., Carr, A. 2014. Development of constitutive model for laminated veneer lumber using digital image correlation technique. *Wood Science and Technology* 48(4): 755-772.

Appendix D: Experimental test setup technical drawings

The technical drawings of the test setup and testing specimens tested as part of the experimental programs shown in Chapters 5 and 6 are here reported. The list of technical drawings is reported below:

1. Test setup (single wall)
2. Test setup (Column-Wall-Column system)
3. Test setup – reaction frame struts
4. LVL wall and boundary elements
5. External dissipaters (fused bar details)
6. Dissipater anchorage
7. U-shaped Flexural Plates
8. U-shaped Flexural Plate Anchorage
9. Column connection
10. Concrete foundation (reinforcement details)
11. Concrete foundation (steel base plate)

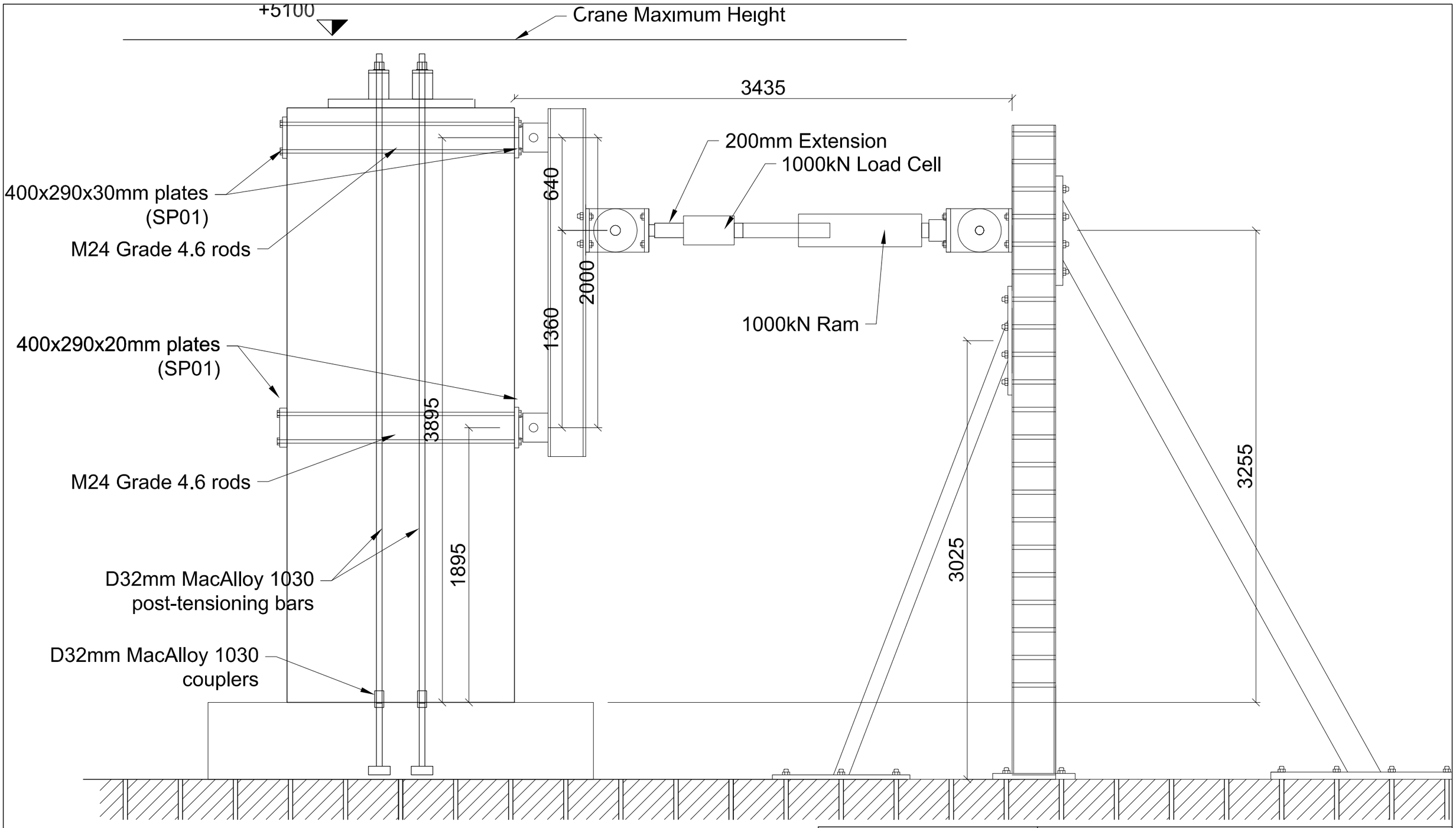

UNIVERSITY OF CANTERBURY
Te Whare Wānanga o Waitaha
CHRISTCHURCH NEW ZEALAND

Title	Test Setup	
By	Francesco Sarti	
Rev.	1	PT bar position, PT plates dimension
	2	
	3	
Date: 06/03/2013		Scale: -
Units: mm		Drawing no.: 1/11

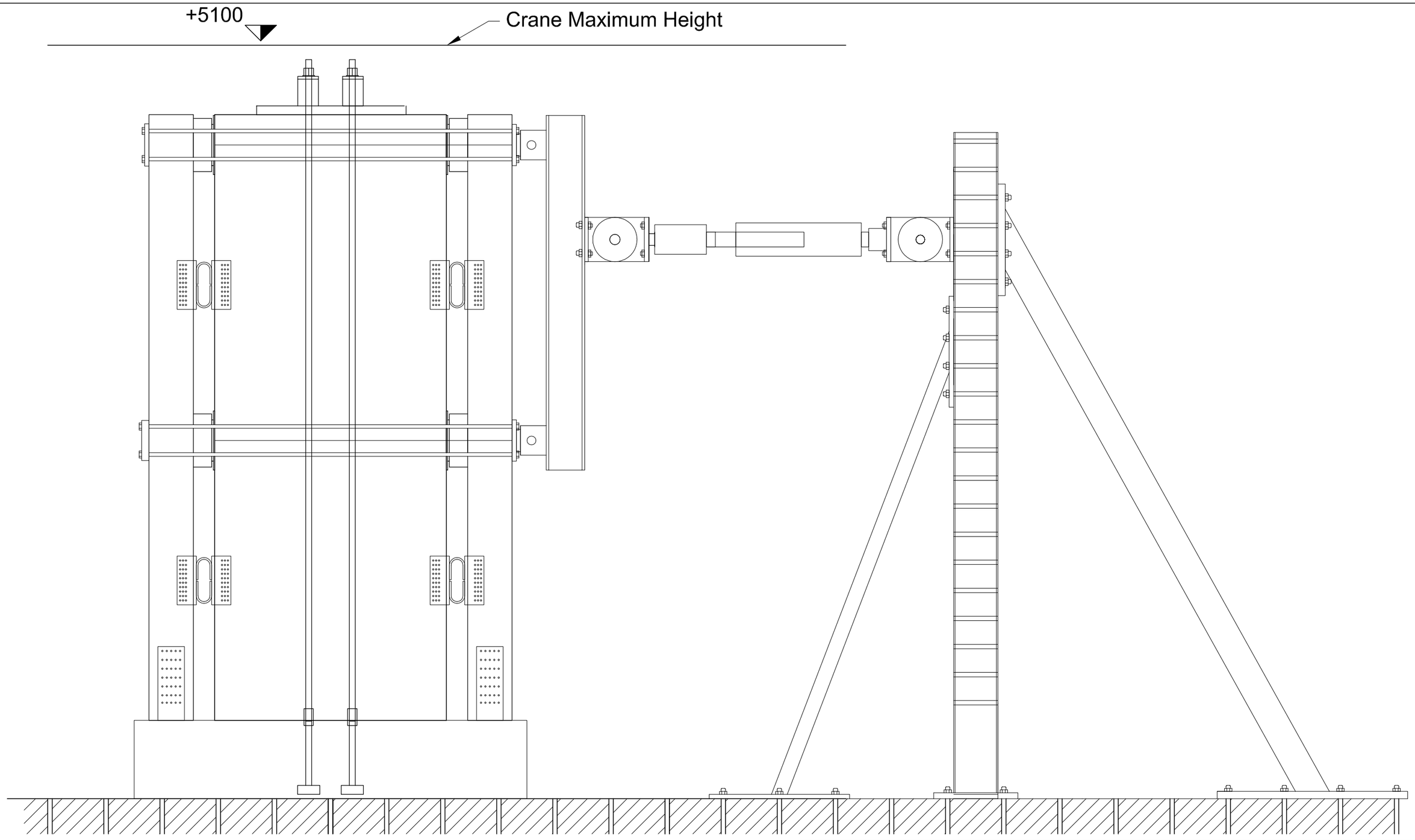

UNIVERSITY OF CANTERBURY
Te Whare Wānanga o Waitaha
CHRISTCHURCH NEW ZEALAND

Title	Test Setup - CWC System	
By	Francesco Sarti	
Rev.	1	PT bar position, PT plates dimension
	2	
	3	
Date: 06/03/2013		Scale: -
Units: mm		Drawing no.: 2/11

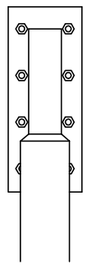

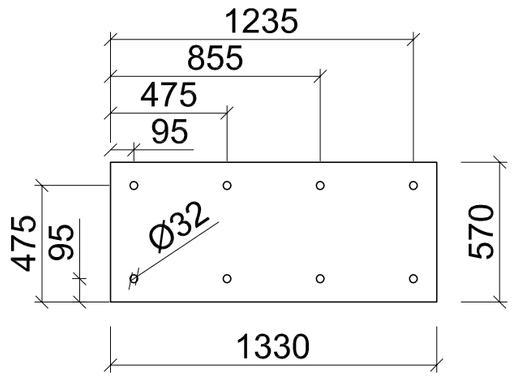

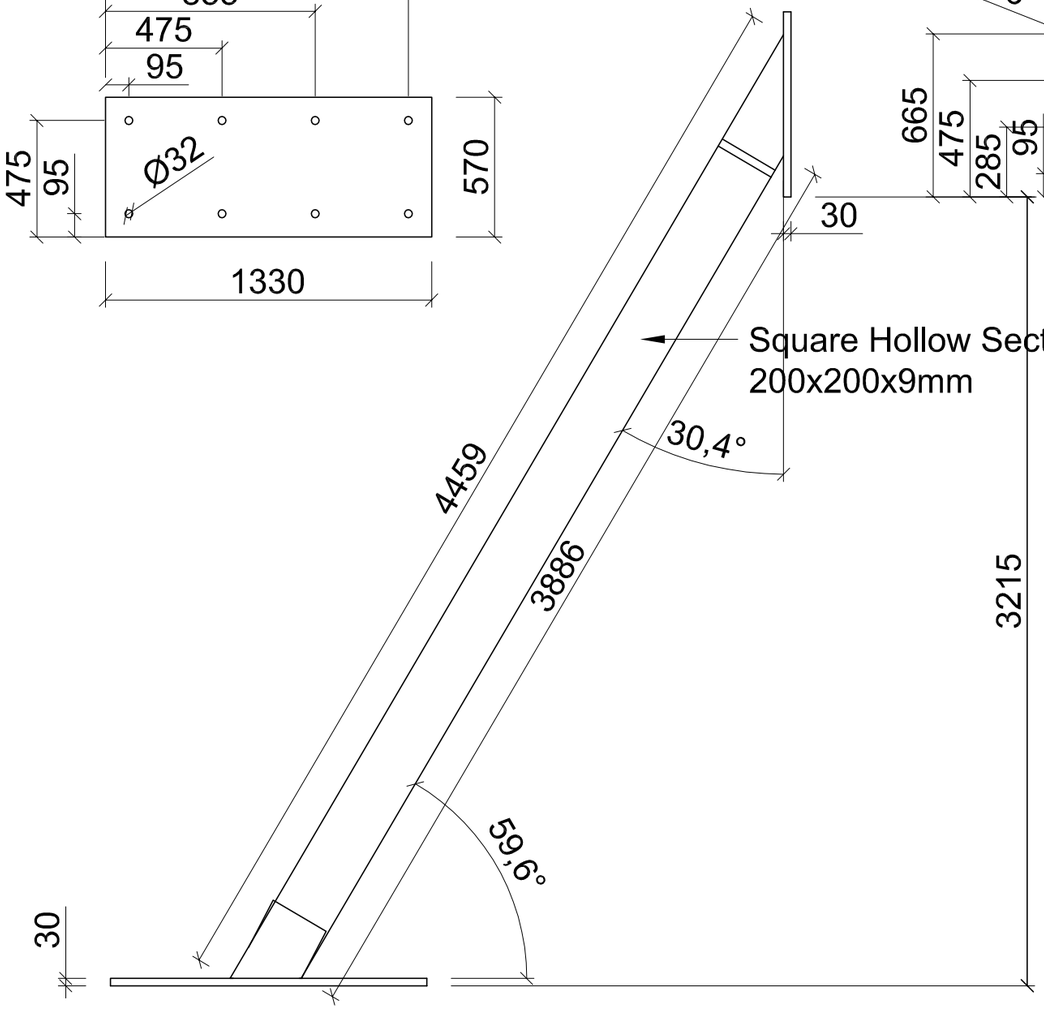

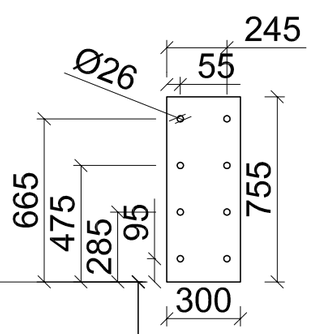

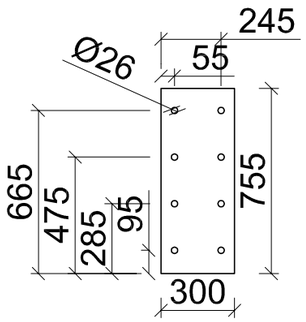

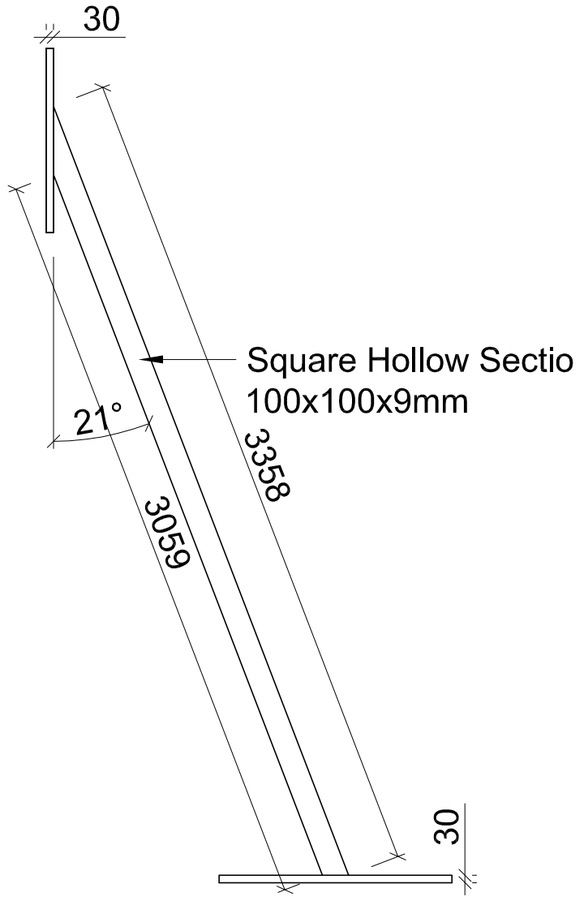

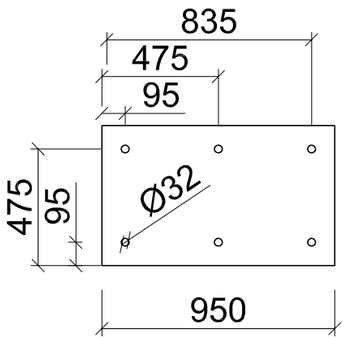

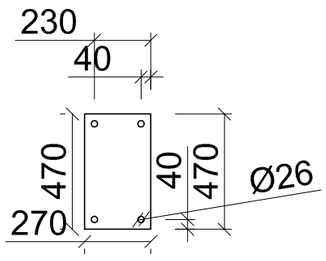

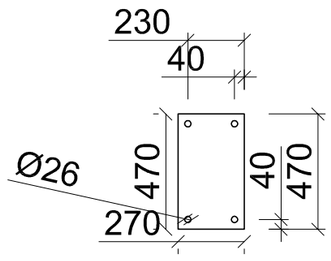

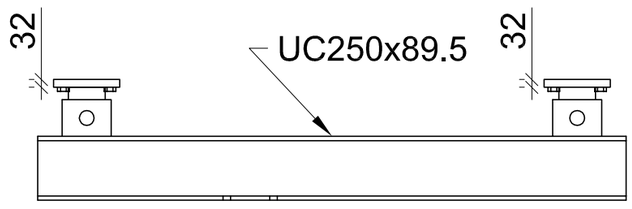

UNIVERSITY OF CANTERBURY
Te Whare Wānanga o Waitaha
CHRISTCHURCH NEW ZEALAND

Title	Test Setup - Reaction frame struts	
By	Francesco Sarti	
Rev.	1	PT bar position, PT plates dimension
	2	
	3	
Date: 06/03/2013		Scale: -
Units: mm		Drawing no.: 3/11

Side View

Wall (1:20)

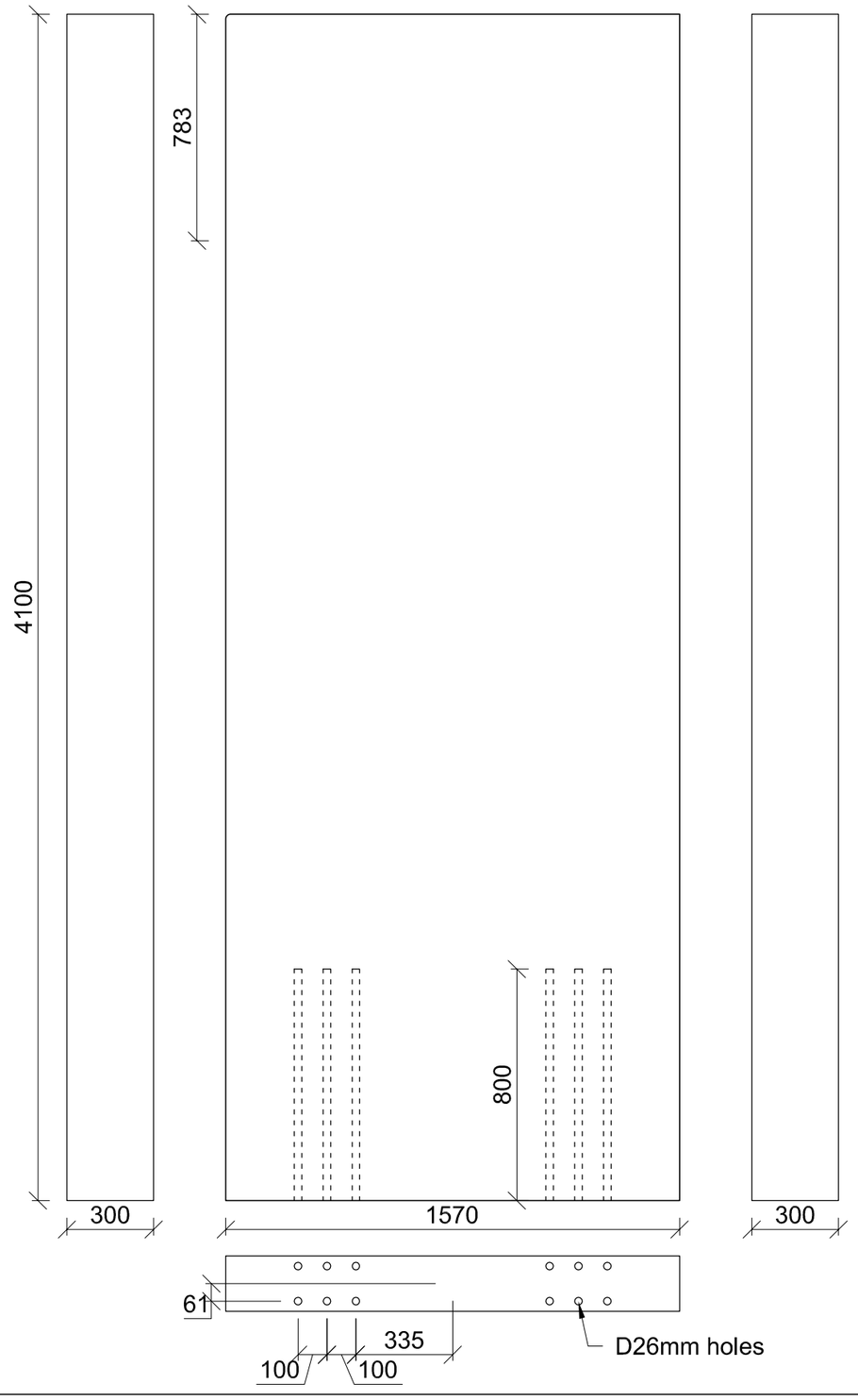

Plan View

Wall Section (1:10)

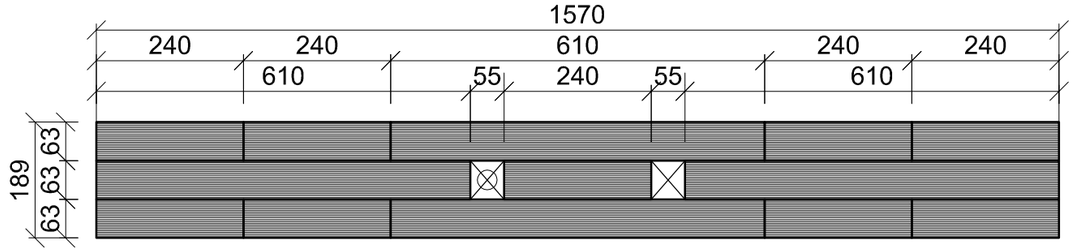

Plan View

Boundary element (1:10)

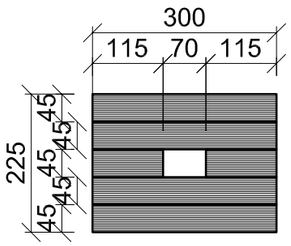

UNIVERSITY OF CANTERBURY
Te Whare Wānanga o Waitaha
CHRISTCHURCH NEW ZEALAND

Title	LVL Wall and boundary elem.	
By	Francesco Sarti	
Rev.	1	Revised dimensions
	2	
	3	
Date: 17/01/2013		Scale: 1:10, 1:20
Units: mm		Drawing no.: 4/11

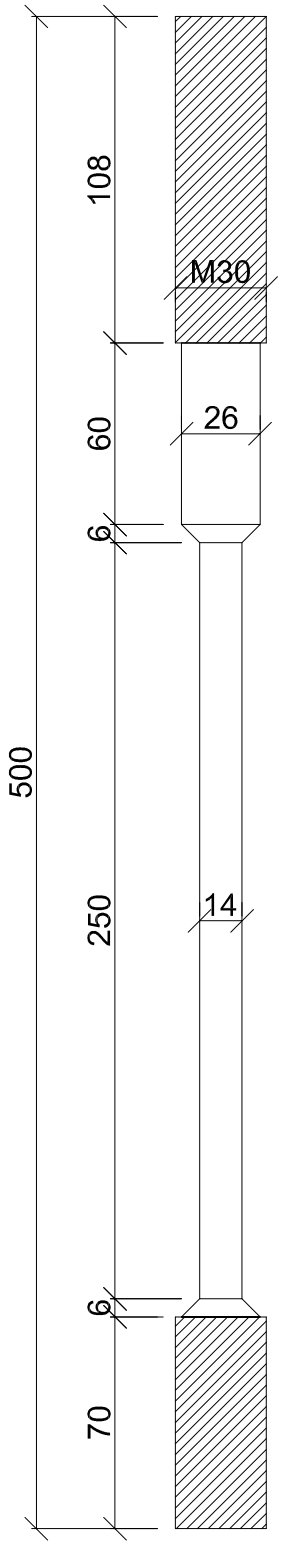

UNIVERSITY OF CANTERBURY
Te Whare Wānanga o Waitaha
CHRISTCHURCH NEW ZEALAND

Title	External Dissipater Fused bar details	
By	Francesco Sarti	
Rev.	1	
	2	
	3	
Date: 18/02/2012		Scale: -
Units: mm		Drawing no.: 5/11

Side View 1
(1:2)

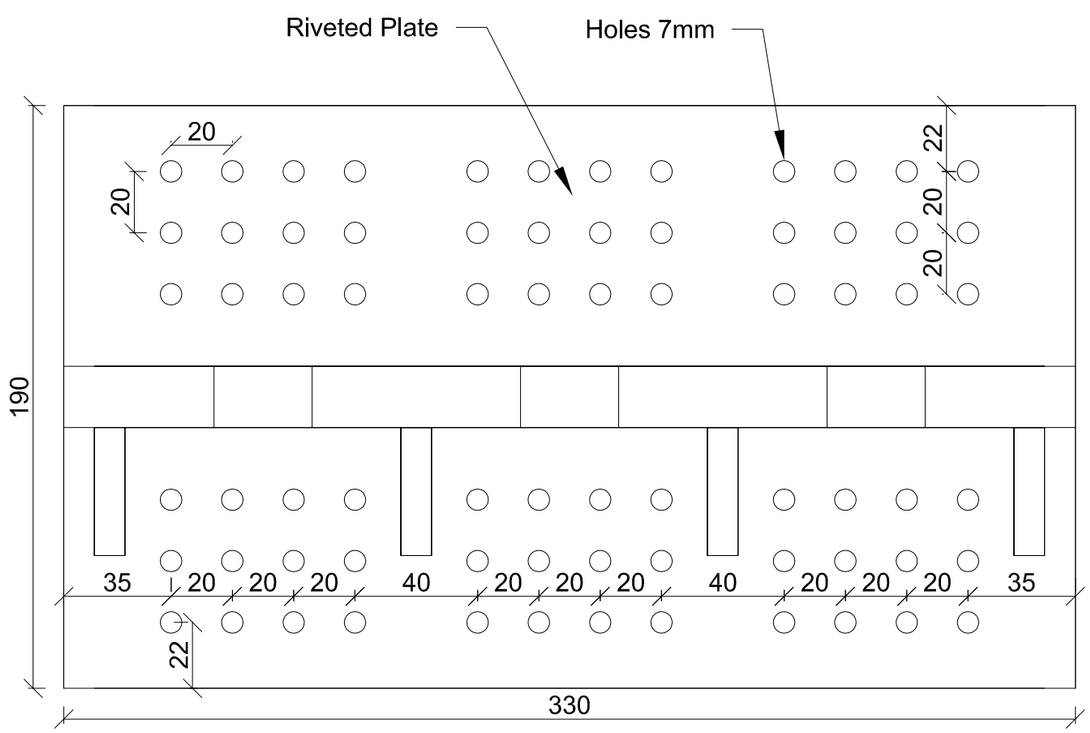

Side View 2
(1:2)

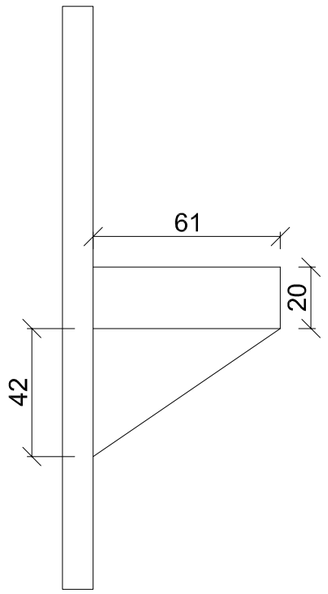

3D View

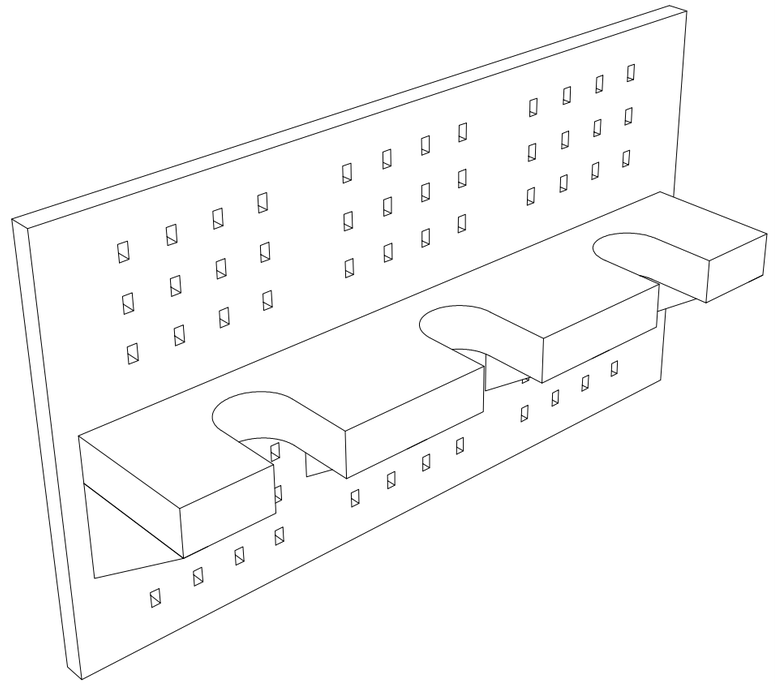

Plan View
(1:2)

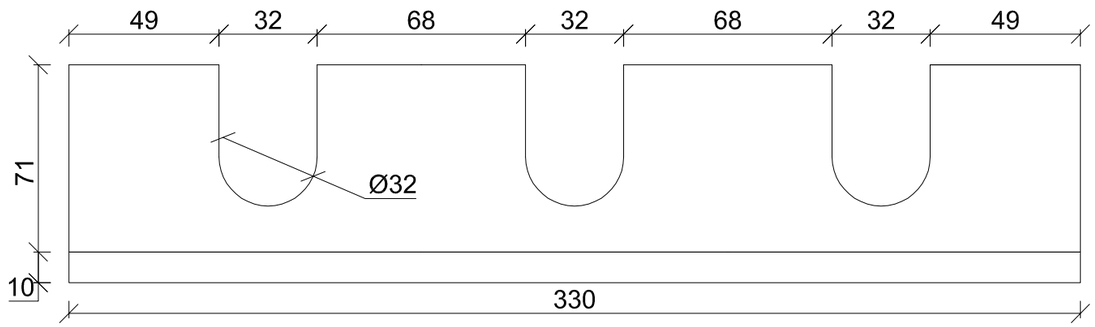

UNIVERSITY OF CANTERBURY
Te Whare Wānanga o Waitaha
CHRISTCHURCH NEW ZEALAND

Title	Dissipater anchorage	
By	Francesco Sarti	
Rev.	1	
	2	
	3	
Date: 21/11/2012		Scale: 1:5, 1:10
Units: mm		Drawing no.: 6/11

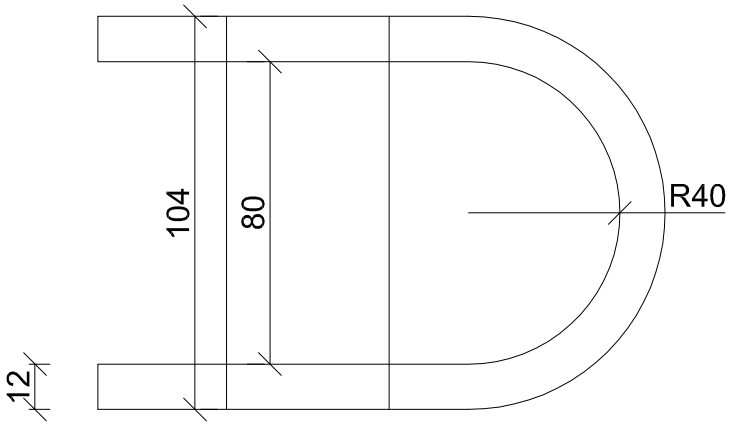

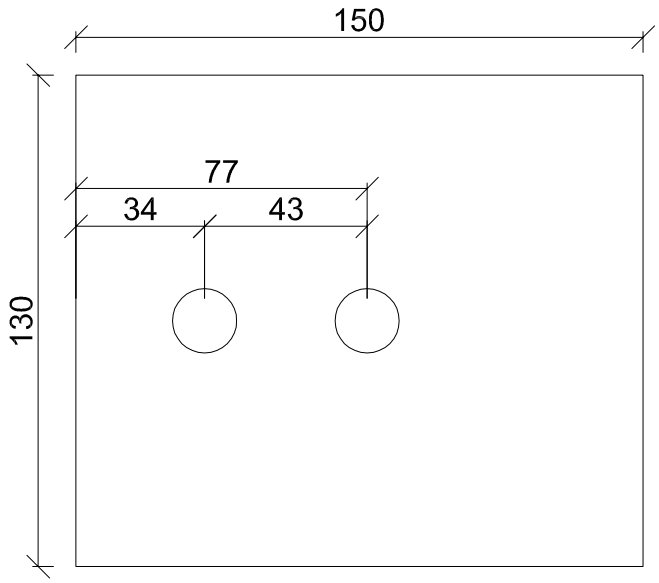

NOTES

- Grade250 Steel

UNIVERSITY OF CANTERBURY
Te Whare Wānanga o Waitaha
CHRISTCHURCH NEW ZEALAND

Title	U-Shaped Flexural Plate	
By	Francesco Sarti	
Rev.	1	
	2	
	3	
Date: 14/03/2013		Scale: 1:2
Units: mm		Drawing no.: 7/11

Side View 1
(1:2)

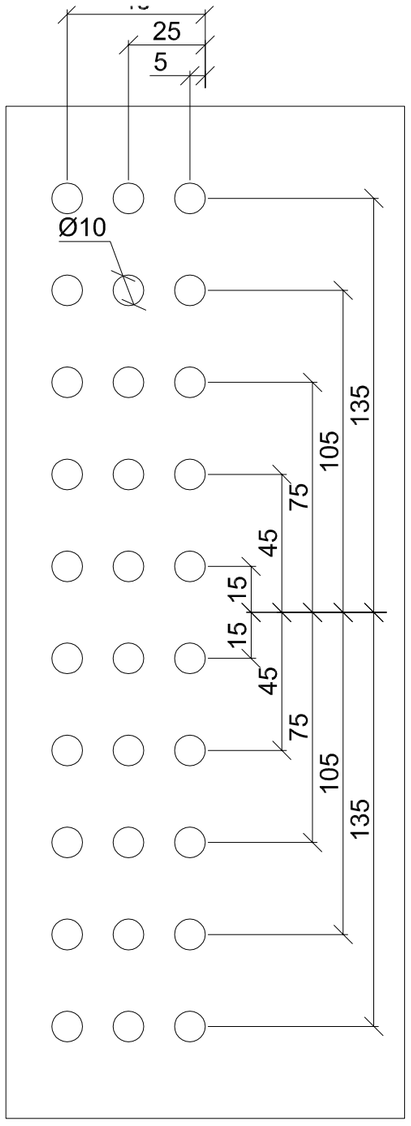

Side View 2
(1:2)

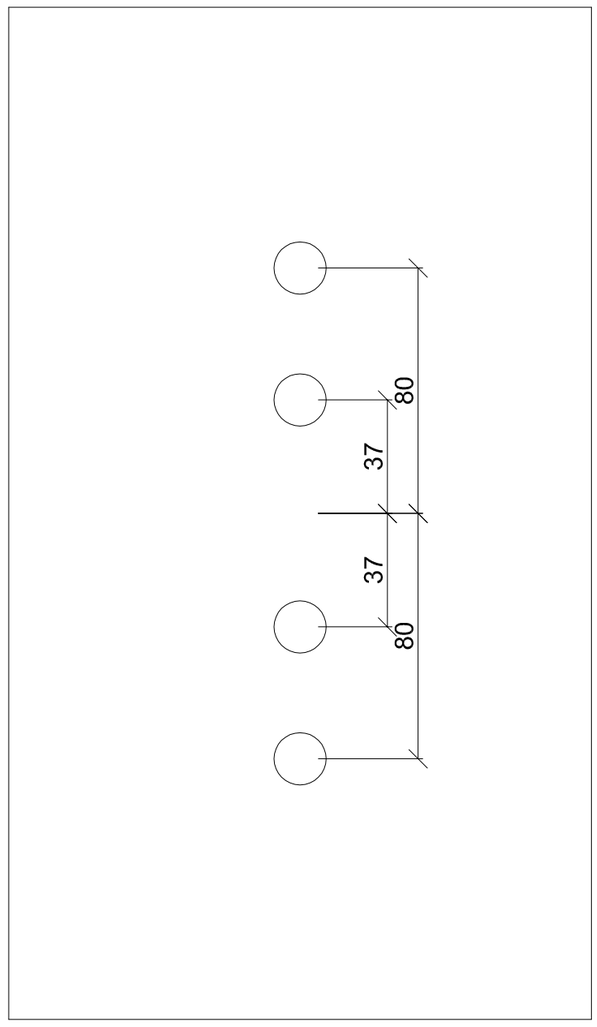

3D View

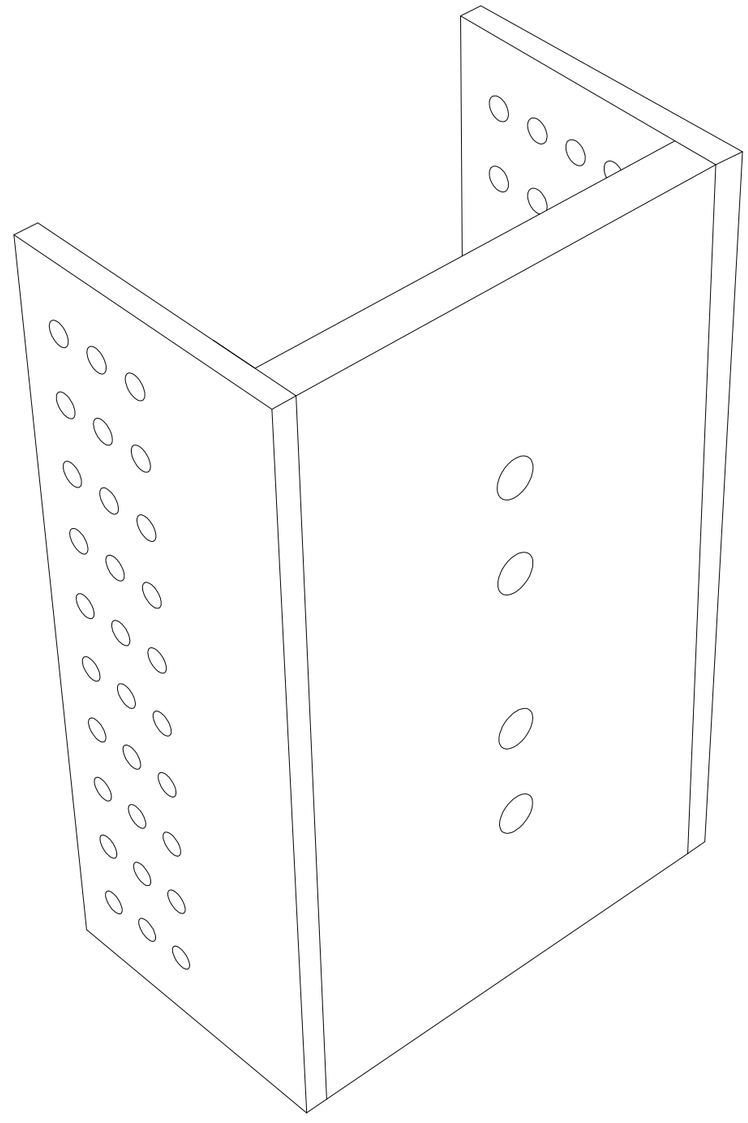

UNIVERSITY OF CANTERBURY
Te Whare Wānanga o Waitaha
CHRISTCHURCH NEW ZEALAND

Title	UFP anchorage	
By	Francesco Sarti	
Rev.	1	
	2	
	3	
Date: 24/05/2013		Scale: 1:2
Units: mm		Drawing no.: 8/11

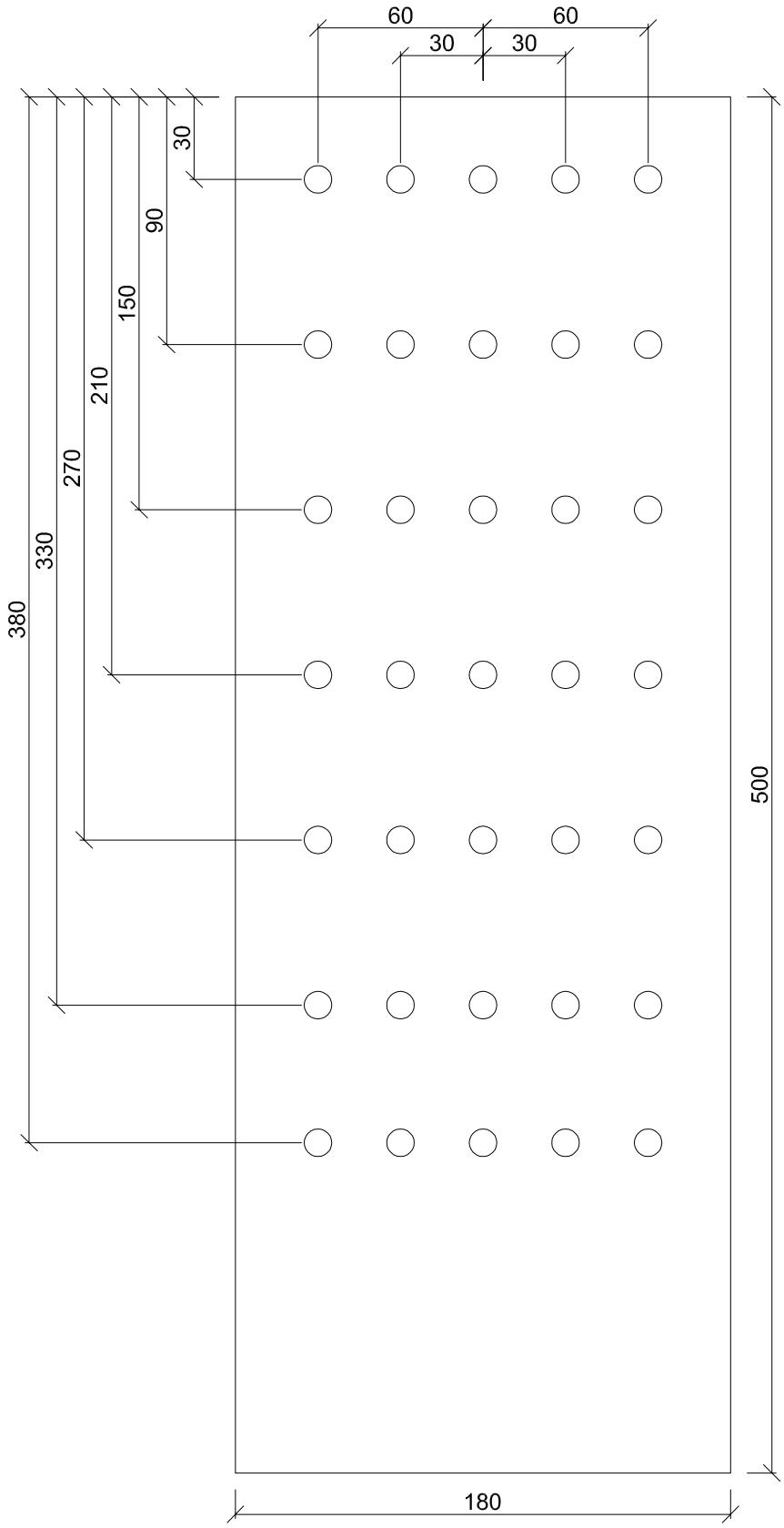

UNIVERSITY OF CANTERBURY
Te Whare Wānanga o Waitaha
CHRISTCHURCH NEW ZEALAND

Title	Column Anchorage	
By	Francesco Sarti	
Rev.	1	
	2	
	3	
Date: 14/03/2013		Scale: -
Units: mm		Drawing no.: 9/11

Plan View

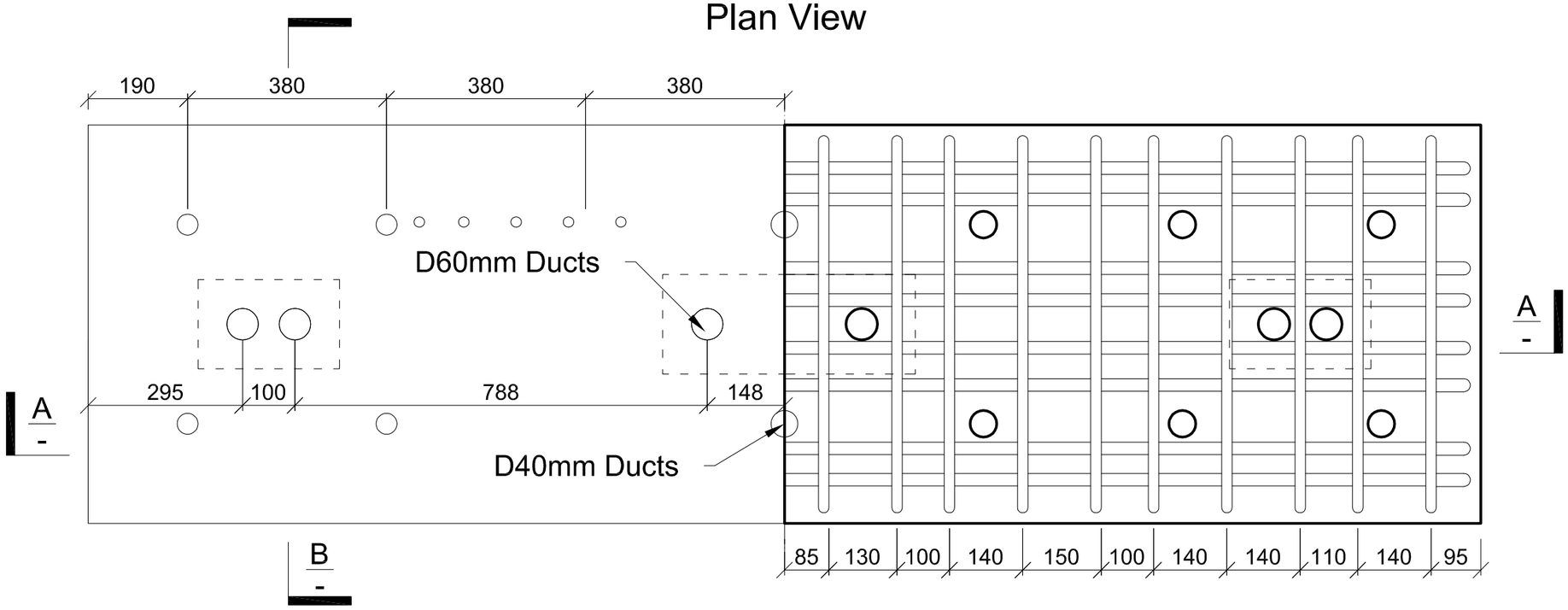

Section B

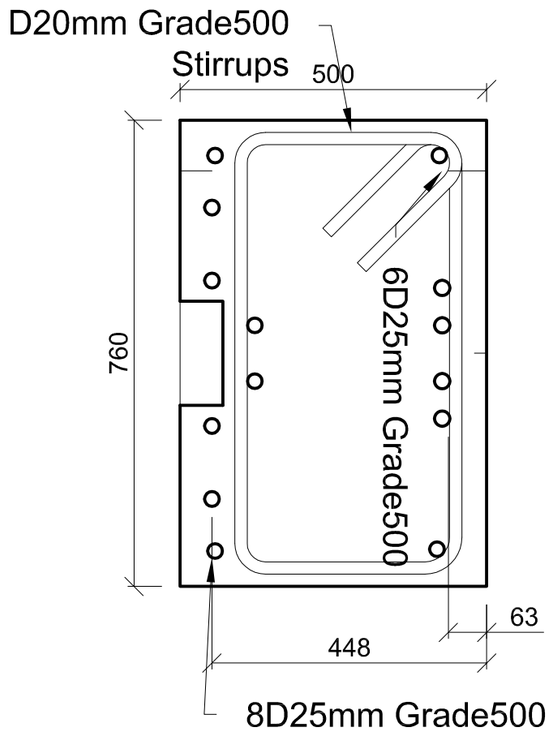

Section A

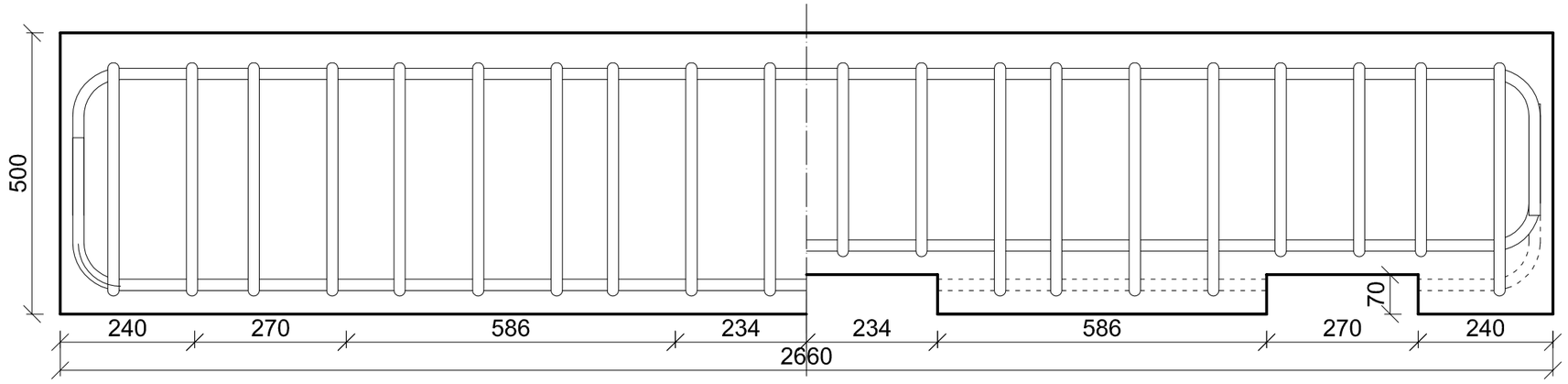

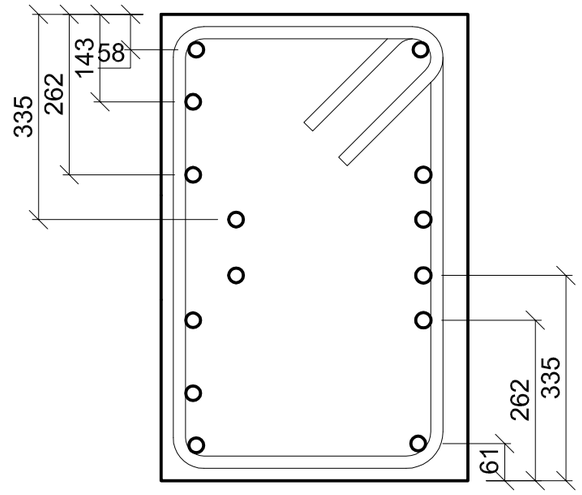

NOTES:

- All reinforcements are Grade500
- Quantitaives
  - Longitudinal 14xD25mmx3000mm
  - Transversal 20xD20mmx2700mm

UNIVERSITY OF CANTERBURY
Te Whare Wānanga o Waitaha
CHRISTCHURCH NEW ZEALAND

Title	Concrete foundation (reinforcement details)	
By	Francesco Sarti	
Rev.	1	
	2	
	3	
Date: 08/11/2012		Scale: 1:10
Units: mm		Drawing no.: 10/11

Plan view

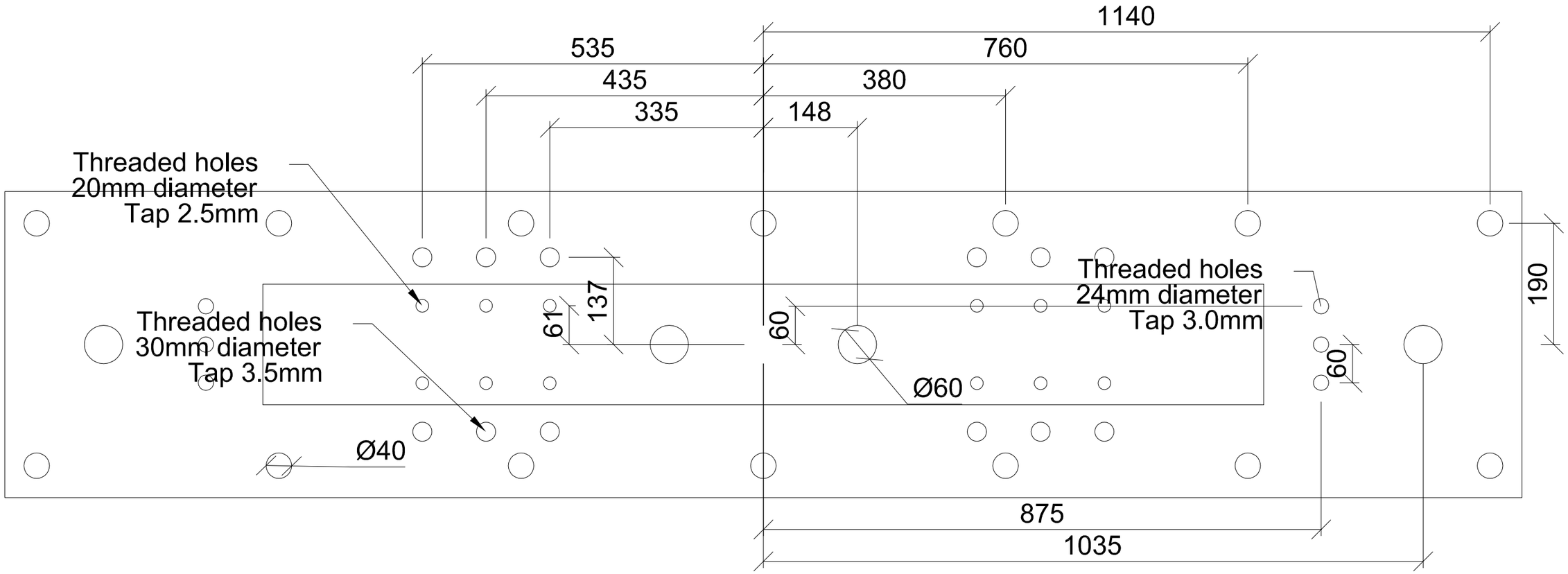

UNIVERSITY OF CANTERBURY
Te Whare Wānanga o Waitaha
CHRISTCHURCH NEW ZEALAND

Title	Concrete foundation (steel base plate)	
By	Francesco Sarti	
Rev.	1	Holes position final
	2	
	3	
Date: 27/11/2012		Scale: -
Units: mm		Drawing no.: 11/11